TRIBO-OXIDATION OF STEELS

BY

PETER MILLS B.Sc.

A thesis submitted for the degree of

DOCTOR OF PHILOSOPHY

THE UNIVERSITY OF ASTON IN BIRMINGHAM

SEPTEMBER 1984

DEDICATED

TO

DAWN

THE UNIVERSITY OF ASTON IN BIRMINGHAM

TRIBO-OXIDATION OF STEELS

By PETER MILLS

A thesis submitted for the degree of

DOCTOR OF PHILOSOPHY

1984

Summary

The present study is concerned with the oxidational wear of EN8 low alloy steel under unlubricated, unidirectional sliding conditions. Wear tests were conducted at various loads and sliding speeds using a pin on disc wear machine in which wear rate, frictional force and pin and disc temperatures were monitored. Wear debris and worn surfaces were examined by means of x-ray diffraction. Scanning electron microscopy was used to gain topographical information of the worn surfaces and also to directly measure the thickness of surface oxide films. Particular emphasis was placed on the analysis of surfaces by Auger electron spectroscopy and x-ray photoelectron spectroscopy, both techniques having been used in conjunction with argon ion etching.

Results of the analyses indicated that the oxide films on the worn surfaces were physically homogeneous films which grew separately on the pin and disc surfaces. Furthermore, transitions in the wear rate versus load curves which were observable at certain critical loads were found to be associated with a change in oxide composition: oxide films consisting predominantly of Fe_3O_4 were found to have greater wear protective properties than those which consisted mainly of αFe_2O_3 or FeO.

A theoretical surface model was used which enabled the contact temperature and the number and size of the asperity contacts to be deduced. Excellent correlation between contact temperatures and the composition of the surface oxides indicated that the contact temperature, and not the much lower general surface temperature, governed the growth of oxide films during wear.

A method was devised for calculating values of activation energy (Qp) and Arrhenius constant (Ap) applicable to tribo-oxidation. Comparison of these values with those relevant to oxidation under static oxidizing conditions indicated that Qp was approximately the same in both cases, but Ap values were much greater in the case of tribo-oxidation.

Wear/Low Alloy Steel/Oxidation/Electron Spectroscopy

ACKNOWLEDGEMENTS

I would like to extend my thanks to my project supervisor, Mr.J.L.Sullivan, for his continued advice and encouragement which was offered throughout the work contained in this thesis.

I am grateful to Mr.A.Abbot and Mr.H.Arrowsmith for their technical assistance. I would like to thank Professor W.E.J.Neal, Head of the Department of Physics, in whose laboratories the majority of the work was conducted. Thanks are also due to the Department of Metallurgy for the liberal use of their facilities.

Financial support for the project was provided by the Science and Engineering Research Council, which I gratefully acknowledge.

I am grateful to Mrs.A.Howell for the typing of the thesis.

I thank my family for their continued interest and encouragement.

Last, but by no means least, I would like to thank my wife for the considerable work carried out in preparing the final diagrams, for her continued support, and for the many sacrifices made.

CONTENTS

FIGURES

TABLES

CHAPTER 1

INTRODUCTION

1.1 Background to the Work

The removal of material from the surfaces of moving mechanical parts which rub against each other constitutes wear of those surfaces. Obviously it is economically desirable to minimize wear in order to prolong the working lifetime of machinery. The presence of an oxide film on rubbing surfaces is one such factor which will often result in a reduction in wear rate, and also in the frictional force between the surfaces. In view of the fact that this reduction in wear rate will typically be a few orders of magnitude, the presence of protective oxide films on rubbing surfaces is highly desirable. However, before we can promote the formation of wear protective oxides, for example by design considerations or surface coatings, it is first necessary to know something of how the oxide films form. In lubricated conditions the oxide films are produced by a chemical reaction between the metal surfaces and the lubricating oil, oil additives, or dissolved oxygen, whereas under dry, unlubricated conditions the oxides form due to a reaction of the metal surfaces with the atmosphere. This atmospheric oxidation may occur at the ambient temperature of the rubbing surfaces, or it may occur at elevated temperatures produced by frictional heating. At present there is still no general agreement on the mechanism of oxide formation and removal, but this is probably partly due to the existence of more than one mechanism, corresponding to differences in mechanical

configuration, type of motion, temperature, load, speed, atmosphere etc., rather than one theory being universally correct. It is the aim of this project to study the mild wear of low alloy steel produced when a horizontal pin is pressed against one face of a vertical rotating disc, with particular emphasis placed on examination of the surface oxides.

1.2 The Oxidation of Metals

1.2.1 General Considerations

The overall driving force behind the reaction of a metal surface with oxygen is the free energy change associated with the formation of the oxide from the reactants. Thermodynamically, the ambient oxygen pressure must be larger than the dissociation pressure of the oxide in equilibrium with the metal in order that the oxide will be formed. Although the free energy change is the driving force it has little bearing on the rate of reaction, this being a kinetic problem. Reaction rates are governed by the slowest step in the reaction mechanism, and the particular mechanism of oxidation which operates will depend upon the physical, chemical and structural properties of the metal and the oxide as well as the specific oxidation conditions.

1.2.2 Initial Stages of Oxidation

The first stage in the oxidation of a true clean metal surface involves the adsorption of oxygen onto the surface, after which rearrangement and incorporation of oxygen into

the metal surface results in some type of oxygen-metal structure (1). The next stage involves the appearance of a number of nuclei on the metal surface (2), which may be due to precipitation when the local concentration of oxygen in the metal surface has reached a critical value (1 , 2), or to the presence of defect sites on the surface (1 , 2). Surface diffusion of matter towards the nuclei occurs so that they grow laterally until the entire surface is covered (1 , 2). This is followed by the growth of an oxide layer on the surface. The metal and oxygen are now separated by an oxide film so that transport of oxygen or metal, or both, through the film must occur in order for the reaction to continue.

1.2.3 Growth of Thin Films

The distinction between thin films, generally formed at relatively low temperatures or in the initial stages of thick film formation, and thick films, formed at higher temperatures, is necessarily arbitrary, but for convenience the boundary between the two is often considered to be a thickness of around a few thousand Angstroms e.g. (3 , 4). Many theories of thin film growth, however, are only applicable for very much thinner films e.g. (5).

The growth of an oxide film on a metal surface at relatively low temperatures is most often characterized by an oxidation rate which is initially very rapid, but which slows down quickly, often becoming negligibly slow. The rate laws which give the best description of such behaviour are direct logarithmic and inverse logarithmic laws.

The Cabrera and Mott theory (5) of thin film formation has been regarded as authoritative for many years, and has formed the basis for many other theories of low temperature oxidation. In their theory they proposed that electrons from the metal are able to travel through the thin oxide film by tunneling in order to fill traps produced by the adsorption of oxygen on the oxide surface. The oxygen ions so produced set up a strong electric field which decreases the activation energy for cation migration through the film. The rate-determining step of the reaction is considered to be the passage of ions into the oxide at the metal/oxide interface. The theory leads to an inverse logarithmic rate law for the oxide thickness x after time t, namely:

$$\frac{1}{x} = A - B\ln(t) \qquad (1.1)$$

where A and B are constants.

More recently Fehlner and Mott (6) have updated the theory of Cabrera and Mott (5) to include anion migration as well as cation migration. The basic assumptions are the same as those proposed in the earlier work but in the case of anion migration it is assumed that there is a constant field, rather than the constant potential across the oxide assumed for cation migration. This arises from the fact that in oxide films which are growing by anion migration the field creating ions and migrating ions are the same. This leads to a direct logarithmic rate law.

Many other theories based on the electric field induced transport of ions through a thin oxide film have been

proposed, and which differ according to the assumed rate-determining process. An inverse logarithmic rate law has been derived by Hauffe (7), and also by Fromhold and Cook (8), on the assumption that the rate-determining process is the transport of ions through the film. Direct logarithmic rate laws have been proposed on the assumption that the rate-determining process is the transport of electrons through the oxide film (Mott (9), Fromhold and Cook(8)), or the chemisorption of oxygen at the oxide surface (Landsberg (10), Ritchie and Hunt (11)). These are only a few examples of the many theories of logarithmic oxidation which have been proposed.

The Cabrera-Mott theory (5) of logarithmic oxide growth is only applicable for oxide films of around 100 Å or less, but Cabrera and Mott (5) have shown that the same basic assumptions can be used in the case of thicker films of up to 2000 Å thickness. In this case, however, the electric field across the film is much weaker and the velocity of the charge carriers becomes proportional to the field (5). This leads to a parabolic rate law for n-type oxides, not to be confused with the very different Wagner theory (12) of thick film parabolic oxidation, and a cubic rate law for p-type oxides. Electron transport by tunneling is replaced by thermionic emission for the thicker films produced at slightly higher temperatures (13).

So far the theories discussed assume the existence of a uniform plane-parallel oxide film. However, many theories of thin film logarithmic oxidation are based on the existence of pores or cavities, and it is worth mentioning these since

the previously discussed theories of logarithmic oxide growth cannot explain logarithmic growth in any but the lowest part of the thin film range (1).

Davies et al (14) proposed a model in which it is assumed that ions diffuse preferentially along paths of low-resistance such as grain boundaries or dislocations. The formation of fresh oxide is considered to cause blockage of neighbouring pores through compressional stress. This leads to a direct logarithmic law, given by:

$$x = A \ln (Bt + 1) \qquad (1.2)$$

where A and B are constants. Evans (15) considered the case in which blockage only occurs in the paths in which the fresh oxide is formed, and this led to an asymptotic rate law. Harrison (16) has treated the case of simultaneous self-blockage and mutual blockage. Evans (15) also proposed a model in which only part of the oxide thickens due to the formation of cavities at the base of the oxide. This can occur when the mechanism of cation transport is via vacancies since the vacancies will accumulate at the metal/oxide interface. A logarithmic rate equation was obtained.

1.2.4 Growth of Thick Films

The growth of oxide on a metal surface at a relatively high temperature which results in the formation of a compact scale will often follow a parabolic rate law (17). In 1933 Wagner (12) developed his theory of parabolic oxidation and this has since become the most well known and thoroughly tested theory of parabolic growth of oxide films at high

temperatures.

Before outlining Wagner's theory it is first instructive to consider the mechanism by which metal and oxygen are able to travel through the growing oxide scale. It is now well established that the diffusion of material through the lattice of a thick oxide scale is associated with the nature of point defects present in the lattice (17 , 18 , 19). Point defects comprise interstitial ions and vacant lattice sites. Nonstoichiometric oxides containing either interstitials or vacancies will also contain electrons or electron defects in order to preserve electrical neutrality. Electrons may be free, while electrons or holes may be associated with cations or anions in normal lattice positions. In the latter cases transport of electrons occurs by an interchange between two cations or two anions of different valency. The different types of oxide, which are illustrated in figure 1.1, can be conveniently classified according to the nature of the defects present in the oxide lattice as follows (17):

(i) Metal excess semiconductors contain interstitial cations plus electrons. Cationic transport occurs via interstials (figure 1.1(a)).

(ii) Anion deficit semiconductors contain anion vacancies plus electrons. Anionic transport occurs via anion vacancies (figure 1.1(b)).

(iii) Metal deficit semiconductors contain cation vacancies plus electron defects. Cationic transport occurs via cation vacancies (figure 1.1(c)).

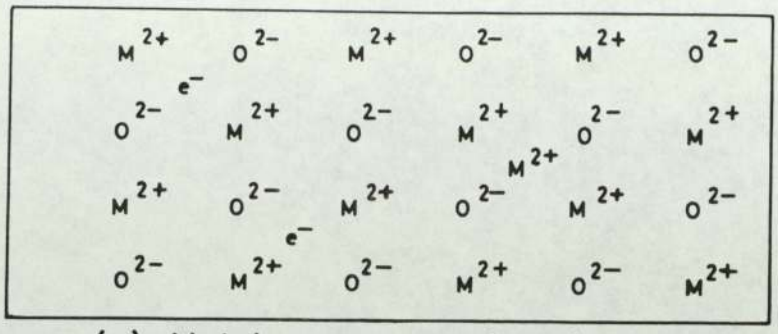

(a) Metal excess semiconductor

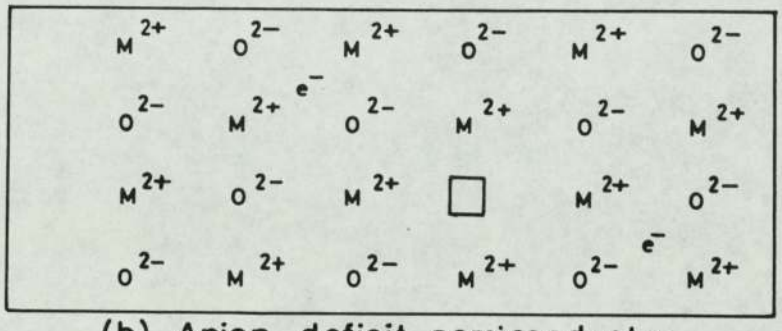

(b) Anion deficit semiconductor

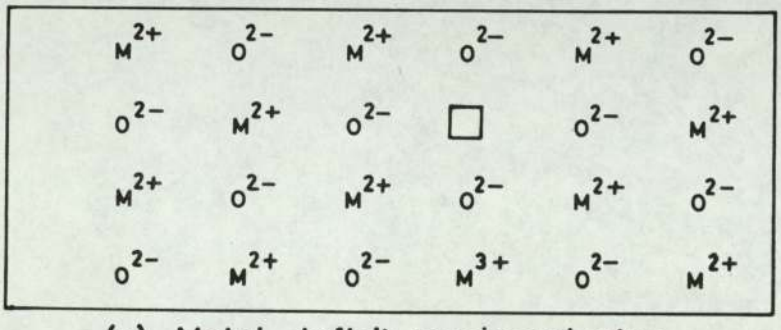

(c) Metal deficit semiconductor

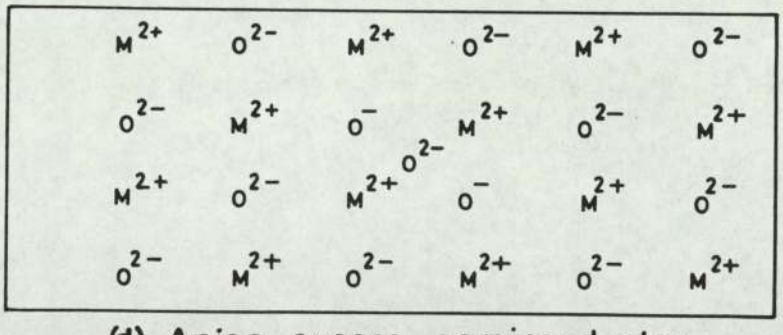

(d) Anion excess semiconductor

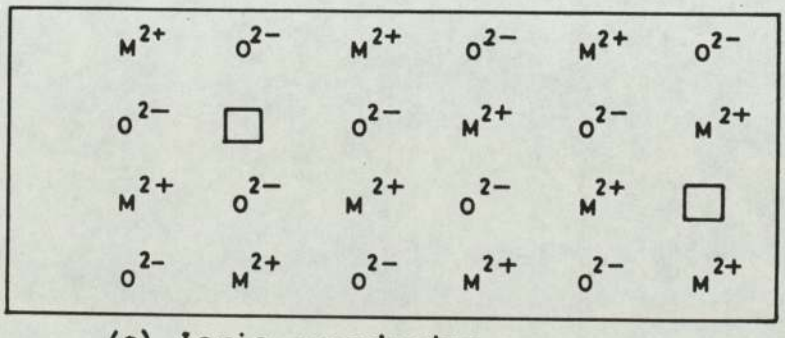

(e) Ionic conductor

Symbols { M = metal ion, O = oxygen ion, □ = vacancy, e^- = electron

FIGURE 1.1 Types of Oxide Defect Structure

(iv) Anion excess semiconductors contain interstitial anions plus electron defects. Anion transport occurs via interstitials (figure 1.1(d)).

(v) Ionic conductors are of stoichiometric composition. They contain an equal number of cation vacancies and cation interstitials, or an equal number of anion vacancies and anion interstitials (Frenkel defects). Alternatively they may contain an equal number of cation and anion vacancies (SchottKey defects). Electron conductivity is negligible (figure 1.1(e)).

Wagner's theory of parabolic oxidation (12) is based on the diffusion of ions through the oxide lattice by the above mechanisms under the influence of an electrochemical gradient. Phase boundary reactions are considered to be rapid, so that the diffusion of ions or transport of electrons through the growing scale determines the reaction rate. It is assumed that there is a thermodynamic equilibrium between metal and oxide at the metal/oxide interface and between oxide an oxygen at the oxide/oxygen interface. Cations, anions and electrons are considered to migrate independently of each other, but since the mobilities or diffusion coefficients of the separate species are generally different this suggests that charge separation occurs. However, the resulting electric field will tend to prevent any further charge separation resulting in electrons or holes being sharply decelerated, while the acceleration of ions is only slight due to their considerably greater mass (18). A stationary state is reached for which there is zero net charge transfer through the oxide and electroneutrality

is maintained for each volume element of the oxide.

The theory commences by using the known laws of diffusion to express the current densities of the individual diffusing species due to the double influence of a chemical potential gradient and an electrical potential gradient. The electrical potential gradient is generally not known (1) but this can be expressed in terms of the chemical potential gradient and transport numbers by making use of the fact that no net current flows through the oxide scale under equilibrium conditions. The final result is an equation relating the number of oxide equivalents formed per unit area per second, dn/dt, to the instantaneous oxide thickness, x, namely:

$$\frac{dn}{dt} = \left\{ \frac{1}{F^2 |Z_o|} \int_{\mu_x^i}^{\mu_x^o} \chi(\tau_m + \tau_o)\tau_e \, d\mu_x \right\} \cdot \frac{1}{x} \qquad (1.3)$$

where:

F = Faraday's constant (= Avagadro No. x electronic charge)

Z_o = valency of the anion

χ = total electrical conductivity

τ_m, τ_o, τ_e = respective transport numbers of the cations, anions and electrons

μ_x = chemical potential

μ_x^i, μ_x^o = chemical potential of oxygen at the oxide/metal and oxide/oxygen interfaces respectively.

The expression in the brackets on the right hand side of equation (1.3) is constant with time (18). The rate of growth of oxide thickness, dx/dt, is related to dn/dt by a

simple constant multiplying factor which converts oxide equivalents per unit area into oxide thickness. Thus, the rate of increase of oxide thickness is given by:

$$\frac{dx}{dt} = \frac{k_p}{2} \cdot \frac{1}{x} \qquad (1.4)$$

where the parabolic rate constant, k_p, is equal to the above mentioned conversion constant multiplied by the bracketted expression of equation (1.3). On integration of equation(1.4), and taking x=0 at t=0, we have the familiar parabolic rate equation, namely:

$$x^2 = k_p t \qquad (1.5)$$

Hence we are able to explain oxidation rates on the basis of the electrical properties of the oxide and on the nature of the point defects present in the oxide, and we are also able to predict oxidation rates from a knowledge of these properties. Furthermore, the theory makes it possible to predict the effect of temperature, pressure and metal impurities on oxidation rate. These factors are responsible for the considerable success of the Wagner theory of parabolic oxidation.

In the case of a metal which forms more than one oxide, providing the oxides are present as separate layers which are compact it is the diffusion of ions through the various layers which controls growth, resulting in a parabolic growth law. The relative thickness of the various layers is dependent upon the diffusion rates of the ions through each layer and upon the differences of the chemical potentials at the

interfaces, and will remain constant with time. For a metal forming two compact oxide layers the ratio of the thickness of each layer is equal to the ratio of the parabolic rate constants for each layer (2) i.e.:

$$\frac{x_1}{x_2} = \frac{k_1}{k_2} \qquad (1.6)$$

The parabolic rate constants k_1 and k_2 will both vary with temperature, and so the relative thickness of each layer will also vary with temperature.

The discussion of thick film growth has so far been concerned with oxides which form compact layers on the metal surface. Often,however, the oxide layer will lose its adhesion to the metal surface, or pores or cracks may form in the oxide. These factors affect the mechanism of growth and the rate of growth of the oxide.

Pilling and Bedworth (20) were the first to emphasize the importance of the relationship between the oxide volume and the volume of the metal on the protectiveness of the oxide scale against further attack. According to these workers a necessary condition for the formation of a compact, non-porous oxide layer is:

$$\frac{\text{molar volume of oxide}}{\text{molar volume of metal}} \geq 1 \qquad (1.7)$$

For values of the ratio less than one the volume of oxide formed does not compensate for the volume of metal consumed producing stresses which result in a porous film. This may not always be so in such cases, however, due to plastic flow of the oxide and metal compensating for the differences in

volume. In fact, it has been shown by Schottky (21) that the primary requirement for the formation of a compact, adherent oxide film is the capability of plastic flow in both metal and oxide.

Pilling and Bedworth (20) considered that for cases where the ratio in equation (1.7) was greater than one a protective film resulted. However, even though lateral compression in a film will tend to prevent the formation of pores or close them up if they form, compressional stresses may also result in the deterioration of a film. The energy needed to overcome the adhesional forces in order that film breakaway from the metal substrate may occur is independent of thickness, but the internal compressional stress per unit area in the film increases with thickness (15). Thus, at a particular film thickness the stresses may become sufficient for breakaway to occur. Compressional stresses causing film deterioration is most pronounced when oxidation is controlled by anion diffusion. Since the oxide is formed at the metal/oxide interface in this case an expansion of the lattice is necessary to provide space for the anions when a layer of metal is transformed into oxide (2). The metal and oxide layers already formed resist this expansion.

When cation migration predominates in the oxidation reaction vacancies accumulate at the metal/oxide interface and may result in the formation of cavities producing lack of film adhesion. This becomes more important at relatively low temperatures when the plasticity of the oxide is often insufficient to compensate for the formation of cavities.

The formation of cracks or pores in an oxide layer which expose the metal surface to direct attack by oxygen frequently results in a linear rate law (18 , 19). Such linear rate laws are generally attributed to phase boundary reactions being rate-determining. Evans (15) proposed a direct logarithmic rate law for the growth of thick oxide scales containing cavities.

1.2.5 Effect of Temperature on Oxidation Rate

The increase in rate of oxide growth with increase in temperature is an exponential relationship, which is characteristic of diffusion processes. To move through an oxide film a diffusing particle requires a certain critical energy in order to "jump" from one position of low potential energy to the next, over an intervening energy barrier. The number of ions which can take part in the diffusion process and which have sufficient energy to make the jump is proportional to $\exp(-E/RT)$ where E is the height of the energy barrier, R is the gas constant, and T is the absolute temperature. As a result the oxidation rate constant, k, can be expressed by an Arrhenius equation, as first pointed out by Dunn (22), which is:

$$k = A \exp(-Q/RT) \qquad (1.8)$$

where A and Q are known as the Arrhenius constant and the activation energy respectively. A and Q are constant for any given temperature range in which there is no change in the oxide formed or in the oxidation mechanism. Hence a plot of k versus the reciprocal of absolute temperature is a straight line from which A and Q can be determined.

A detailed physical interpretation of A and Q presents a major theoretical problem (19). Qualitatively, the value of Q gives a measure of the energy needed for diffusion through the oxide film; the greater the value of Q the greater is the energy needed to overcome the potential energy barriers, which is necessary for diffusion. The Arrhenius constant, A, depends upon the degree of disruption of the oxide; the greater the density of grain boundaries and dislocations the greater is the value of A.

Q may also depend upon the degree of disruption of the oxide since diffusion will also occur along grain boundaries and dislocations as well as through the oxide lattice. This "short-circuit" diffusion as it is frequently termed has a lower activation energy than lattice diffusion (19). As a result of this, short-circuit diffusion becomes increasingly important at lower temperatures, and according to Hauffe (18) short-circuit diffusion does not play a significant role at high temperatures. However, Caplan et al (23) observed an order of magnitude variation in the parabolic oxidation rate of iron-carbon alloys at 500^{o}C, and this was attributed to variations in the Fe_3O_4 grain size, the higher oxidation rate occurring at the smaller grain size.

1.2.6 Oxidation of Iron and Low Alloy Steel

When iron or low alloy steel is heated in air at atmospheric pressure three primary oxides are formed: haematite (Fe_2O_3), magnetite (Fe_3O_4) and wustite (FeO). The latter oxide, FeO, is unstable below 570^{o}C, so that thick oxide films formed below this temperature consist only of Fe_2O_3 and Fe_3O_4,

although all these different oxides are usually present in the oxide film as separate layers having the structure $Fe/FeO/Fe_3O_4/Fe_2O_3/O_2$ (17 , 18 , 19).

The growth of thin films on iron at relatively low temperatures exhibits a logarithmic rate law (17). The Cabrera-Mott theory (5) can be used to explain this behaviour for very thin films, but for films above a few hundred Angstroms in thickness this is no longer applicable and a theory based on the blocking of pores or dislocations, such as that due to Evans (15), provides the explanation. Both of these theories were covered briefly in section 1.2.3.

Above 200°C to 300°C the rate law for oxide growth is parabolic (15 , 17), the exact temperature at which the transition from logarithmic to parabolic growth occurs being dependent on surface condition and pretreatment (15). The oxidation rate law is parabolic since the separate oxides all form compact layers, so that the growth of each layer is diffusion controlled. This conforms with the prediction of Pilling and Bedworth's (20) relation (equation (1.7)) since the ratio of molar volume of iron oxide to molar volume of iron is 2.10 for Fe_3O_4 and 2.14 for Fe_2O_3 (17).

The oxides of iron are not of exactly stoichiometric composition. Their structures and mechanisms of growth are described briefly below:

(i) FeO is a p-type semiconductor. It contains less iron than the formula suggests due to the presence of Fe^{2+} vacant lattice sites. Growth occurs almost entirely

due to the diffusion of cations, which occurs via these vacancies (17 ,18).

(ii) Fe_3O_4 grows by the diffusion of both cations (Fe^{2+} and Fe^{3+}) and anions. Kubachewski and Hopkins (17) state that anion diffusion is predominant, while Boltaks (24) states that the contribution from anions is appreciable. In contrast, Hauffe (18) states that cation diffusion is predominant.

(iii) Fe_2O_3 is an n-type semiconductor. It contains more metal than the formula suggests due to the presence of O^{2-} vacant lattice sites. Growth occurs due to the diffusion of anions, which occurs via these vacancies (17 ,18).

Figure 1.2 is a schematic diagram of the diffusion processes and phase boundary reactions occurring during the growth of a multilayer oxide on the surface of iron due to Hauffe (18)

Above 570°C the greatest part of the scaling layer consists of FeO, with only a thin covering of Fe_3O_4 and Fe_2O_3 (18). The relative thickness of each layer is governed by the relative diffusion rates of ions in each phase (19), and the FeO layer is thickest due to the fact that it posesses the highest conductivity (25). According to Lustman (25), at a temperature of around 600°C the proportions of the three oxides in the scale are: 85-90% FeO, 10-15% Fe_3O_4, and 0.5-2% Fe_2O_3. Below 570°C the scale consists of Fe_2O_3 and Fe_3O_4, but at lower temperatures Fe_2O_3 is the main constituent of the oxide, while at higher temperatures within this range the oxide is mainly Fe_3O_4. The temperature at which

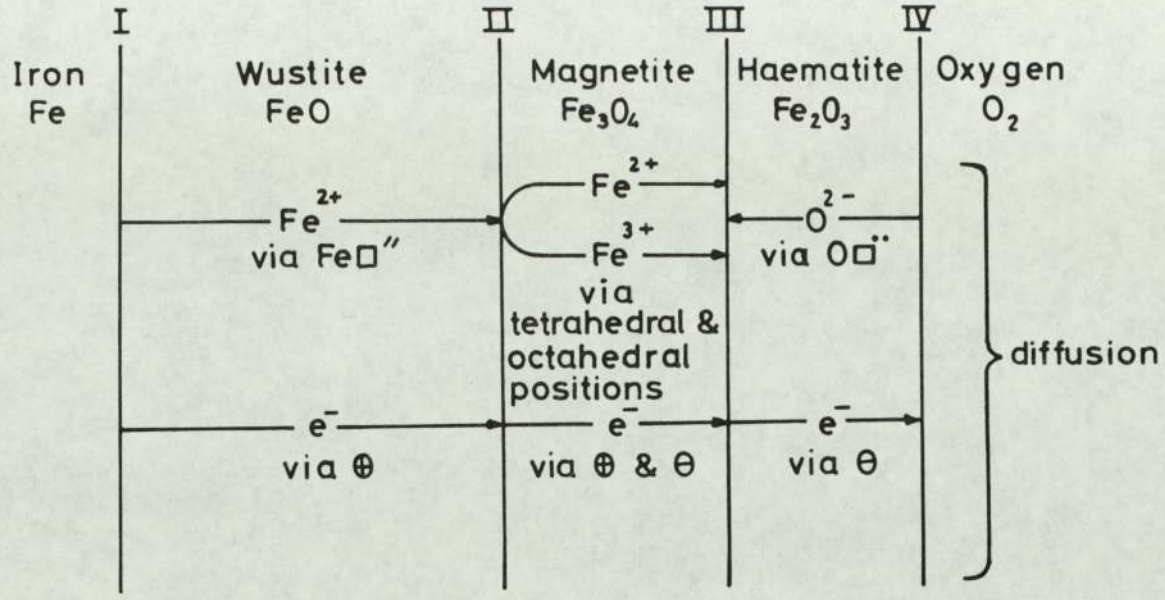

Phase boundary reactions

I $Fe\ (metal) + (Fe\square'' + 2\oplus)_{in\ FeO} \leftrightharpoons Null$

II $Fe_3O_4 \leftrightharpoons (4FeO + 4Fe\square'' + 2\oplus)_{in\ FeO}$ (Fe_3O_4 decomposition)
& $\oplus_{inFeO} + (Fe\square'' + Fe\square''')_{vacant\ tetrahedral\ positions\ in\ Fe_3O_4}$
$\leftrightharpoons$ filled lattice positions $+ (2Fe\square'')_{inFeO}$

III $12Fe_2O_3 \leftrightharpoons 9Fe_3O_4 + (Fe\square'' + 2Fe\square''' + 8\oplus)$ (Fe_2O_3 decomposition)
$2Fe_3O_4 \leftrightharpoons 3Fe_2O_3 + (O\ddot{\square} + 2\Theta)_{in\ Fe_2O_3}$ (Fe_2O_3 formation)

IV $\frac{1}{2}O_2\ (g) + (O\ddot{\square} + 2\Theta)_{in\ Fe_2O_3} \leftrightharpoons Null$

Symbols:

$\square$	=	lattice vacancy
N°. of primes	=	N°. of negative excess charges
N°. of dots	=	N°. of positive excess charges
Θ	=	conduction electrons
⊕	=	holes
Null	=	stoichiometric crystal without lattice defects

FIGURE 1.2 Diffusion Processes and Phase Boundary Reactions in Iron Oxide (18).

Fe_2O_3 is replaced by Fe_3O_4 as the main oxide varies according to surface pretreatment of the iron (26). In a multi-layer scale in which one particular layer is much thicker than the other two the rate of growth of the scale is essentially the rate of growth of the thicker layer since this is obviously increasing in thickness at a much greater rate than the other layers. This corresponds to the three oxidation regions for iron, except near the transition temperatures where the thickness of two layers can be similar. Hence a plot of $\ln(k_p)$ versus the reciprocal of absolute temperature will produce three straight lines for the growth of thick films on iron, in accordance with equation (1.8), corresponding to the parabolic growth of Fe_2O_3, Fe_3O_4 and FeO.

1.2.7 Experimental Determination of Oxidational Parameters

The measurement of oxidation rate can be performed by various methods, and the more well-known of these are briefly outlined below:

(i) Thermogravimetric method. This involves measuring increases in weight due to the oxidation reaction. This may be done by heating a sample in a furnace for a given period of time, after which the sample is removed, cooled, weighed on a microbalance and re-inserted into the furnace for a further period of oxidation. According to Kubachewski and Hopkins (17) this method is completely satisfactory for the investigation of thick scales which do not crack on cooling. Alternatively, a more convenient method is to

continuously monitor increases in weight by suspending a metal specimen inside a furnace by means of a wire attached to a microbalance (18 , 19). A final method involves measuring the loss of weight of a metal specimen after removing the oxide scale.

(ii) Volumetric and manometric methods. This involves measuring changes in volume or pressure as a result of oxygen consumed as the reaction proceeds (18 , 19).

(iii) Electrometric method. This is particularly useful for determining the thickness of thin oxide films on metals. The specimen of interest is made the cathode in a suitable electrolyte and the time taken to reduce the oxidation product by a small known current is measured (17).

(iv) Ellipsometric method. This method uses the fact that a beam of polarized light reflected from a metal surface undergoes a change in its state of polarization, and the degree of this change depends upon the incident angle and the optical properties of the metal and surface film. Knowledge of these properties permits the calculation of the film thickness. Thus examination of the oxidized surface after successive periods of oxidation enables the oxidation rate to be determined. This method is only suitable for very thin transparent films (27).

As mentioned in section 1.2.5, a plot of the natural logarithm of the oxidation rate constant versus (1/T) enables the activation energy and Arrhenius constant to be determined.

1.3 Application of Electron Spectroscopy to the Study of Oxidized Steel Surfaces

One of the main uses of x-ray photoelectron spectroscopy (XPS) in the study of surfaces is in determining the chemical nature of a surface by means of measurements of shifts in electron binding energies. The shift in the binding energy of a core-level electron in a compound from its value in the free atom depends basically upon two factors (28 , 29). Firstly, there is a change in binding energy because of the removal from, or addition of, one or more electrons to the valence shell of the parent atom, which provide the chemical bonds with neighbouring atoms in the compound. A positive change in oxidation state produces a slight increase in binding energy and vice versa for a negative change in oxidation state. The second factor which has an effect upon the binding energy of core-level electrons is the electrostatic interaction between the electron on the ion of interest and the other ions in the compound. This second point implies that the binding energy of a given core-level electron of an atom of a given element having a given oxidation state may vary from compound to compound as a result of differences in the spatially averaged electostatic potentials exerted upon the electron.

In view of the above we expect small differences in the binding energy values of the core-level electrons of the three oxides Fe_2O_3, Fe_3O_4 and FeO since they contain differing amounts of Fe^{2+} and Fe^{3+} ions and the three structures have differing spatial distributions of the various ions. FeO contains exclusively Fe^{2+} ions, the ions being

octahedrally coordinated in a cubic lattice. Fe_3O_4 contains both Fe^{2+} and Fe^{3+} ions in an inverse cubic spinel structure, with the Fe^{2+} ions in octahedral sites and Fe^{3+} ions half in octahedral and half in tetrahedral sites. α-Fe_2O_3 contains exclusively Fe^{3+} ions in a lattice having the rhombahedral Al_2O_3 structure. Thus XPS is a useful tool in the examination of oxidized iron and steel surfaces since it enables chemical identification of the oxides present.

Auger electron spectroscopy (AES) is another useful technique for the examination of oxidized surfaces and, although it can be used for observing chemical shifts (28), it is frequently used for determining the relative concentrations of the various constituents in the surface layers of a sample. In the case of oxidized steel surfaces analysis could typically be performed to determine the concentration of an alloying element in the oxide phase (30). This type of analysis is most frequently performed in conjunction with ion sputtering so that a concentration versus depth profile can be built up for each element in the oxide layer. A useful extension of the technique is scanning Auger analysis in which a two dimensional map shows the variation in concentration of a selected element over the surface and this can be particularly useful for showing the extent to which an oxide film covers a surface, such as the oxide plateaux often observed on worn steel surfaces (31).

1.4 Wear

1.4.1 General Mechanisms of Wear

Archard and Hirst (32) broadly classified wear into two main types, severe wear and mild wear, and this classification has since been widely adopted. In severe wear the wear rates are relatively high, surfaces are considerably roughened, and the wear debris consists mainly of metallic particles of up to a fraction of a millimetre in size. Mild wear results in relatively low wear rates, surfaces which have a smooth appearance, and wear debris which is composed mainly of small oxide particles, typically 1μm in size. Many different mechanisms of wear make up these two broad wear types.

Burwell and Strang (33) and Burwell (34) classified wear according to the mechanism of material removal. In this classification system any wear process can be categorized by one or more of the following wear types: adhesive, corrosive, surface fatigue, abrasive, or fretting wear. Each of these will now be considered briefly.

(i) Adhesive Wear

When two surfaces touch contact only occurs between microscopic asperities of each surface, and adhesive forces are produced at these contact junctions as a result of atomic attraction (35). In the case of two surfaces which are sliding against each other these junctions are continually being formed and then broken, and adhesive wear results when

the shear strength of some of the junctions is greater than that of the material on one side of the junction, so that shearing often occurs a little distance within the softer material and not at the junction interface itself. A wear particle may be formed immediately or transfer of the fragment to the opposite surface may occur first, after which it may become detached e.g. due to a fatigue process (32). Adhesive wear can generally be regarded as a severe wear mechanism (32).

(ii) Corrosive Wear

This form of wear results from a chemical reaction between the wearing surfaces and the surrounding environment. The mechanism of wear involves the continuous process of formation and removal of the reaction product on the wearing surfaces. This may lead to relatively high wear rates if the reaction film is easily broken down thus giving poor protection. In some cases, however, a protective film is produced which results in relatively low wear rates, and a good example of this is the smooth oxide films which often form on the surface of metals during wear due to reaction with the atmosphere (36 , 37). These oxide films prevent intermetallic contact and hence lead to reductions in friction and wear.

(iii) Abrasive Wear

This type of wear occurs when material is ploughed out of a surface by a harder body, resulting in the formation of a wear particle. The harder body may be the other surface which is in contact, or in some cases hard particles may be

present between the two sliding surfaces (38). These hard particles may be embedded in one of the surfaces, such as in emery paper, or they may be present as a result of wear fragments which have become work hardened. Some oxide films are very hard e.g. aluminium oxide, and so their presence can result in abrasive wear.

(iv) Surface Fatigue

This form of wear occurs when part of a surface is repeatedly loaded and unloaded, where the resulting periodic stresses lead to the nucleation and propagation of surface and sub-surface cracks. Surface fatigue wear is commonly observed in rolling contact, such as in roller bearings, where the formation of cracks leads to large scale surface damage and pitting (34). In this latter case surface fatigue gives rise to severe wear. However, it is considered that the detachment of oxide particles from the wear protective oxide films developed on metal surfaces during sliding could also be due to a fatigue mechanism (31), and in this case surface fatigue is associated with mild wear.

(v) Fretting Wear

This form of wear arises when contacting surfaces undergo relative tangential displacements of a small amplitude in an oscillatory manner. Fretting wear generally includes a number of different wear mechanisms acting together (39) e.g. fretting resulting in the adhesive wear of a metal in which the wear particles corrode to form a hard oxide which then acts as an abrasive (35). Most commonly fretting is combined with corrosion in which case the wear is known as

fretting corrosion. Oxides formed during the reciprocating sliding of metal surfaces may also form a protective surface layer which reduces wear and friction (40).

1.4.2 The Unlubricated Wear of Steels

Before considering the different mechanisms which have been proposed for the oxidative wear of steels it is perhaps useful to briefly discuss the wear of steels in general and, in particular, the conditions which promote the formation of protective surface oxides during wear. One of the most comprehensive works on this subject was that due to Welsh (41). He showed that for a steel pin wearing against a steel ring at a given speed there are three critical loads, which he denoted by T_1 , T_2 and T_3. Below T_1 mild wear occurs by the removal of oxide which is supported on a work hardened layer. Above the T_1 transition the higher bulk temperatures result in plastic deformation of the substrate and the load is now sufficiently high to cause breakdown of the surface oxide so that severe wear occurs. Above T_2 the surface temperature is high enough for phase hardening (martensitic phase transformation) so that a hard "white layer" structure is produced. The higher temperatures and the hardened surface layers produced above T_2 promote the formation of a protective surface oxide so that mild wear occurs once again. Above the T_3 transition permanent phase hardening occurs so that oxide formation is no longer necessary for the mild wear behaviour to be sustained. Factors which affect the positions of the load transitions are hardness, speed and carbon content of the steel.

An important point which emerges from this work as regards oxidative wear is that it appears that the wear protective oxides observed on worn steel surfaces are supported by a work hardened layer. The recent work of Sullivan and Athwal (31), however, suggests that the presence of a work hardened layer is not a necessary condition for the formation of a wear protective oxide.

1.4.3 Oxidative Wear Theories

A number of theories have been proposed to explain the oxidative wear of metal surfaces (37 , 40 , 42 , 43 , 44) and while all of these theories assume that wear occurs predominantly by the removal of oxidized metal, they differ in the mechanisms proposed for the growth of the oxide layer and its subsequent removal, and in the temperature at which oxidation is thought to occur.

Yoshimoto and Tsukizoe (42) used a simple model, in which there is an even depth distribution of conical asperities, to represent the profile of a metal surface. In the case of two metal surfaces in sliding contact oxidative wear is considered to occur by complete removal of the oxide film from a contact area during contact, after which the film grows again to a constant thickness before the next encounter. This is illustrated in figure 1.3. The removal of oxide from an area of contact is considered to take place by shearing at the oxide/metal interface. However, Archard (45) considered that the production of a wear particle at every encounter, as suggested in this model, is most unlikely.

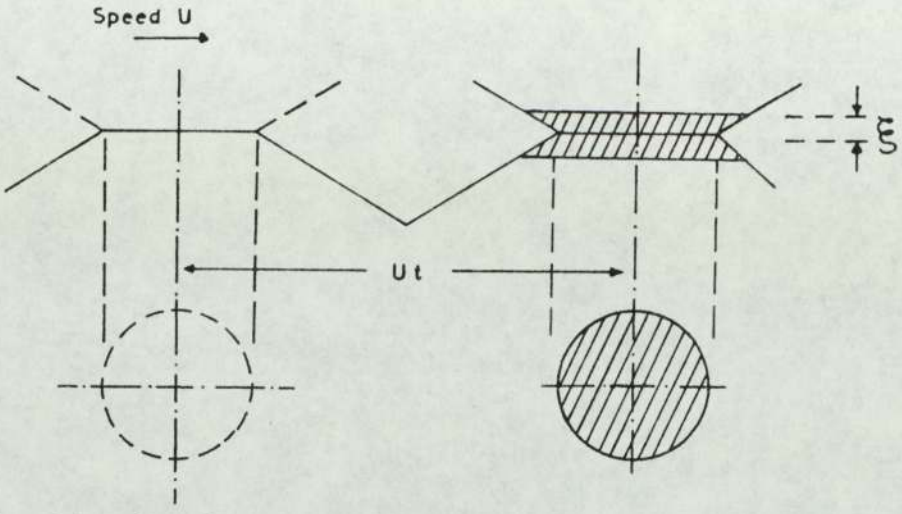

FIGURE 1.3 Idealized Model of Oxidative Wear due to Yoshimoto and Tsukizoe (42).

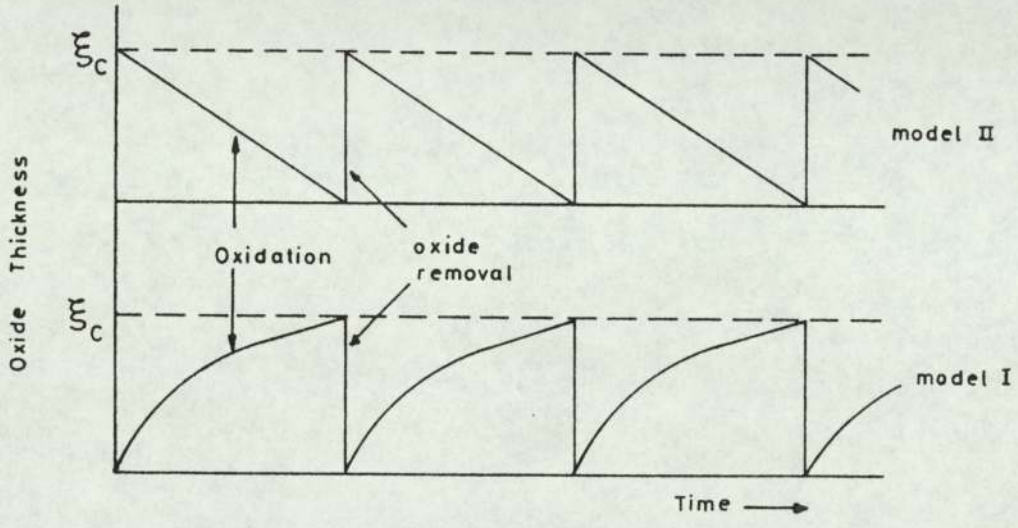

FIGURE 1.4 Theoretical Models for Oxidative Wear due to Tao (37).

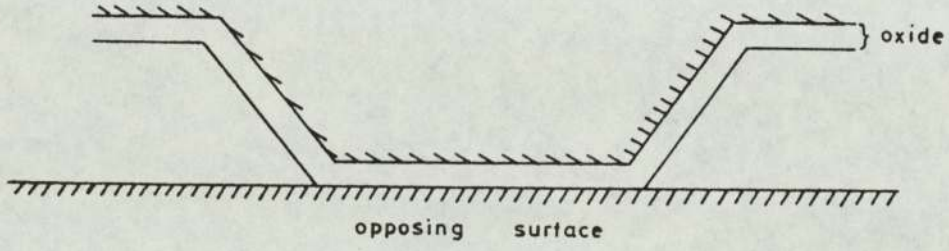

FIGURE 1.5 Typical Asperity Contact - Tenwick and Earls (43).

The rate of growth of oxide in the theory of Yoshimoto and Tsukizoe is considered to obey a logarithmic law, but since the growth rate is also considered to be very rapid in the period between successive asperity contacts this approximates to a linear law. Recent SEM oxide thickness measurements (31), however, have shown that the oxide films produced during the unidirectional sliding wear of low alloy steel are relatively thick ($\sim 4\mu m$) and in this case we would expect a parabolic rate law to be applicable (17).

An expression for film wear rate per unit sliding distance was derived and this predicts that wear rate is approximately directly proportional to the square root of the load, and inversely proportional to the sliding speed. Furthermore, the theory predicts that oxide thickness is inversely proportional to sliding speed, and that it decreases slightly with increasing load. Recent SEM measurements (31) have shown, however, that such a variation in oxide thickness is not found in the case of low alloy steel wear tests.

The theory of Yoshimoto and Tsukizoe was one of the earliest to be proposed for oxidative wear but no real experimental evidence was provided in support of it.

Tao (37) considered two models which represent two possible extreme situations which could theoretically occur when a surface wears due to growth and subsequent removal of an oxide layer. The first model assumes that the oxide grows gradually until it reaches a critical thickness, ξ_c , after which it is removed instantaneously by the rubbing action. In contrast the second model assumes that the time taken for

the oxide to grow to ξ_c is negligible in comparison to the time taken for its subsequent rubbing off. Both of these models are illustrated diagramatically in figure 1.4. Application of these models to experimental wear data suggested that the first model is the one which is representative of the real wearing situation, thus indicating that the rate of metal oxidation, rather than oxide removal is the important factor in determining wear rate. This model is applicable to the formation of thick, homogeneous oxide films, and it must be noted that other types of oxide film can be formed during wear. Tao also assumed that oxidation occurred at the hot-spot temperatures and that the rate of oxide growth obeyed a parabolic rate law. The proposed model predicted that the activation energy relevant to oxidation during wear was somewhat smaller than that for static oxidation due to the mechanical disruption of the oxide providing easy diffusion paths. This is in contrast to the work of Quinn et al (46) who assume that the activation energy for both tribological and static oxidation will be the same.

Tenwick and Earles (43) proposed a simple model for the contacting surfaces in order to develop an expression for the wear of one surface in terms of temperature and load. The surface model assumes that contact between the sliding surfaces occurs at only one asperity, as shown in figure 1.5. The asperity is assumed to remain continuously in contact with the opposing surface until an oxide layer of critical thickness builds up, after which it becomes detached to form a wear particle. The process is then repeated with another asperity. The rate of oxide growth was considered to follow

a logarithmic law, but this approximated to a linear law for the relatively short period required to reach the critical thickness. The expression derived for the wear rate, ω (volume removed per unit time) is:

$$\omega = \frac{W A}{P_m B} \exp(-Q / R T_s) \qquad (1.9)$$

where:

W = applied load

T_s = general surface temperature

P_m = hardness of metal at T_s

A = Arrhenius constant for linear oxidation

Q = activation energy

R = gas constant

B = constant

Tenwick and Earles proposed that T_s is the effective temperature at which oxide growth takes place, rather than the hot-spot temperature at the contact, since they considered that each asperity spends a much greater length of time out of contact than in contact. The range of T_s values for which they considered their theory to be applicable is around 300°C to 500°C, and modifications to Quinn's oxidational wear theory (44) carried out by Athwal (47) also indicates that out of contact oxidation is responsible for oxide growth at these high T_s values.

The rate of growth of thick oxide films on metal surfaces usually follows a parabolic law, and Tenwick and Earles replaced their linear rate law by a parabolic law to account for this. They failed to apply this to their experimental results, however, because the new wear rate equation

contained the critical oxide thickness, which they could not determine.

Quinn's oxidational wear theory (44) assumes that oxide growth takes place during the successive contact periods of an asperity, and that oxide growth continues until it reaches a critical thickness, after which it becomes unstable and an oxide wear particle is formed. This theory is discussed in detail in section 6.2.

The theories discussed so far have been based on the growth of a physically uniform oxide film at the elevated temperatures produced at the wearing surfaces, much in the same way that an oxide film grows on a heated metal surface under static oxidizing conditions. The theory of oxide 'glazes' proposed by Stott and co-workers (40 , 48), however, is based on a completely different mechanism. These glazes are considered to develop as a result of oxide debris which has been fragmented, compacted and then undergone plastic deformation. Oxides do not usually exhibit any significant plastic flow under tensile stress since they are often brittle, fracturing at a relatively low stress. However, plastic flow of the oxide is considered to occur in the development of glazes as a result of both the Auerbach effect, in which very small indenters such as asperities can significantly increase the maximum value of tensile stress at which fracture first occurs, and the presence of hydrostatic pressures in the glaze.

Oxide glazes can develop in a number of ways. They may develop following compaction of oxide or oxide coated debris

produced during sliding, as mentioned above, and in these cases the smooth oxide glaze typically forms on top of a compressed particulate region. Sometimes, however, they may develop on oxides which were present on the metal surfaces prior to the commencement of sliding. In this case glazes may form immediately on the oxide surface, appearing as a 'polished section' through the pre-formed oxide or, in cases where the interfacial adhesion between the oxide and metal surface is poor, the oxide will break up on commencement of sliding and the debris so produced will be compacted enabling a glaze to eventually develop.

Relatively low wear rates are observed when glazes are present on the wearing surfaces since the oxide wear debris which is produced consists of very fine oxide particles which can be recompacted into the glaze during further sliding.

It seems likely that the development of glazes is favoured by sliding conditions in which wear debris is easily trapped, such as reciprocating sliding having a small amplitude of oscillation or an interface between two sliding surfaces which is in a horizontal plane so that loose debris is not removed by gravity.

1.5 Mechanisms of Friction

Friction is the force which resists motion when one surface slides over another. There are two basic laws of friction which have been established empirically, and these are:

(i) The frictional force, F, is proportional to the normal load, W, pressing the two bodies together i.e.

$$F = \mu W \tag{1.10}$$

where μ is the coefficient of friction. μ is a constant for a given pair of materials under a given set of ambient conditions.

(ii) F is independent of the apparent area of contact. This holds true for most materials but not elastomers.

The Bowden and Tabor (49) theory of friction is based on the shear strength of the junctions which are formed at the points of contact between the two surfaces. If the average shear strength of the junctions is s, and the real area of contact between the surfaces is A_r then according to Bowden and Tabor:

$$F = A_r s + P \tag{1.11}$$

where P is a term which represents the force required to 'plough' hard asperities through a softer surface. P can usually be neglected in the case of metals sliding against each other under unlubricated conditions.

It is considered that the surface asperities deform plastically and in this case A_r is given by (49):

$$A_r = \frac{W}{P_m} \tag{1.12}$$

where P_m is the yield pressure of the softer material. Neglecting the ploughing term in equation (1.11) and combining equations (1.10), (1.11) and (1.12) we have:

$$\mu = \frac{s}{P_m} = \frac{\text{shear strength of the softer metal}}{\text{yield pressure of the softer metal}} \qquad (1.13)$$

The ratio s/P_m is roughly the same for most metals and this explains the observation that μ does not vary greatly from metal to metal (equation (1.13) predicts that $\mu \simeq 0.2$).

In the case of a metal surface which is covered by a thin film e.g. of lubricant or oxide, then film/metal or film/film type contacts may predominate, and so equation (1.13) must now be replaced by the equation:

$$\mu = \frac{\text{shear strength of the interface } (s_i)}{\text{yield pressure of the bulk metal } (P_m)} \qquad (1.14)$$

A reduction in the frictional force between metal surfaces in sliding contact due to the presence of surface oxide films has been reported on numerous occassions. Surface oxides reduce frictional force since they prevent or reduce the occurrence of metallic contact between surfaces, and it is usually easier to shear oxide junctions than metallic junctions (49). It is found experimentally that some oxides give relatively low friction values, while others do not (50). According to Bowden and Tabor (49) the overriding factor which determines whether an oxide will support a given load is the relative mechanical properties of the oxide and the underlying metal. If the oxide film is very hard and the underlying metal relatively soft (aluminium oxide on aluminium, tin oxide on tin) then small loads will deform the substrate so that breakthrough of the surface film occurs, and in this case μ is determined by mainly metallic contact. However, if the hardness of the oxide and metal are similar then the oxide film will deform with the

substrate, breakthrough will not occur, and μ will be fairly low (copper oxide on copper).

Wilson et al (51) proposed a model based on the adhesion theory of friction which relates μ to the extent of oxide coverage on the worn surfaces in terms of the shear strengths and junction growth constants of metal/metal, metal/oxide, and oxide/oxide asperity junctions. Comparison of theoretical and experimental friction results indicated that metal/oxide asperity interactions are not very critical in determining frictional behaviour, although the oxide junction growth constant is important.

Rigney and Hirst (52) proposed an alternative theory to the traditional theories of friction. They proposed that the frictional force arises due to the work required for plastic deformation in the near surface region, described in terms of work hardening, recovery and cellular microstructure existing during steady state sliding.

1.6 Temperatures Generated During Sliding

When two surfaces are sliding against each other the energy resulting from frictional contact of asperities on the opposing surfaces is largely dissipated as heat. This causes sudden temperature rises at the points of contact which only last for a very short period of time, since the heat is quickly conducted along the asperities into the bulk. The heat conducted into the bulk results in a rise in the temperature over the surface as a whole, but this temperature rise is generally much lower than the temperature rise

produced at the contacting asperities, known as the "flash temperature". If external heating is applied to the sliding bodies this will result in an increase in both of the above mentioned temperatures. Thus there are two temperatures to be considered, and there has always been some controversy over which temperature governs the growth of oxides during wear. Some oxidative wear theories propose that the majority of oxide growth occurs at the flash temperature (37 , 44), and much of the evidence which has been presented in support of this is based on a comparison of estimates of flash temperature with oxidation temperatures to be expected on the basis of oxide composition (36). Other theories consider that oxide growth occurs at the general surface temperature (43). More recently Athwal (47) has modified Quinn's oxidational wear theory (44) to include oxidation at the general surface temperature, and this modified theory predicts that oxidation at the general surface temperature is unimportant if this temperature is relatively low, but becomes the dominant mechanism at temperatures above approximately 300^{o}C. Sullivan and Athwal (31) have presented results of experimental wear tests carried out on low alloy steel which support this finding.

It is usually possible to measure the general surface temperature experimentally, but this is very difficult to do in the case of the flash temperature since they only occur for very brief periods over an extremely small contact area. Dynamic thermocouples have been used to measure flash temperatures (53 , 54) but these tend to be restrictive as regards the choice of sliding material combinations and are insensitive to the rapid transients which occur during

sliding. As a result flash temperatures are often estimated from theoretical analyses. Flash temperature theories have been presented by Blok (55) and Jaeger (56), while Archard (57) has presented a simplified version of Jaeger's theory.

Surface temperatures have also been deduced from calculations of heat flow rates performed from thermocouple measurements of temperature at strategic points along one of the sliding bodies (58 , 59). Such a method due to Quinn (59) is given in detail in section 2.5.

1.7 Research Programme

The presence of oxide films on surfaces during sliding contact usually leads to a significant decrease in wear rate and a corresponding decrease in frictional force. Various theories have been proposed for the continuous process of formation and removal of oxide from a surface during wear, but there is still no general agreement regarding this mechanism. This is probably partly due to the existence of more than one mechanism of oxidative wear, corresponding to different wearing situations. The present project is concerned with establishing the mechanism of the oxidative wear of low alloy steel in unlubricated, unidirectional sliding conditions when a horizontal pin is loaded against the polished face of a rotating vertical disc.

A range of wear tests were performed in air at various loads and speeds using a low alloy steel (EN8). A few selected wear tests were also carried out in which an EN8 pin was

loaded against a 9% Cr steel disc, the purpose of which was to test for oxide transfer using Auger electron spectroscopy. Wear rate, frictional force, and pin and disc temperatures were recorded.

Various methods of analysis were used. Powder x-ray diffraction was used to examine wear debris while glancing angle x-ray diffraction was used to identify the constituents of the surface oxide films. Scanning electron microscopy was used for examining the topographies of the worn surfaces and also for directly measuring the thickness of the oxide films. Particular emphasis was placed on surface analysis by Auger electron spectroscopy and x-ray photoelectron spectroscopy. Both techniques were used in conjunction with argon ion etching, the former technique being used to build up concentration versus depth profiles of the elements in the surface films, while the latter technique was used to identify the chemical state of the oxide films at successive depths. For the purpose of comparison of oxide composition, some of the above analytical techniques were also performed on surface oxides which had been produced on low alloy steel under static oxidizing conditions at various selected temperatures.

A theoretical surface model was used which enabled the contact temperature, the number of contacts and the average asperity contact radius to be deduced. From this theory it was also possible to calculate values of activation energy and Arrhenius constant for oxide growth during wear, and these values were compared with those relevant to the oxidation of low alloy steel under static conditions. The

values of activation energy and Arrhenius constant for static oxidation were calculated from oxidation rate constants, which had been determined earlier for a wide range of selected temperatures by measurements of mass increase with time, or, in the case of relatively low temperatures, by measurements of increase in film thickness.

CHAPTER 2

EXPERIMENTAL DETAILS OF MECHANICAL WEAR TESTS

2.1 Introduction

This chapter describes the experimental instrumentation and methods used in investigating the unlubricated wear of EN8 steel. All experiments were conducted in an air environment and no external heating was applied, so that the elevated temperatures at the pin and disc surfaces were due entirely to frictional heating.

The subsequent analysis of the worn surfaces is described in Chapter 3.

2.2 The Wear Test Rig

The wear test rig used for conducting the wear experiments consisted essentially of a horizontal pin loaded pneumatically against a vertical rotating disc, resulting in a circular wear track. A general view of the rig is shown in figure 2.1, while the diagram of figure 2.2 shows the main features of the rig.

The pin was held inside a calorimeter which was secured firmly on a sub-assembly attached to the front end of the main supporting shaft, such that the axis of the pin was parallel, but not coincident, with the axis of the main shaft. The shaft was supported by double row radial ball bearings enabling it to rotate, in order to facilitate

FIGURE 2.1 The Wear Test Rig.

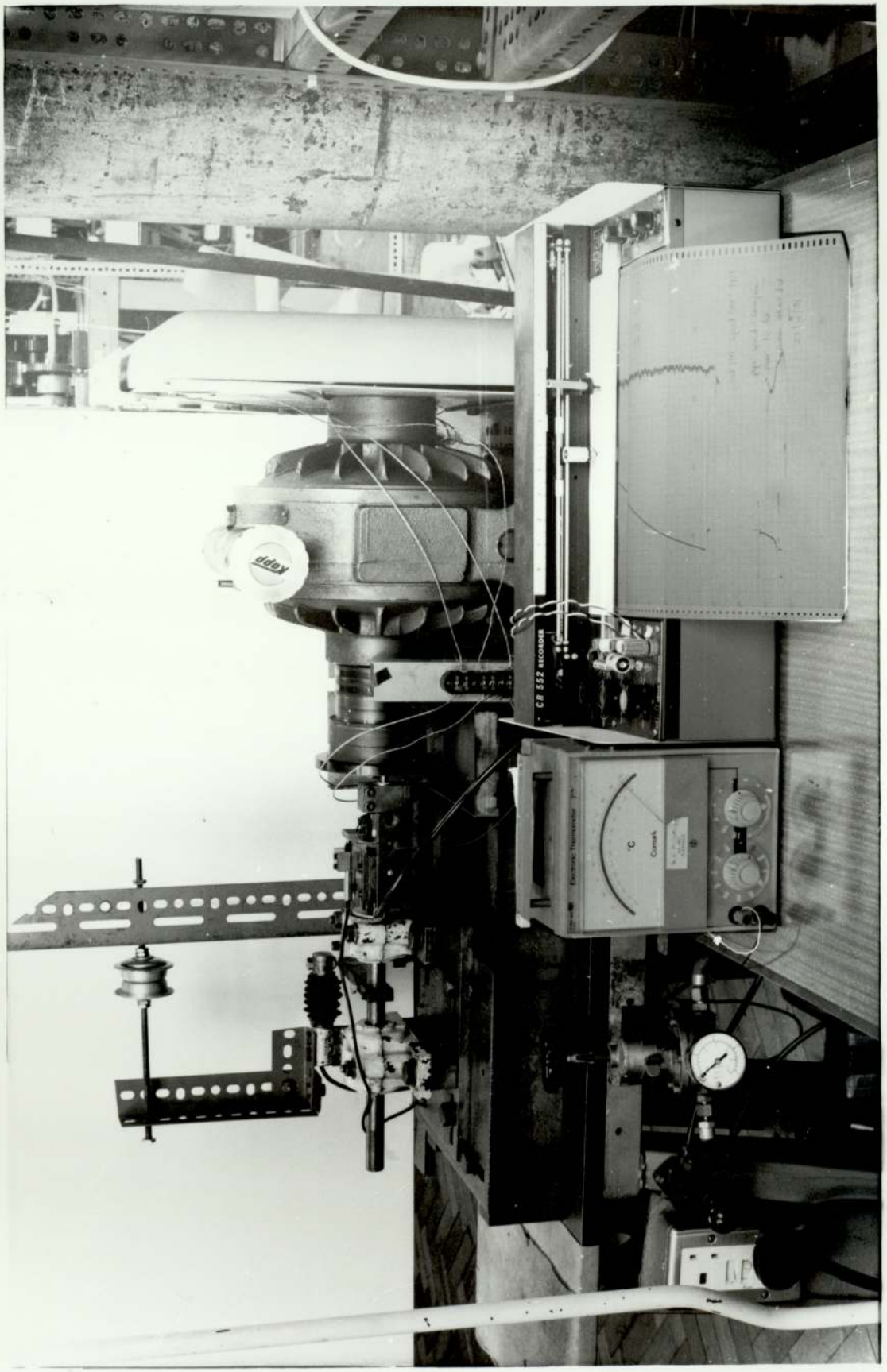

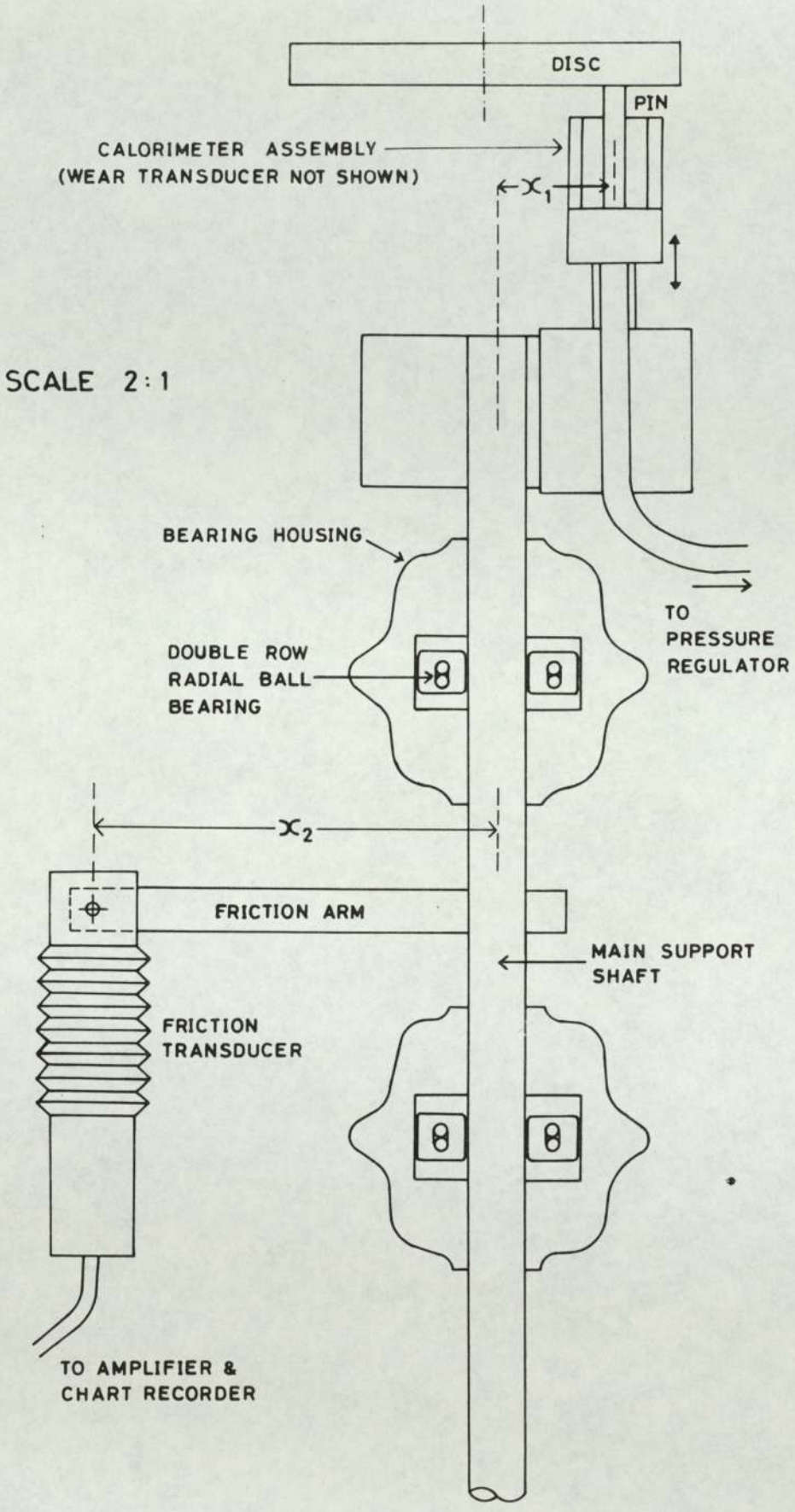

FIGURE 2.2 Main Features of the Wear Test Rig.

the measurement of the frictional force on the pin from torque considerations (see section 2.4). Loading of the pin against the disc was accomplished by means of compressed air fed from a cylinder to a pneumatic piston at the rear of the calorimeter. A pressure valve equipped with a gauge was situated in the compressed air line and could be used to vary the load between 5 N and 58 N.

The disc was held in a vertical position by a single bolt through its centre which secured it to the shaft of a Kopp variable speed drive. The variable speed drive was driven by a pulley connected to a 3 phase, 5 H.P. electric motor. Rotational disc speeds in the range from 120 r.p.m. to 2047 r.p.m. were available corresponding to linear disc on pin velocities in the range 0.5 ms^{-1} to 8.5 ms^{-1}. Calibration of the rotational speeds, which had been carried out previously, was checked frequently using a light beam/ photocell tachometer pointed at the edge of the rotating disc. A circular wear track was produced on the disc face having a mean track radius of 40 mm.

Additional features of the wear test rig comprised equipment for measuring and recording the wear rate, frictional force, and various temperatures.

An aluminium tray was positioned under the pin and disc interface in order to collect debris which had fallen under the influence of gravity.

2.3 Measurement of Wear Rates

Measurement of pin wear rates was achieved by means of a Linear Voltage Differential Transducer. The transducer was fixed firmly in a horizontal position such that it was in contact with a flat vertical plate attached to the pin/calorimeter assembly (figure 2.3). Forward movement of the plate due to wearing of the pin was detected by the transducer, whose output was amplified and fed to one channel of a duel channel chart recorder.

For most experiments the chart recorder channel was operated on a 0-1 volt range, although for the lower wear rates a 0-0.1 volt range was favoured. On each of these ranges full scale deflection was 200 mm.

Instrument calibration was carried out using a micrometer. It was found that 0.635 mm displacement of the pin corresponded to a pen recorder deflection of 157 mm on the 0-1 volt range setting. The calibration factor was found to be a factor of ten times greater in sensitivity on the 0-0.1 volt range demonstrating that the transducer characteristic was linear over the range of experimental conditions used.

The slope of the equilibrium wear trace was used to calculate the equilibrium wear rate. The slope was a measure of the decrease in length of the pin per unit time. Multiplying this factor by the cross-sectional area of the pin and dividing by the linear speed of the disc against the pin gave the volume of pin removed per unit sliding

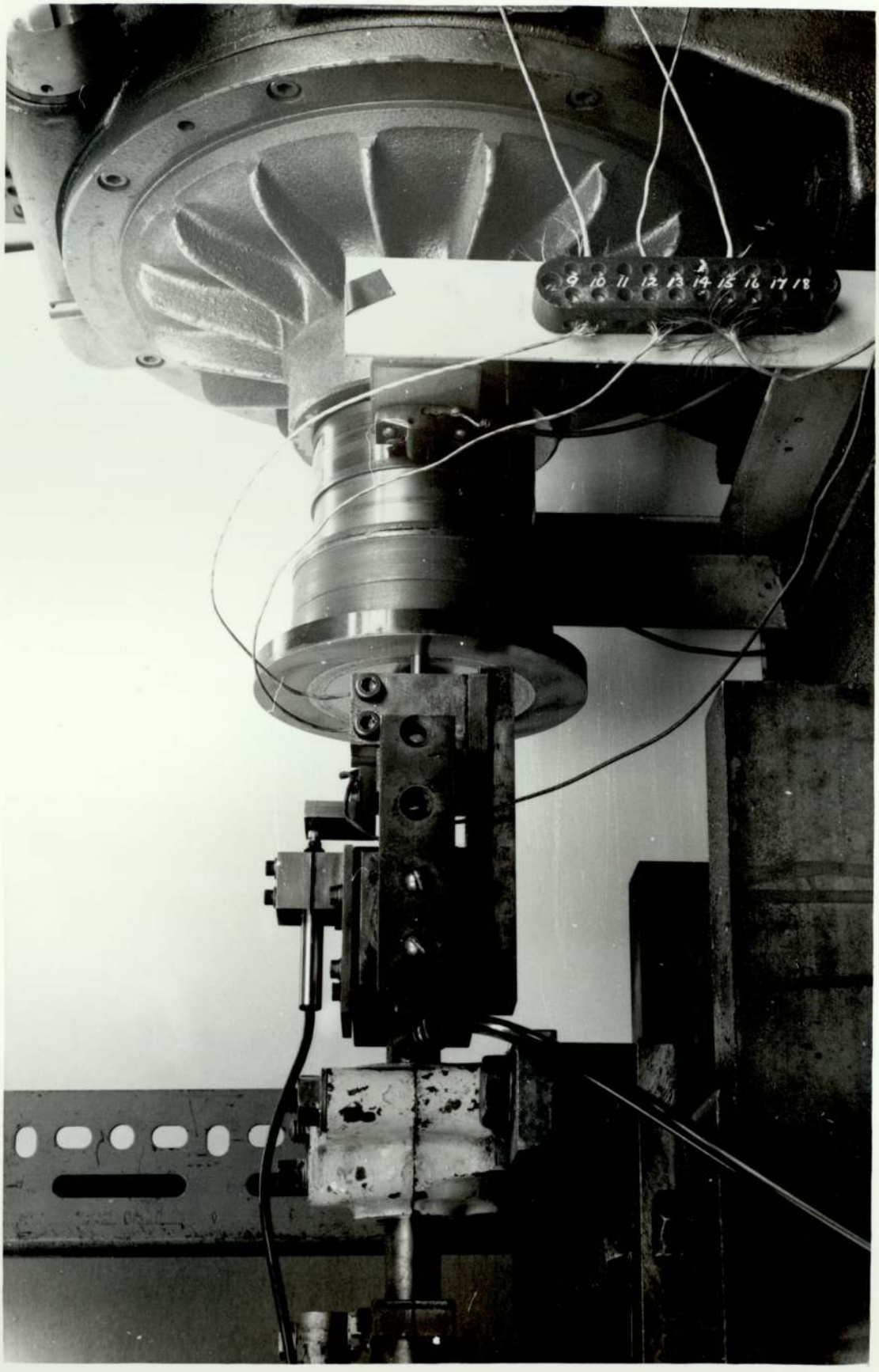

FIGURE 2.3 Close Up View of the Pin on Disc Assembly.

distance (m^3m^{-1}). All wear rates are expressed in this latter form.

2.4 Measurement of Friction

The frictional drag of the rotating disc on the pin caused the pin assembly to rotate about the axis of the main supporting shaft, this rotation being of a small magnitude so that the position of the pin with respect to the rotating disc appeared fixed throughout the wear test. This rotation was transmitted to a friction transducer via an arm attached perpendicularly to the main shaft. Considerations of moments enabled the upward force on the friction transducer to be correlated with the downward frictional force of the pin on disc. From figure 2.2

$$F_{friction} = \frac{x_2}{x_1} \cdot F_{transducer} \qquad (2.1)$$

where x_1 and x_2 are the perpendicular distances of the pin axis and transducer contact point from the main shaft axis respectively. The transducer output was amplified and fed to the second channel of the duel channel chart recorder for continuous recording.

Calibration of the friction transducer was accomplished by suspending known masses from a single pulley system which was connected to the transducer. A calibration factor of 0.167 N of frictional force per mm of pen recorder deflection was obtained for the 0-0.1 volt range setting of the recorder, which was the setting used for all of the experiments conducted. This factor was found to be constant

over the specified range.

2.5 Heat Flow Measurements

Temperatures at strategic points along the pin were measured by means of chromel-alumel thermocouples. The thermocouple wires were spot welded to the pin, after which it was fitted inside a sindanyo insulating jacket and placed inside a hollow cylindrical copper calorimeter. A diagram showing the arrangement of the pin-calorimeter assembly is shown in figure 2.4. The calorimeter was fixed securely inside the cylindrical hollow of a rectangular metal block by means of screws. The rear end of the pin was in contact with a copper disc situated inside the block. Outputs from the thermocouple wires were fed to an electronic thermometer.

From the measured temperatures various parameters could be determined according to the method used by Quinn (59), namely the general surface temperature of the pin, T_S, and the heat flow per second into the pin at the pin/disc interface, H_1. These quantities are given by:

$$T_S = (T_A - T_C)\cosh\left(\frac{L_1}{ZR_t}\right) + \frac{ZH_2}{K_S \pi R_t}\sinh\left(\frac{L_1}{ZR_t}\right) + T_C \qquad (2.2)$$

and

$$H_1 = \frac{\pi R_t K_S}{Z}\left[(T_A - T_C)\sinh\left(\frac{L_1}{ZR_t}\right) + H_2\cosh\left(\frac{L_1}{ZR_t}\right)\right] \qquad (2.3)$$

where:

$$Z = \left(\frac{K_S}{2R_t h}\right)^{\frac{1}{2}} \qquad (2.4)$$

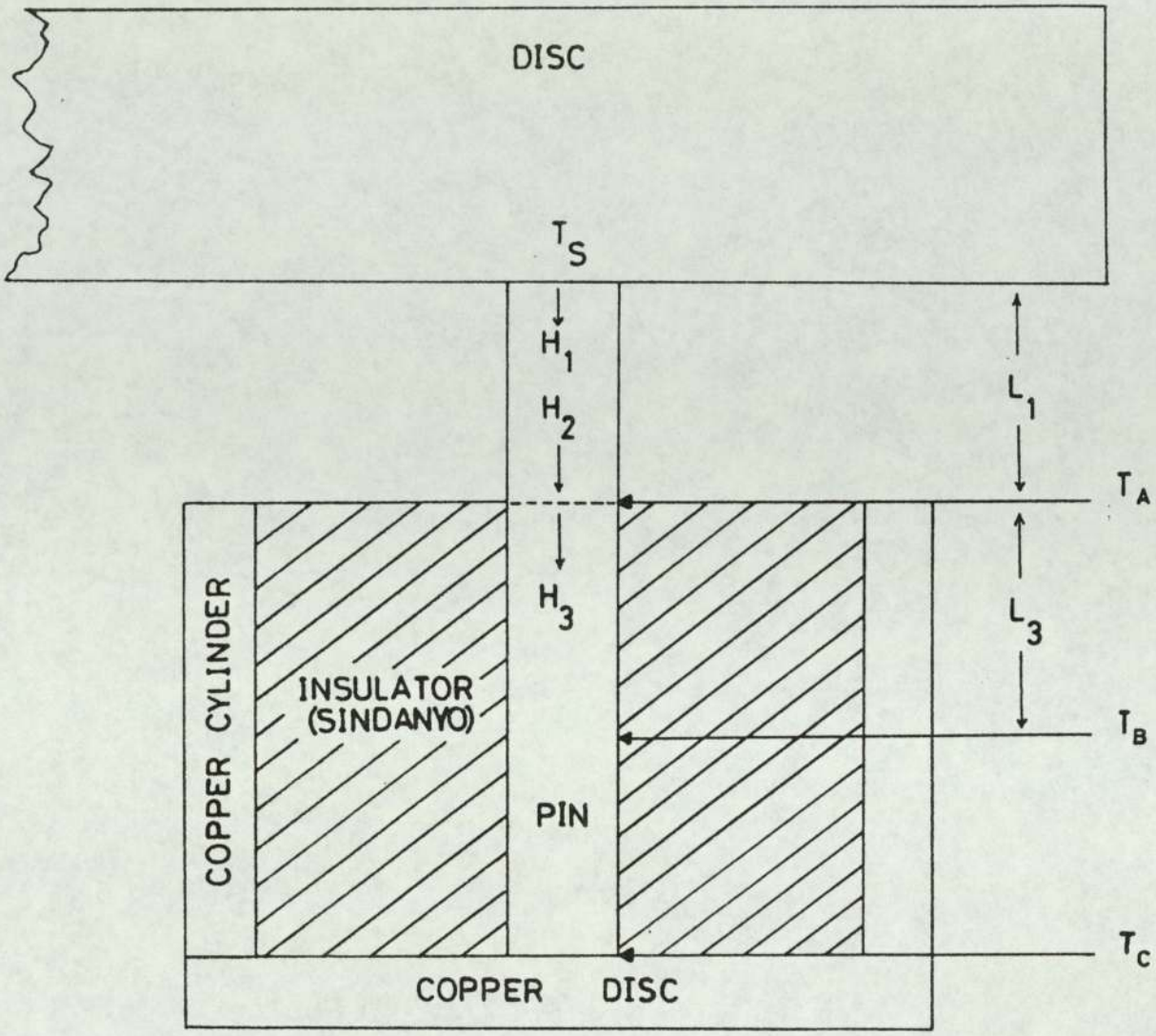

FIGURE 2.4 Cross sectional Diagram of the Calorimeter Assembly Showing Heat Flow and the Thermocouple Positions.

$$H_2 = H_3 + \frac{C(T_A - T_C)}{R_d - R_t} \qquad (2.5)$$

$$H_3 = K_s \pi R_t^2 M \left[\frac{(T_A - T_C)\cosh(ML_3) - (T_B - T_C)}{\sinh(ML_3)} \right] \qquad (2.6)$$

$$M^2 = \frac{2K_i}{K_s R_t^2 \ln(R_d/R_t)} \qquad (2.7)$$

h = heat transfer coefficient between exposed cylindrical surface of pin and the air

K_s = thermal conductivity of steel

K_i = thermal conductivity of insulating material

R_t = radius of the pin

R_d = outer radius of insulating material

C = conductance of thermocouple wire

L_1 = length of pin exposed to air between holder and disc

L_3 = length of pin between thermocouples measuring the temperatures T_A and T_B

General disc surface temperatures were measured by holding a thermocouple onto the disc face close to the wear track.

2.6 Specimen Materials

The materials used in the wear experiments were BS970 EN8, a low-alloy medium carbon steel, and a 9% chromium steel. The composition of these steels by mass is shown below:

Element	% composition BS970 EN8	9% Cr steel
C	0.35 - 0.45	0.11
Si	0.05 - 0.35	0.66
Mn	0.6 - 1.0	0.42
S	0.06 max	0.010
P	0.06	0.005
Cr	_	8.89
Mo	_	1.00
Ni	_	0.24
Fe	Remainder	Remainder

Both EN8 and 9% Cr steel were used as disc material, but only EN8 as pin material throughout the experiments.

2.7 Specimen Preparation

Pins of length 38 mm and diameter 6.35 mm were machined from EN8 cold-rolled rods and turned to a smooth finish of about 5μm Centre Line Average (CLA). The bulk hardness of the pins, measured using a Vickers Hardness Tester, was found to be 250±5 VPN.

Discs of 120 mm diameter and 12.5 mm thickness were cut from EN8 black bars and ground to a surface finish of approximately 0.2μm CLA. In order to facilitate surface examination of the worn discs, two tapered studs were inserted in each disc prior to surface grinding. The bulk hardness of the EN8 discs was 200±5 VPN.

The 9% Cr steel discs had a diameter of 127 mm and were 12 mm thick. As with the EN8 discs, two tapered studs were inserted in each disc prior to surface grinding to a 0.2μm CLA finish. The bulk hardness of the 9% Cr steel discs was 238±5 VPN.

Before each wear experiment both the pin and disc were degreased by washing in detergent and rinsing in water, followed by a thorough washing in acetone.

2.8 Wear Tests

EN8 wear tests were carried out at loads of between 5 N and 58 N, in increments of approximately 5 N, for speeds of $2.0\,ms^{-1}$ and $4.0\,ms^{-1}$.

At the beginning of each experiment there was a "running in" period during which there was a relatively high, non-uniform wear rate and frictional force. The debris produced during this period consisted mainly of large metallic particles indicating a severe wear regime. The end of this running in period, which usually lasted no longer than half an hour, was witnessed by a falling and levelling out of the wear rate and frictional force accompanied by a change in the nature of the wear debris to mainly oxide. It was this mild wear regime which was of interest in the present study.

Wear rates and frictional forces were recorded continuously on the duel channel chart recorder and the temperatures

T_A, T_B and T_C (figure 2.4) were measured regularly on the electronic thermometer and recorded. Debris was collected for each experimental run once it had been fully "run in" and mild wear had ensued.

Wear tests using EN8 pins loaded against 9% Cr steel discs were conducted at loads of between 10 N and 50 N in increments of 10 N for a speed of 2.0 ms^{-1}. The purpose of this was to test for oxide transfer from the disc to the pin. Any transfer, which would result in chromium being present in the oxide layer on the pin surface, could be detected by depth profiling in Auger electron spectroscopy.

CHAPTER 3

EXPERIMENTAL DETAILS OF SURFACE AND DEBRIS ANALYSIS

3.1 Introduction

This chapter describes the experimental methods used for investigating the growth of oxides on low alloy steel surfaces, under both static and tribological conditions.

In Section 3.3 the techniques employed in the investigation of the growth rates of oxides on low alloy steel under static conditions are described. The remaining sections are concerned with the analysis of a range of statically and tribologically produced oxide surfaces by various physical techniques. The analysis of successive layers in the surface oxide by means of Auger electron and x-ray photo-electron spectroscopy in conjunction with argon ion etching is described in Section 3.4, while Sections 3.5 and 3.6 give an account of the technique of x-ray diffraction for identifying the constituents of wear debris and surface oxides respectively. In Section 3.7 the use of scanning electron microscopy for the characterisation of worn surfaces and measurement of oxide thickness on worn surfaces is described.

3.2 Specimen Materials

The investigation of the static oxide growth rates on low alloy steel (Section 3.3) made use of two steels. The low

alloy steel used for the high temperature experiments above 450°C was commercially available feeler gauge strip, manufactured by Moore and Wright of Sheffield. It has the following percentage composition by mass:-

Element	% Composition
C	1.2 - 1.3
Si	0.3 max
Mn	0.25 - 0.45
P	0.025
S	0.025
Cr	0.15 - 0.3
Fe	Remainder

For the lower temperature, ellipsometric study of oxide growth rates BS970 EN8 low alloy steel was used, the composition of which has already been given in Section 2.6.

The specimens analysed by the various physical methods of analysis detailed in this chapter were either of the composition listed above, EN8, or 9% Cr steel.

The need for various standards in the x-ray photoelectron spectroscopic analyses introduced the use of various additional materials. High purity gold, silver and copper were used in calibrating the energy scale of the spectrometer. Commercially obtained, high purity powders α-Fe_2O_3, Fe_3O_4 and FeO along with 99.9% purity iron metal were used in obtaining standard XPS spectra of iron and its three oxides. Mounting of these powders for analysis

in the spectrometer involved the use of 99.9% pure soft lead sheet, supplied by Goodfellows Metals, Cambridge, along with 60 mesh gold powder obtained from Johnson Matthey Chemicals, Herts.

3.3 Oxidational Rate Constant Measurements

3.3.1 Introduction

In this section the methods used for measuring the rate of growth of oxides on low alloy steel under static conditions are described. The plotted rate curves could be described by established rate laws, and rate constants were measured. Using these rate constants it was possible to determine the activation energy, Q, and Arrhenius constant, A, for static oxidation.

3.3.2 Ellipsometry

Initially the sample was placed on a flat aluminium tray which was inserted into an electrically heated tubular furnace, which had been pre-heated to the required temperature. The ends of the furnace were blocked in order to maintain static air conditions around the sample. A chromel/alumel thermocouple was attached to the tray at a point very close to the sample and the temperature was monitored on an electronic thermometer. Temperature variation inside the oven did not exceed $\pm 5^{o}C$. After heating in the oven for a given period of time the sample was removed and the surface oxide film thickness measured

using an ellipsometer. The sample was then readmitted to the furnace for a further period of time after which it was again removed and analysed on the ellipsometer. This process was repeated several times so that the variation of film thickness with time could be determined.

Ellipsometry is a technique that enables the thickness of a thin film on a substrate to be determined by measurement of the change in the state of polarisation of light reflected from the film covered surface. It involves the determination of the optical properties of the surface film, which in turn enables the film thickness to be calculated.

The state of polarization of light is characterised by the phase and amplitude relationships between two component plane waves of the electric field vector into which the polarized oscillation may be resolved. The resolved components of the plane polarised light which is incident on the specimen are designated p and s, and represent the components parallel and perpendicular to the plane of incidence respectively. Reflection at the specimen surface causes a change in the relative phases of the p and s waves and a change in the ratio of their amplitudes, resulting in the reflected light being elliptically polarized. The elliptically polarized light then passes through a compensator (a ¼ wave plate) the purpose of which is to revert the light back to plane polarized light for analysis by the analyser. A diagram showing the arrangement of the ellipsometer components is shown in figure 3.1.

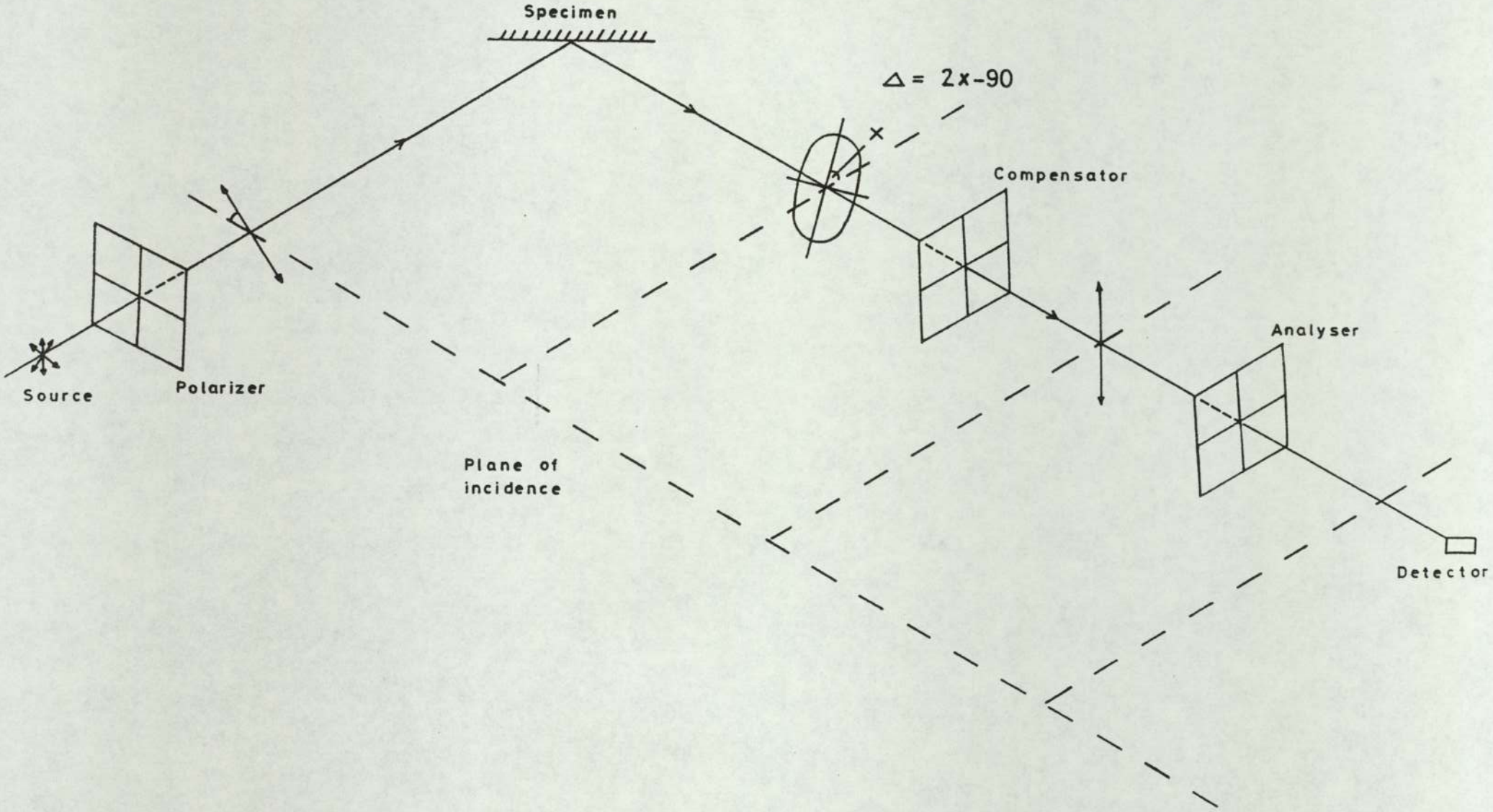

FIGURE 3.1 Arrangement of Ellipsometer Components

Analysis of each sample was performed with the compensator axis set at 45^{o} to one of its azimuthal directions. The polarizer was then rotated so that the axes of the ellipse produced by reflection at the sample surface also lay inclined at 45^{o} to the compensator azimuth. The resulting plane polarized light emerging from the compensator was then extinguished by rotation of the analyser. Four polarizer and four analyser extinction directions were obtainable with the compensator axis set at -45^{o} to an azimuthal direction and also with the axis set at $+45^{o}$ to this direction.

The basic equation of ellipsometry is:

$$\frac{r(p)}{r(s)} = \tan\psi . e^{i\Delta} \qquad (3.1)$$

where r(p) and r(s) are the respective Fresnel reflection coefficients parallel and perpendicular to the plane of incidence, $\tan\psi$ is the relative amplitude reduction ratio, and Δ is the relative phase difference. The purpose of the experimental ellipsometry was to determine the parameters ψ and Δ. The parameter ψ was determined from the polarizer extinction settings and reference azimuths as shown in figure 3.2(a), while figure 3.2(b) shows how Δ is related to the corresponding analyser settings. A full description of the method of determining ψ and Δ from the experimental readings is given by McCrackin et al (60).

In order to determine film thicknesses it was also necessary to determine the optical constants, n and k, both of the film and of the substrate. The optical

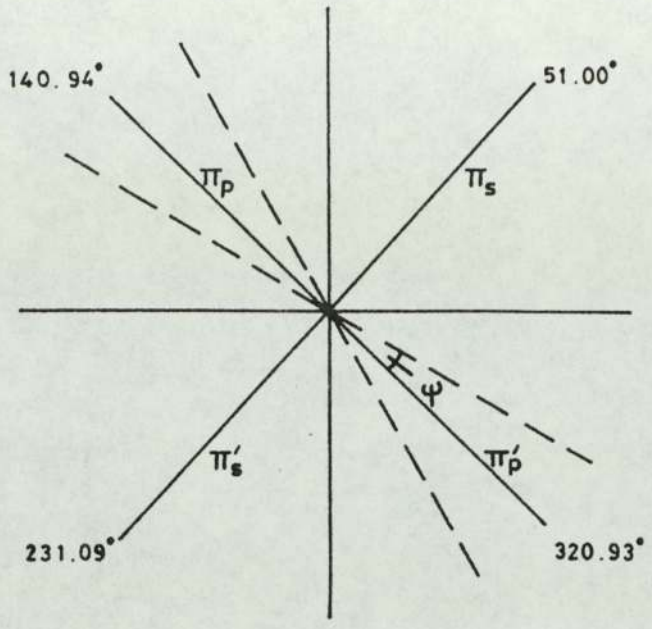

FIGURE 3.2 (a) Polariser Azimuths and Experimental Exctinction Directions.

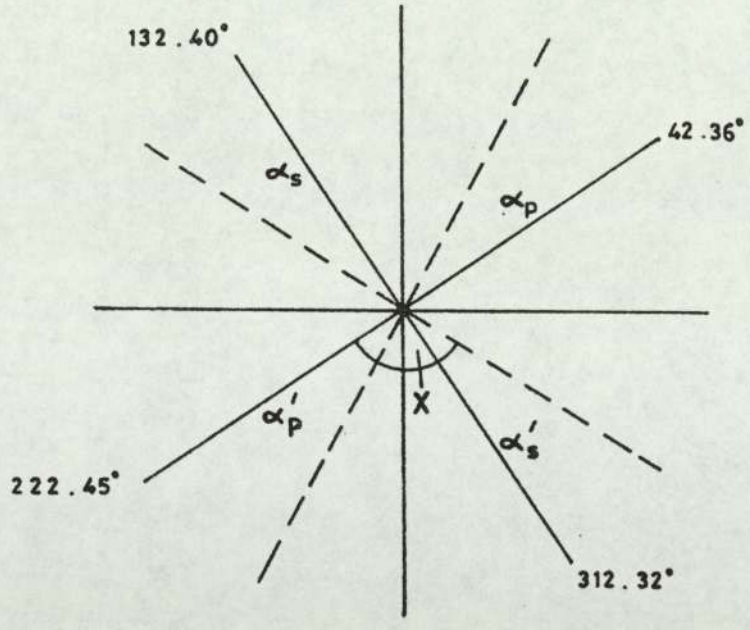

FIGURE 3.2 (b) Analyser Azimuths and Experimental Exctinction Directions.

— — — Experimental extinction directions (with compensator set at ±45° to one of its azimuths)

——— Polarizer and analyser azimuths.

constants of the substrate were determined by measuring the optical parameters Ψ and Δ of the polished metal surface, although a very thin film of oxide would always be present when exposed to air. The calculation of these substrate constants was performed by means of a computer program based on the Ditchburn equations (61), which express n and k for the substrate in terms of the angle of incidence, wavelength of light, and the measured values of Ψ and Δ . The wavelength of light used was 5461 $\mathring{A}$ and its angle of incidence to the sample surface was 1.0685 radians. The values obtained from the computer program were:-

$$n(\text{substrate}) = 2.34$$
$$k(\text{substrate}) = 3.32$$

The oxide thickness values corresponding to the measured Ψ and Δ values were also determined by means of a computer program (62). The optical constants n and k for the oxide were varied to give a range of theoretical $\Psi - \Delta$ - thickness curves. Values for n and k were chosen which gave the best fit between the experimental $\Psi - \Delta$ curves and the theoretical computer generated $\Psi - \Delta$ curves. The optical constants which gave the best fit were:-

$$n(\text{oxide}) = 2.88$$
$$k(\text{oxide}) = 0.37$$

The oxide thicknesses corresponding to the measured Ψ and Δ values were then obtained from the theoretical $\Psi - \Delta$ - thickness curve generated by these n and k values.

3.3.3 Mass Increase Method

Above 450°C the oxides produced were sufficiently thick as to allow the rate of oxide growth to be determined by measurement of increases in mass.

All samples were rectangular in shape. The samples oxidised at 600°C and below were held in a specially constructed sample holder which secured each corner of the sample by means of small screws and washers. The washers very slightly overlapped each corner of the sample. This was necessary in order to prevent curling of the sample, which would have resulted in cracking or peeling of the oxide scale. The design of the holder was such that both sides of the sample were exposed to air.

Above 600°C thicker samples were used, since the thinner samples soon became completely oxidised at these higher temperatures. These samples resisted curling under high temperature conditions enabling the use of a simpler sample holder, namely a glass boat. The curvature and size of the glass boat was such that each sample was only in contact with the boat along both edges of its length. Again both sides of each sample were exposed to air.

Each sample was first cleaned and dried thoroughly before its initial weighing on an electric balance, calibrated to read to an accuracy of 0.1 mg. It was then mounted carefully in the sampler holder after which the holder was inserted into a tubular furnace which had been pre-heated

to the required temperature. A chromel/alumel thermocouple was attached to the sample holder at a point very close to the sample. The temperature was monitored on an electronic thermometer, and variations in the sample temperature did not exceed $\pm 5^{o}C$. After a given period of time the sample was removed from the furnace, cooled and re-weighed. It was then returned to the oven for a further period of time after which it was again removed and re-weighed. This procedure was repeated several times in order that the mass increase as a function of time could be determined.

3.3.4 Specimen Preparation

The samples used in the ellipsometric oxidation studies were circular discs of EN8 steel, 12 mm in diameter and approximately 1.27 mm thick. One face of the sample was polished using a series of silicon carbide wheels before being diamond polished to a 1μm finish. The sample was then cleaned by washing in detergent and water followed by a thorough washing in acetone. After allowing the sample to dry completely it was ready for oxidation and analysis by the ellipsometer.

For the determination of oxidation rates by the mass increase method low alloy steel in the form of thin strips was used. The strips were of width 12.5 mm and were cut into 30 mm lengths. Three thicknesses were used. For the experiments between $450^{o}C$ and $600^{o}C$ the samples were 0.0254 mm thick. At temperatures above $600^{o}C$ thicker samples were used, of thickness 0.127 mm and 0.254 mm, since samples

of only 0.0254 mm thickness soon became completely oxidised. Each sample was thoroughly degreased by washing in detergent and water followed by washing in acetone. After being allowed to dry completely the sample was ready to be given its initial weighing.

3.3.5 Range of Experiments

The investigation of oxidation rates by means of ellipsometric oxide thickness measurements was carried out for oxidation temperatures of 150°C, 180°C, 200°C, 250°C and 300°C. Above 300°C the oxide films produced were too thick to enable thickness determination by means of ellipsometry.

The mass increase method was employed to determine the oxidation rate at temperatures of 450°C, 470°C, 500°C, 550°C, 600°C, 650°C, 700°C, 750°C and 800°C. At temperatures below 450°C the mass increases due to oxidation were too small to enable accurate measurement.

The measurement of oxidation rates over this wide range of temperatures enabled the determination of the activation energy and Arrhenius constant for the three different temperature regions of iron oxidation, corresponding to the predominant oxide being α-Fe_2O_3, Fe_3O_4 or FeO.

3.4 Auger Electron Spectroscopy (AES) and X-ray Photoelectron Spectroscopy (XPS)

3.4.1 General Features of the Electron Spectrometer

The electron spectrometer used for the analysis of surfaces was an XSAM 800 instrument manufactured by Kratos. It is based on a hemispherical electrostatic electron energy analyser but it is fitted with a sophisticated electron optical system which enables high resolution x-ray photoelectron spectroscopy to be combined with a high transmission (high sensitivity) Scanning Auger microprobe (SAM) in the same instrument.

The essential features of the electron spectrometer are excitation sources for the production of Auger electrons and photoelectrons in the sample surface, an electron energy analyser which sorts out the electrons emitted from the surface according to their energy, a detector system for detecting the electrons emerging from the analyser, an ion etching gun for depth profiling, and an ultra-high vacuum (UHV) system. Figures 3.3(a) and 3.3(b) show the arrangement of the main components around the specimen analysis chamber (SAC). Figure 3.4 is a photograph of the whole spectrometer system, and figure 3.5. is a schematic diagram of the scanning Auger facility.

3.4.2 Spectrometer Excitation Sources

The spectrometer has two excitation sources, a duel anode

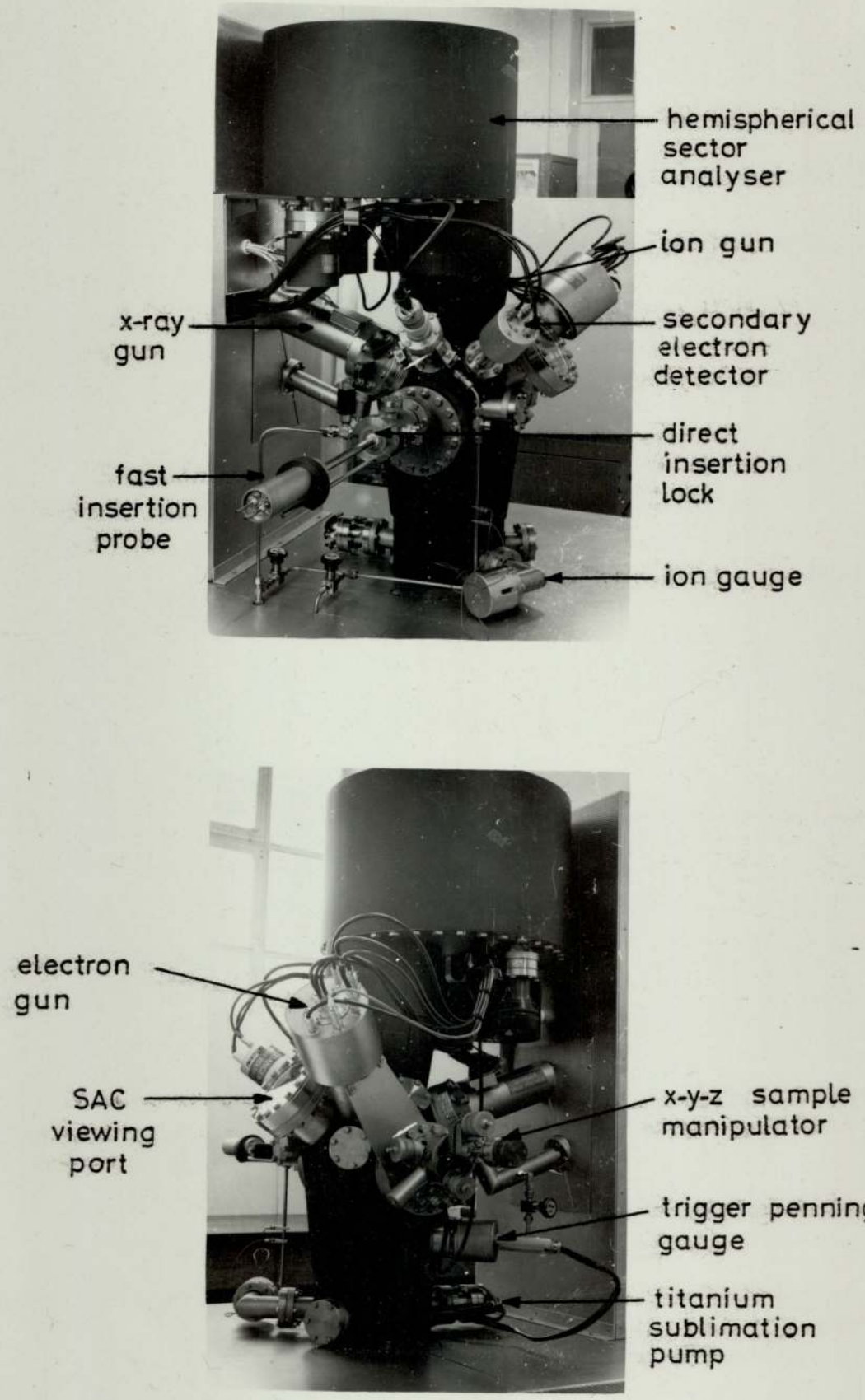

FIGURE 3.3 Arrangement of Main Components Around Specimen Analysis Chamber.

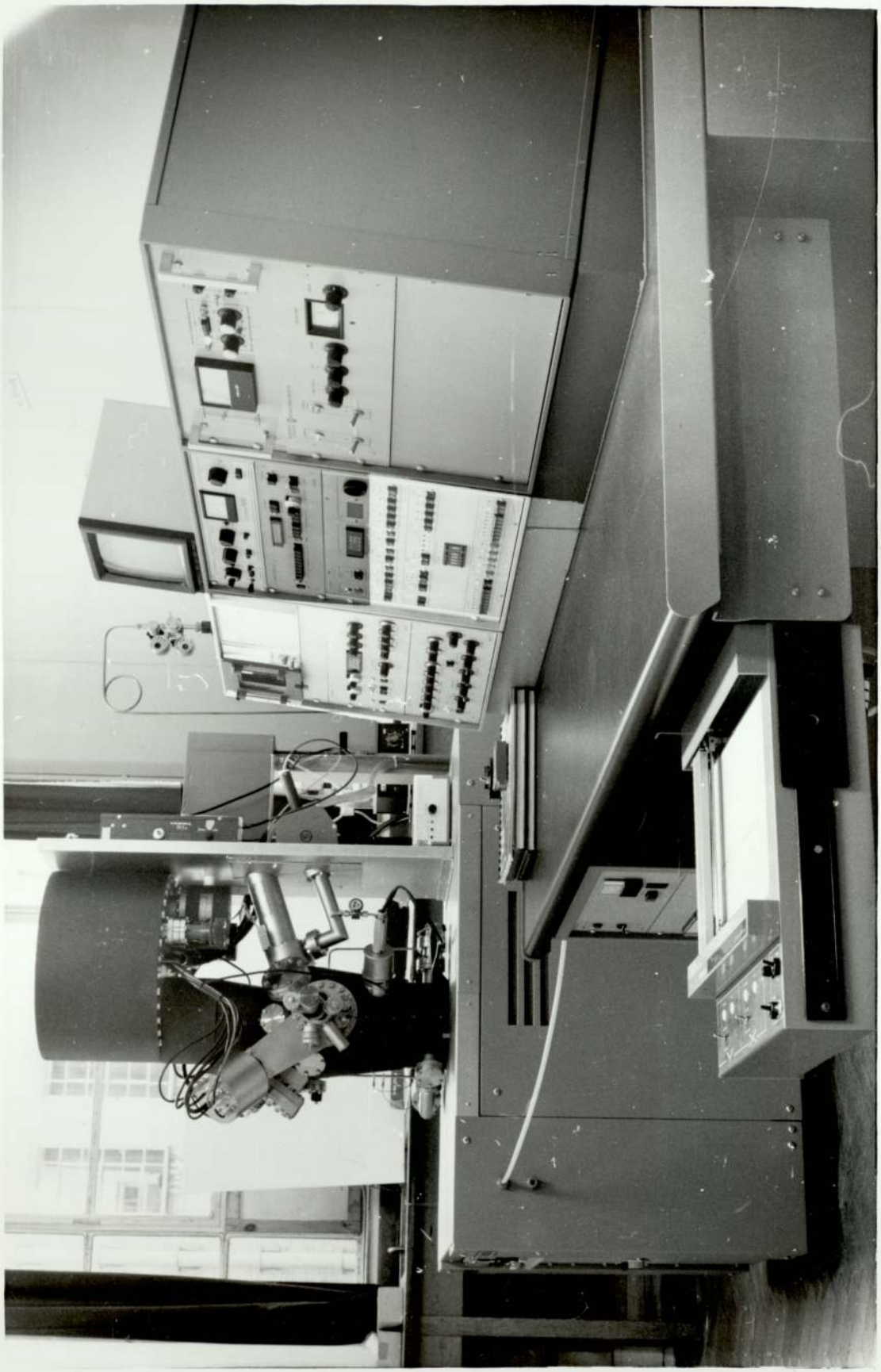

FIGURE 3.4 The XSAM 800 Electron Spectrometer.

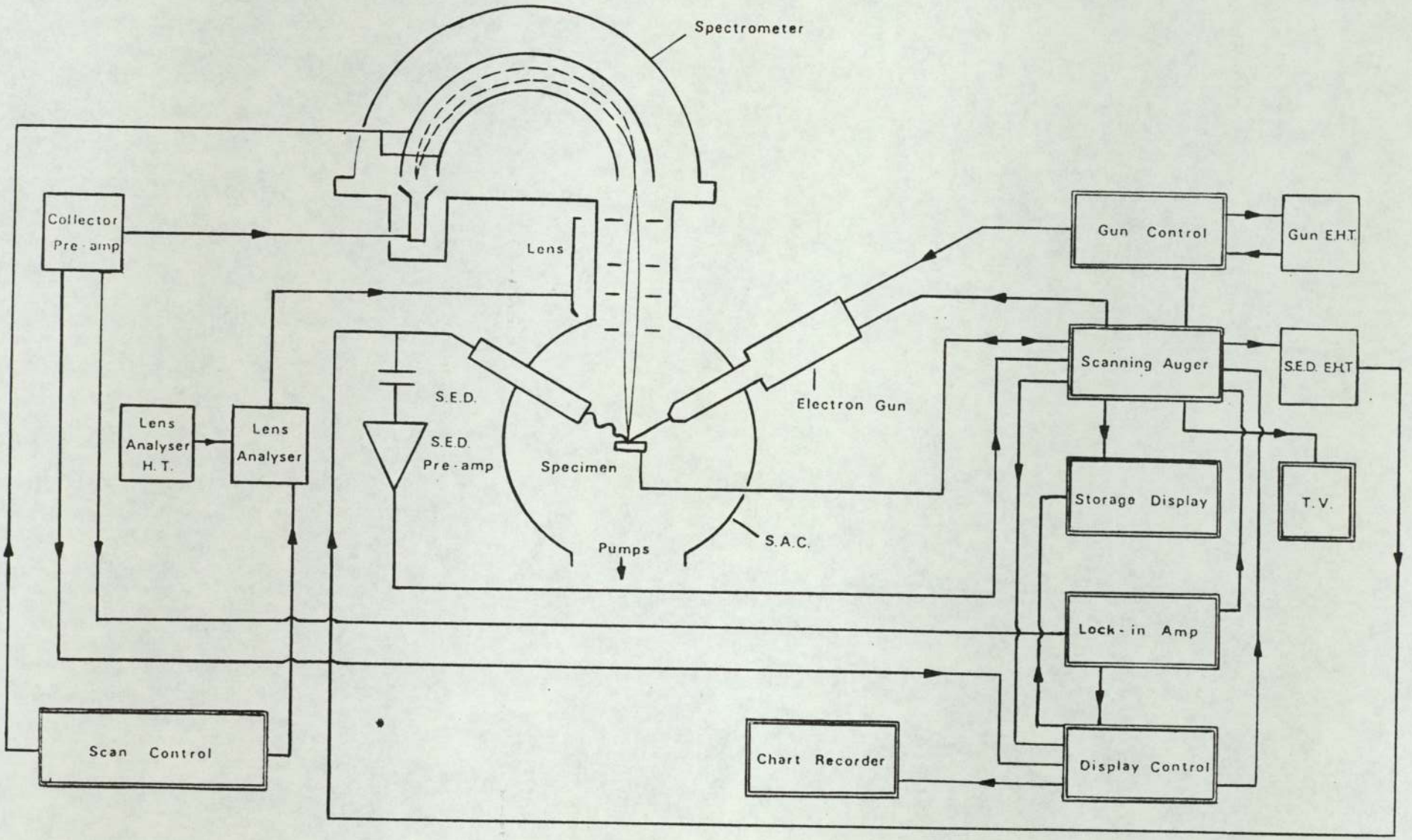

FIGURE 3.5 Schematic Diagram of the XSAM 800 Scanning Auger Facility.

x-ray gun and an electron gun. The duel anode x-ray gun produces Mg(Kα) or Al(Kα) radiation having respective energies of 1253.6 eV and 1486.6 eV which provides the exciting radiation for XPS analysis. The electron gun, for use in AES, consists of a heated tungsten filament in a triode emission assembly followed by a demagnifying/ focussing lens system which reduces the apparent diameter of the source and focusses the beam onto the specimen. Two pairs of orthogonal deflection plates are mounted after the final focussing lens and these serve to vary the position of the beam spot on the surface. A range of spot sizes down to less than 1μm in diameter can be produced by the electron gun.

3.4.3 The Electron Energy Analyser

The spectrometer electron energy analyser is a type of dispersive electrostatic analyser known as a hemispherical sector analyser (HSA). The main feature of the dispersive electrostatic analyser is that it only admits electrons in the energy range E to E+ΔE, where E is the pass energy and ΔE is the energy window. The HSA is generally noted for its high energy resolution capability, but in the present case high resolution has been combined with high transmission by means of an aberration compensated input lens (ACIL). The way in which this is achieved may be illustrated by a simple example. The resolving power of an HSA for a point source imaged into a point image may be stated in its simplest form as:

$$\text{Resolving power} = \frac{E}{\Delta E} = \frac{2R}{W} \qquad (3.2)$$

where R is the mean radius of the analyser, and W is the average width of the slits at the entrance and exit of the analyser. Using this expression it can be seen that a mean analyser radius of 127 mm and a mean slit width of 3 mm, which are typical XSAM 800 analyser operating conditions, results in a resolving power of ~85. Thus for a 1000 eV electron the resolution is 11.8 eV, which is inadequate for XPS and AES work. The input lens overcomes this problem by retarding the electrons to a fixed energy of say 65 eV so that the resolution becomes 0.76 eV. In fact three transmission energies of 20, 38 and 65 eV are available on the XSAM 800. The main disadvantage in using the retardation input lens is that the collected photoelectron current is made smaller on account of the acceptance angle of the input lens being smaller than that of the energy analyser.

An additional means of controlling instrument resolution and sensitivity is provided by two adjustable slits at the entrance and exit of the spectrometer analyser. A single control alters the width of both slits simultaneously, slit widths of 1, 2, 3 and 5 mm being available. The smaller slit width provides maximum resolution with minimum sensitivity. The AES and XPS spectra presented in this thesis were conducted with the slit widths adjusted to the largest settings in order to obtain maximum sensitivity.

Two modes of spectrometer magnification are possible as a consequence of using an input lens. These are denoted by high and low settings on the control console. In low

magnification the input lens accepts electrons only through a narrow angle although a large number of cones can be accepted resulting in a wide area of surface analysis. This is ideal for maximising the signal intensity in XPS analysis where the area of the sample illuminated by the x-ray source is relatively large. In the high magnification mode the input lens accepts electrons through a wide angle which have originated from a small spot on the surface, making it ideal for AES analysis. The low magnification mode was employed to produce the XPS spectra presented in this thesis, while the high magnification mode was used to produce the Auger spectra.

In addition to the various resolutions, sensitivity and magnification settings which have been discussed there are also two general analyser operating modes known as Fixed Analyser Transmission (FAT) and Fixed Retarding Ratio (FRR). In the FAT mode the transmission energy of the analyser is maintained constant so that electrons entering the HSA have their energies retarded by a varying proportion, depending upon their kinetic energy. Three transmission energies are possible on the XSAM 800, as mentioned earlier, and these are selected by a resolution setting on the spectrometer operating console. The transmission energies of 20, 38 and 65 eV correspond to the respective resolution settings of high, medium and low. In the FAT mode the resolution is constant throughout the whole kinetic energy range, but the sensitivity is inversely proportional to the kinetic energy.

In the FRR mode electrons entering the analyser system have their energy retarded by a constant proportion of their initial energy. Throughout the energy scan range the transmission energy of the analyser is continuously varied in order to maintain the constant retarding ratio. Four retarding ratios are possible and these are set by the resolution and magnification settings. In this mode the resolution and sensitivity vary with kinetic energy, the sensitivity being proportional to the kinetic energy at the sample.

The analyser mode chosen depends upon the type of information required. The AES and XPS spectra presented in this thesis were obtained with the analyser operating in the FRR mode. This mode was chosen for a number of reasons. Firstly, it is desirable that inter-spectrometer spectrum comparisons be made in the future. This is difficult at low energies when operating in the FAT mode since under these conditions the transmission behaviour is a very individual property of the analyser (63). Secondly, the great difference produced in the intensities of the high and low energy Auger electron peaks in the FAT mode make the spectra inconvenient to use (63). Thirdly, the AES and XPS peaks of interest obtained using the FRR mode were of adequate intensity.

A low resolution setting was used to obtain all Auger spectra in this present work since it gave maximum sensitivity while providing more than adequate resolution for the Auger peaks of interest. For the generation of XPS

spectra, where the determination of accurate binding energies was required, a higher resolution was needed. It was found that a medium resolution setting provided adequate resolution while maintaining a reasonable signal intensity.

3.4.4 The Electron Detection System

The electrons which are allowed to pass through the electron energy analyser are detected by an electron multiplier of the Channeltron type, the output of which is amplified by a pre-amplifier before being fed to a ratemeter. Two detection modes are available in this system, these being the pulse mode (Δq) and current mode ($\int$). The pulse mode gives a true count rate, on the ratemeter, while the current mode is particularly useful at very high count rates when the multiplier operated in the pulse mode can become saturated. Both detection modes were used in producing the spectra displayed in this thesis. The preamplifier also has a lock-in setting for when the lock in amplifier is used to obtain differentiated Auger spectra.

3.4.5 Recording of Surface Analysis Information

In this section the various forms in which the surface analysis data was obtained is described, along with the spectrometer apparatus which facilitated the recording of the data in these forms.

In the analysis of surfaces by x-ray photoelectron spectroscopy spectra have been presented in the conventional manner i.e. the number of electrons with energy E emitted from the surface N(E) as a function of the electron energy E. Strictly speaking, however, EN(E) as a function of E is obtained using a hemispherical sector analyser operating in the FRR mode (or $E^{-1}N(E)$ as a function of E in the FAT mode except at low energies) (64).

In the case of Auger analysis, spectra were almost always obtained in the conventional differentiated mode, and all of the Auger spectra presented in a later chapter are in this form. There are a number of reasons for this. Firstly, most Auger spectra are presented in this mode today. This is probably as a result of the ease of measuring relative elemental concentrations from peak to peak heights and also as a consequence of the majority of data banks of elemental sensitivity factors being presented for use with differentiated spectra. Secondly, differentiation of the spectra reduces the large secondary electron background upon which the Auger electrons are superimposed, which is the historical reason for developing this technique.

The electronic device used to differentiate the Auger signal was a lock-in amplifier. It does this by first supplying a signal at a set frequency which is used to modulate the Auger electron energy. The modulated signal from the electron detector is then fed to the lock-in amplifier which contains a phase sensitive detector running synchronously with the modulation frequency. The phase

sensitive detector produces an output only for signals which are in phase and of the same frequency as the modulation frequency, the resultant output being a differentiated, amplified signal with the background component largely removed (65). When this signal is displayed against the spectrometer pass energy the dN(E)/dE spectrum is obtained.

In the analysis of surfaces by XPS the area of the sample analysed was relatively large since it is not possible to focus an X-ray source into a fine beam. By contrast electrons can be focussed into a fine beam, and this enabled the Auger analysis of small surface areas, typically of the order of a few μm in diameter. In addition to Auger point analysis it was also possible to produce elemental maps of the surface, which reveal the variation in concentration of a selected element over the surface. This was accomplished by means of a scanning Auger microprobe (SAM) facility. It operates by rastering the electron beam across the surface of the sample. The pass energy of the electron energy analyser is pre-set at the negative excursion of the Auger peak of interest, and the detected electron signal is fed to the lock-in amplifier, the output of which is used to modulate the brightness of a cathode ray tube (CRT) display which is scanning in synchronism with the electron beam scan. Thus, the intensity of the display at any point is a measure of the selected Auger peak height at that point. Elemental maps of interest were photographed by a camera which could be mounted on the front of the CRT display.

A secondary electron image of each surface could also be obtained by operating the system as a scanning electron microscope. The method is similar to that for obtaining Auger elemental maps only in this case the secondary electron signal is used to modulate the CRT display. SEM photographs of selected areas of samples were taken, and these were particularly useful when compared with the corresponding elemental maps, so that topographical features could be correlated with the concentrations of particular elements. In addition to the CRT display, the SEM image could also be shown on a T.V. monitor.

The Auger and XPS spectra could be recorded on the display of the CRT, but usually they were permanently recorded by means of an x-y chart recorder.

3.4.6 The Vacuum System

The spectrometer pumping system consists essentially of a diffusion pump backed by two rotary pumps. A liquid nitrogen filled baffle mounted above the mouth of the diffusion pump provides a cold trap for reducing the amount of pump fluid entering the vacuum system, while the rotary pumps are equipped with molecular sieve traps. In addition, a titanium sublimation pump provides a means of pumping active gases by chemical combination, using the active surface gettering method. This pump was used intermittently, a few minutes of pumping every ten hours being required in the pressure range 10^{-9}-10^{-10} torr (66). The twin anode x-ray gun is pumped independently by an ion pump. The sample

analysis chamber (SAC) was baked at 150°C fairly regularly to expel any adsorbed gases on the SAC walls.

The pumping system was used to maintain UHV conditions inside the SAC during surface analysis, the pressure being around 10^{-9} torr. Pressure monitoring in the SAC is provided by means of an ionisation gauge, and also a trigger-penning gauge for accurate measurement in the UHV range.

A direct insertion lock enables samples to be admitted into the SAC in a matter of only a few minutes without degradation of the vacuum.

3.4.7 Spectrometer Operating Conditions

The following spectrometer operating conditions were employed for the analysis of surfaces and the production of the spectra displayed in this thesis, unless otherwise stated.

(a) Auger Electron Spectroscopy

Electron gun EHT : 5 kV

Electron gun filament current : 2.75 A

Spot size : 4($\leqslant 5\mu m$) or 2($\leqslant 20\mu m$)

Analyser mode : FRR

Analyser slit widths : 5 mm (max settings)

Resolution : low

Magnification : high

Spectrum mode : dN(E)/dE

Scan time : 300 s, 1000 s

Time constant : various

Signal sensitivity : various

Modulation : 5 V p : p, or 2 V p : p for higher resolution work

Pre-amplifier setting : lock-in

SAC pressure : $\sim 1 \times 10^{-9}$ torr

Oxygen map : 125 lines, 100 s frame period, lock-in time constant 30 ms

SEM image : 500 lines, 10 s frame period, N(E) mode

(b) X-Ray Photoelectron Spectroscopy

X-ray source EHT : 15 kV

X-ray source filament current : 30 mA, unless otherwise specified

Analyser mode : FRR

Analyser slit widths : 5 mm

Resolution : medium

Magnification : low

Spectrum mode : N(E)

Scan time : 300 s, 1000 s

Response time : various

Pre-amplifier setting : both pulse mode (Δq) and current mode ($\int$) were used

SAC pressure : $\sim 1 \times 10^{-9}$ torr

(c) Argon Ion Etching

Ion gun EHT : 2 kV

Ion gun emission current : 25 mA

Argon pressure in SAC during etching : $\sim 5 \times 10^{-5}$ torr

Specimen current : varies, but usually 15-25 μA

3.4.8 Specimen Types and Preparation

A variety of samples were analysed by means of AES and XPS, but these can be divided into four main groups:-

(i) Metal foils which were used to set up the spectrometer energy scale and to provide reference binding energies.

(ii) Low alloy steel oxidised in a furnace (Section 3.3.2 & 3.3.3)

(iii) Tribological samples produced using the wear test rig (Section 2.2)

(iv) Oxide powders which were used to obtain standard spectra of the three oxides of iron in order to facilitate accurate determinations of the spectral

peak chemical shifts with change in oxide

The metal foils were cut into rectangular strips having approximate dimensions of 15 mm by 4 mm, in order to facilitate mounting onto the sample holder. The surfaces were cleaned using Brasso followed by a thorough washing in acetone, before being mounted ready for insertion into the SAC.

The statically oxidised samples were of two types: low alloy steel sheet (Section 3.2), and low alloy steel circular discs, one surface of which had been finely polished prior to being oxidised (Section 3.3.4). The oxidised steel sheet was cut into rectangular strips as for the metal foils. The oxidised discs were cut in half to produce semicircular samples in order that they could be inserted through the entrance port to the analysis chamber. No surface cleaning or treatment was applied to the samples as this would obviously have contaminated the oxide surface.

The tribological samples comprised worn pins and worn studs taken from discs (Section 2.7). The pins and studs had to be cut to a length of approximately 2 mm in order for them to be inserted through the entrance port of the sample analysis chamber. Sample surfaces which had a relatively high degree of oxide debris present were repeatedly wiped with dry cotton wool before being admitted into the SAC. No other surface treatment was carried out.

The oxide powders could not be admitted into the UHV of the analysis chamber in loose powder form and so it was decided to mount them on lead sheet. This was accomplished by first covering one half of a small sheet of lead (approximately 40 mm x 40 mm) with the oxide powder. The other half of the lead sheet was then folded over the powder and the two halves compressed together in a vice, embedding the powder into the surface of the soft metal. The two halves were then separated yielding two specimens for analysis. Any loose powder remaining on the surface was removed by gently tapping the sample. Prior to this mounting procedure the oxide powder was intimately mixed with gold powder in order to provide a reference binding energy. Once the mounting of the powder had been completed a rectangular sample of dimensions 15 mm x 4 mm was cut from the sheet ready for fixing onto the sample holder.

Careful sample handling techniques were followed at all times. Vinyl gloves were worn when preparing samples and when mounting them on sample holders ready for insertion into the analysis chamber, and whenever possible samples were held with tweezers. These procedures were followed in order to minimise hydrocarbon contamination of the sample surface and to help maintain UHV conditions within the sample analysis chamber.

3.4.9 Calibration of the Spectrometer Energy Scale

A gold foil sample was used in calibrating the energy scale of the spectrometer. After cleaning, the rectangular

foil sample was secured onto a sample holder by means of small clips, and this in turn was attached to the end of the fast insertion probe (FIP). This device enables specimens to be admitted into the sample analysis chamber (SAC) via the direct insertion lock in a matter of only a few minutes without degradation of the vacuum. Once inside the SAC the sample was positioned so that the surface to be examined was in the correct position with respect to the x-ray gun. This was simply accomplished manually using the end of the FIP while viewing the sample through the window port of the SAC. The sample was then earthed by connecting the end of the FIP to the metallic spectrometer casing.

The spectrometer was calibrated by the single sample, dual anode x-ray source method. Adjustments were made to the coarse and fine potentiometers located on the analyser high voltage supply and this altered the relation between energy scale digi-switch settings on the operating console and analyser voltages. Now the kinetic energy of a photo-electron as passed by the spectrometer (E_{KE}) is given by:

$$E_{KE} = h\nu - E_{BE} - \phi_A \qquad (3.3)$$

where $h\nu$ is the energy of the incidence x-ray photons

$h\nu$ = 1253.6 eV for Mg($K\alpha$) radiation

= 1486.6 eV for Al($K\alpha$) radiation

E_{BE} is the binding energy of the emitted photoelectron

ϕ_A is the spectrometer work function

Since the difference between the photon kinetic energies

of Mg(Kα) and Al(Kα) radiation is assumed to be exactly 233.0 eV, then we would expect from equation (3.3) above that the separation between a photoelectron peak produced by Mg(Kα) and the corresponding peak produced by Al(Kα) would also be 233.0 eV for a correctly calibrated energy scale. Thus the potentiometer adjustments were made until this was so for the standard $Au4f_{7/2}$ photoelectron peak. The digi-switch settings now differed from tabulated kinetic energies by an amount equal to the spectrometer work function. The calibration of the energy scale and the value of the spectrometer work function were checked regularly during the surface analysis work presented in this thesis.

Silver and copper foils were also used as a check that correct calibration had been achieved. Separations of the $Ag3d_{5/2}$ peaks, and of the $Cu2p_{3/2}$ peaks, produced by Mg(Kα) and Al(Kα) radiations were 233.0 eV indicating a correctly calibrated, linear energy scale.

3.4.10 Analysis of Iron and Iron Oxide Standards

The three oxide powder surfaces which were studied by means of XPS were α-Fe_2O_3, Fe_3O_4 and FeO. The purpose of this study was to obtain core level electron spectra characteristics of the three oxides and to determine any chemical shifts in the photoelectron peak binding energies. This information could then be used as a reference in identifying the chemical composition of oxides produced in various ways on low alloy steel surfaces.

The rectangular sample having the oxide powder surface to be analysed was secured onto a sample holder by means of small screws, and inserted into the SAC on the end of the FIP. The sample was then earthed to the metallic spectrometer casing.

XPS analysis of the oxide powder surfaces was carried out using the operating conditions stated in Section 3.4.7. $Fe2p_{3/2}$, $2p_{1/2}$, 3p, 3s, O1s and $Au4f_{7/2}$ spectra were recorded. Binding energy measurements were made relative to the $Au4f_{7/2}$ peak at 84.0 eV. It was also considered useful to record the C1s spectra due to hydrocarbons on the sample surfaces as the binding energy of this line is often used as a reference value in XPS work.

Initially spectra were recorded for unetched oxide powder surfaces. The surfaces were then etched with Ar^+ ions under the conditions stated in Section 3.4.7 before being re-analysed. Periods of etching were varied from less than one minute up to a total of one hour. Etching of the oxide powder surfaces was performed for two reasons: firstly to remove any surface contaminant layers to reveal the true oxide underneath, and secondly to investigate the effect of etching upon the composition and structure of the oxide itself.

In the case of Fe_3O_4 a sample was also electrically heated under the UHV conditions of the SAC. This was carried out in an attempt to remove any adsorbed water on the sample surface, and also to decompose any α-Fe_2O_3 which

was present as a result of surface oxidation. The sample was heated up to a maximum indicated probe temperature of 600°C in steps of 100°C. Each temperature was maintained for a period of around two hours, while monitoring the Fe and O photoelectron spectra.

Fe metal was also analysed by XPS, both in the unetched and etched states. The rectangular iron sheet sample was analysed while attached to the end of the FIP, as for the iron oxide powder samples.

3.4.11 Analysis of Statically Oxidised Samples

Selected low alloy steel samples which had been oxidised at various temperatures in a furnace were analysed by means of XPS. Each sample was analysed while mounted on a holder attached to the end of the FIP. $Fe2p_{3/2}$, $2p_{1/2}$, O1s and C1s photoelectron peaks were recorded, and the Fe3p and 3s peaks were occasionally obtained also.

Each sample was first analysed in the unetched state. It was then argon ion etched for successive periods, from less than one minute up to a total of around one hour, under the conditions stated in Section 3.4.7. The photoelectron spectra of concern were recorded at the end of each of the etching periods.

3.4.12 Analysis of Worn Surfaces

Worn surface specimens in the form of pins and round studs

taken from discs were analysed by XPS and AES. Initially the sample to be analysed was mounted on a metallic stub fixed onto the end of the FIP. After being inserted into the SAC, the stub containing the worn sample was transferred from the end of the FIP to a specimen holder situated in the analysis area. The orientation and position of this specimen holder can be varied by an x-y-z manipulator. In addition, modulation can be applied to the sample via the sample holder when analysis in the differentiated Auger mode is required.

The initial step in the anlysis was to view the worn surface in the SEM mode on the TV monitor screen. The x-y-z manipulator was adjusted until a suitable area of the surface was in view, usually a well defined oxide plateau. When this had been done an SEM image was also produced on the CRT display situated on the spectrometer operating console. The incident electron beam on the sample surface was then displayed as a small spot on the SEM image. The position of the spot was altered until it was suitably placed, usually in the centre of an oxide plateau. The sample had now been set up for the point Auger analysis of an oxide plateau on the worn surface.

Point Auger analysis and XPS analysis of the worn surface were carried out in conjunction with argon ion etching. A period of etching would be followed by the plotting of an Auger spectrum in the differentiated mode, usually a large energy range scan containing all the peaks of interest (C, O, Fe, Cr), plus narrow energy range XPS scans of these

elements. In this way relative elemental concentrations in the surface layers of the sample were obtained (AES) along with information on their chemical states (XPS). In addition to the spectra, SEM images and corresponding oxygen maps of the worn surfaces were also monitored. Selected images and maps were photographed.

Selected samples from experiments where EN8 pins were worn against EN8 discs were analysed in this manner. Samples produced in experiments where EN8 pins had been worn against 9% Cr discs were also analysed in this way, although in this case more emphasis was placed on Auger analysis.

3.5 Powder X-Ray Diffraction of Wear Debris

The constituents of the debris from each wear experiment were identified by means of x-ray diffraction using the Debye-Scherrer technique. The debris was placed in a fine glass capillary tube of 0.5 mm diameter, which was then mounted in a conventional powder diffraction camera. The camera had an inside diameter of 180 mm, so that 1 mm displacement of the x-ray film corresponded to 1^{o} in the angle 2θ (where θ is the Bragg angle), enabling direct measurement of 2θ values. Cobalt Kα radiation was used to irradiate the debris as it has a relatively low mass adsorption coefficient for iron. The x-ray tube was operated at 40 kV and 30 mA, with exposure times of around 1 hour being typical. The constituents of the debris were identified by comparison of the interplanar spacings

obtained from the diffraction pattern with interplanar spacings listed in the x-ray powder data file of the American Society for Testing and Materials (ASTM) (67).

3.6 Glancing Angle X-Ray Diffraction

Glancing angle diffraction analysis was carried out on selected worn pin and disc (stud) surfaces and also on statically oxidised steel surfaces. In this technique the sample was positioned at the centre of a powder camera such that the impinging x-rays were incident on the edge of the sample surface at a glancing angle of around 20^{o}-30^{o}. As for the powder diffraction analysis of the wear debris, samples were irradiated with cobalt Kα x-rays for around one hour using x-ray tube settings of 40 kV and 30 mA. Identification of oxide constituents was carried out by comparison of interplanar spacings determined from the diffraction pattern with interplanar spacings listed in the x-ray powder data file of the American Society for Testing and Materials (ASTM) (67).

3.7 Scanning Electron Microscopy

A scanning electron microscope (SEM), capable of image resolution down to a few microns, was used to study the worn surfaces produced in the wear experiments. The purpose of this was twofold. Firstly, to observe the general characteristics of the surface, such as extent of oxide coverage, and secondly, to measure the thickness of the surface oxide.

The tilt control of the instrument was especially useful when measuring oxide film thicknesses. The orientation of the sample was adjusted until the angle made by the viewing direction with the sample surface was relatively small (usually around 45^{o} or less). This enabled the edges of oxide plateaux to be viewed clearly so that thickness measurements could be made. A tilt correction control of the instrument was used to make the magnification of the SEM image equal in both vertical and horizontal image directions. Thickness measurements were made against a scale marker at the bottom corner of the viewing screen. Around ten to fifteen oxide thickness measurements were made on each worn surface and an average thickness value obtained.

Often it was found almost impossible to measure the oxide thickness on a worn surface, either because of the large amount of debris on the sample surface obscuring the oxide plateaux edges, or because of an almost complete oxide covering with very few visible oxide edges. In the case of a large amount of debris the problem was largely overcome by wiping the sample surface in order to remove the debris. This did not affect the continuous compact oxide film on the surface since it was very adherent. However, when dealing with surfaces with very few visible oxide edges due to a relatively large oxide covering, more severe measures had to be taken. In this case the pin in question was placed in a mechanical vice and a compressive force applied to the cylindrical stem of the pin just below the worn surface. This caused the worn pin surface to become

slightly convex in shape, and the resulting surface stresses produced cracking and separation of the oxide at various regions on the surface. The oxide edges produced in this way were clearly visible and their thicknesses could be easily measured.

The scanning electron microscope was also used briefly to examine surface oxides grown on steel under static conditions.

Scanning electron micrographs of the samples examined using the SEM were taken by means of a single lens reflex camera attached to the SEM, and these are shown in Chapter 5.

Mounting of the samples for analysis by the SEM was accomplished by cementing the sample onto an aluminium stud using silver conducting paint.

CHAPTER 4

RESULTS OF MECHANICAL WEAR TESTS

4.1 Introduction

The results of the wear rate, friction value, and pin and disc temperature measurements, recorded during the wear experiments, are given in this chapter. In addition, section 4.5 gives an account of the theoretical determination of a number of parameters associated with the surface asperities in contact.

4.2 Wear Results

4.2.1 Wear of EN8

The variation in wear rate with applied load for BS970 EN8 steel at sliding speeds of 2.0 ms^{-1} and 4.0 ms^{-1} is shown in figures 4.1 (a) and 4.1(b) respectively. It can be seen from these wear characteristics that wear rate increases linearly with applied load, and also that step-like transitions occur in the characteristics at certain critical loads. Two transition are observable in figure 4.1(a) for wear tests run at 2.0 ms^{-1} and these occur at loads of around 12 N and 38 N. Only one transition occurs in the wear characteristic for 4.0 ms^{-1} as shown in figure 4.1(b) and this occurs at a load of approximately 35 N. Although other possible interpretations could be applied to these graphs, the author believes the present interpretation to be correct particularly in view of the fact that previous graphs of wear rate versus

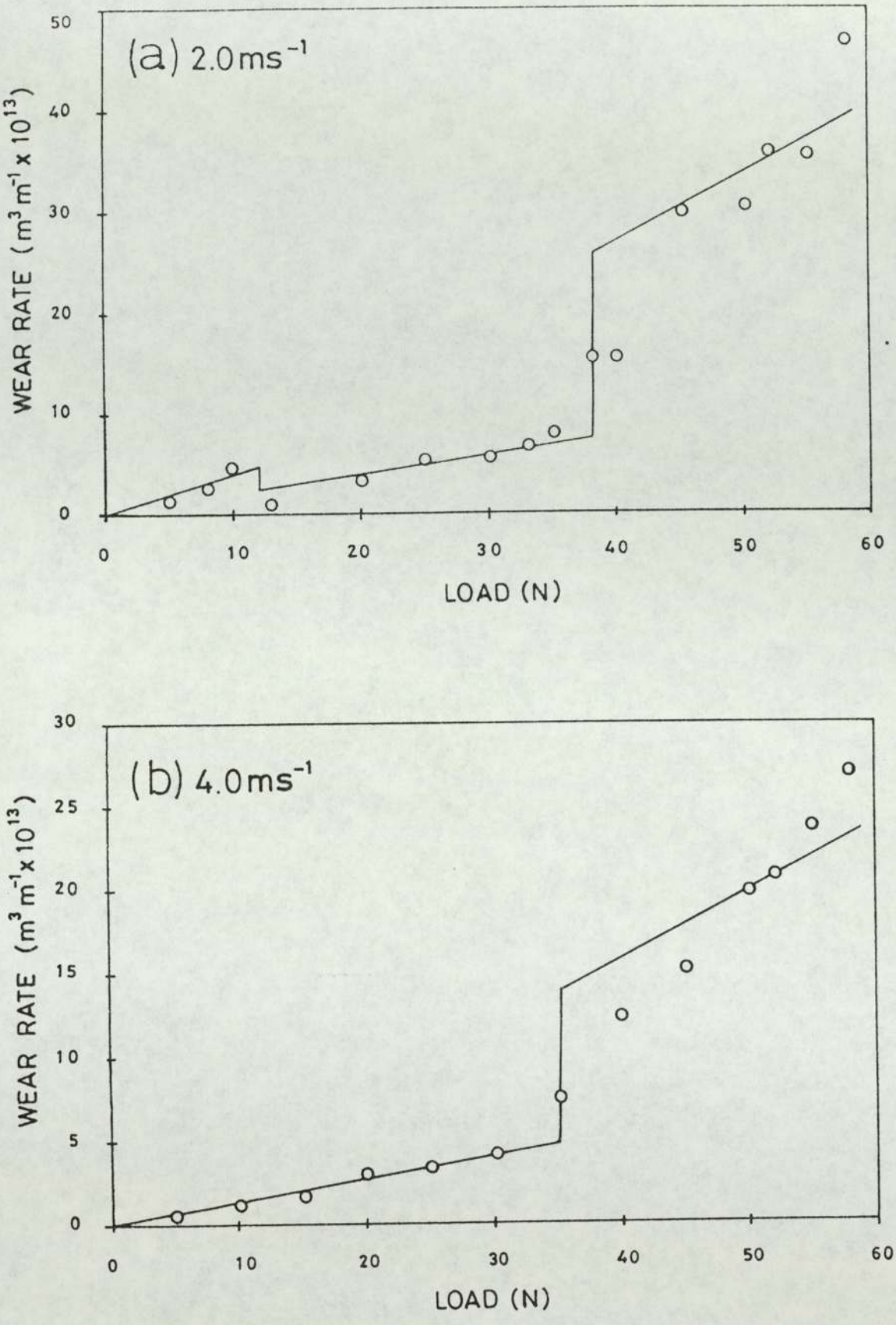

FIGURE 4.1 Variation in Wear Rate with Load for EN 8 Wear Tests.

load resulting from similar pin on disc wear tests also exhibited step-like transitions when plotted on a linear scale (46, 68), and also in view of the fact that the present interpretation is consistent with the Archard Wear Law. In addition, the transitions coincide with the first appearance of Fe_3O_4 or FeO in the oxide debris (section 5.2.1) which suggests that the transitions are associated with a change in the chemical composition of the oxide.

For wear experiments carried out below the 12 N transition at 2.0 ms^{-1}, the debris consisted of fine red-brown oxide powder with traces of bright metallic particles. Patches of loose red-brown oxide debris covered a high proportion of the worn disc surfaces.

The debris produced in wear experiments carried out below the transition load at 4.0 ms^{-1}, and in those experiments conducted between the two transition loads of 12 N and 38 N at 2.0 ms^{-1}, also consisted of fine red-brown oxide powder having traces of metallic particles. In this case, however, the worn disc surfaces contained little observable wear debris and were very smooth in appearance.

Wear experiments carried out at loads above the transition in the 4.0 ms^{-1} wear characteristic, and those run at loads above the 38 N transition at 2.0 ms^{-1}, produced debris which consisted of fine black oxide powder having traces of metallic particles. Patches of loose black oxide debris covered large areas of the worn disc surfaces.

A feature common to all of the wear tests was that the worn

pin surfaces always appeared fairly smooth and had little or no observable debris covering them.

4.2.2 Wear of EN8 /9% Chromium Steel System

The purpose of conducting the wear experiments in which an EN8 pin was loaded against a 9% chromium disc under identical conditions of load and speed to selected EN8 pin / EN8 disc wear tests was to determine if any oxide transfer takes place from the disc to the pin during mild, oxidational wear. In order for the results of this investigation to be meaningful it was first necessary to establish that mild, oxidational wear was the wear regime followed in the EN8 / 9% Cr experiments. For this reason, wear rates, frictional forces and strategic pin and disc temperatures were monitored in addition to the various surface and debris analyses, in order to build up a complete picture of the wear regime.

Figure 4.2 shows the variation in wear rate with load for the EN8 /9% Cr wear tests. It is clear that there is a linear relationship between wear rate and load. Wear rates were much lower than those produced in wear tests in which an EN8 pin was worn against an EN8 disc at similar applied loads. In all cases the wear debris was a fine black powder containing traces of metallic particles.

4.3 Friction Results

The frictional force was measured continuously for each wear experiment which was conducted. In the initial stages

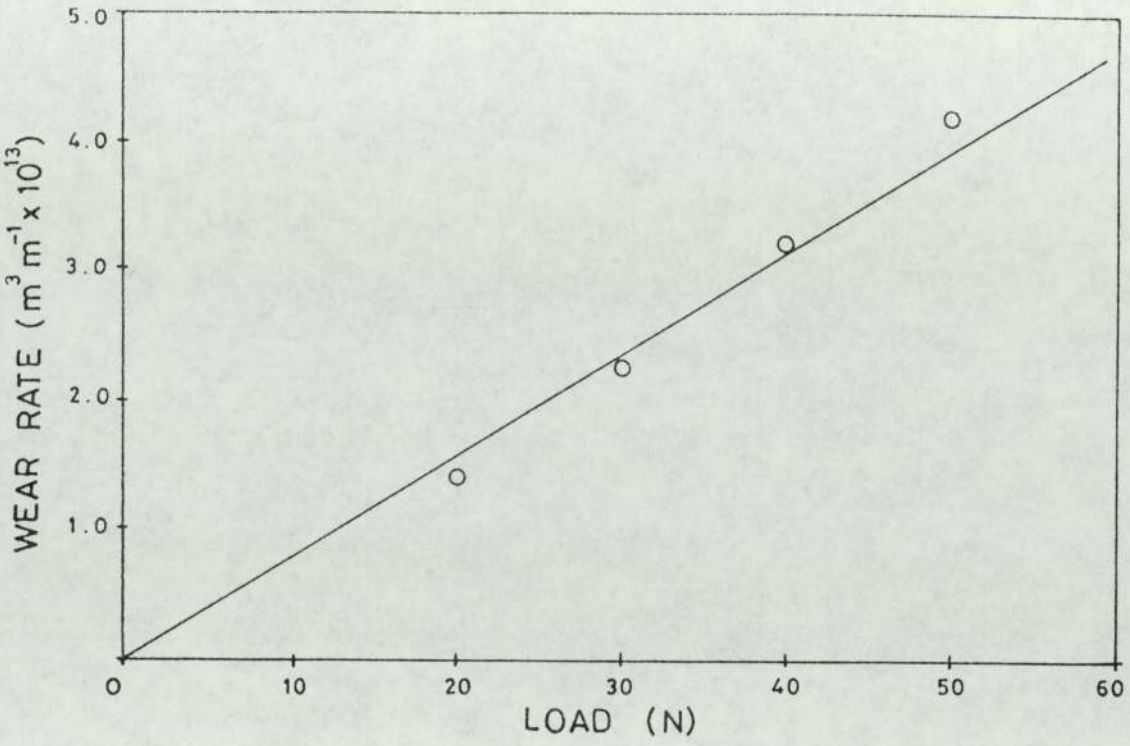

FIGURE 4.2 Variation in Wear Rate with Load for EN8/9% Cr Wear Tests

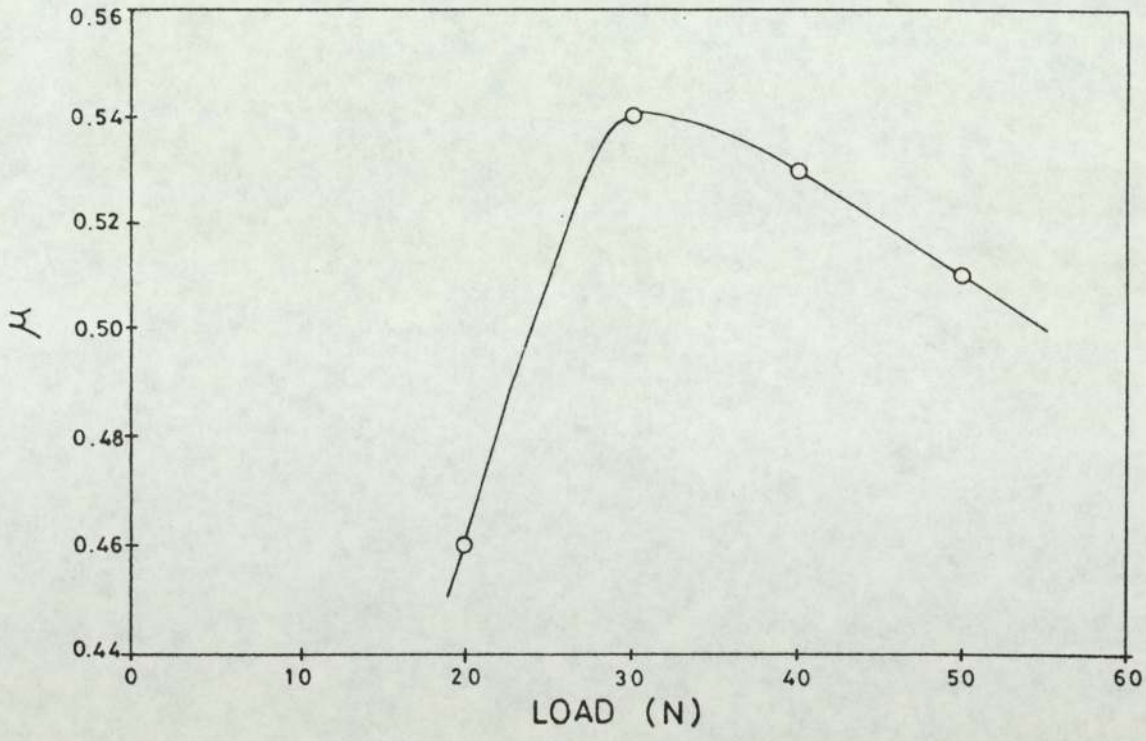

FIGURE 4.4 Variation in Coefficient of Friction (μ) with Load for EN8/9% Cr Wear Tests

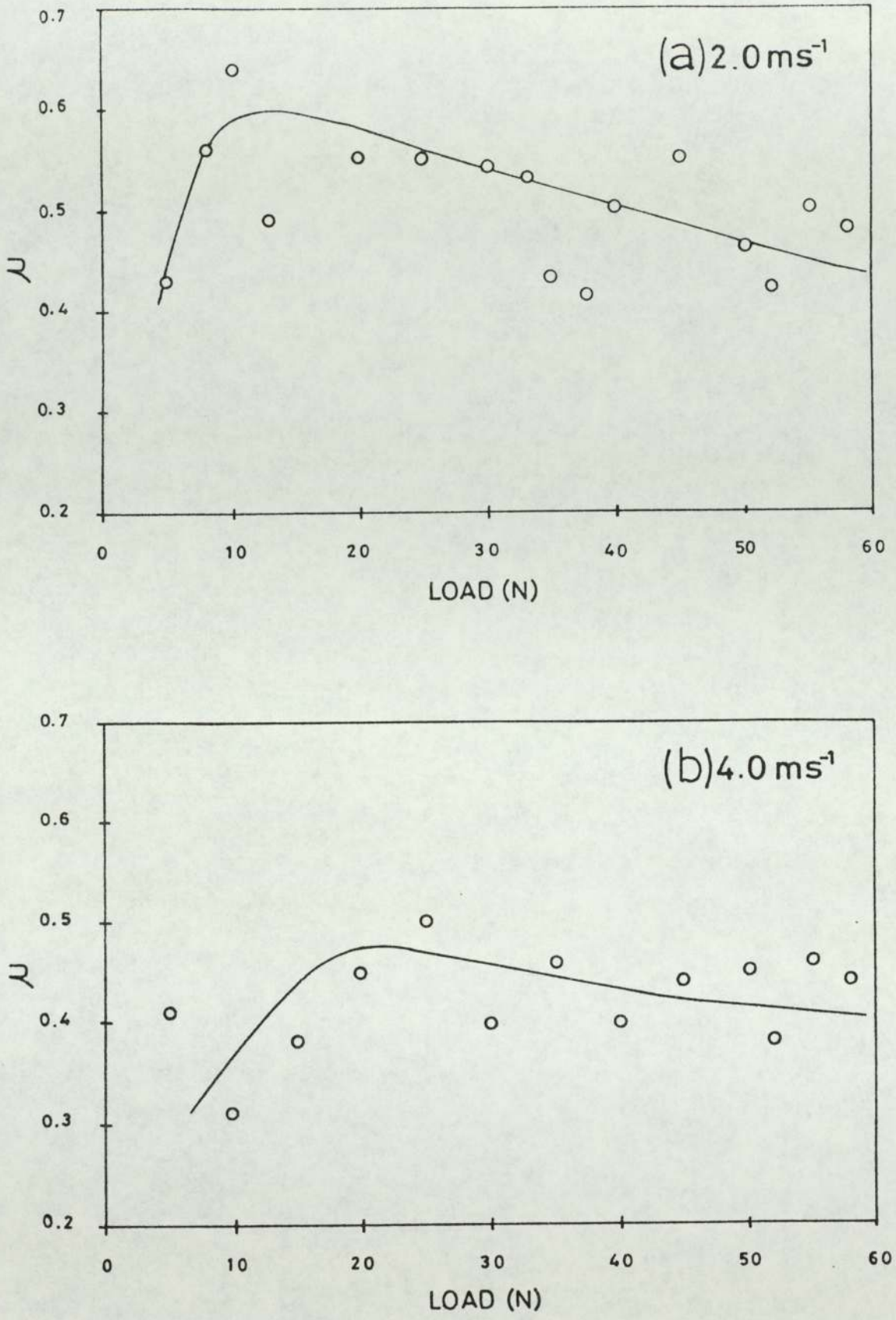

FIGURE 4.3 Variation in Coefficient of Friction (μ) with Load for EN8 Wear Tests.

of each experiment the wear was severe,and the associated frictional force was erratic with relatively high values of coefficient of friction, μ. Once the experiment had been "run in", however, and mild wear had ensued, then the value of μ remained at a reasonably steady level.

4.3.1 EN8 Wear Tests

Figures 4.3(a) and 4.3(b) show the variation of μ with applied load for experiments conducted at $2.0\,ms^{-1}$ and $4.0\,ms^{-1}$ respectively. As can be seen from these figures, there is a relatively high scatter of experimental points, making it difficult to determine the exact form of variation of μ with load. However, similar wear tests have been conducted using the same material and experimental conditions as in the present investigation, but which were carried out on a different experimental test rig (**47**), and the friction results from these tests, together with the present friction results, lead the author to believe that the variation of μ with load is of the form shown by the curves in figures 4.3(a) and 4.3(b). The curves initially rise rapidly, peak at a relatively low load, and then gradually decrease with further increase in load. By comparison with the transitionary behaviour of the wear rate graphs it seems that the frictional force is independent of the wear rate.

4.3.2 EN8 / 9% Chromium Steel Wear Tests

The variation in the coefficient of friction with applied load for the EN8 / 9% Cr wear tests is shown in figure 4.4. The form of the curve is similar to that of the curves of

figure 4.3 for the EN8 wear tests, and the magnitude of μ for both sets of experiments was also similar.

4.4 Heat Flow Results

The heat flow results associated with the EN8 wear experiments conducted at 2.0 ms^{-1} and 4.0 ms^{-1} are given in tables 4.1(a) and 4.1(b) respectively. The quantities l_1, l_3, T_A, T_B, T_C, T_D, T_S and H_1 have already been defined in section 2.5. The T_A, T_B, T_C and T_D values in the tables are those steady state values recorded immediately before the wear experiment was terminated. The quantities l_1 and l_3 were measured after the experiment had ended. The general surface temperature, T_S, and the heat flow per second into the pin, H_1, were calculated from the thermocouple readings T_A, T_B and T_C, from various calculated heat flow quantities, and from various measurements and physical quantities associated with the steel pin, as shown in equations (2.2) and (2.3) respectively. The rate of production of heat, H_T, due to the two surfaces sliding together is given by the product of the frictional force at the interface between the pin and the disc, F, and the linear speed of the pin with respect to the disc, U. The experimentally determined division of heat (flowing into the pin) at the pin-disc interface is given by:

$$\delta_{exp} = \frac{H_1}{H_T} \qquad (4.1)$$

Figures 4.5(a) and 4.5(b) show the variation of T_S with applied load for EN8 steel wear experiments carried out at linear sliding speeds of 2.0 ms^{-1} and 4.0 ms^{-1} respectively.

LOAD (N)	ℓ_1 (mm)	ℓ_3 (mm)	T_A (°C)	T_B (°C)	T_C (°C)	T_S (°C)	T_D (°C)	H_I (W)	H_T (W)	δexpt (%)
5	8	15	33	30	27	37	31	0.44	4.26	10.2
8	8	15	47	40	34	52	36	1.00	8.88	11.3
10	9.5	15	50	44	35	55	36	0.96	12.80	7.5
13	9.5	15	52	42	36	60	40	1.42	12.80	11.1
20	8.5	17	63	46	38	73	44	2.12	22.04	9.6
25	8	17	68	47	36	80	40	2.62	27.36	9.6
30	10	16	70	46	38	88	46	3.16	32.34	9.8
33	10	15	84	56	44	106	46	3.93	34.84	11.3
35	9	15	94	59	45	118	50	4.80	30.00	16.0
38	9	16	100	60	45	126	52	5.20	30.92	16.8
40	9	16	124	80	53	154	56	5.92	40.20	14.7
45	7	15	140	88	58	168	53	7.04	49.71	14.2
50	8	15	141	81	56	178	52	8.11	45.84	17.7
52	7	16	145	80	61	177	63	8.07	43.30	18.6
55	8	15.5	158	92	64	198	55	8.70	54.64	15.9
58	6	15.5	172	91	65	207	63	10.18	55.28	18.4

TABLE 4.1(a) Heat Flow Data for EN8 Wear Tests Conducted at 2.0ms^{-1}.

LOAD (N)	ℓ_1 (mm)	ℓ_3 (mm)	T_A (°C)	T_B (°C)	T_C (°C)	T_S (°C)	T_D (°C)	H_I (W)	H_T (W)	δ_{expt} (%)
5	10	15.5	34	30	28	37	33	0.59	8.12	7.2
10	9.5	16	42	34	29	48	34	1.16	12.56	9.2
15	10	15	52	39	32	63	38	1.97	23.00	8.5
20	10.5	15	61	44	36	76	42	2.57	35.84	7.2
25	10	16	76	55	38	93	50	3.17	50.08	6.3
30	9	16	89	69	48	104	52	3.05	48.04	6.4
35	8	15.5	135	95	60	161	52	5.90	64.96	9.1
40	8.5	15.5	146	99	57	179	57	7.05	64.28	11.0
45	8	16	138	95	60	165	55	6.15	79.16	7.8
50	7	16	212	136	67	253	65	10.72	90.00	11.9
52	9	15.5	160	108	65	198	75	7.83	78.48	10.0
55	8	15.5	168	106	77	206	80	8.61	101.40	8.5
58	11	15	186	120	73	247	70	10.53	101.48	10.4

TABLE 4.1(b) Heat Flow Data for EN8 Wear Test Conducted at 4.0 ms^{-1}

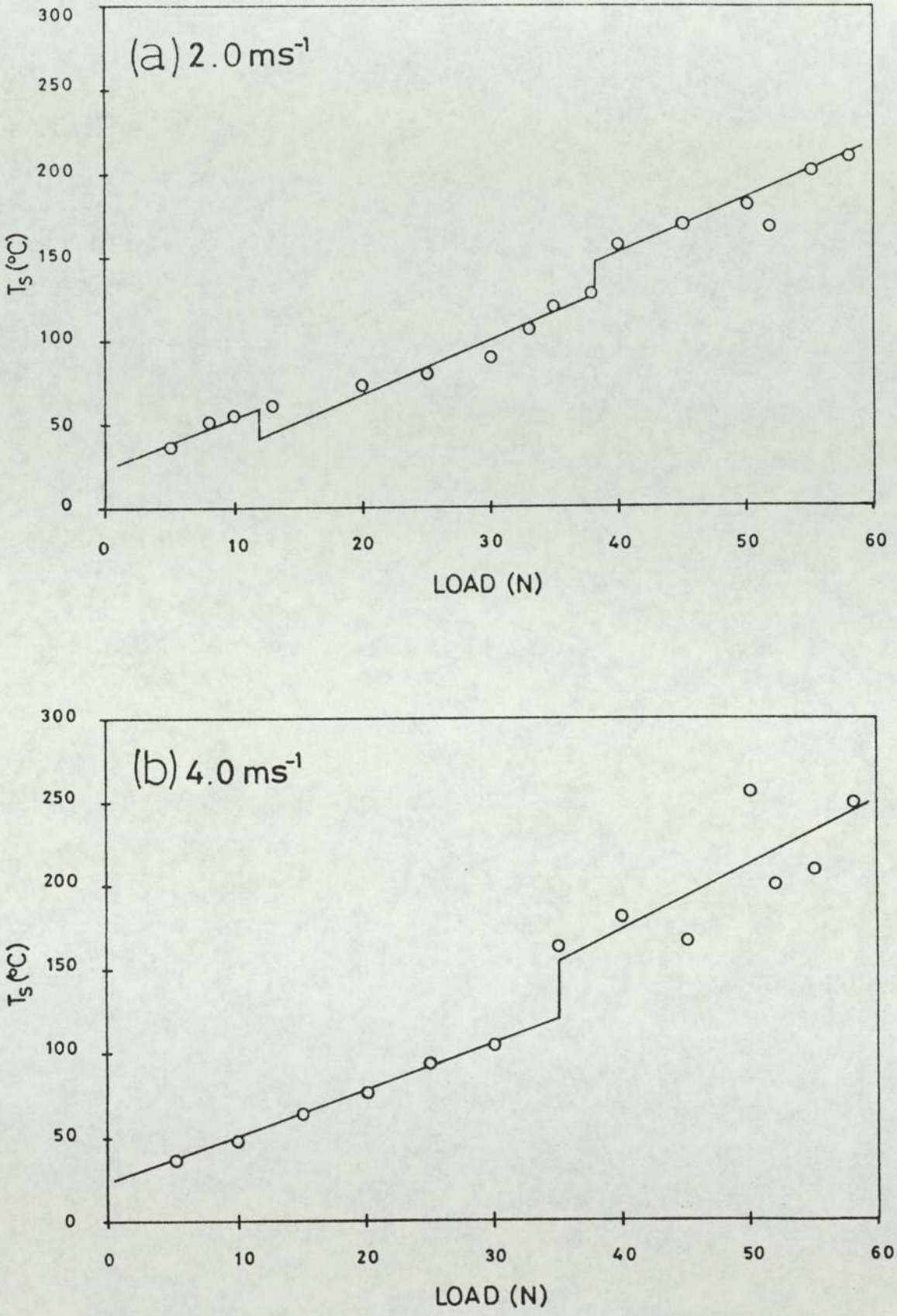

FIGURE 4.5 Variation in General Surface Temperature with Load for EN8 Wear Tests.

T_s increases linearly with applied load and, in addition, step-like transitions occur at certain critical loads. From comparison of these graphs with the wear rate characteristics of figure 4.1 it can be clearly seen that the form of the two sets of curves is very similar.

4.5 Theoretical Determination of Surface Parameters Associated with Contacting Asperities

4.5.1 Introduction

Section 4.5 is an account of the method used for the calculation of parameters associated with the actual surface asperities in contact. Parameters which have been evaluated are average contact temperature of the asperities, T_o, average asperity contact radius, a, and number of contacting asperities, N, and, in addition, it was possible to obtain a theoretical value for the division of heat at the pin-disc interface, δ_{th}.

Section 4.5.2 shows how consideration of a surface model led to the development of equations for the surface parameters mentioned above, while section 4.5.3 gives an account of the iterative process used to calculate the surface parameters from these equations. Section 4.5.4 summarises the results of the calculations of the surface parameters, and shows how they vary with applied load and sliding speed.

4.5.2 Derivation of Equations for the Evaluation of T_o, a, N & δ_{th}

The starting point in the present derivation of equations which enable the surface parameters T_o, a, and N to be calculated is the consideration of a surface model. The model assumes that the worn surface consists of N circular areas of contact (of radius 'a'), and on each of these contacting asperities there is an oxide film (of thickness ξ_p and ξ_D for the pin and disc surfaces respectively). This model is very similar to that used by Quinn (59), and differs only in the assumption of an oxide film on the disc as well as on the pin.

For this surface model the real area of contact, A_r, is given by:

$$A_r = N\pi a^2 \qquad (4.2)$$

For plastic deformation of the surface A_r is given by the ratio of the applied load, W, to the hardness of the steel, P_m, (49) so that the equation relating the number of contacts, N, to the average asperity contact radius, a, is:

$$N\pi a^2 = \frac{W}{P_m} \qquad (4.3)$$

Theoretical considerations of heat flow between disc and pin are essential to the present derivation of equations for calculating T_o, a, N and δ_{th}. A theoretical expression for the proportion of the total heat which goes into the pin, δ_{th}, has been given by Archard (57):

$$\delta_{th} = \frac{\Theta_D}{\Theta_D + \Theta_P} \qquad (4.4)$$

where θ_p is the "fictitious" flash temperature obtained by assuming that a heat flow rate of H_T is supplied to the pin only, and similarly θ_D is the "fictitious" flash temperature assuming that a heat flow rate of H_T is supplied to the disc only.

According to Quinn (59) the fictitious flash temperature θ_p for the present surface model can be expressed as:

$$\theta_p = \frac{H_T}{4aNK_s} + \frac{H_T \xi_p}{N\pi a^2 K_o} \qquad (4.5)$$

The equation for θ_D depends upon the speed of sliding (57). Following the approach of Quinn et al (69), who conducted wear tests under very similar conditions to those employed in the present work, an expression for medium speeds has been used, namely:

$$\theta_D = \left(0.8605 - 0.1021 \frac{Ua}{2\chi_s}\right) \frac{H_T}{4aNK_s} \qquad (4.6)$$

where χ_s is the thermal diffusivity of the disc material (steel) and U is the linear sliding speed. In the derivation of equation (4.6), however, no account has been taken of the oxide on the disc and in previous work (59) this has until recently (31) been neglected. SEM oxide thickness measurements given in section 5.5 show that the oxide films on the pin and the disc are of approximately the same thickness, so that the effect of an oxide on the disc should be taken into account. This can be done by modifying equation (4.6) slightly to give:

$$\theta_D = \frac{\alpha H_T}{4aNK_s} + \frac{\alpha H_T \xi_D}{N\pi a^2 K_o} \qquad (4.7)$$

where α is given by the expression:

$$\alpha = \left(0.8605 - 0.1021 \frac{Ua}{2\chi_o}\right) \qquad (4.8)$$

and χ_o is the thermal diffusivity of the disc oxide.

The real flash temperature for the pin is given the equation (4.5) with H_T replaced by H_1, the heat flow per second into the pin at the pin-disc interface. The average contact temperature of the pin, $T_o(PIN)$, is equal to the general pin surface temperature plus the real flash temperature, so we have:

$$T_o(PIN) = T_S + \frac{H_1}{4aNK_S} + \frac{H_1 \xi_p}{N\pi a^2 K_o} \qquad (4.9)$$

Similarly, the real flash temperature for the disc is given by equation (4.7) with H_T replaced by $(H_T - H_1)$, the heat flow per second into the disc at the pin-disc interface. The average contact temperature of the disc, $T_o(DISC)$, is equal to the general disc surface temperature plus the real flash temperature, so that:

$$T_o(DISC) = T_D + \frac{\alpha(H_T - H_1)}{4aNK_S} + \frac{\alpha(H_T - H_1)\xi_D}{N\pi a^2 K_o} \qquad (4.10)$$

where T_D is the general disc surface temperature, measured approximately by holding a thermocouple onto the disc at a point very close to the wear track.

Equating (4.9) and (4.10) for the average temperature of the contacting asperities, and eliminating N by the use of equation (4.3), gives us a quadratic equation in the contact radius, a, of the form:

$$Aa^2 + Ba + C = 0 \qquad (4.11a)$$

where:

$$A = \frac{0.1021\,\pi\,P_m\,U\,(H_T - H_1)}{8\chi_0 K_S W} \qquad (4.11b)$$

$$B = \frac{P_m}{W}\left\{\frac{H_1\pi}{4K_S} - \frac{0.8605\pi(H_T - H_1)}{4K_S} + \frac{0.1021U(H_T - H_1)\xi_D}{2\chi_0 K_0}\right\} \qquad (4.11c)$$

$$C = \frac{P_m}{W}\left\{\frac{H_1\xi_P}{K_0} - \frac{0.8605(H_T - H_1)\xi_D}{K_0}\right\} + T_S - T_D \qquad (4.11d)$$

For the present oxidational wear experiments the coefficients A and B were always found to be positive and C was always negative. This gives two real solutions for the average contact radius, a, one positive and one negative. However, equation (4.7) is valid for medium speeds and holds true for $0 < Ua / 2\chi_0 < 5$ (59) so that the positive solution to equation (4.11a) is appropriate. Thus, a value for the average contact radius was found from the equation:

$$a = \frac{-B + \sqrt{B^2 - 4AC}}{2A} \qquad (4.12)$$

In order to calculate a value for 'a' we need to evaluate the A, B and C terms in equation (4.12). As can be seen from equation (4.11b), (4.11c) and (4.11d) these terms contain various physical quantities which were determined experimentally from measurements recorded during, or after the termination of, each wear test (W, U, F, T_S, T_D, H_1, H_T, ξ_P and ξ_D), and also the material properties χ_0, K_0, P_m and K_S. These material properties are temperature dependent, and so a problem arises as to what temperature these properties should be taken at. Following the work of Sullivan and Athwal (31) it was decided that the physical properties of the substrate metal, P_m and K_S should be taken at the general surface temperature, whereas the oxide properties, χ_0 and K_0, should be evaluated at the contact temperature.

The effect of evaluating these quantities at any other temperature between T_s and T_o, and also the effect of varying oxide thickness values within the limit of experimental uncertainty, is discussed in Chapter 7.

The variation of P_m with temperature is shown in figure 4.6 (47) and it can be seen that for temperatures up to around 300°C, corresponding to the range of general surface temperature values produced in the present wear tests, the hot hardness is approximately constant. A constant value of 256 VPN was therefore assumed for P_m. The variation in K_s with temperature for EN8 steel is shown in figure (4.7) (70). Similarly, it can be seen that the variation in K_s up to temperatures of around 300°C is fairly small, so that a constant value of 52 $Wm^{-1}°C^{-1}$ was assumed in the present work.

The oxide properties χ_o and K_o are connected in that the thermal diffusivity, χ_o, is given by the equation:

$$\chi_o = \frac{K_o}{\rho_o c_o} \qquad (4.13)$$

where ρ_o and c_o are the density and specific heat capacity of the oxide respectively. Molgaard and Smeltzer (71) have shown that for haematite ($\alpha-Fe_2O_3$) and magnetite (Fe_3O_4) the thermal conductivity, K_o, varies with absolute temperature, T, according to the equations:

$$\alpha-Fe_2O_3 \; : \; K_o = (8.39 - 6.63 \times 10^{-3} T) \quad Wm^{-1} K^{-1} \qquad (4.14a)$$

$$Fe_3O_4 \; : \; K_o = (4.23 - 1.37 \times 10^{-3} T) \quad Wm^{-1} K^{-1} \qquad (4.14b)$$

Where $\alpha-Fe_2O_3$ was the predominant oxide, equation (4.14a)

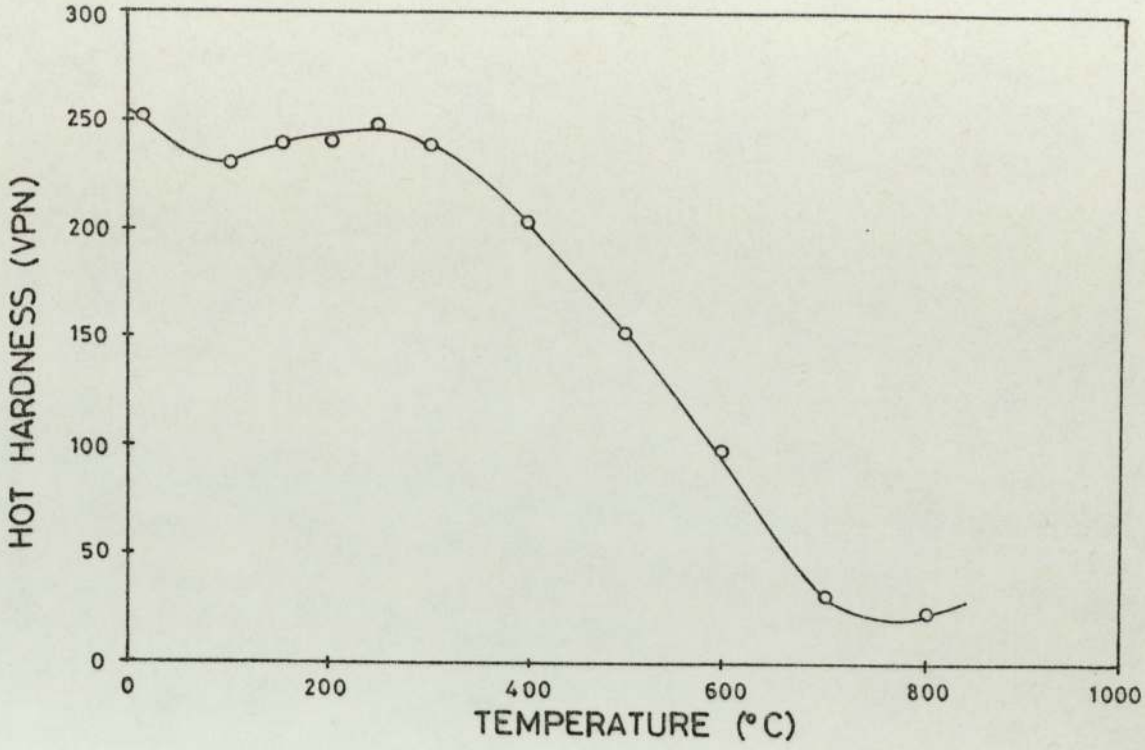

FIGURE 4.6 Hot Hardness versus Temperature for EN8 Steel (47)

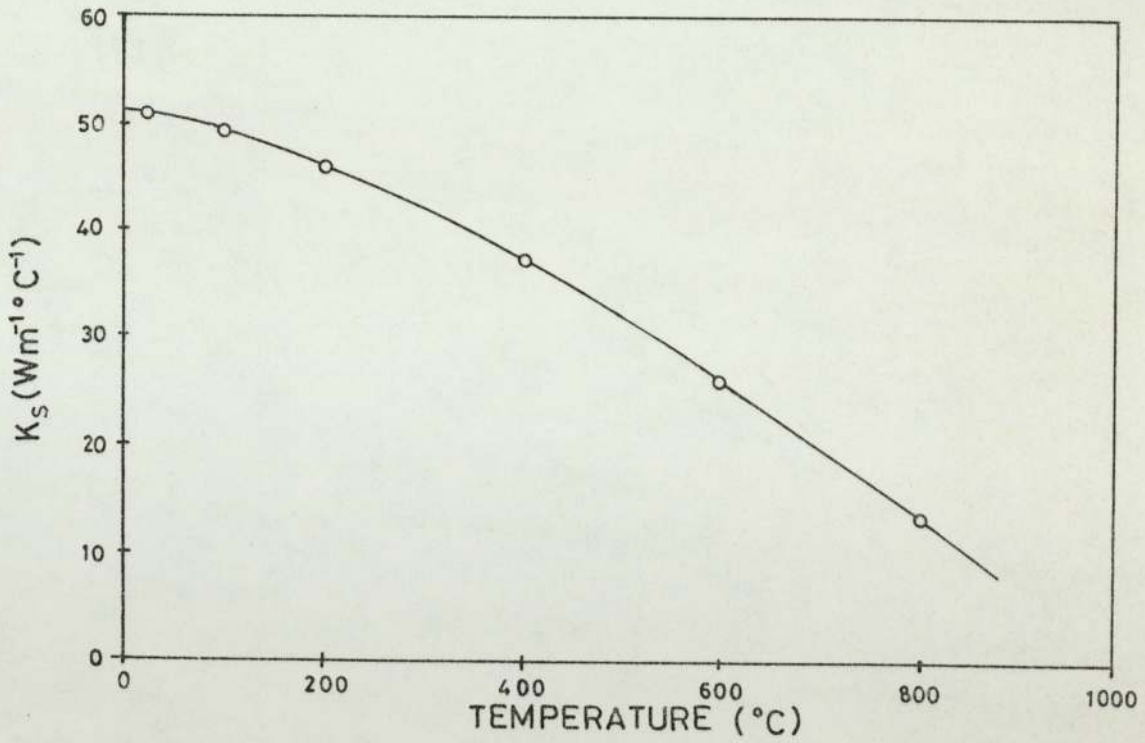

FIGURE 4.7 Thermal Conductivity (K) versus Temperature for EN8 Steel (70)

was used to calculate K_o, whereas, equation (4.14b) was used when the oxide was mainly Fe_3O_4. At present no data is available on the variation of K_o with temperature for FeO and so equation (4.14b) was also used for the calculation of K_o values when the oxide was predominantly FeO.

For the calculation of χ_o values from equation (4.13) we also need to know ρ_o and c_o, which both vary with temperature. No comprehensive data on the variation of ρ_o and c_o with temperature was found in the literature, and so values of ρ_o at 20°C (72) and values of c_o at 100°C (72) were used throughout. These values were 5.24×10^3 kgm^{-3} and 5.18×10^3 kgm^{-3} for the densities of $\alpha-Fe_2O_3$ and Fe_3O_4 respectively, and 761.7 $J\,kg^{-1}\,°C^{-1}$ and 749.1 $J\,kg^{-1}\,°C^{-1}$ for their respective specific heat capacities. Since ρ_o and c_o vary in opposition with temperature it was hoped that the product $\rho_o c_o$ would not vary greatly with temperature.

In order to calculate the surface parameter 'a' (and subsequently the parameters N and T_o) it is also necessary to know the critical thickness of the oxide on the worn surfaces. This was done by scanning electron microscopy (section 5.5.1) and the results are summarised in tables 5.10(a) and 5.10(b). Occasionally only the pin or disc oxide thickness has been measured and in these cases the critical oxide film thickness on the worn surfaces of the two members of the sliding pair was assumed to be of equal magnitude. Although this will not be strictly true since there will be differences in the thermal and mechanical stresses experienced by the oxide on the pin and disc, it can be seen from table 5.10 that ξ_p and ξ_D are not very

different and are approximately equal within the experimental uncertainties.

4.5.3 Iterative Calculation for the Determination of Surface Parameters

Since it was assumed that the physical properties of the oxide should be taken at the average contact temperature, T_o, and this is one of the surface parameters which we are trying to determine, it was necessary to calculate the surface parameters by means of an iterative process. This process will now be described.

First of all a value for K_o at the general surface temperature, T_s, was calculated from equation (4.14) and this in turn enabled a value to be calculated for χ_o from equation (4.13). All of the variables in the equations (4.11b), (4.11c) and (4.11d) defining the quadratic coefficients A, B, and C were now known so that values for these coefficients could be calculated, thus enabling a value for the average contact radius, a, to be calculated from equation (4.12). Once a value for this latter quantity had been obtained it was inserted into equations (4.3) and (4.6) to enable the calculation of the number of contacts, N, and average contact temperature, T_o, respectively. This completed one step of the calculation. In the second step of the iteration process new values for K_o and χ_o were calculated at this contact temperature, and this in turn resulted in new values for a, N and T_o. This procedure was repeated until two subsequent contact temperatures were within 5^oC of each other, after which the iterative process was terminated. The

resulting values for T_o, a and N were taken to be representative of the average contact temperature, average contact radius, and number of contacting asperities respectively. A theoretical value for the division of heat at the pin-disc interface, δ_{th}, could be calculated from equation (4.4) and comparison with the experimentally determined division of heat, δ_{exp}, provided a means of testing theory against experiment. The computer program used for the iterative calculation of a, T_o, N and δ_{th} is listed in Appendix.

4.5.4 Determined Values of T_o, a, N and δ_{th}

This section gives the results of the calculations based on the theoretical analysis outlined in the previous sections. In particular we are concerned with how the various calculated surface parameters vary with applied load and sliding speed, since we are interested in correlations between variations in the calculated parameters and variations in experimentally determined quantities such as wear rate and general surface temperature.

Tables 4.2(a) and 4.2(b) summarise the results of the calculations for the wear tests carried out at $2.0\,ms^{-1}$ and $4.0\,ms^{-1}$ respectively. In addition, experimentally determined values for the division of heat, δ_{exp}, are included for comparison with their theoretically determined counterparts, δ_{th}. It can be seen that agreement between δ_{th} and δ_{exp} is good, especially considering the experimental errors involved in measuring δ_{exp}.

LOAD (N)	K_o ($Wm^{-1}K^{-1}$)	$\bar{a}$ (μm)	N	T_o (°C)	δ_{exp} (%)	δ_{th} (%)
5	4.99	9.28	7	238	10.2	10.5
8	4.46	8.02	15	317	11.3	11.9
10	4.85	9.39	14	261	7.5	8.1
13	3.27	6.16	43	427	11.1	11.6
20	3.23	6.24	64	459	9.6	10.3
25	3.25	6.31	78	442	9.6	10.5
30	3.17	6.07	101	502	9.8	10.7
33	3.05	5.63	129	589	11.3	12.5
35	2.99	4.93	179	632	16.0	17.7
38	3.09	4.96	192	556	16.8	19.2
40	2.99	5.02	197	634	14.7	17.2
45	3.05	5.10	215	602	14.2	17.3
50	3.02	4.67	284	613	17.7	21.7
52	2.79	4.22	363	779	18.6	21.4
55	2.88	4.59	324	711	15.9	19.5
58	2.86	4.33	384	732	18.4	22.4

TABLE 4.2(a) Calculated Values of $\bar{a}$, N, T_o and δ_{th} for EN8 Wear Tests Conducted at $2.0 ms^{-1}$.

LOAD (N)	K_o ($Wm^{-1}K^{-1}$)	a (μm)	N	T_o (°C)	δ_{exp} (%)	δ_{th} (%)
5	3.31	3.33	56	403	7.2	7.3
10	3.32	3.23	119	388	9.2	9.6
15	3.23	3.20	182	459	8.5	9.1
20	3.17	3.19	245	501	7.2	7.7
25	3.17	3.26	292	502	6.3	7.0
30	3.10	3.12	382	556	6.4	7.0
35	3.06	2 98	490	580	9.1	11.2
40	3.02	2.73	667	606	11.0	13.7
45	3.03	2.95	643	600	7.8	9.6
50	2.76	2.36	1117	795	11.9	15.4
52	2.99	2.87	783	631	10.0	12.5
55	2.90	2.78	888	698	8.5	10.4
58	2.84	2.57	1088	744	10.4	13.6

TABLE 4.2 (b) Calculated Values of a, N, T_o and δ_{th} for EN8 Wear Tests Conducted at 4.0 ms^{-1}.

The variation in average contact temperature, T_o, with load for the 2.0 ms^{-1} and 4.0 ms^{-1} wear tests is shown in figures 4.8(a) and 4.8(b) respectively. It can be seen that T_o varies linearly with W and, in addition, it is possible to interpret the graphs as having transitions in T_o at certain applied loads, corresponding to the transitions in the wear rate versus load and general surface temperature versus load graphs of figures 4.1 and 4.5 respectively. The transition in figure 4.8(b) for the 4.0 ms^{-1} wear tests is less pronounced than the transitions in the 2.0 ms^{-1} wear test graph of figure (4.8a), but it is considered that definite transitions do occur in both cases, and this view is supported by T_o transitions observed in similar wear tests reported by Sullivan and Athwal (31). Comparison of the T_o versus W graphs with the results of x-ray diffraction analysis (section 5.2) indicate that the transitions in T_o at certain loads are associated with a change in the composition of the oxide on the worn surfaces.

Figures 4.9(a) and 4.9(b) show the variation in average contact radius, a, with load for the 2.0 ms^{-1} and 4.0 ms^{-1} wear tests respectively, while figures 4.10(a) and 4.10(b) show the variation in the number of contacts, N, with load for these respective sliding speeds. It can be seen that 'a' decreases with load, the decrease being very slight over the range of loads used in the 4.0 ms^{-1} wear tests, while 'a' halves in value over this same range of loads for wear tests carried out at 2.0 ms^{-1}. The increase in N with load follows a smooth curve for both sliding speeds investigated, the increase in N for the 4.0 ms^{-1} experiments being approximately double the increase for the 2.0 ms^{-1} experiments over the range of loads employed.

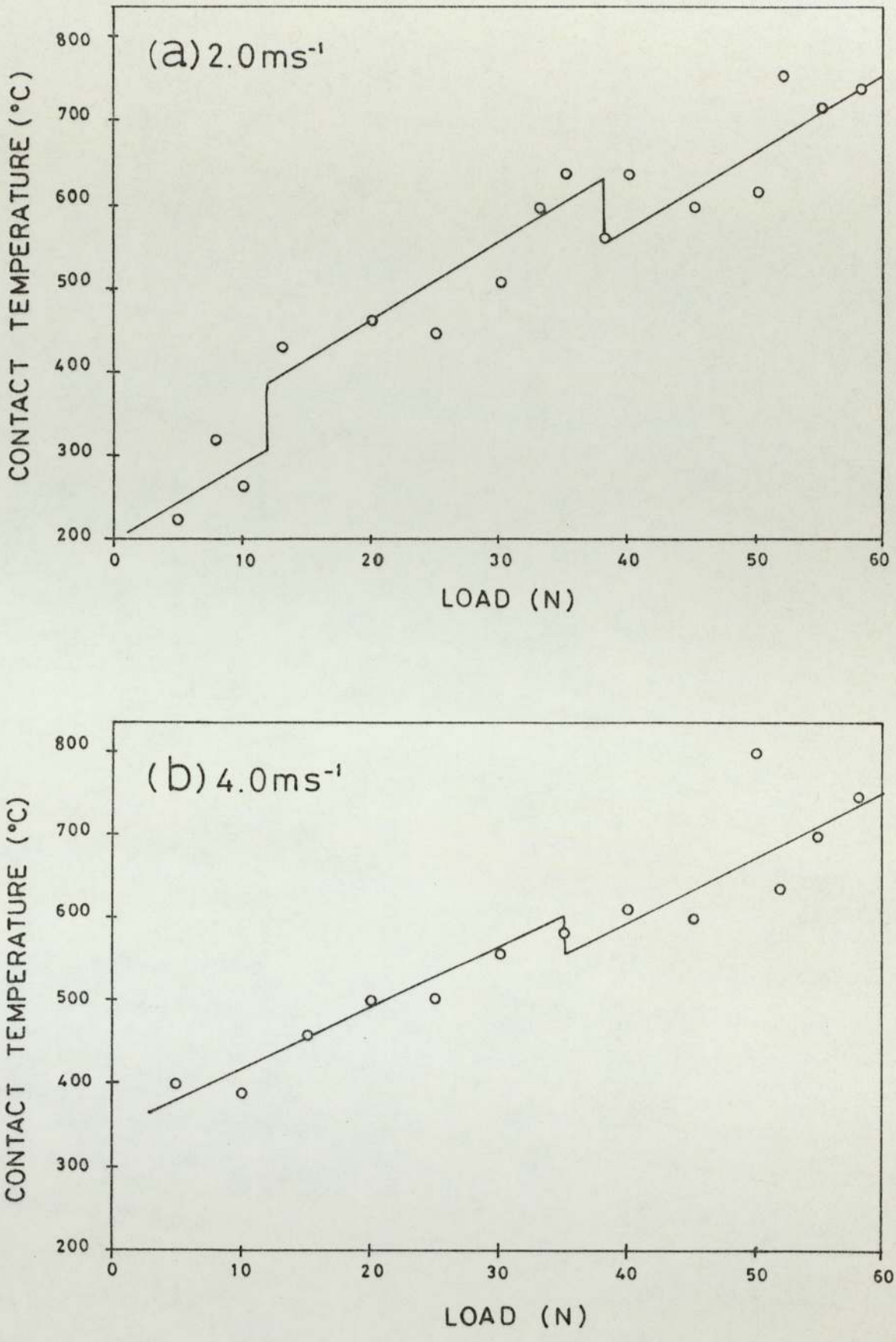

FIGURE 4.8 Variation in Contact Temperature with Applied Load for EN8 Wear Tests.

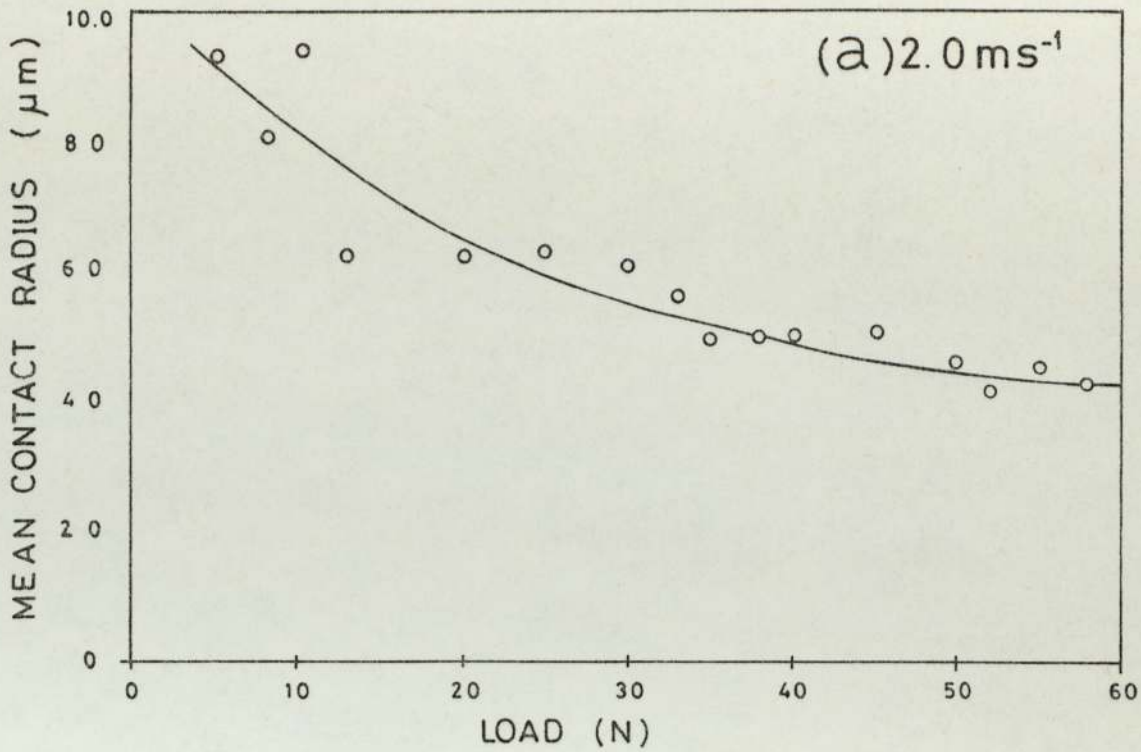

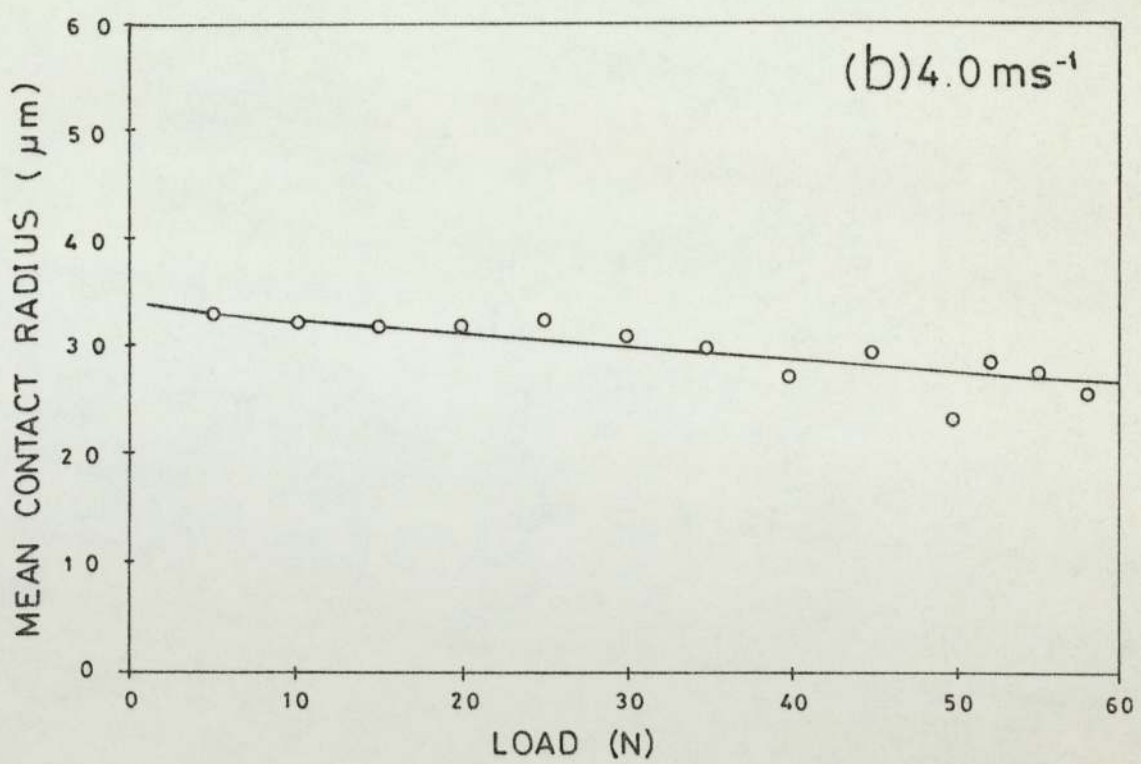

FIGURE 4.9 Variation in Mean Contact Radius with Applied Load for EN8 Wear Tests.

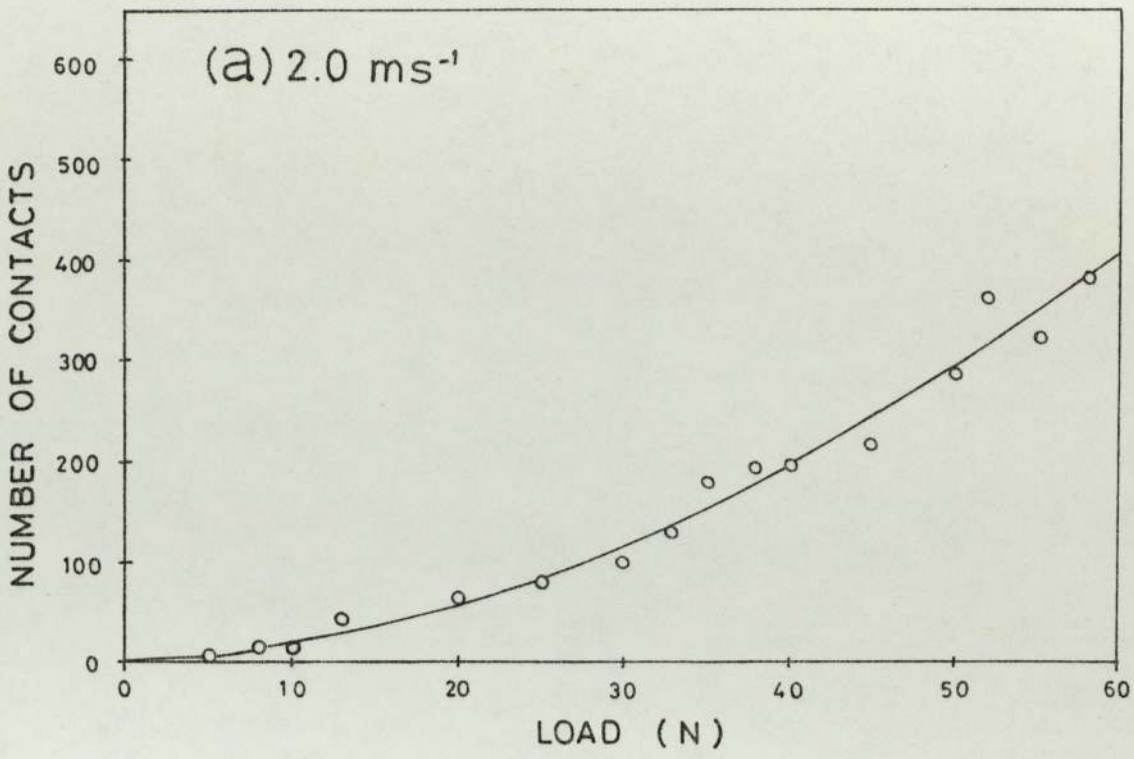

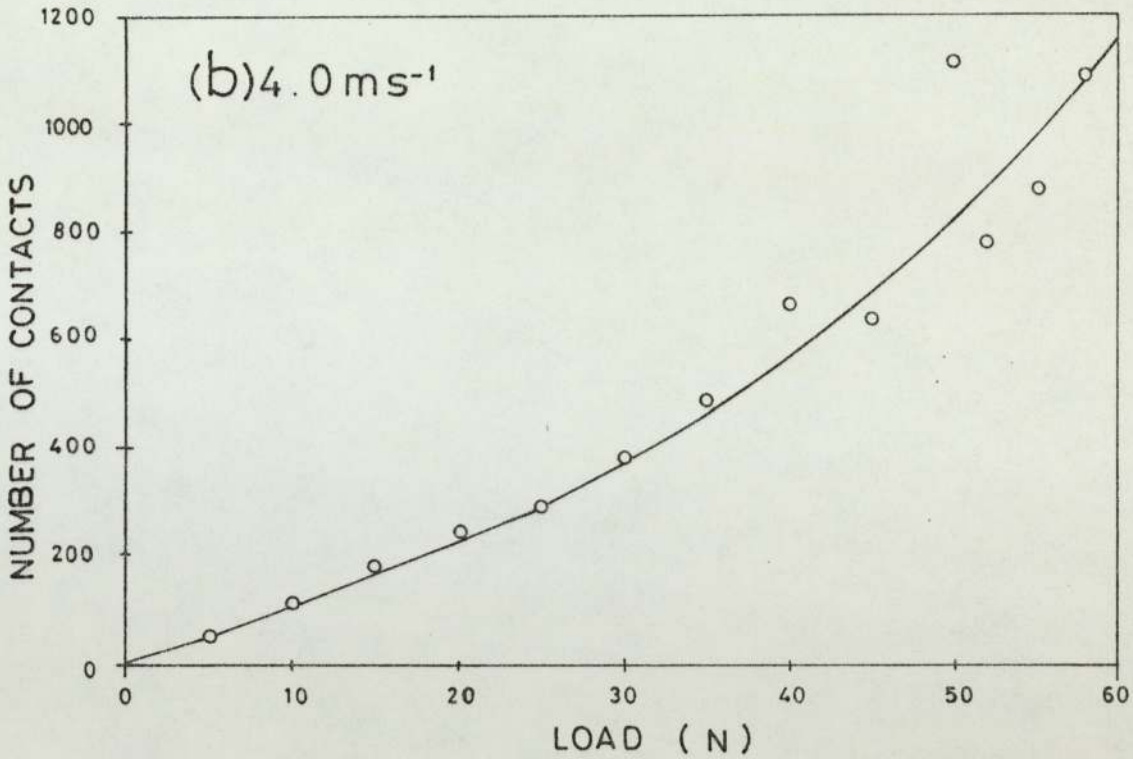

FIGURE 4.10 Variation in Number of Contacts with Applied Load for EN8 Wear Tests.

CHAPTER 5

RESULTS OF SURFACE ANALYSIS AND WEAR DEBRIS ANALYSIS

5.1 Oxidational Constants

5.1.1 Ellipsometric Results

In the temperature range investigated by ellipsometry (150°C to 300°C) the oxidation of low alloy steel was found to obey a logarithmic rate law of the form:

$$y = c_1 \ln(k_l t + c_2) \qquad (5.1)$$

where: y = increase in oxide thickness

k_l = logarithmic rate constant

c_1, c_2 = constants

t = length of oxidation period

It was assumed that $c_2 = 1$ since the thickness was taken to be zero when $t = 0$. The two constants k_l and c_1 were calculated by a method due to Davies et al (14). From equation (5.1) we have:

$$\exp\left(\frac{y}{c_1}\right) = k_l t + 1 \qquad (5.2)$$

A plot of $\exp(y/c_1)$ versus t is a straight line for a logarithmic law. For each temperature investigated a value of c_1 was chosen which gave a straight line of unity intercept on the $\exp(y/c_1)$ axis. The rate constant for a particular oxidation temperature was then determined from the gradient of the straight line obtained for that temperature. Table 5.1 gives the values of the constants k_l and c_1

T (°C)	k_l ($s^{-1} \times 10^2$)	C_1 (cm $\times 10^7$)
150	0.25	0.5
200	1.03	1.72
250	2.73	2.85
280	2.80	3.57
300	7.97	3.91

TABLE 5.1 Constants for Logarithmic Oxidational Growth Rates.

TEMP RANGE (°C)	Q_l ($kJ\ mol^{-1}$)	A_l (s^{-1})
150 - 300	43 ± 5	450

TABLE 5.2 Activation Energy and Arrhenius Constant for Logarithmic Oxidation.

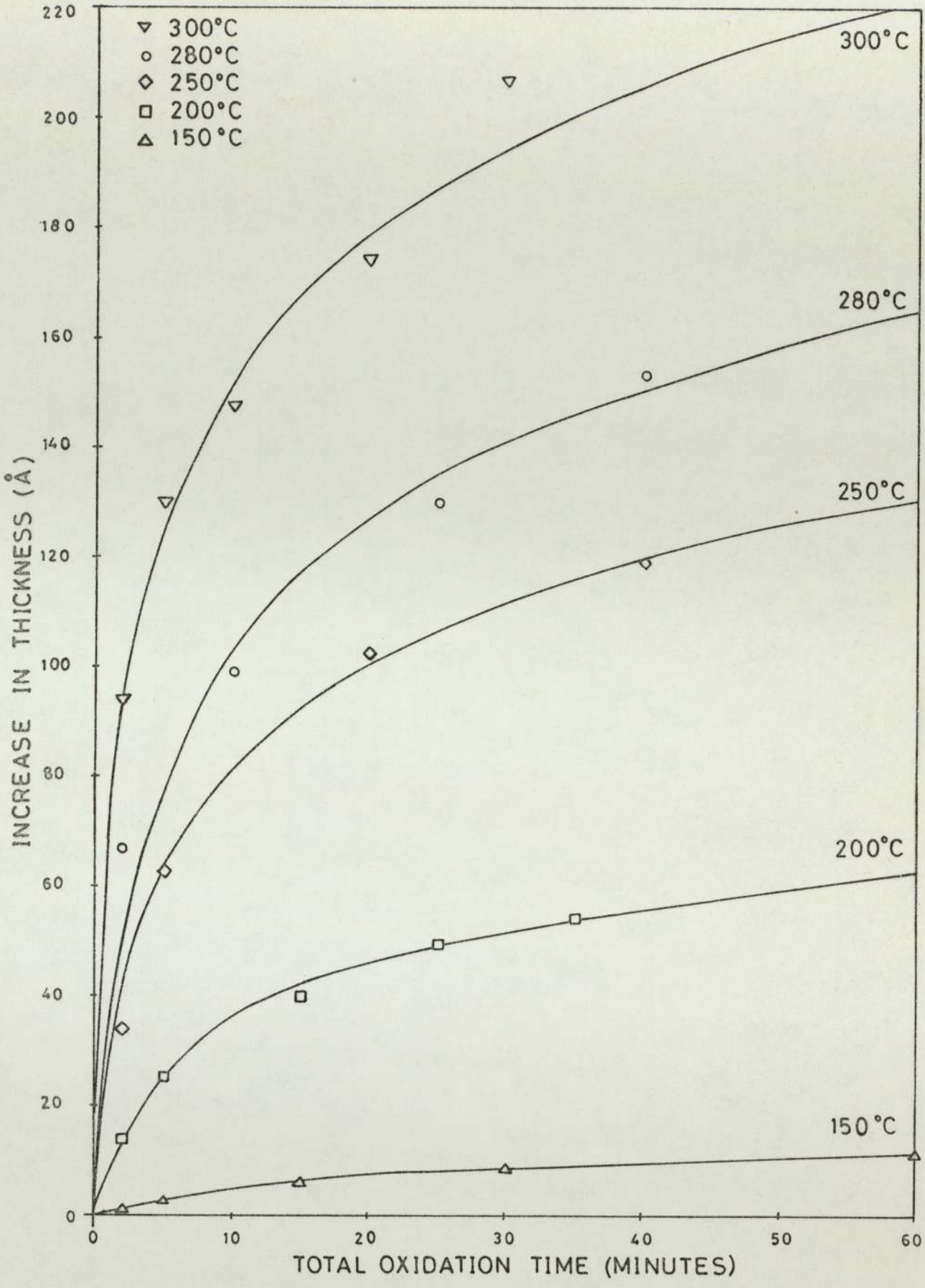

FIGURE 5.1 Logarithmic Oxide Growth Curves for Temperatures in the Range 150°C to 300°C.

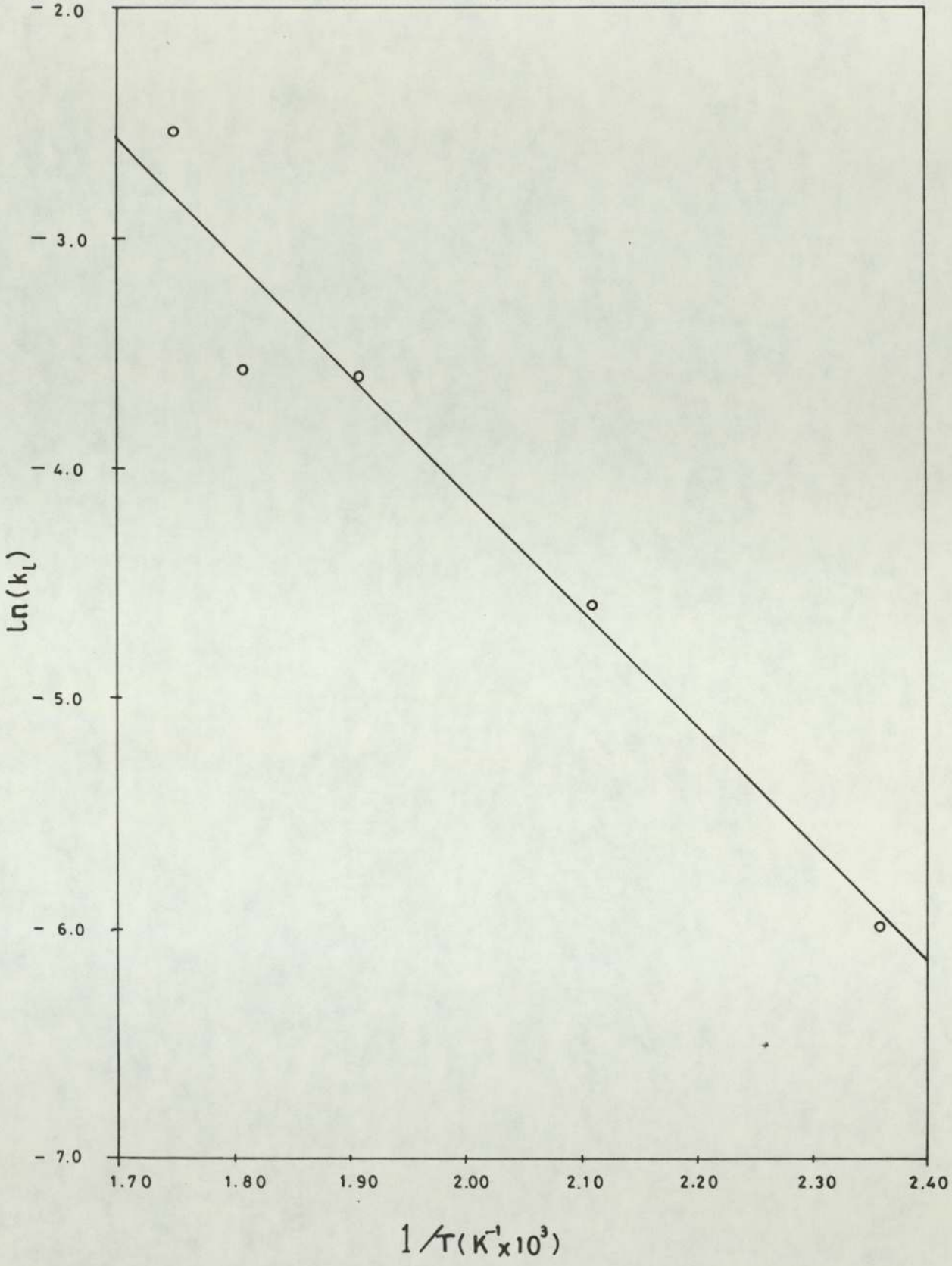

FIGURE 5.2 Logarithm of Oxidational Rate Constant versus Reciprocal of Absolute Temperature for the Temperature Range 150°C to 300°C.

obtained for each oxidation temperature, while figure 5.1 shows the corresponding logarithmic rate curves.

The variation of oxidational growth rate with temperature is described by the Arrhenius equation:

$$k = A \exp\left(\frac{-Q}{RT}\right) \qquad (5.3)$$

where: k = oxidational growth rate constant

A = Arrhenius constant

Q = activation energy for oxidation

R = gas constant = $8.310\ J\ K^{-1}\ mol^{-1}$

T = oxidation temperature

Thus a plot of $\ln(k)$ versus $(1/T)$ is a straight line of slope $(-Q/R)$ and intercept $\ln(A)$ on the $\ln(k)$ axis. In the case of a logarithmic rate law, the quantities k, A and Q in equation (5.3) can be represented by k_L, A_L and Q_L for logarithmic oxidation. Figure 5.2 is a plot of $\ln(k_L)$ versus $(1/T)$ for the temperature range 150-300°C investigated by ellipsometry, while table 5.2 gives the resulting Q_L and A_L values.

5.1.2 Mass Increase Results

In the temperature range 450°C to 800°C oxidation rates of low alloy steel were determined by means of mass increase measurements. The growth of oxide at all temperatures investigated in this range was found to follow a parabolic rate law of the form:

$$(\Delta m)^2 = k_p t + c_3 \qquad (5.4)$$

where: Δm = mass increase per unit area

k_p = parabolic rate constant

c_3 = a constant

t = length of oxidation period

Figures 5.3(a) to 5.3(i) are plots of $(\Delta m)^2$ versus t for oxidation temperatures between 450°C and 800°C. It can be seen that the straight line plots often do not pass through the origin, ie. $c_3 \neq 0$, as we would intuitively expect if $\Delta m = 0$ at time $t = 0$. However, the simple explanation of this is that the oxidational rate law is not truly parabolic in the very early stages of oxidation, but is most likely linear. This transitory linear stage is very brief, after which a different rate law ensues, this being a parabolic rate law at the relatively high temperature employed in the present mass increase investigation.

Tables 5.3(a) and 5.3(b) give the calculated parabolic rate constants (k_p) for oxidation in the temperature ranges 450°C to 600°C and 600°C to 800°C respectively. Separation of the results into two distinct temperature regions follows the work of Caplan and Cohen (26) and is due to the fact that FeO is present in the oxide above, but not below, a temperature of 570°C.

Equation (5.3) also applies to parabolic oxidation. Figure 5.4 is a graph of $\ln(k_p)$ versus $(1/T)$ for the temperature region between 450°C and 800°C. The activation energy (Q_p) and Arrhenius constant (A_p) for parabolic oxidation, determined from this figure, are given in tables 5.4(a) and 5.4(b).

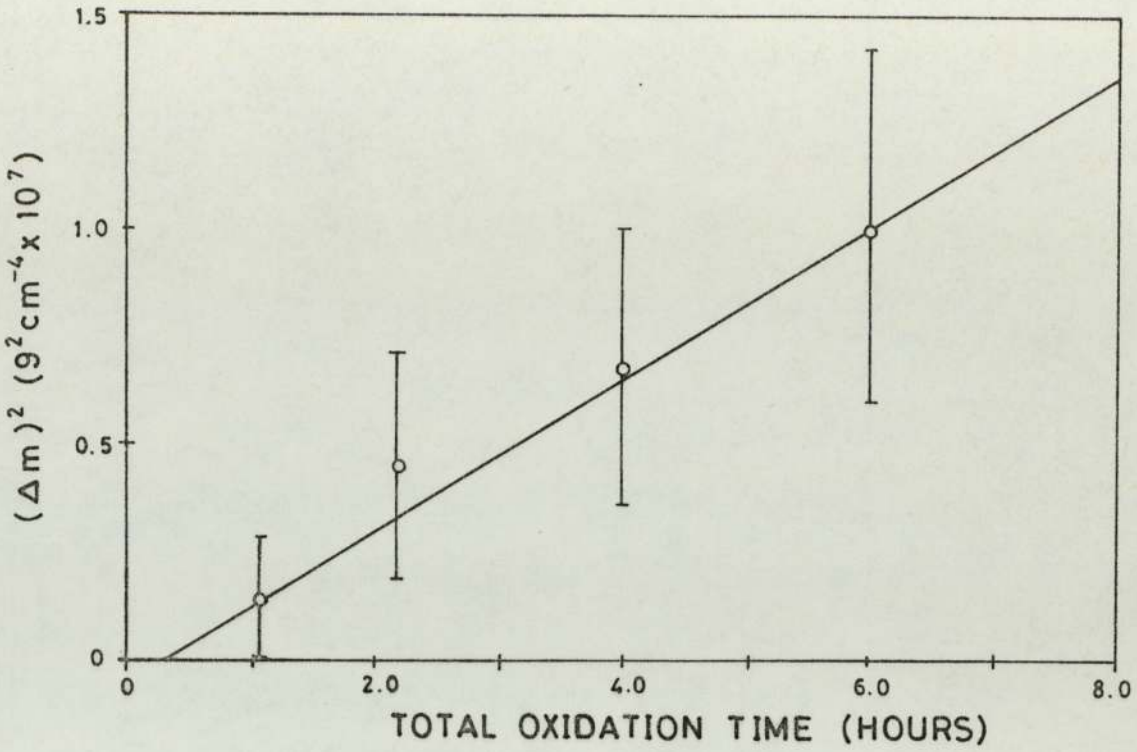

FIGURE 5.3(a) Square of Mass Increase versus Time for Oxidation at 450°C.

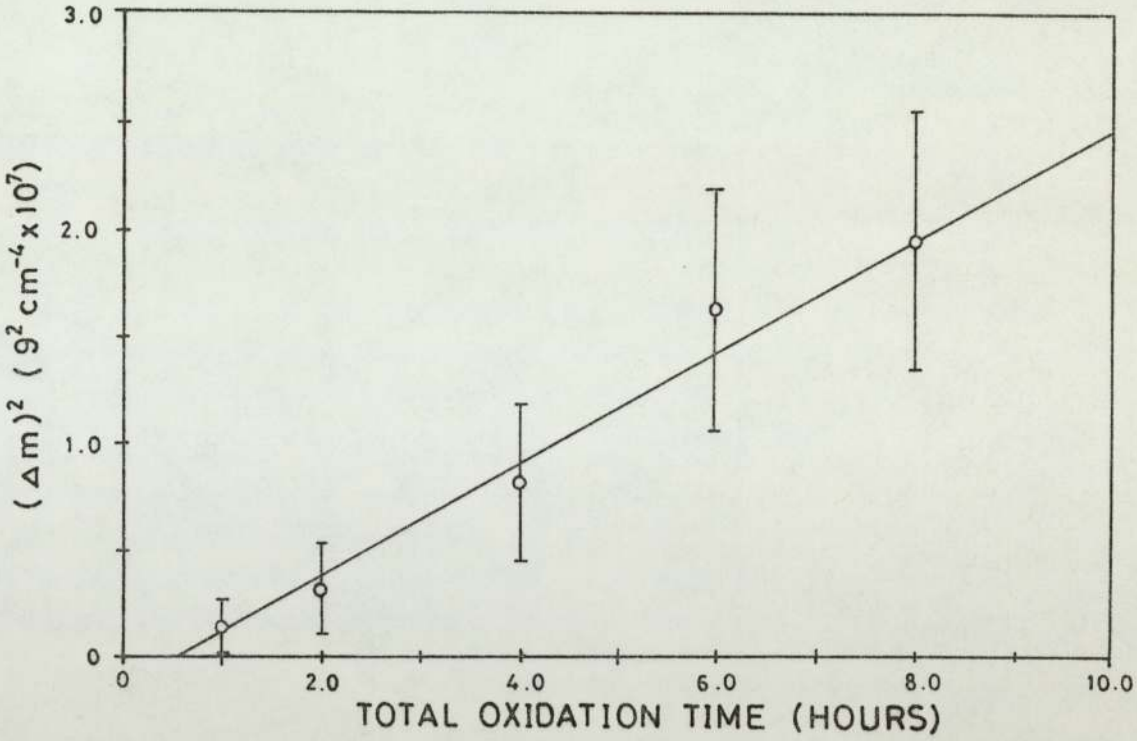

FIGURE 5.3 (b) Square of Mass Increase versus Time for Oxidation at 470°C.

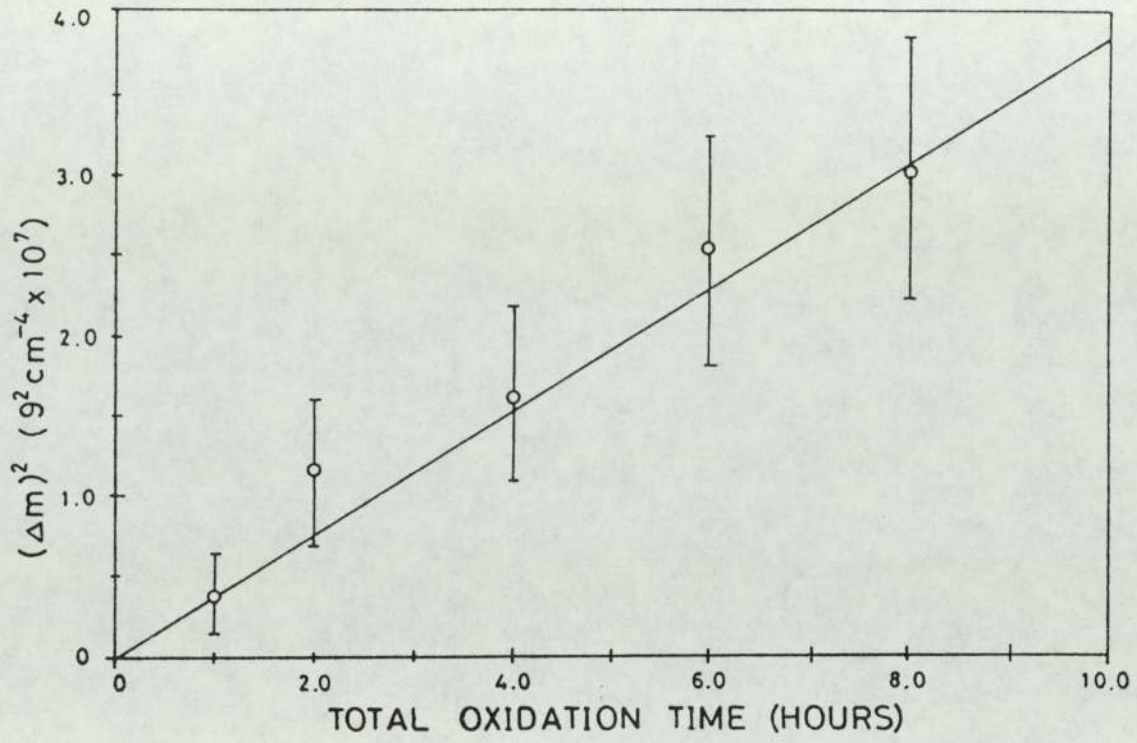

FIGURE 5.3 (c) Square of Mass Increase versus Time for Oxidation at 500°C.

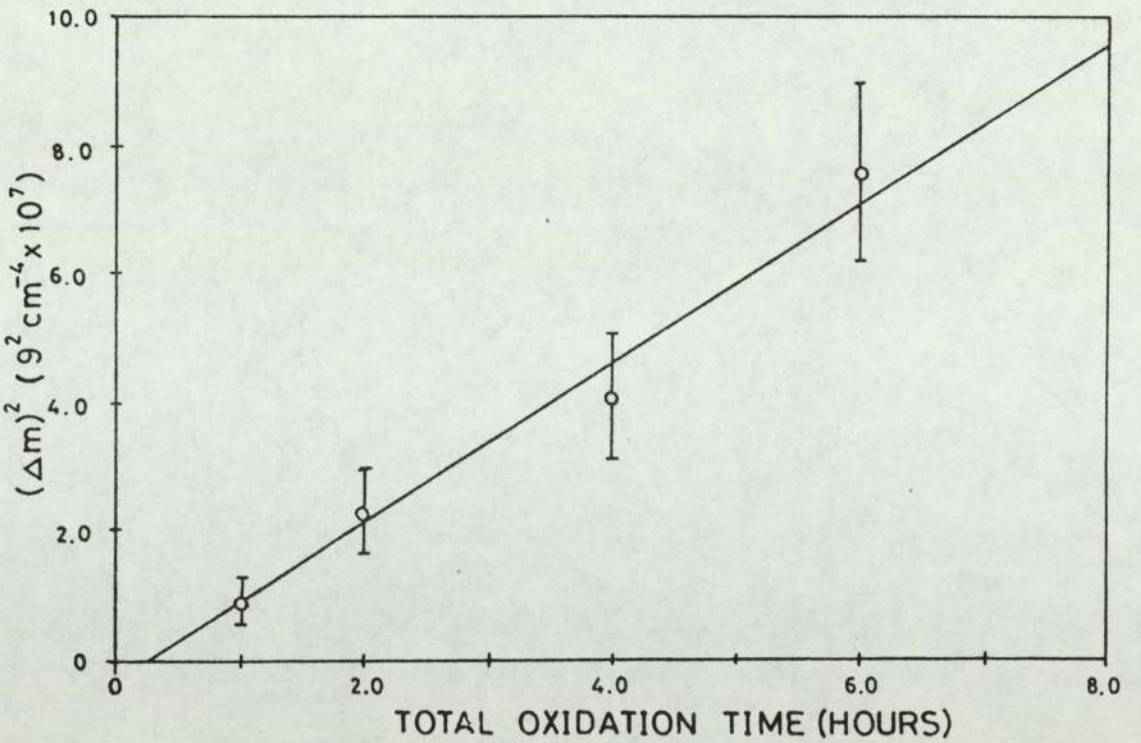

FIGURE 5.3 (d) Square of Mass Increase versus Time for Oxidation at 550°C.

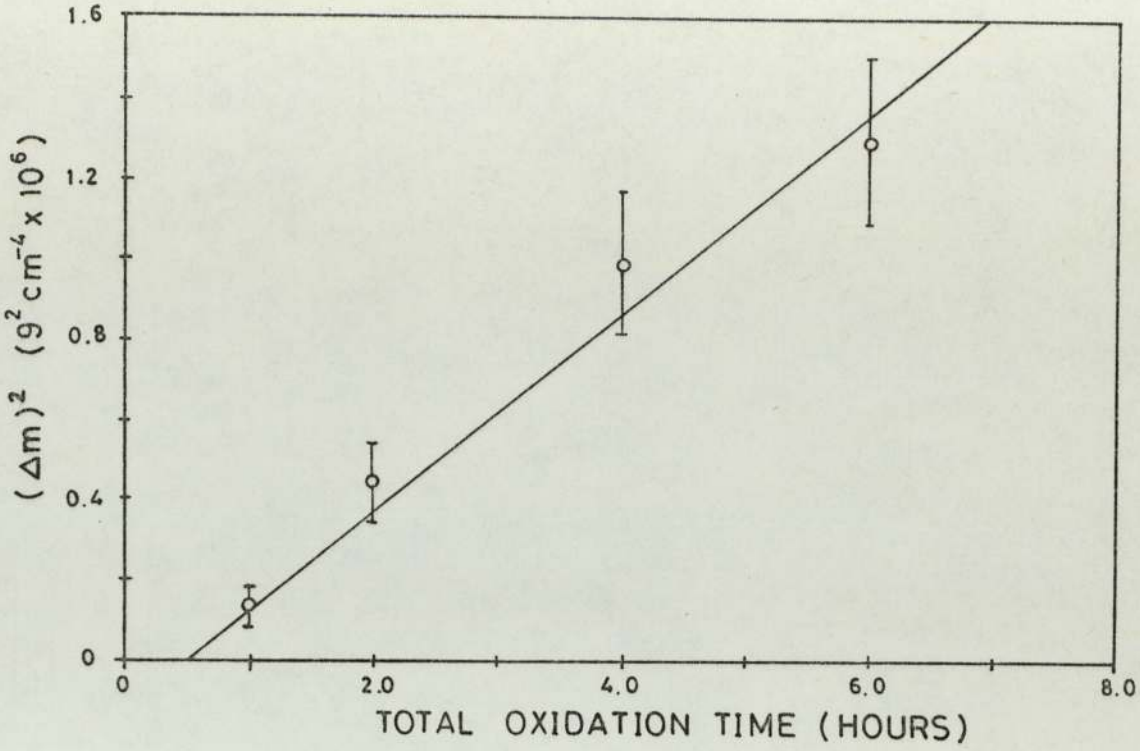

FIGURE 5.3(e) Square of Mass Increase versus Time for Oxidation at 600°C

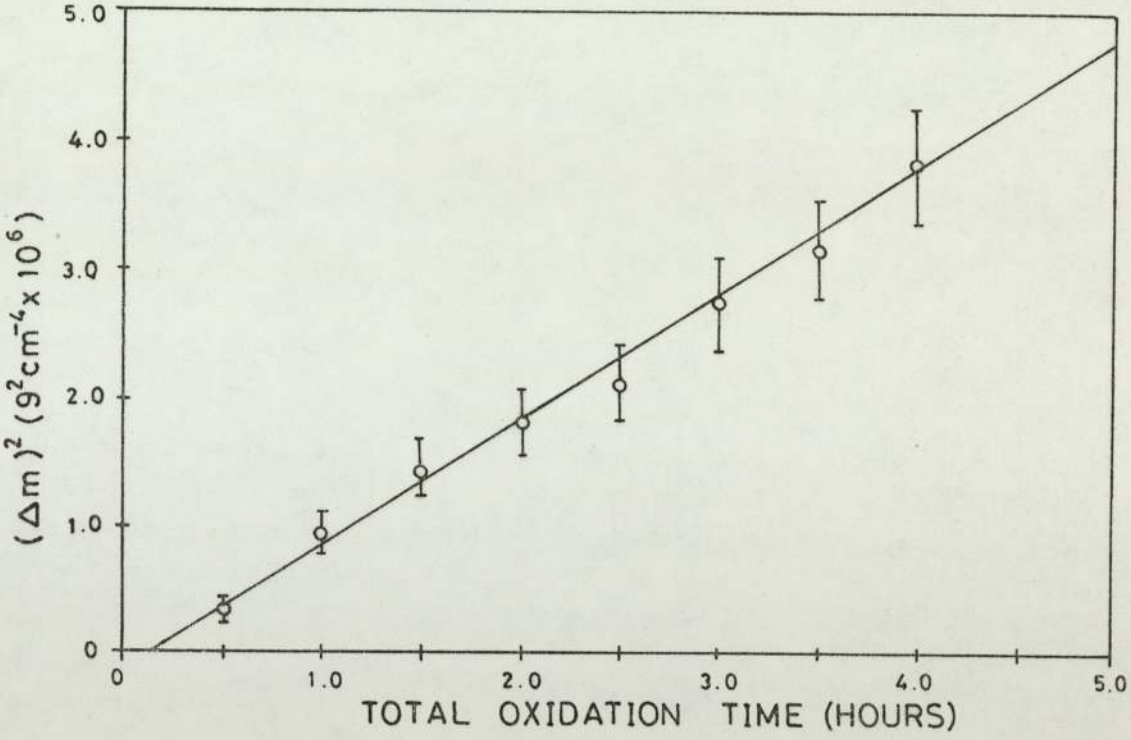

FIGURE 5.3(f) Square of Mass Increase versus Time for Oxidation at 650°C.

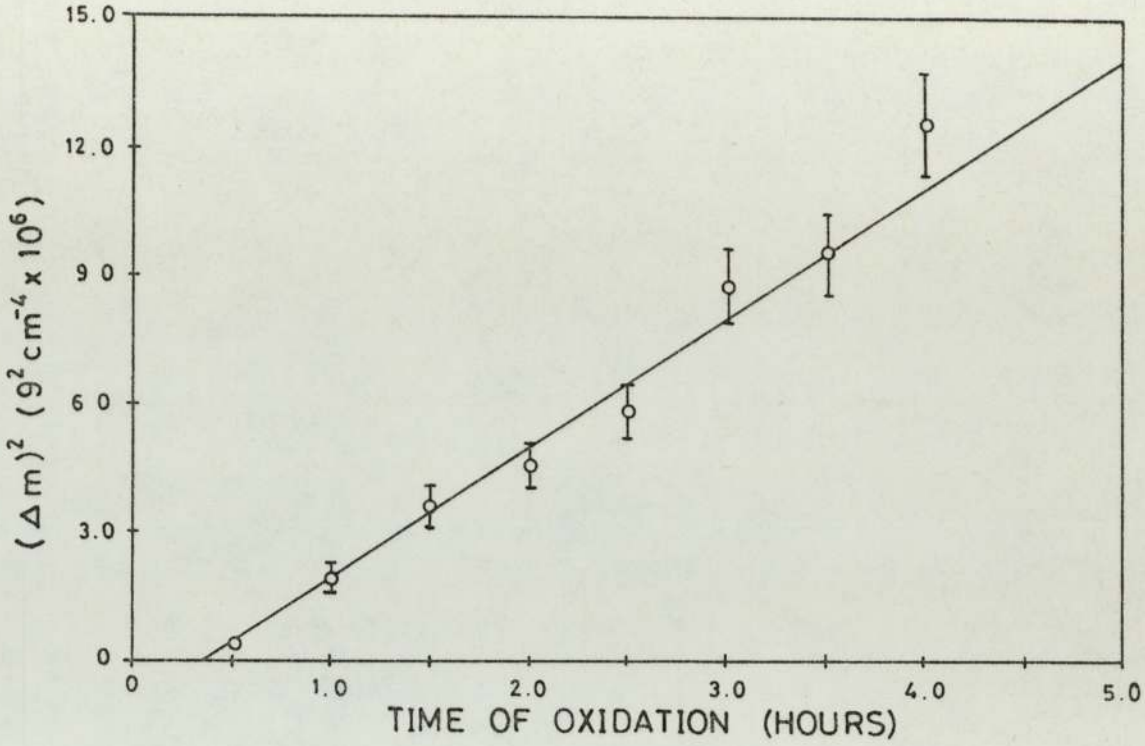

FIGURE 5.3 (g) Square of Mass Increase Versus Time for Oxidation at 700°C.

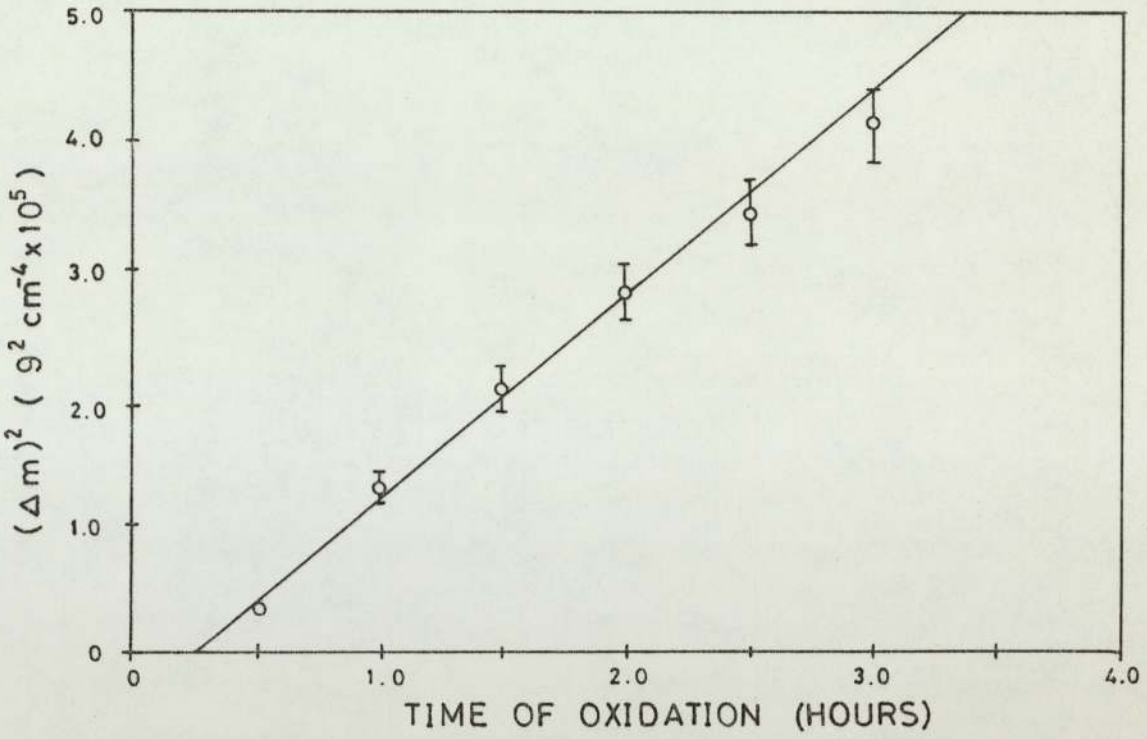

FIGURE 5.3 (h) Square of Mass Increase Versus Time for Oxidation at 750°C

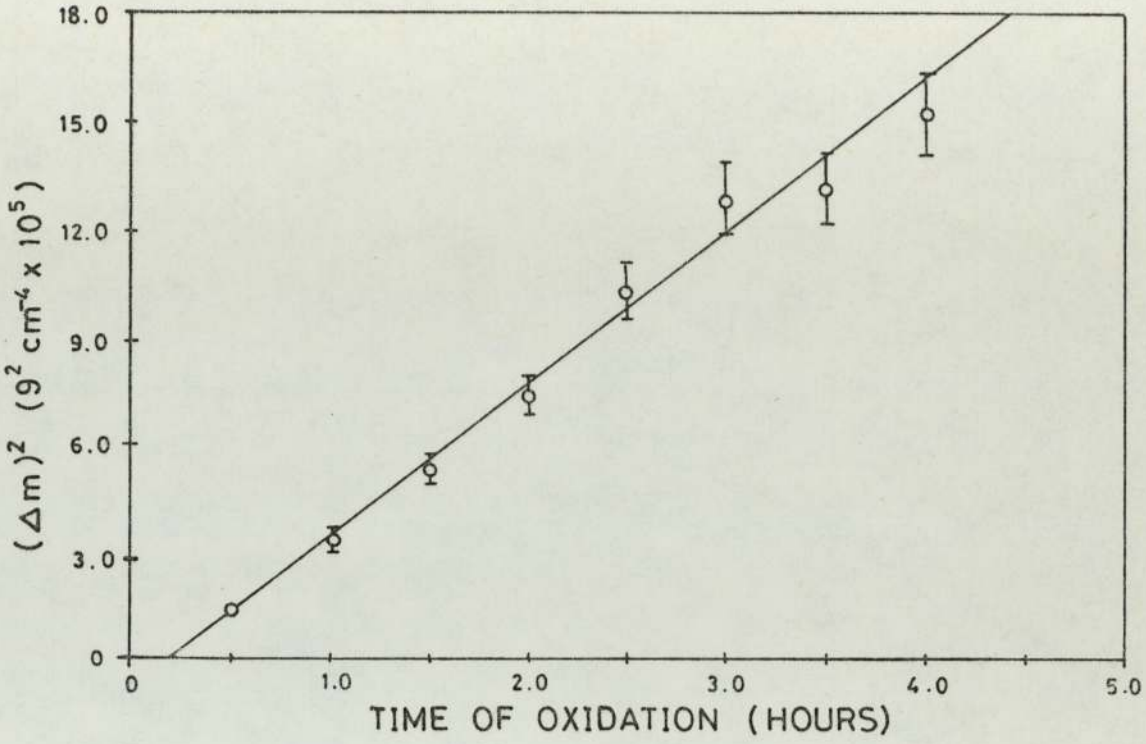

FIGURE 5.3 (i) Square of Mass Increase versus Time for Oxidation at 800°C.

T (°C)	k_p ($9^2 cm^{-4} s^{-1} \times 10^{11}$)
450	0.49 ± 0.31
470	0.72 ± 0.29
500	1.05 ± 0.42
550	3.39 ± 0.72
600	6.6 ± 1.3

TABLE 5.3(a) Parabolic Oxidational Rate Constants for Temperatures below 600°c.

T (°C)	k_p ($9^2 cm^{-4} s^{-1} \times 10^{10}$)
600	0.66 ± 0.13
650	2.72 ± 0.43
700	8.4 ± 1.0
750	44 ± 6
800	118 ± 18

TABLE 5.3(b) Parabolic Oxidational Rate Constants for Temperatures above 600°c.

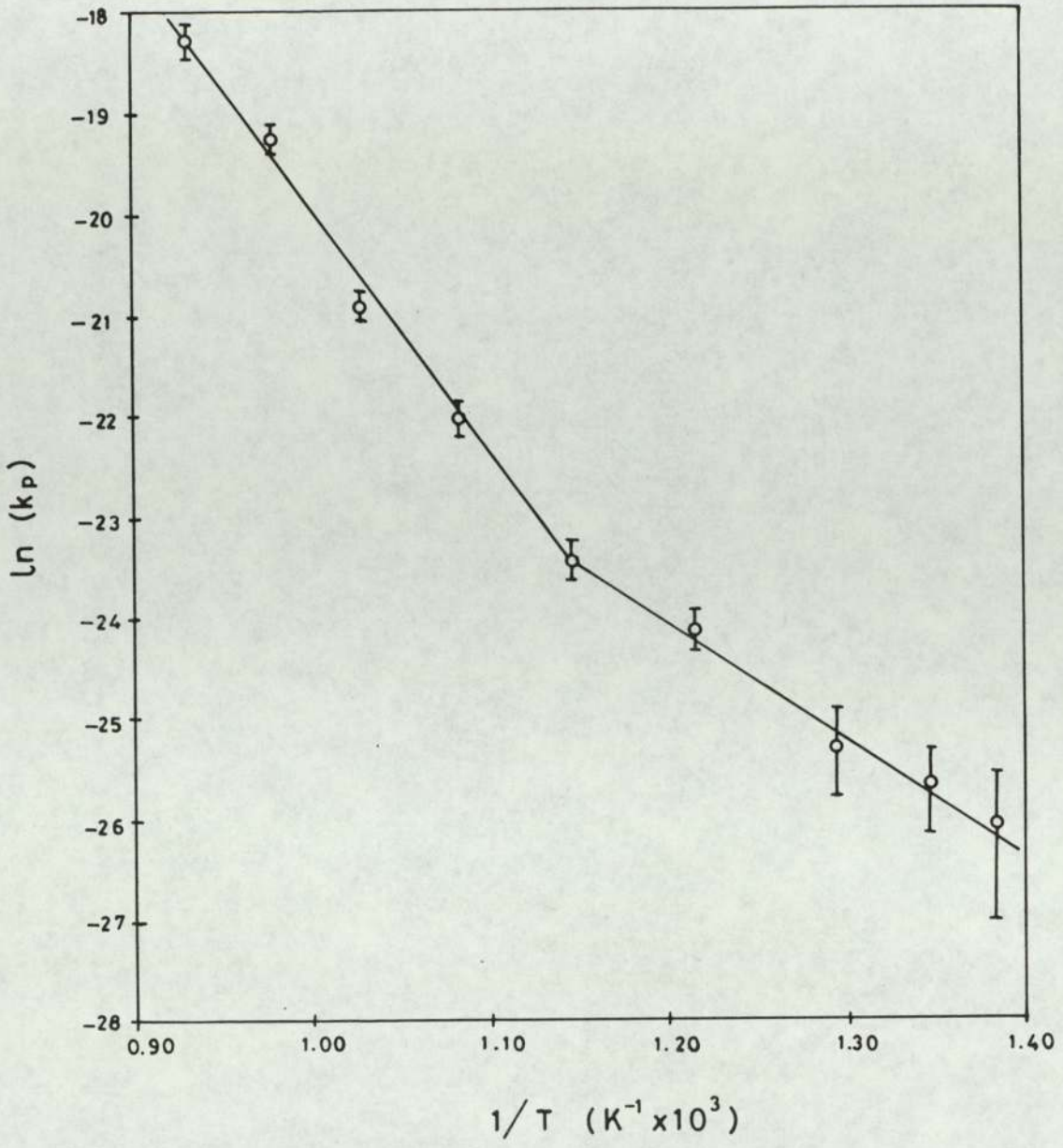

FIGURE 5.4 Logarithm of Parabolic Rate Constant versus Reciprocal of Absolute Temperature for the Temperature Range 450°C to 800°C.

TEMP RANGE (°C)	Q_P (kJ mol^{-1})	A_P ($kg^2 m^{-4} s^{-1}$)
450 - 600	96 ± 25	$(3.7^{+134}_{-3.6}) \times 10^{-3}$

TABLE 5.4(a) Activation Energy and Arrhenius Constant for Parabolic Oxidation below 600°C.

TEMP RANGE (°C)	Q_P (kJ mol^{-1})	A_P ($kg^2 m^{-4} s^{-1}$)
600 - 800	201 ± 20	$(7.1^{+83}_{-6.6}) \times 10^{3}$

TABLE 5.4 (b) Activation Energy and Arrhenius Constant for Parabolic Oxidation above 600 °C.

5.2 X-Ray Diffraction Results

5.2.1 Powder X-Ray Diffraction of Debris from EN8 Wear Tests

Tables 5.5(a), (b) and (c) give the relative intensities and interplanar spacing values (d_{hkl}) of experimentally obtained diffraction lines and demonstrate how these were compared with standard values for iron and its oxides in order to identify the constituents of the wear debris. These three particular examples were chosen because they represent the three distinct regions observed in the wear rate versus load and surface temperature versus load graphs associated with the EN8 wear experiments at 2.0 ms^{-1}.

The constituents of the wear debris, identified by x-ray diffraction, are listed in tables 5.6(a) and 5.6(b) for wear experiments conducted at linear sliding speeds of 2.0 ms^{-1} and 4.0 ms^{-1} respectively. Comparison of the wear rate versus load graphs (figures 4.1(a) and (b)) with these tables clearly indicates that there is a connection between the magnitude of the wear rate and the composition of the debris.

5.2.2 Glancing Angle X-Ray Diffraction of Worn Surfaces from EN8 Wear Tests

Selected worn surfaces from the EN8 wear tests were analysed by glancing angle x-ray diffraction. Pins and discs (studs) from wear experiments run at 2.0 ms^{-1} and loads of 10 N, 20 N, 30 N and 58 N were analysed, as were pins and discs taken from experiments run at 4.0 ms^{-1} and loads of 5 N, 30 N and

EXPERIMENTAL VALUES				POSSIBLE IDENTITY (ASTM INDEX d_{hkl} (Å) VALUES)*				
LINE	RELATIVE STRENGTH	2θ (DEG)	d_{hkl} (Å)	γ-Fe_2O_3	α-Fe_2O_3	Fe_3O_4	FeO	α-Fe
1	v. faint	28.0	3.697	$3.73^{(5)}$	$3.68^{(25)}$	-	-	-
2	medium	38.7	2.700	-	$2.69^{(100)}$	-	-	-
3	medium	41.5	2.525	$2.52^{(100)}$	$2.51^{(50)}$	$2.532^{(100)}$	-	-
4	faint	47.7	2.212	$2.23^{(.5)}$	$2.201^{(20)}$	-	-	-
5	strong	52.3	2.030	-	-	-	-	$2.03^{(100)}$
6	faint	58.3	1.836	-	$1.838^{(40)}$	-	-	-
7	medium	63.6	1.697	$1.70^{(12)}$	$1.690^{(60)}$	$1.715^{(10)}$	-	-
8	faint	74.0	1.486	$1.48^{(53)}$	$1.484^{(35)}$	$1.485^{(40)}$	-	-
9	faint	76.0	1.453	-	$1.452^{(35)}$	-	-	-
10	faint	77.5	1.429	$1.43^{(1)}$	-	-	-	$1.433^{(20)}$
11	v. faint	86.0	1.312	$1.32^{(7)}$	$1.310^{(20)}$	-	-	-
12	medium	99.8	1.169	-	-	-	-	$1.170^{(30)}$
13	v. faint	108.0	1.106	-	$1.102^{(14)}$	-	-	-
14	v. faint	115.3	1.059	-	$1.055^{(18)}$	$1.050^{(6)}$	-	-
15	faint	124.0	1.013	-	-	-	-	$1.0134^{(10)}$
CONCLUSION : Debris consists of α-Fe_2O_3 and α-Fe								

* Small bracketed numbers are the index values for the intensity of each diffraction line relative to the most intense line (intensity 100) for that compound.

TABLE 5.5 (a) Identification of Debris from EN8 Wear Experiment at 8N and 2.0 ms^{-1}

EXPERIMENTAL VALUES				POSSIBLE IDENTITY (ASTM INDEX d_{hkl} (Å) VALUES)				
LINE	RELATIVE STRENGTH	2θ (DEG)	d_{hkl} (Å)	γ-Fe_2O_3	α-Fe_2O_3	Fe_3O_4	FeO	α-Fe
1	v.faint	28.0	3.697	$3.73^{(5)}$	$3.68^{(25)}$	–	–	–
2	strong	38.7	2.700	–	$2.69^{(100)}$	–	–	–
3	strong	41.5	2.525	$2.52^{(100)}$	$2.51^{(50)}$	$2.532^{(100)}$	–	–
4	faint	48.0	2.199	–	$2.201^{(20)}$	–	–	–
5	strong	52.3	2.030	–	–	–	–	$2.030^{(100)}$
6	faint	58.5	1.831	–	$1.838^{(40)}$	–	–	–
7	medium	63.8	1.693	$1.70^{(12)}$	$1.690^{(60)}$	$1.715^{(10)}$	–	–
8	faint	67.5	1.610	$1.61^{(33)}$	–	$1.616^{(30)}$	–	–
9	faint	74.0	1.486	$1.48^{(53)}$	$1.484^{(35)}$	$1.485^{(40)}$	–	–
10	faint	76.0	1.453	–	$1.452^{(35)}$	–	–	–
11	v.faint	86.0	1.312	$1.32^{(7)}$	$1.310^{(20)}$	–	–	–
12	medium	99.9	1.169	–	–	–	–	$1.1702^{(30)}$
CONCLUSION: Debris consists of α-Fe_2O_3, Fe_3O_4 and α-Fe								

TABLE 5.5 (b) Identification of Debris from EN8 Wear Experiment at 25N and 2.0ms^{-1}

EXPERIMENTAL VALUES				POSSIBLE IDENTITY (ASTM INDEX d_{hkl} (Å) VALUES)				
LINE	RELATIVE STRENGHT	2θ (DEG)	d_{hkl} (Å)	γ-Fe_2O_3	α-Fe_2O_3	Fe_3O_4	FeO	α-Fe
1	faint	42.2	2.485	–	$2.51^{(50)}$	–	$2.49^{(80)}$	–
2	medium	49.2	2.149	–	–	–	$2.153^{(100)}$	–
3	strong	52.3	2.030	–	–	–	–	$2.03^{(100)}$
4	faint	72.2	1.518	$1.53^{(1)}$	–	–	$1.523^{(60)}$	–
5	faint	77.5	1.437	$1.43^{(1)}$	–	–	–	$1.433^{(20)}$
6	v.faint	87.0	1.299	–	–	–	$1.299^{(25)}$	–
7	v.faint	92.0	1.243	–	–	–	$1.243^{(15)}$	–
8	medium	99.8	1.170	–	–	–	–	$1.1702^{(30)}$
9	faint	124.0	1.013	–	–	–	–	$1.0134^{(10)}$
CONCLUSION : Debris consists of FeO and α-Fe								

TABLE 5.5 (c) Identification of Debris from EN8 Wear Experiment at 50N and 2.0ms^{-1}

EXPERIMENTAL LOAD (N)	DEBRIS COMPOSITION			
	α-Fe_2O_3	Fe_3O_4	FeO	α-Fe
5	✓	—	—	✓
10	✓	—	—	✓
13	✓	✓	—	✓
20	✓	✓	—	✓
25	✓	✓	—	✓
35	✓	✓	—	✓
40	—	✓	✓	✓
45	—	—	✓	✓
50	—	—	✓	✓
55	—	—	✓	✓

TABLE 5.6 (a) Composition of Wear Debris from EN8 Experiments at 2.0 ms^{-1}.

EXPERIMENTAL LOAD (N)	DEBRIS COMPOSITION			
	α-Fe_2O_3	Fe_3O_4	FeO	α-Fe
10	✓	✓	—	✓
20	✓	✓	—	✓
30	✓	✓	—	✓
35	✓	✓	✓	✓
40	—	✓	✓	✓
45	—	—	✓	✓
52	—	—	✓	✓
58	—	—	✓	✓

TABLE 5.6 (b) Composition of Wear Debris from EN8 Experiments at 4.0 ms^{-1}.

58 N. The results of the identification of the surface oxides by glancing angle x-ray diffraction analyses are shown in tables 5.7(a) and 5.7(b) for experiments carried out at linear sliding speeds of 2.0 ms^{-1} and 4.0 ms^{-1} respectively. The composition of the wear debris was found to be in good agreement with the composition of the surface oxide for each particular wear experiment, as we would expect. Thus, the transitions in wear rate at particular applied loads are, in fact, connected with changes in the composition of the oxide on the worn pin and disc surfaces.

5.2.3 Powder X-Ray Diffraction of Wear Debris from EN8 / 9% Cr Wear Tests

Since the purpose of the EN8 / 9% Cr wear experiments was to determine if there was any transfer of oxide from the disc to the pin during oxidational wear, it was first necessary to establish that the wear regime in this case was, in fact, oxidational. X-ray diffraction was one of the techniques employed for this purpose.

The debris produced in all of the EN8 / 9% Cr wear tests ie. for loads of 20 N, 30 N, 40 N, and 50 N, was a fine black powder containing traces of metallic particles. X-ray diffraction revealed that in all cases the constituents of the debris had α-Fe_2O_3, Fe_3O_4, FeO and α-Fe structures. Chromium was almost certainly present in the oxide debris, in addition to the iron oxide, since it was detected by AES in the surface oxide on the worn discs, but it was difficult to detect by XRD as the diffraction line spacings of chromium, iron and mixed iron/chromium oxides having similar

EXPERIMENTAL LOAD (N)	COMPOSITION			
	α-Fe_2O_3	Fe_3O_4	Fe O	α-Fe*
10	✓	–	–	✓
20	✓	✓	–	✓
30	✓	✓	–	✓
58	–	–	✓	✓

TABLE 5.7(a) Glancing Angle XRD Results for Worn Surfaces from EN8 Experiments Conducted at 2.0 ms^{-1}.

EXPERIMENTAL LOAD (N)	COMPOSITION			
	α-Fe_2O_3	Fe_3O_4	Fe O	α-Fe*
5	✓	✓	–	✓
30	✓	✓	–	✓
58	–	–	✓	✓

TABLE 5.7(b) Glancing Angle XRD Results for Worn Surfaces from EN8 Experiments Conducted at 4.0 ms^{-1}.

* The α-Fe detected in all instances was present in the bulk metal since the depth analysed was greater than the thickness of the surface oxide.

OXIDATION CONDITIONS*	OXIDE COMPOSITION		
	α-Fe_2O_3	Fe_3O_4	FeO
6 hours at 450°C	✓	✓	—
8 hours at 500°C	✓	✓	—
6 hours at 550°C	✓	✓	—
4½ hours at 650°C	✓	✓	✓
4½ hours at 800°C	✓	✓	✓

* All samples were oxidised in air at atmospheric pressure.

TABLE 5.8 Glancing Angle XRD Results for Low Alloy Steel Surfaces Oxidised under Static Conditions

structures are almost identical. It is likely that chromium ions were incorporated in the iron oxides forming mixed oxides such as $(Fe,Cr)_2O_3$ and $FeCr_2O_4$ (18).

5.2.4 Glancing Angle X-Ray Diffraction of Statically Oxidized Surfaces

Selected low alloy steel samples, oxidized at various temperatures in a furnace, were analysed by glancing angle x-ray diffraction. The results are shown in table 5.8. It can be seen that there is a transition temperature between 550°C and 650°C above which FeO is detectable. This was expected since it is well known that FeO only forms at temperatures of 570°C and above. It was not possible to identify the oxides present on the samples oxidized at temperatures of 300°C and below by glancing angle x-ray diffraction because the oxide films were too thin.

5.3 X-Ray Photoelectron Spectroscopy (XPS) Results

All XPS spectra presented in this section were produced by Magnesium Kα incident radiation generated using an x-ray source operating at an EHT and filament current of 15 kV and 30 mA respectively, unless otherwise stated (see section 3.4.7 for full operating conditions).

5.3.1 Calibration of the Spectrometer Energy Scale

Figures 5.5(a), (b) and (c) show the respective $Au4f_{7/2}$, $Ag3d_{5/2}$ and $Cu2p_{3/2}$ photoelectron peaks obtained once the energy scale of the electron spectrometer had been correctly

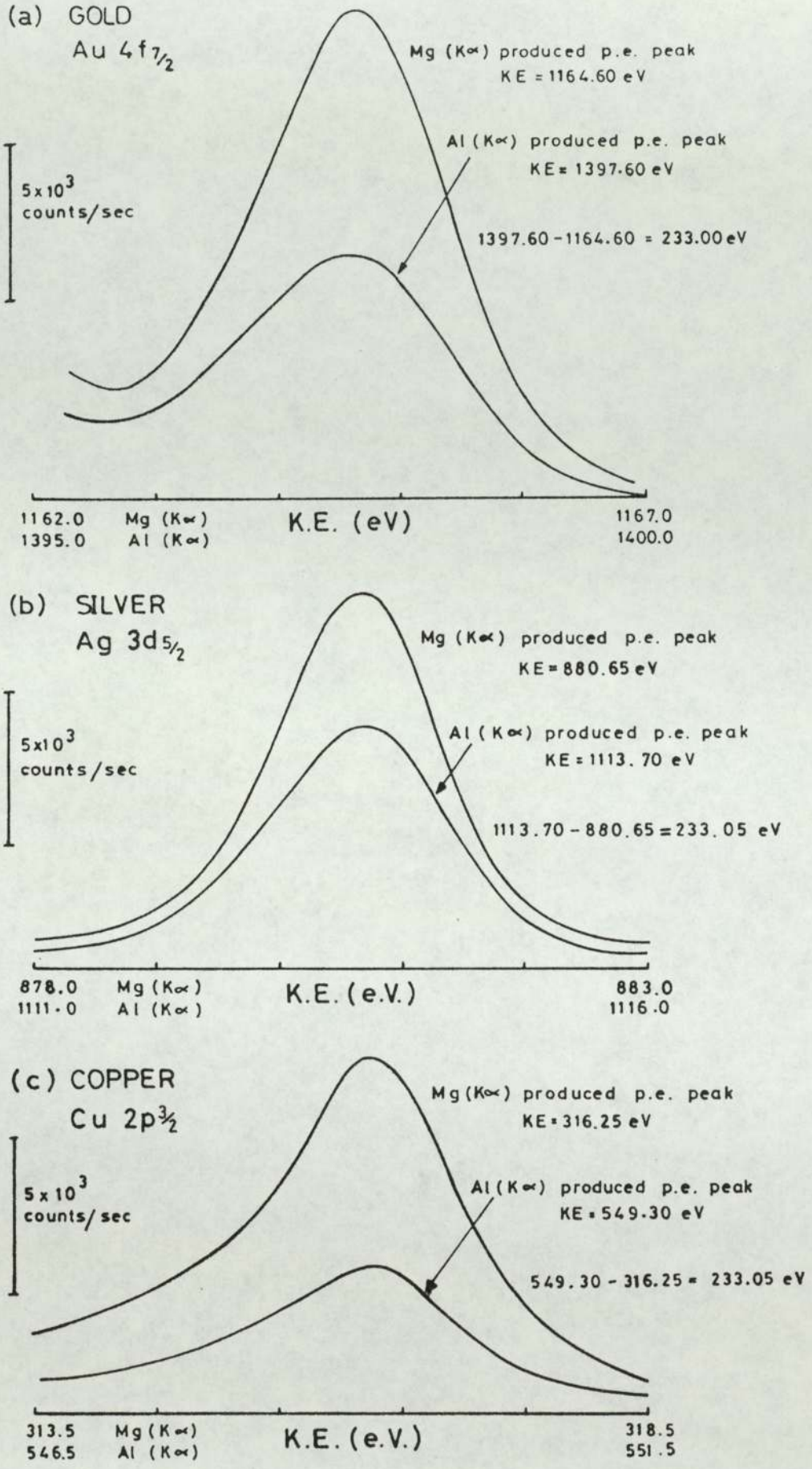

FIGURE 5.5 Photoelectron Peaks of Metal Standards

calibrated. Measured kinetic energy values now differed from tabulated kinetic energy values by an amount equal to the spectrometer work function. In order to calculate the work function from equation (3.3) it was first necessary to assign a value to the binding energy of the $Au4f_{7/2}$ line produced from the primary gold standard. A value of 84.0 eV was chosen for this latter quantity in accordance with the work of Allen et al (73) and McIntyre et al (74). It was found that :

spectrometer work function, ϕ = 5.0 eV

5.3.2 XPS Core Level Spectra of Iron and its Three Oxides

Iron and iron oxide standards were studied by means of XPS in order to obtain core level electron spectra characteristic of Fe, α-Fe_2O_3, Fe_3O_4 and FeO surfaces, and, in particular, to accurately determine core level electron binding energies for these surfaces. The results obtained could then be used as standards, against which the photoelectron peaks produced from analysis of other oxidized iron and steel surfaces could be compared, so that the oxides present on these surfaces could be identified. In the present investigation the standard binding energy values were used to facilitate the identification of oxides produced on the worn steel surfaces, and also for identifying statically grown oxides on low alloy steel.

The iron oxide samples were in the form of powder, while the iron sample was in the form of a flat sheet. Full

details of sample preparation and mounting are given in section 3.4.8, while details of the subsequent spectroscopic examination are given in section 3.4.10.

The C1s peak was invariably the most intense spectral peak for all samples in the unetched state. Measurements for this peak and for the $Fe2p_{3/2}$ peaks for FeO, Fe_3O_4 and α-Fe_2O_3 show relative intensities of 4.6, 5.6 and 3.2 respectively in the unetched condition. Estimated values of carbon present in all three cases, expressed as an atomic fraction, were about 0.7. These are semi-quantitative estimates based on peak area measurements, and cross-section values due to Scofield (75). No account was taken of photoelectron angular intensity distributions or analyser or detector efficiency variation with photoelectron energy.

These latter quantities have as yet not been reliably determined for the instrument used in this investigation. More reliable quantitative results may perhaps be obtained from the very comprehensive data of Evans et al (76) recorded on an AEI ES-200 spectrometer together with angular intensity distributions taken from the work of Reilman et al (77). However, serious quantitative analyses can be attempted only when a full appraisal of the XSAM 800 instrumental characteristics has been undertaken, and this was outside the scope of this project.

After a period of a few minutes of ion etching under the conditions stated in section 3.4.7 the carbon peak had fallen to a negligible level, indicating that carbon contamination had been effectively removed.

The results of the XPS analysis of each oxide will now be considered separately.

FeO (Wustite)

Figure 5.6(a) shows the Fe2p spectrum of an air exposed FeO powder surface. The maxima of the $Fe2p_{3/2}$ and $Fe2p_{1/2}$ photoelectron peaks occur at binding energy values of 710.7 eV and 724.4 eV respectively and, in addition, a satellite peak is observable 8.0 eV above the $Fe2p_{3/2}$ peak. The corresponding O1s spectrum is shown in figure 5.11(d), and it is considered that the peak at around 530.1 eV is due to the oxide, while that at 531.4 eV is due to a surface adsorbed species. Upon etching the FeO sample surface very briefly with Ar^+ ions, the higher binding energy peak in the O1s spectrum diminished considerably, with a corresponding change in the Fe2p spectrum. The $Fe2p_{3/2}$ and $Fe2p_{1/2}$ peak maxima shifted to the lower values of 709.6 eV and 722.9 eV respectively, while the satellite peak previously present disappeared, to be replaced by another satellite peak centred 6.0 eV above the $Fe2p_{3/2}$ peak maximum. Another feature of the Fe2p spectrum was the appearance of a small peak on the low binding energy side of each of the two main photoelectron peaks. These additional peaks were due to the presence of atomic Fe, produced by ion beam reduction of the Fe ions of the oxide. Further etching did not result in any further change in the XPS spectra except for a slight increase in intensity of the Fe^o peaks. It was concluded that any surface layers produced by adsorption on, or oxidation of, the FeO surface had now been removed so that the underlying FeO was exposed.

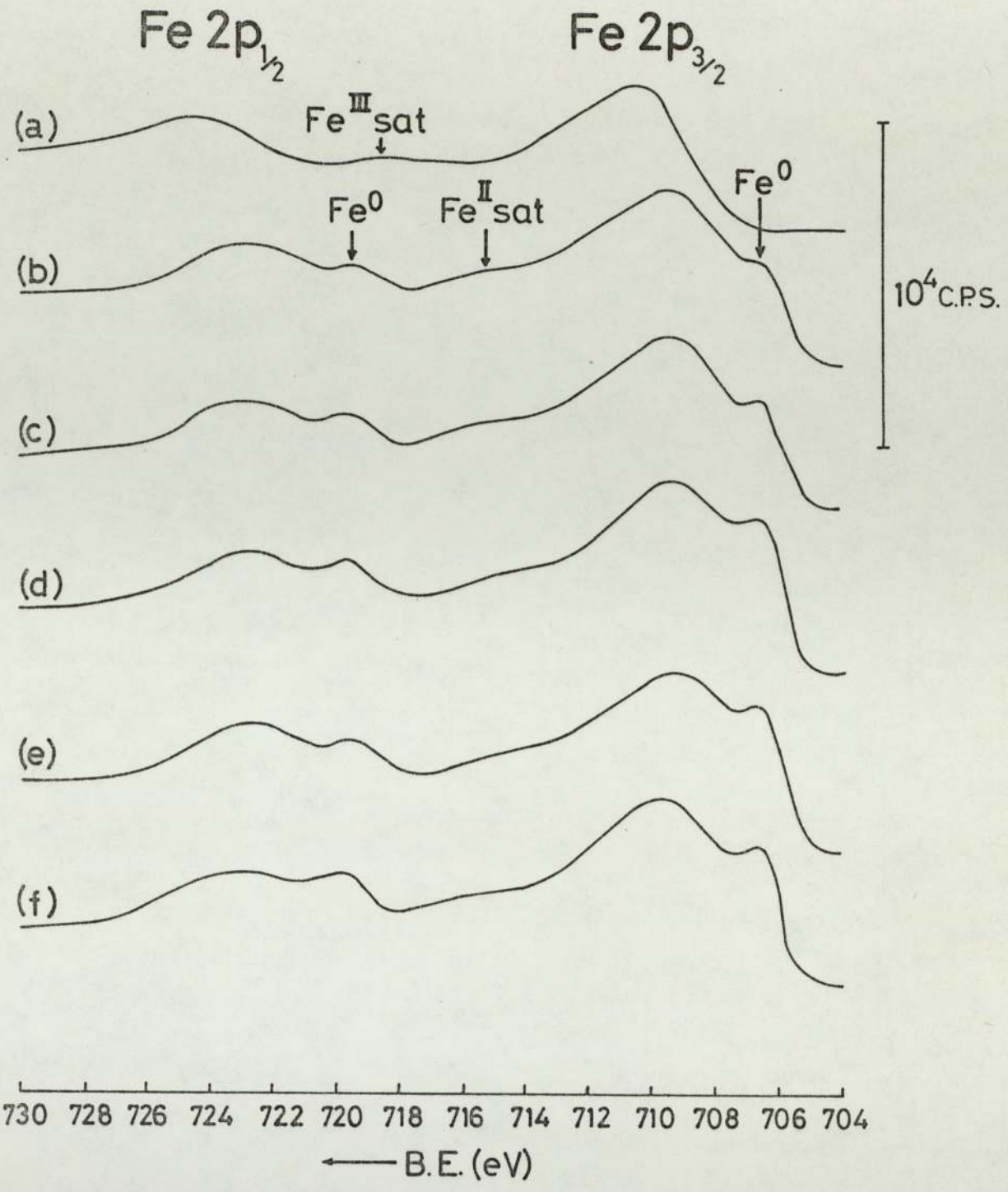

(a) unetched, air exposed sample
(b) 15 min etch
(c) 30 min etch
(d) 45 min etch
(e) 60 min etch
(f) 90 min etch

FIGURE 5.6 Effect of Ar^+ Etching on Fe2p Spectra of Fe O Powder Surface.

Fe_3O_4 (Magnetite)

The initial Fe2p spectrum of an air exposed Fe_3O_4 powder surface varied slightly from sample to sample. Usually the $Fe2p_{3/2}$ photoelectron peak maximum occurred at 710.8 eV, but occasionally it would be higher, sometimes as high as 711.6 eV. It was postulated that this variation was due to differing degrees of surface adsorption. This view was supported by observation of the corresponding O1s spectra, as will be seen when the heating of an Fe_3O_4 sample under UHV conditions is discussed shortly.

The O1s spectrum corresponding to an initial $Fe2p_{3/2}$ peak maximum at 710.8 eV was a broad unresolved double peak having a maximum around 530.7 eV as shown in figure 5.11(c). After a very brief period of etching the sample surface the higher binding energy peak in the O1s spectrum had almost disappeared, leaving the peak due to the oxide. The binding energy values of the corresponding $Fe2p_{3/2}$ and $Fe2p_{1/2}$ peak maxima were 710.3 eV and 723.5 eV respectively. At this point the XPS spectra were considered to be representative of an Fe_3O_4 surface. Further etching resulted in the Fe2p peak maxima shifting to even lower energies, until after only a few minutes they coincided with the binding energies determined for an FeO surface, indicating that a full reduction of Fe^{3+} species to Fe^{2+} had taken place. No further change in the photoelectron spectra was observed when etching of the surface was continued, except for a slight increase in the intensity of the $Fe^{o}2p$ peaks, produced by ion beam reduction of the oxide. Figure 5.7. shows the effect which ion beam etching had upon the Fe2p spectra of the Fe_3O_4

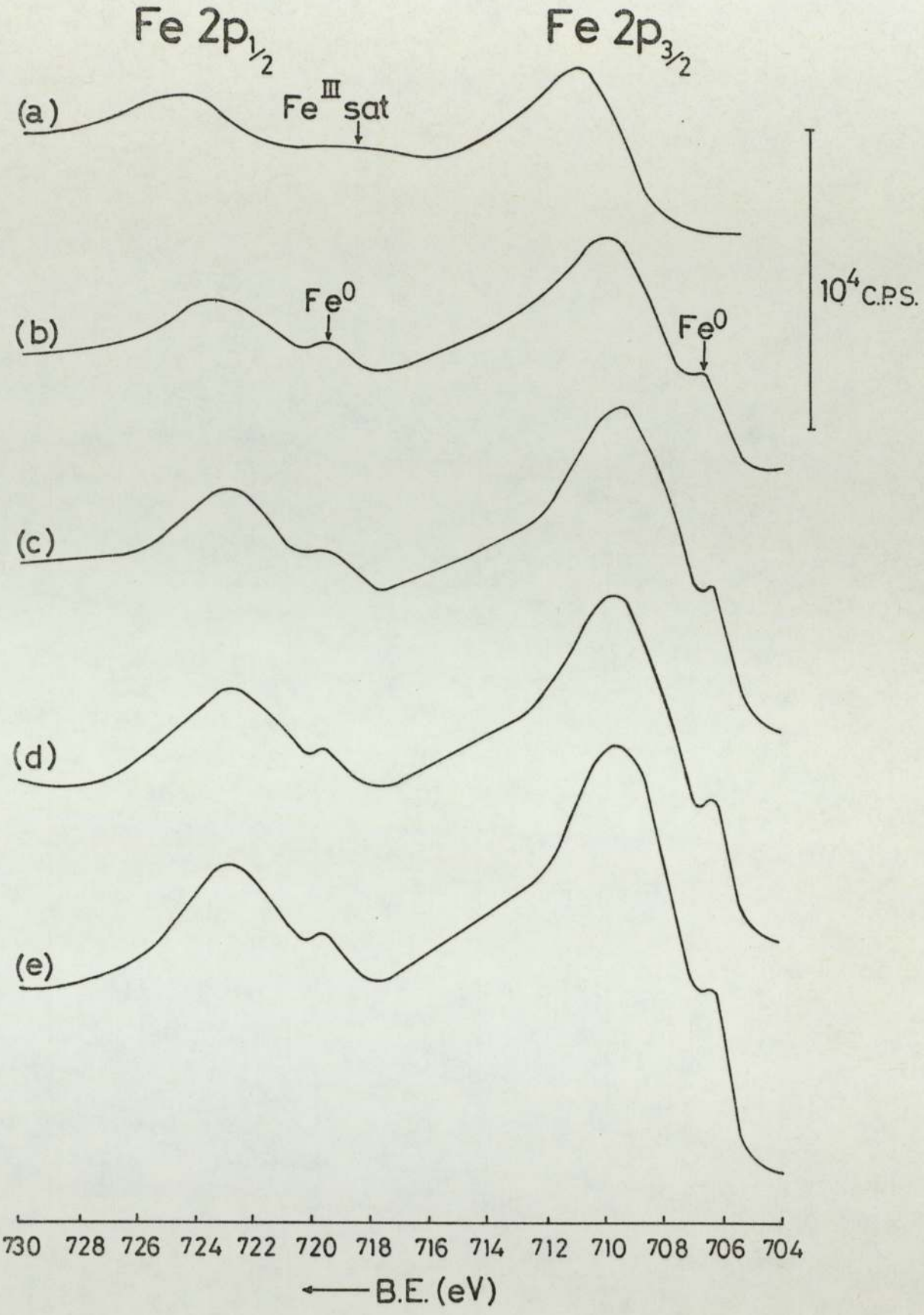

(a) unetched, air exposed sample
(d) 1 min etch
(c) 5 min etch
(d) 15 min etch
(e) 60 min etch

FIGURE 5.7 Effect of Ar^+ Ion Etching on Fe2p Spectra of Fe_3O_4 Powder Surface.

powder surface, while figure 5.12 shows the corresponding O1s spectra.

XPS analysis of an Fe_3O_4 powder surface was also carried out while gradually heating the sample under UHV conditions in the sample analysis chamber. An Fe_3O_4 surface was chosen which exhibited a high degree of adsorbed species as witnessed by the dominant higher binding energy peak in the O1s spectrum. The corresponding $Fe2p_{3/2}$ and $Fe2p_{1/2}$ peak maxima were at 711.5 eV and 725.0 eV respectively. Prolonged heating of the sample at 100°C resulted in the maximum of the unresolved peak doublet shifting from 531.4 eV to 531.0 eV, while the maxima of the photoelectron peaks in the Fe2p spectrum moved 0.5 eV in the direction of decreasing binding energy. At 200°C the O1s peak maximum shifted to an even lower value of 530.7 eV indicating that a considerable amount of the adsorbed species had been removed. The new $Fe2p_{3/2}$ and $Fe2p_{1/2}$ peak maxima were at 710.8 eV and 724.3 eV respectively. Further heating at 200°C, 300°C and 400°C produced no further change in the Fe2p spectra, although the O1s adsorption peak was diminished slightly more, now being visible as a high binding energy shoulder on the O1s oxide peak. It was considered that this surface was almost certainly α-Fe_2O_3, formed by air oxidation of Fe_3O_4. If it was then, according to Allen et al (73), further heating above 500°C at a pressure of 10^{-8}-10^{-9} torr should result in a decomposition of this surface layer of α-Fe_2O_3 to form Fe_3O_4. Further heating of the sample at 500°C did in fact result in a change in the Fe2p spectrum reinforcing our belief that an α-Fe_2O_3 layer had been present. The $Fe2p_{3/2}$ and $Fe2p_{1/2}$ peak maxima shifted to the lower binding energy

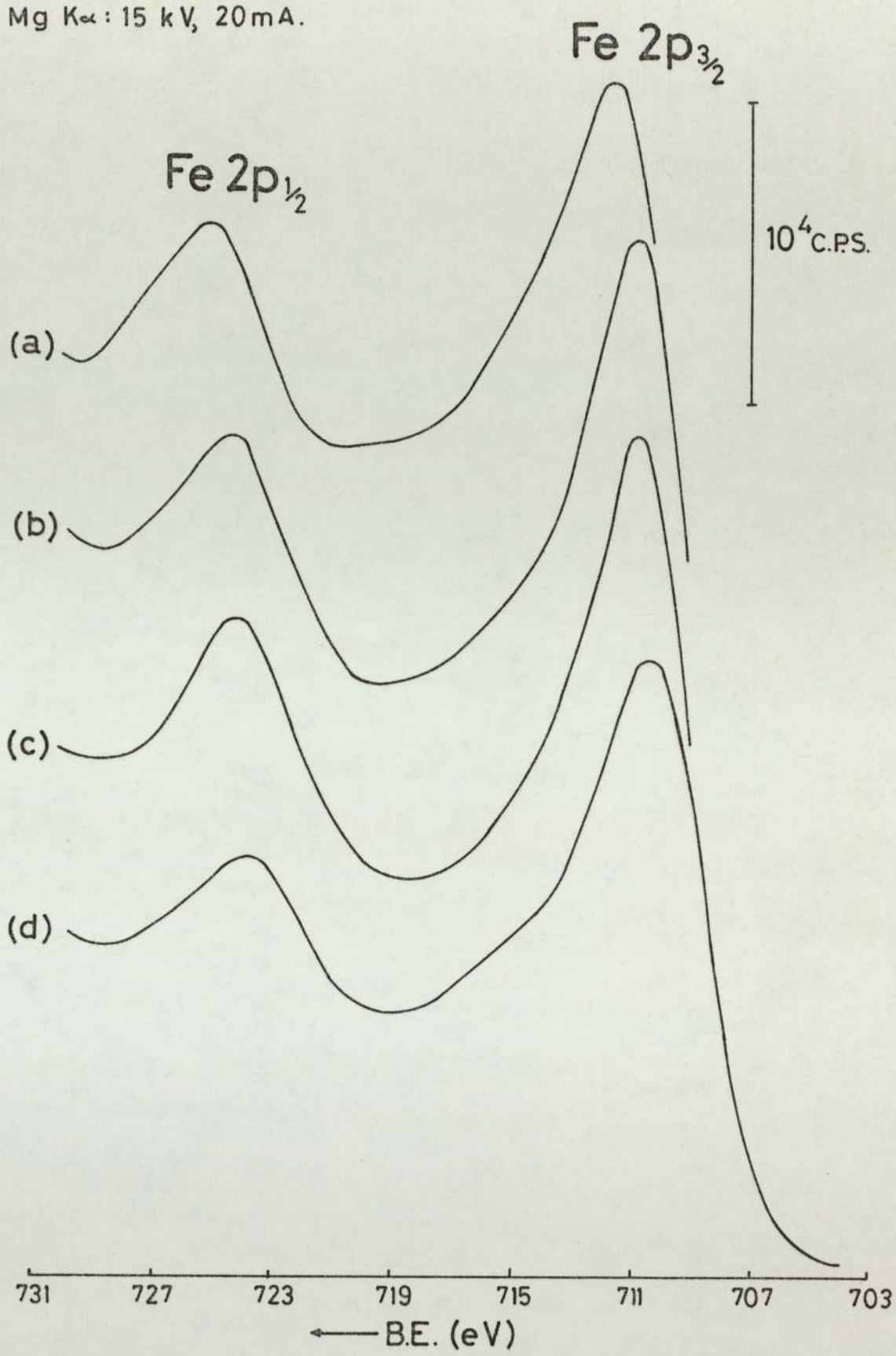

(a) Room temperature
(b) 30 mins at 200°c
(c) Further 80 mins at 400°c
(d) Further 115 mins at 600°c

FIGURE 5.8 Effect of Heating on Fe 2p Spectra of Fe_3O_4 Powder Surface.

values of 710.3 eV and 723.5 eV respectively, while there was no change in the O1s spectrum. Prolonged heating of the sample at 500°C and 600°C produced no further change in any of the photoelectron spectra indicating that a full reduction of the α-Fe_2O_3 layer had taken place. The sample surface was now considered to be Fe_3O_4 and the associated photoelectron spectra were considered to be respresentative of an Fe_3O_4 surface. Figure 5.8 shows a series of Fe2p spectra obtained while heating the Fe_3O_4 powder surface under UHV.

α-Fe_2O_3 (Haematite)

The O1s spectrum of an air exposed α-Fe_2O_3 powder surface is shown in figure 5.11(b), the dominant photoelectron peak at 531.4 eV indicating a high degree of surface adsorption. The corresponding $Fe2p_{3/2}$ and $Fe2p_{1/2}$ photoelectron peaks have maxima occurring at 711.6 eV and 725.1 eV respectively and, in addition, a satellite peak is observable 8.0 eV above the more intense $Fe2p_{3/2}$ peak. Ion beam etching of the sample surface for a few minutes resulted in an almost complete extinction of the higher binding energy O1s peak, while the $Fe2p_{3/2}$ and $Fe2p_{1/2}$ photoelectron peak maxima shifted to the lower binding energy values of 710.0 eV and 723.3 eV respectively. This indicated that the adsorbed layer had been almost completely removed and also that some ion beam reduction of the underlying α-Fe_2O_3 surface had taken place. Further etching for up to 1 hour duration produced no further shift in the photoelectron peaks. This is in contrast to Fe_3O_4 for which the results indicated that a full reduction of the Fe^{3+} ions to Fe^{2+} had occurred after only 5 minutes of ion etching. Figure 5.9 shows the effect

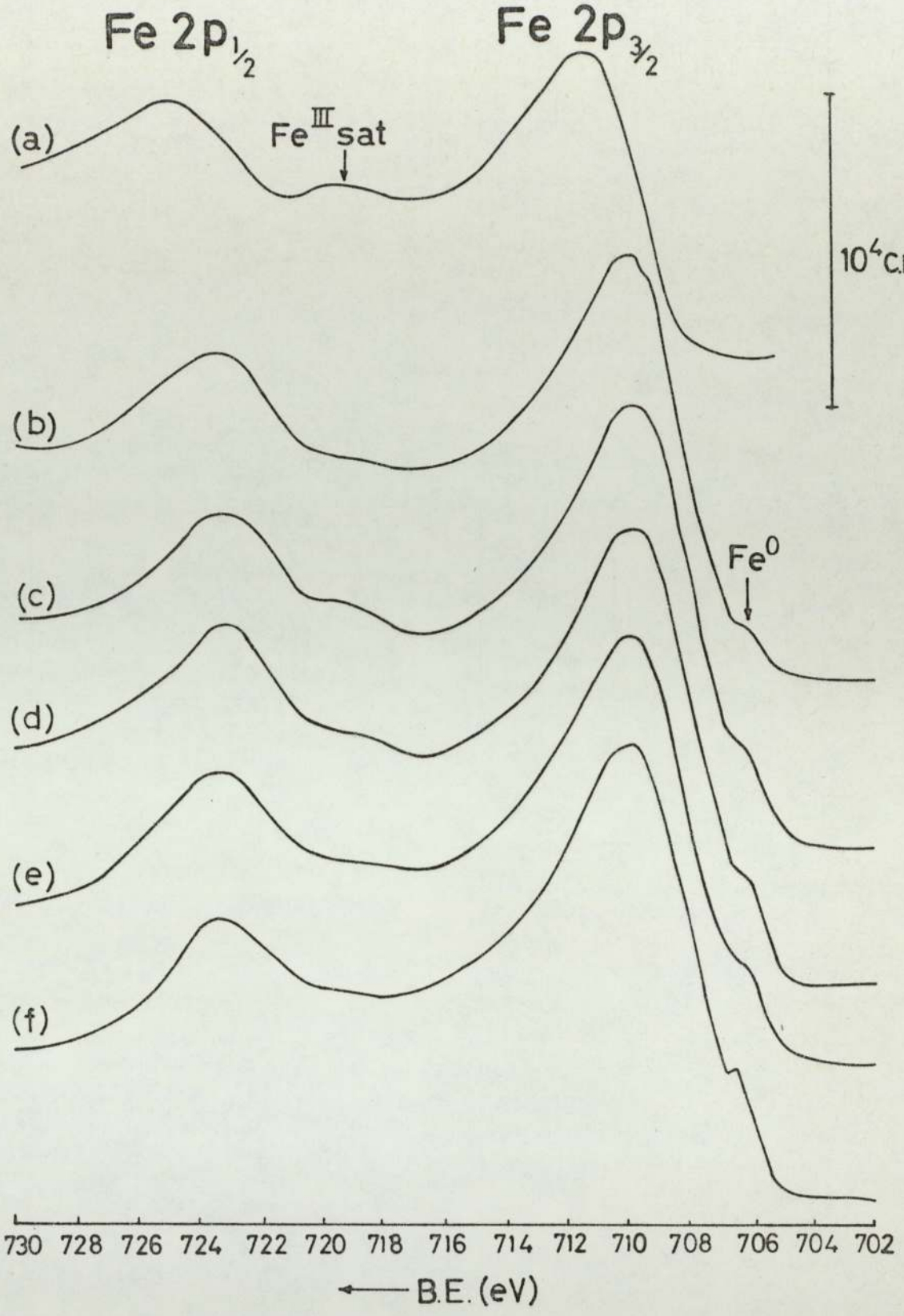

(a) unetched, air exposed surface
(b) 1 min etch
(c) 5 min etch
(d) 15 min etch
(e) 30 min etch
(f) 60 min etch

FIGURE 5.9 Effect of Ar^+ Ion Etching on Fe 2p Spectra of α-Fe_2O_3 Powder Surface.

which argon ion etching of the oxide sample had upon the Fe2p photoelectron spectra.

Fe metal

Figure 5.10 shows the Fe2p spectra recorded for Fe metal. In figure 5.10(a) for the air exposed metal surface the maxima of the $Fe2p_{3/2}$ and $Fe2p_{1/2}$ photoelectron peaks occur at 710.8 eV and 724.4 eV respectively and a satellite peak is present 8.0 eV above the former, more intense peak. From the conclusions drawn from the analyses of the three iron oxides, this suggests the presence of Fe^{3+} species on the sample surface. After etching the iron sample for a few minutes the Fe2p photoelectron peaks became much narrower, as can be seen in figure 5.10(b), and the $Fe2p_{3/2}$ and $Fe2p_{1/2}$ peak maxima shifted to the considerably lower binding energy values of 706.5 eV and 719.7 eV respectively. Continued etching did not result in any further change in the Fe2p photoelectron spectrum, except for perhaps a slight diminishing of the shoulders on the high binding energy side of the sharp photoelectron peaks, which were present as a result of remaining oxide on the surface. It was concluded that the Fe2p photoelectron spectrum of figure 5.10(b) is representative of a metallic Fe surface.

Two peaks were present in the O1s spectrum of the air exposed Fe surface, in common with the air exposed oxide spectra, but in this case the higher binding energy peak was approximately 2.0 eV above the oxide peak. The higher binding energy peak was the more intense of the two, as can be seen in figure 5.11(a), but it rapidly disappeared upon etching.

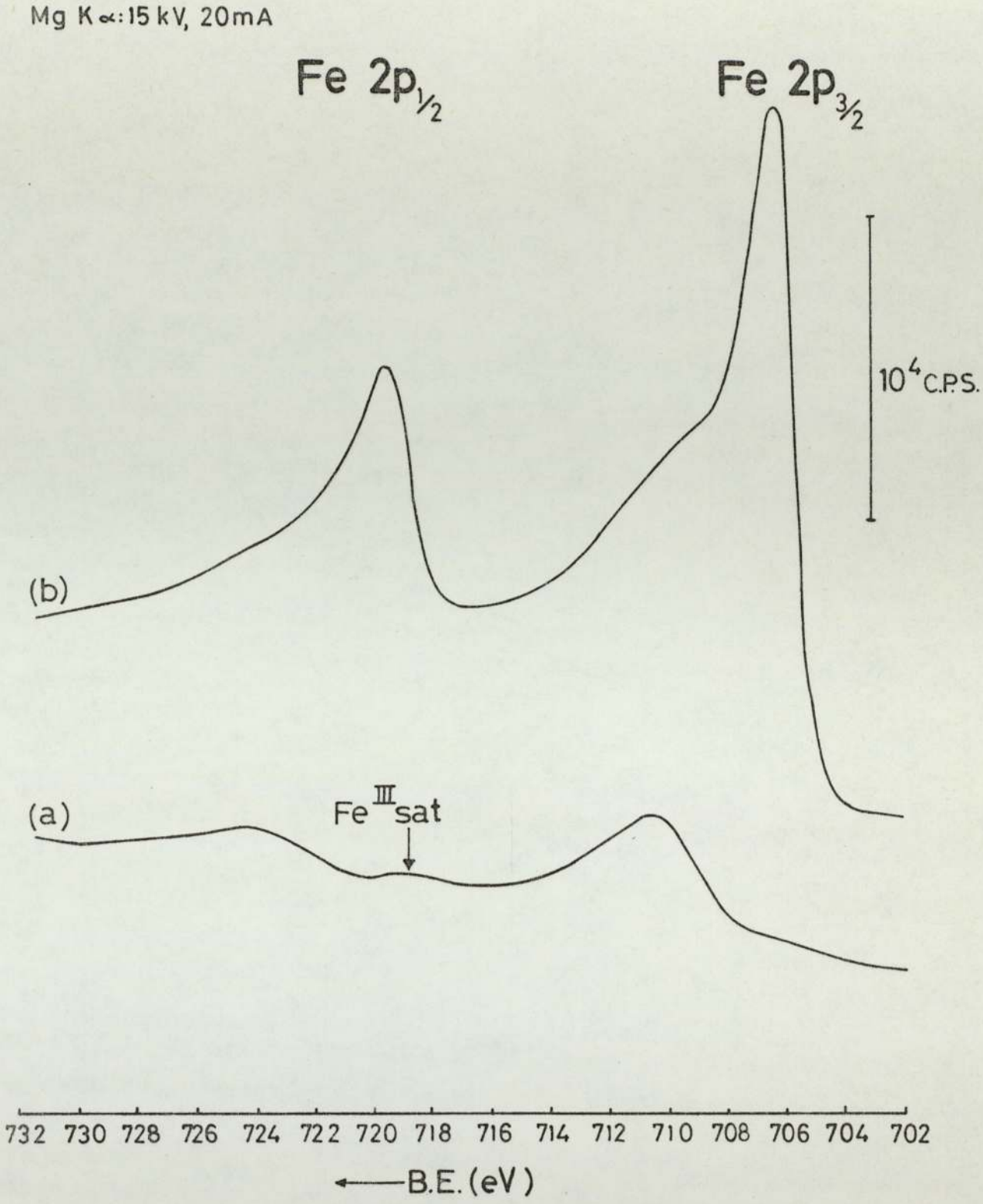

(a) unetched, air exposed metal surface.
(b) 5 min etch.

FIGURE 5.10 Effect of Ar^+ Ion Etching on Fe 2p Spectra of Fe Metal Surface.

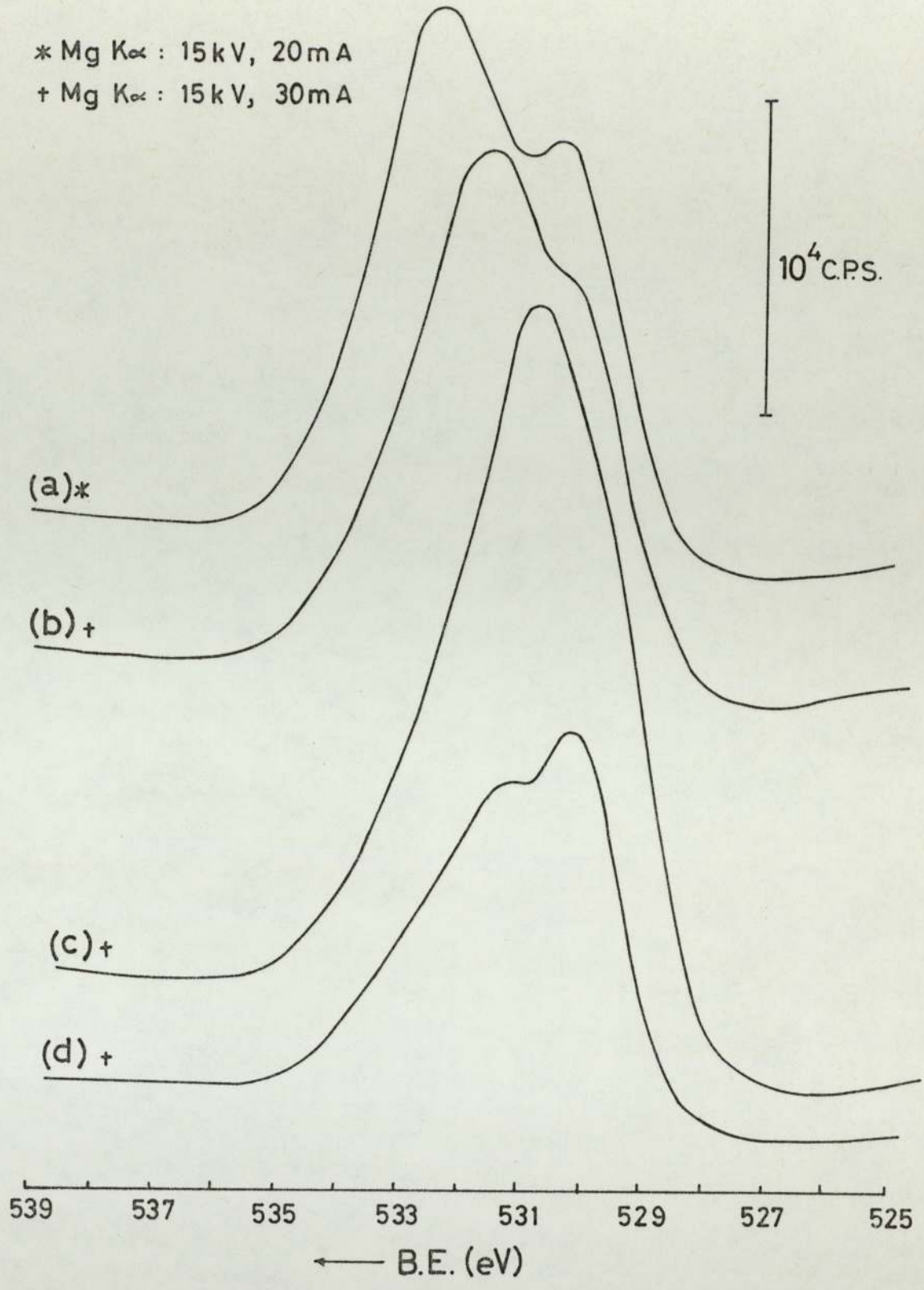

(a) Fe metal
(b) α-Fe_2O_3 powder
(c) Fe_3O_4 powder
(d) Fe O powder

FIGURE 5.11 01s Spectra of Air Exposed Iron & Iron Oxide Surfaces.

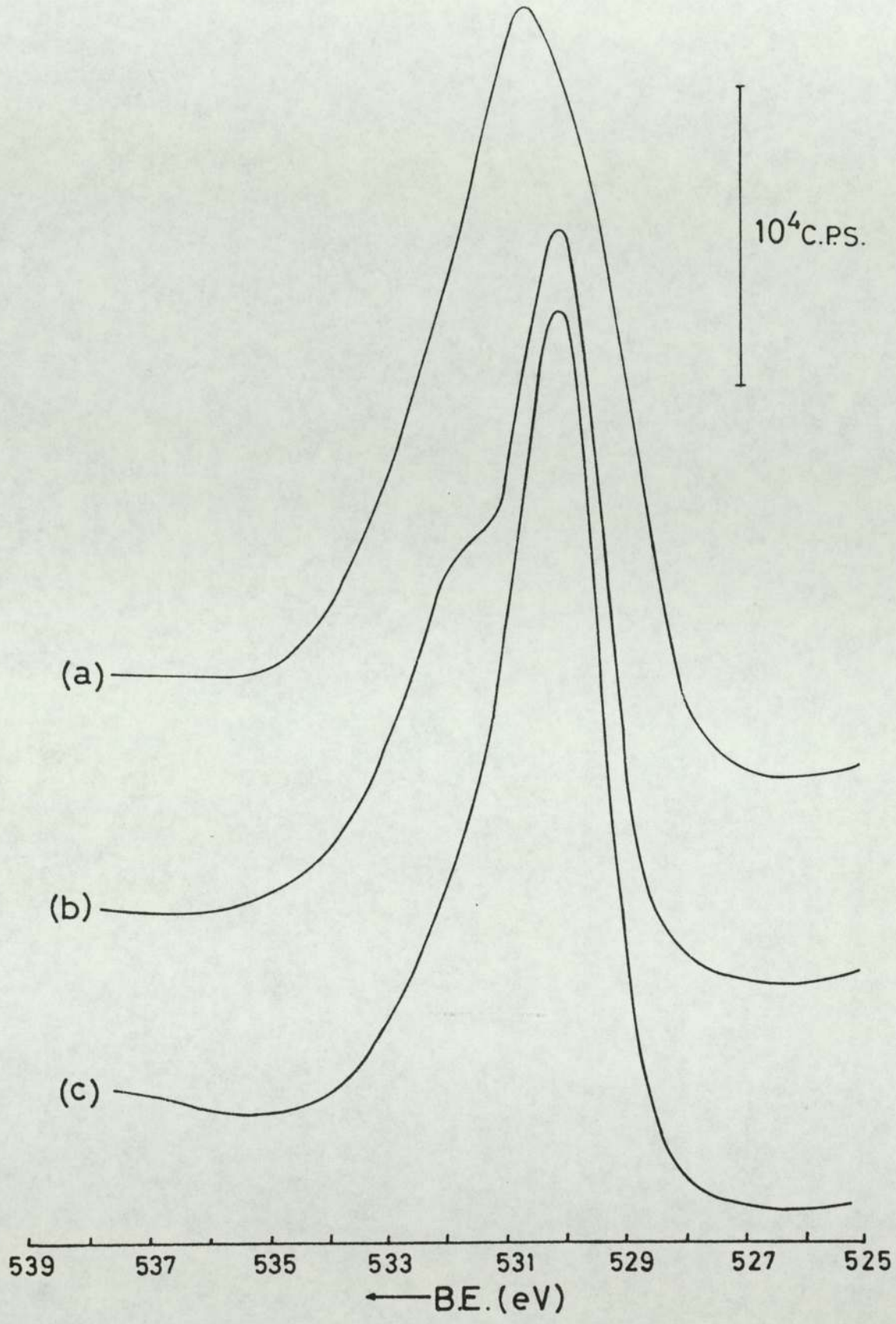

(a) Unetched, air exposed sample
(b) 2 minute etch
(c) 5 minute etch

FIGURE 5.12 Effect of Ar^+ ion Etching on O1s Spectrum of Fe_3O_4 Powder Surface.

	Fe $2p_{3/2}$ BE (±0.2)	FWHM	Fe $2p_{1/2}$ BE (±0.2)	FWHM	Fe 3p BE (±0.2)	Fe 3s BE (±0.2)	O 1s BE (±0.2)	C 1s† BE (±0.2)
Fe metal	706.5	2.6	719.7	3.0	52.9	91.3	530.1 & 532.4 †††	284.9
FeO	709.6	5.0	722.9	4.3	54.9	93.3 ± 0.5	530.1	284.8
Fe_3O_4*	710.3	5.0	723.5	4.4	56.0 & 55.2 ††	93.6 ± 0.5	530.1	284.8
α-Fe_2O_3	710.8	4.1	724.4	4.1	56.0	93.4	530.2	284.8
Hydroxide**	711.6	4.4	725.1	4.1	56.5	93.9	531.4	284.8

TABLE 5.9 Core Level Electron Binding Energies (eV) for Iron and Iron Oxides.

* These are not true B.E.'s since Fe_3O_4 contains Fe^{2+} and Fe^{3+} ions, but are the measured maxima of the photoelectron peaks.

** These are the electron B.E.'s of the adsorbed layer, which is most likely a hydroxide of iron.

† These are the electron B.E.'s of carbon present as a contaminant on the oxide sample surfaces.

†† Separate peaks due to Fe^{2+} and Fe^{3+} species are just observable.

††† On unetched metal surface.

Table 5.9 gives a summary of the core-level electron binding energies in iron and its three oxides determined from this present study, together with photoelectron peak widths expressed as full width at half maximum (FWHM). A full discussion of the characteristic features of the spectra and of the observed chemical shifts is given in Chapter 7.

5.3.3 XPS Analysis of Worn Surfaces from EN8 Wear Tests

Worn surfaces which were representative of the three different predominant surface oxides as revealed by x-ray diffraction were selected for analysis by XPS.
Worn pins and discs produced in wear tests run at a speed of 2.0 ms^{-1} and loads of 10 N, 20 N, 33 N and 50 N were analysed by XPS. Each analysis will now be considered separately, and, since a common feature throughout was a marked similarity in the results for the pin and corresponding disc, the results given in each case relate to both the pin and the disc. The results are interpreted on the basis of the XPS analysis of the standard iron oxide powder surfaces. Only a few sets of representative spectra are shown since the results of the XPS analyses were found to be very similar for all loads.

10 N, 2.0 ms^{-1}

Initially the $Fe2p_{3/2}$ and $Fe2p_{1/2}$ peak maxima occurred at binding energy values of 710.9 eV and 724.5 eV respectively and, in addition, an Fe^{3+} satellite was observable 8.0 eV above the more intense $Fe2p_{3/2}$ peak. The corresponding O1s spectrum consisted of a peak due to the oxide at 530.1 eV

and a higher binding energy peak at 531.4 eV due to some adsorbed species, the peak at 530.1 eV being the more intense of the two. These results indicate that the uppermost surface layers of the oxide consisted mainly of α-Fe_2O_3, although there was some adsorbed species present.

Upon argon ion etching of the worn surface for a few minutes the higher binding energy peak in the 01s spectrum diminished in intensity and the $Fe2p_{3/2}$ and $Fe2p_{1/2}$ peak maxima shifted to the lower values of 709.7 eV and 722.9 eV respectively, characteristic of an FeO surface. This must have been due to the reduction of Fe^{3+} ions to Fe^{2+} since x-ray diffraction had revealed that the surface oxide consisted of α-Fe_2O_3, no Fe_3O_4 or FeO being present. Thus it seems that, just as in the case of the iron oxide powder surfaces, the oxides on the worn surfaces are susceptible to ion beam reduction. Figures 5.13 and 5.14 show the effect of etching upon the respective Fe2p and 01s spectra of the worn pin surface.

The Fe2p peaks due to metallic iron appeared on the low binding energy side of the Fe2p oxide peaks after a few minutes of etching. This was expected since the oxide plateaux do not cover the entire surface and the area analysed by XPS is relatively large. For a given length of etching time the intensity of the $Fe^{o}2p$ peaks relative to the Fe2p oxide peaks was greater for the disc surface than for the pin surface. This agrees well with the SEM findings (section 5.5), which showed that the pin surface usually had a higher surface area coverage of oxide than the disc surface.

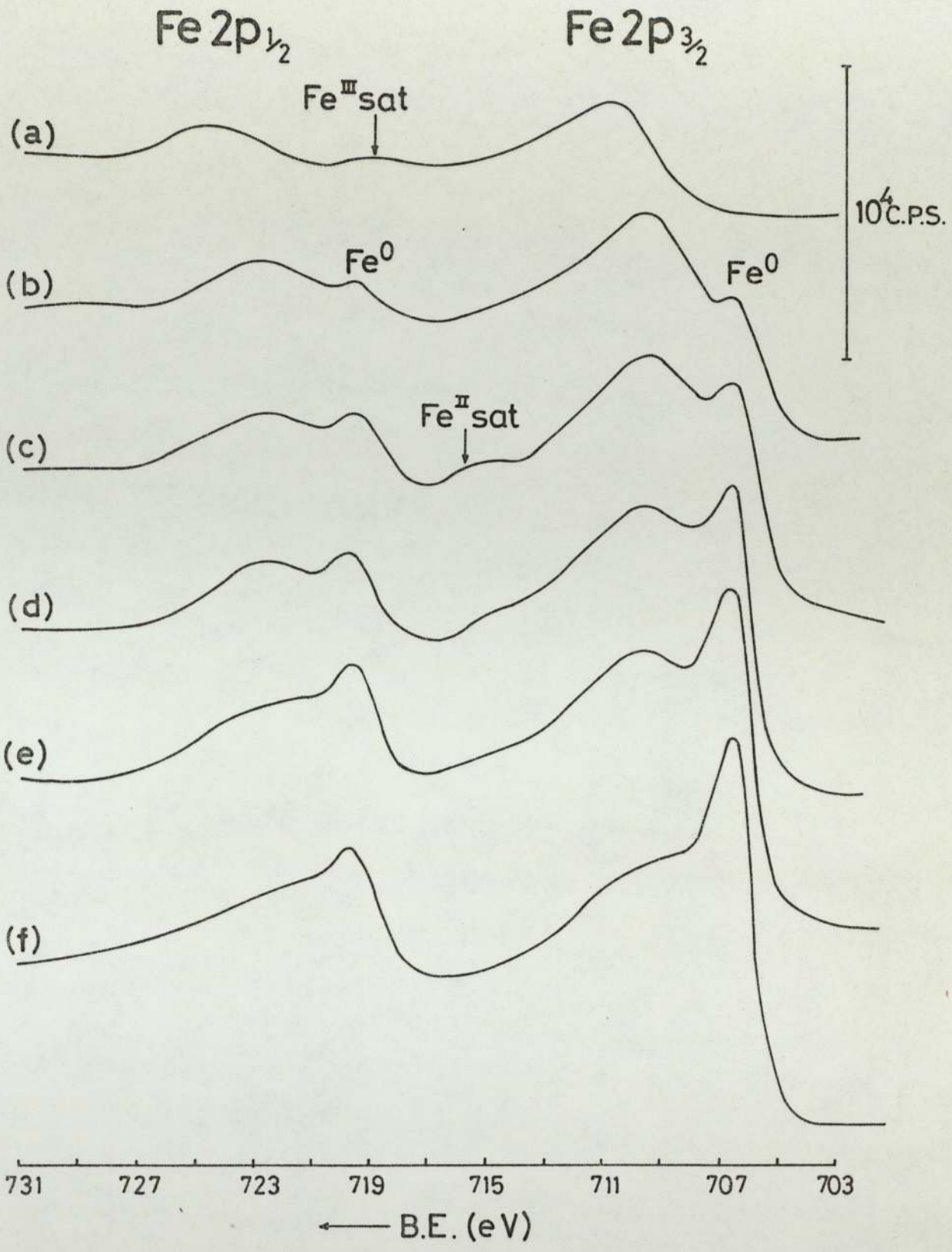

(a) unetched surface
(b) 2 min etch
(c) 15 min etch
(d) 30 min etch
(e) 90 min etch
(f) 150 min etch

FIGURE 5.13 Fe 2p Spectra of Worn Pin Surface from EN8 Wear Test at 2.0 ms^{-1}, 10 N.

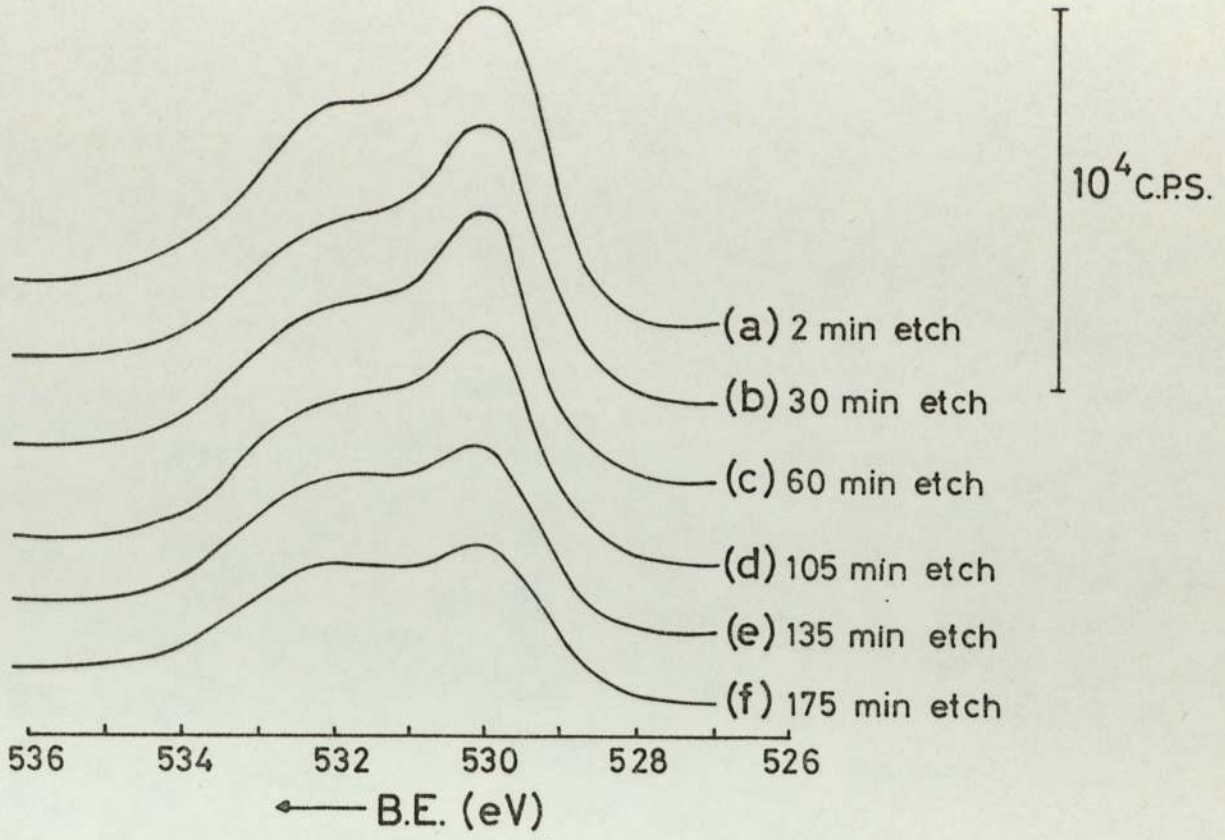

FIGURE 5.15 O1s Spectra of Worn Pin Surface from EN8 Wear Test at 2.0 ms^{-1}, 33N.

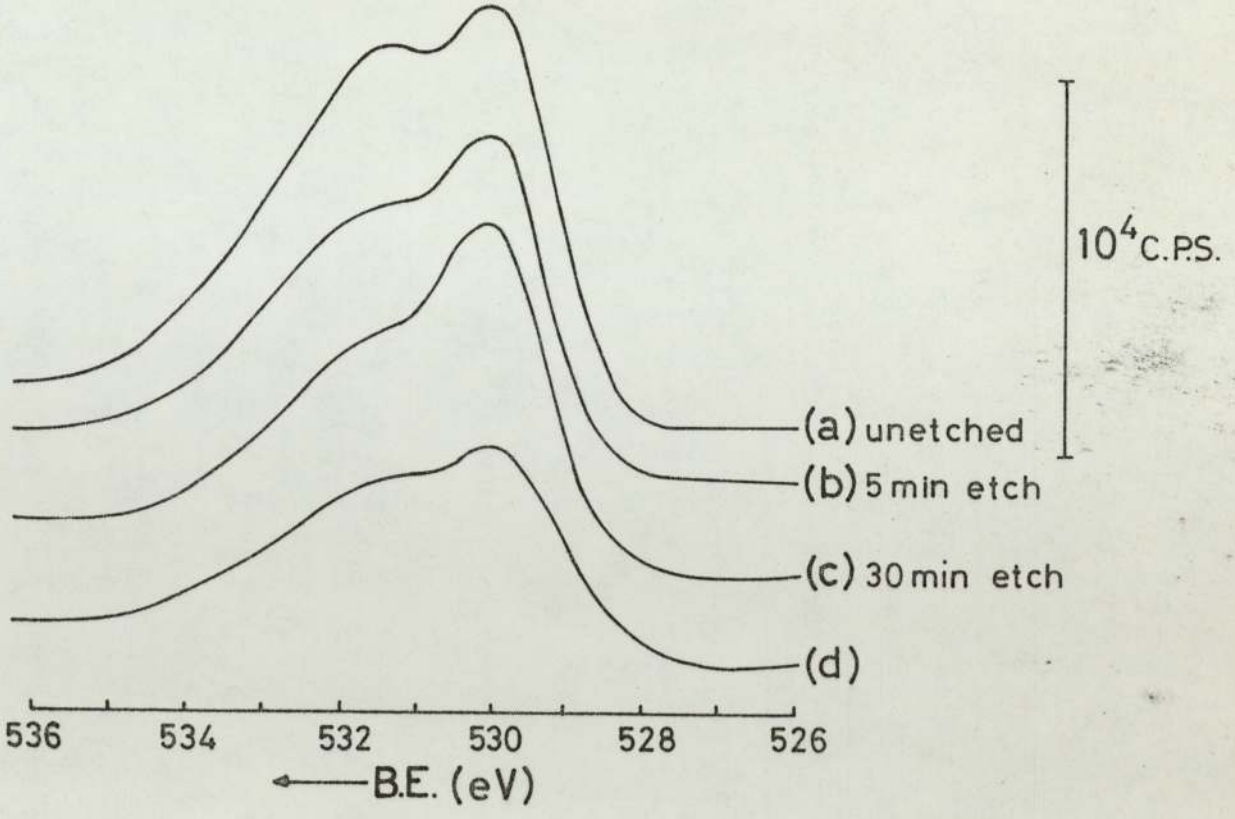

FIGURE 5.14 O1s Spectra of Worn Pin Surface from EN8 Wear Test at 2.0 ms^{-1}, 10N.

20 N, 2.0 ms^{-1}

The results of the XPS analyses of the worn pin and disc surfaces produced in the 20 N wear test were similar to the above results. This may seem surprising since x-ray diffraction revealed that the oxide on the worn surfaces produced in the 20 N experiment consisted of Fe_3O_4 and α-Fe_2O_3, whereas the oxide on the surfaces from the 10 N experiment was α-Fe_2O_3 alone. However, if we again take into account the effect of argon ion reduction the results can easily be explained.

33 N, 2.0 ms^{-1}

The results from the XPS analysis of the worn pin and disc produced in the wear test conducted at a load of 33 N were very similar to the results stated above for load of 10 N and 20 N, again indicating that reduction of the surface oxide was caused by the argon ion etching process. One noticeable difference between the results for this pin and the results for the previous samples was the position of the higher binding energy peak in the O1s spectrum. In this case the peak maximum occurred at the higher binding energy value of 532.1 eV, and was probably due to a different adsorbed species on the sample surface. Figure 5.15 shows the O1s spectra recorded during the analysis of the worn pin surface.

50 N, 2.0 ms^{-1}

The XPS analysis of the worn surfaces produced in the wear test at 50 N gave results which were very similar to those

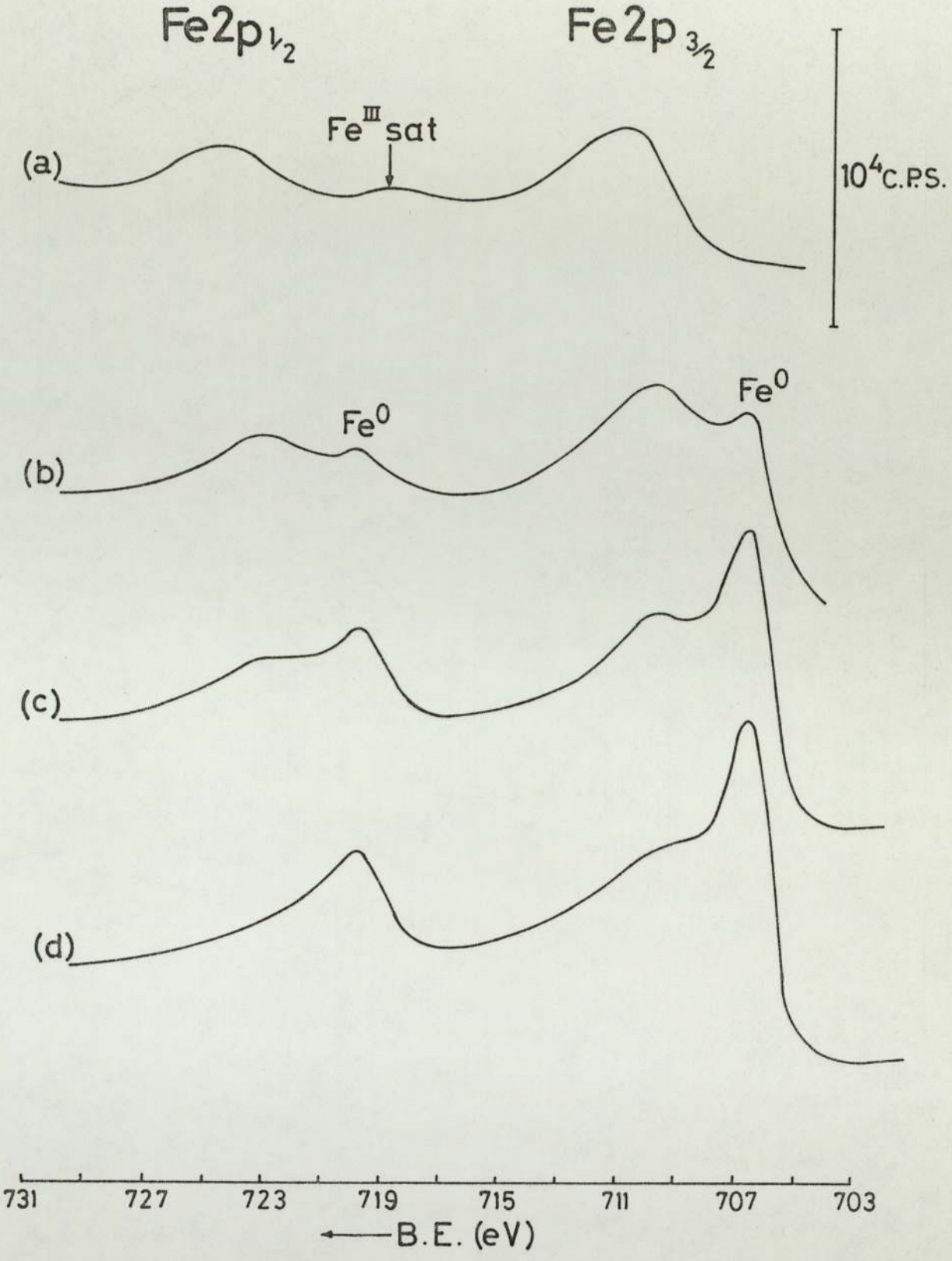

(a) unetched surface
(b) 5 min etch
(c) 60 min etch
(d) 120 min etch

FIGURE 5.16 Fe2p Spectra of Worn Pin Surface from EN8 Wear Test at 2.0 ms^{-1}, 50N.

obtained for the worn surfaces from the 10 N and 20 N wear tests described previously. The initial spectra indicated that the surface of the oxide was mainly α-Fe_2O_3, and after a few minutes of etching the spectra obtained were characteristic of an FeO surface. In this case we would expect this since x-ray diffraction indicated that the oxide was predominantly FeO, but it was impossible to determine whether the initial detection of FeO was due to true FeO present in the oxide or whether it was due to ion beam reduction of higher oxides in the surface layers. The Fe2p spectra of the pin surface worn in the 50 N wear test are shown in figure 5.16.

5.3.4 XPS Analysis of Worn Surfaces from EN8 / 9% Cr Wear Tests

Most of the emphasis for the analysis of worn surfaces from the EN8 / 9% Cr wear tests was placed on AES, since the primary concern was the determination of the relative concentration of chromium in the oxide on the worn pins and discs. In addition, it was considered that XPS of selected worn surfaces might provide extra useful information. Since powder x-ray diffraction revealed that the constituents of the wear debris were identical for all of the EN8 / 9% Cr wear tests (20 N, 30 N, 40 N and 50 N) it was decided to analyse only the worn surfaces produced in the 50 N wear tests. Unfortunately, it was only possible to analyse the pin surface.

Results of the XPS analysis of the worn pin from the EN8 / 9% Cr wear test were similar to those obtained in the analyses of

surfaces from the EN8 wear tests (section 5.3.3). The initial spectra for the unetched pin surface indicated the presence of α-Fe_2O_3; the $Fe2p_{3/2}$ and $Fe2p_{1/2}$ peak maxima occurred at binding energies of 710.7 eV and 724.4 eV respectively, while the O1s spectrum consisted of two overlapping peaks, one centred at 530.1 eV due to the oxide, and another, slightly less intense peak at 532.1 eV due to an adsorbed species. After one minute of argon ion etching the $Fe2p_{3/2}$ and $Fe2p_{1/2}$ peak maxima shifted to the lower values of 709.8 eV and 723.3 eV respectively and, in addition, the Fe^{3+} satellite peak previously observable in the Fe2p spectrum had now disappeared to be replaced by an Fe^{2+} satellite centred 6.0 eV above the more intense $Fe2p_{3/2}$ peak. After a few more minutes of etching the Fe2p peak positions corresponded to those of Fe^{2+} in FeO, and the Fe^{o} peaks were just observable on the low binding energy side of the oxide peaks. Further etching resulted in an increase in the intensity of the Fe^{o} peaks with respect to the oxide peaks, which remained at binding energy values characteristic of FeO. Argon ion etching initially caused the higher binding energy peak in the O1s spectrum to diminish in intensity, after which its intensity remained fairly constant.

The more intense XPS peak of chromium, $Cr2p_{3/2}$, was just about detectable at each depth investigated. The peak had a binding energy of 576.1 ± 0.2 eV, and this value remained constant throughout the oxide indicating that only one species of chromium was present, probably Cr^{3+} (78).

Figures 5.17, 5.18 and 5.19 show the respective Fe2p, O1s and $Cr2p_{3/2}$ spectra obtained in the XPS analysis of the worn

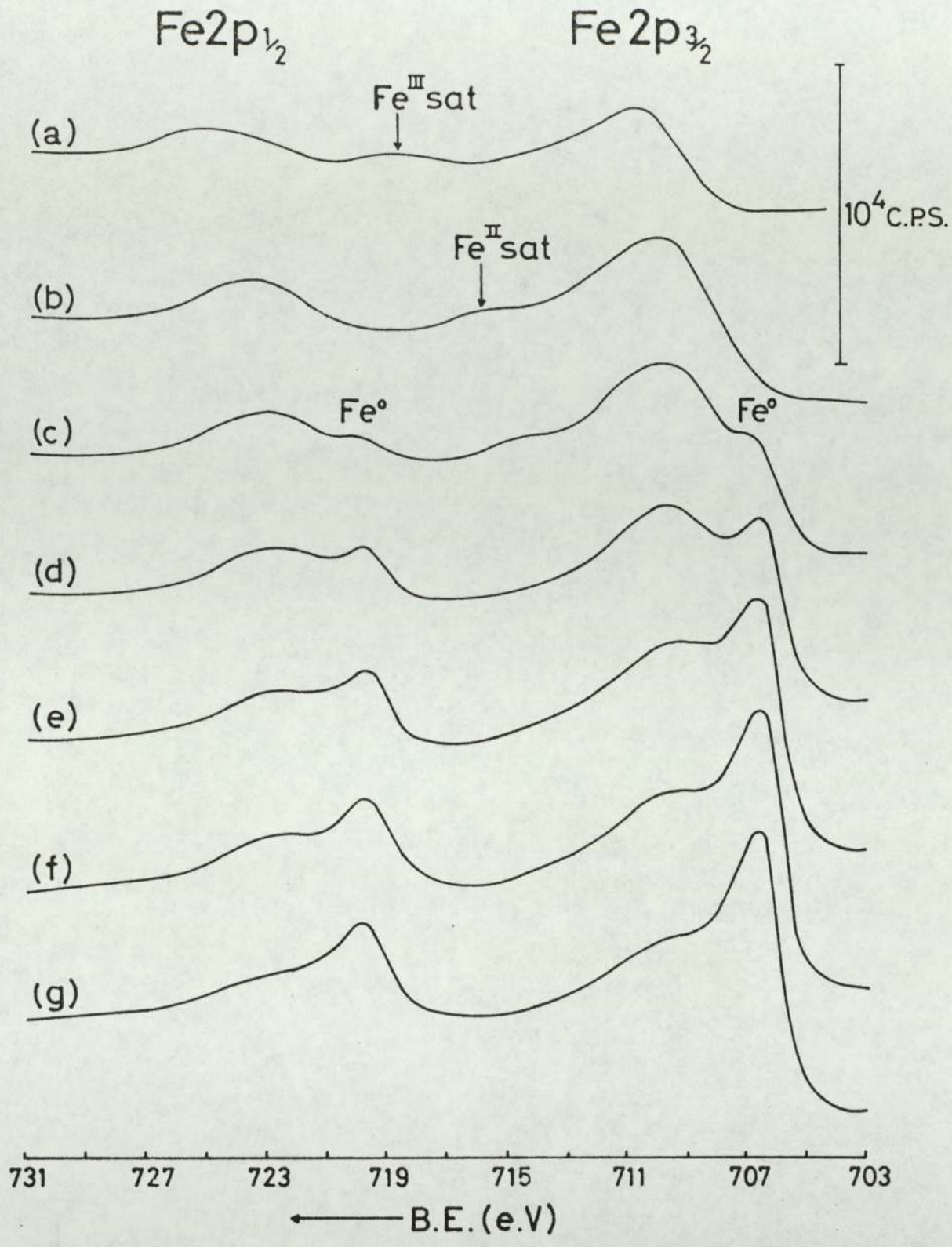

(a) unetched surface
(b) 1 min etch
(c) 5 min etch
(d) 30 min etch
(e) 90 min etch
(f) 150 min etch
(g) 270 min etch

FIGURE 5.17 Fe 2p Spectra of Worn Pin Surface from EN8/9% Cr Wear Test at 2.0 ms^{-1}, 50N.

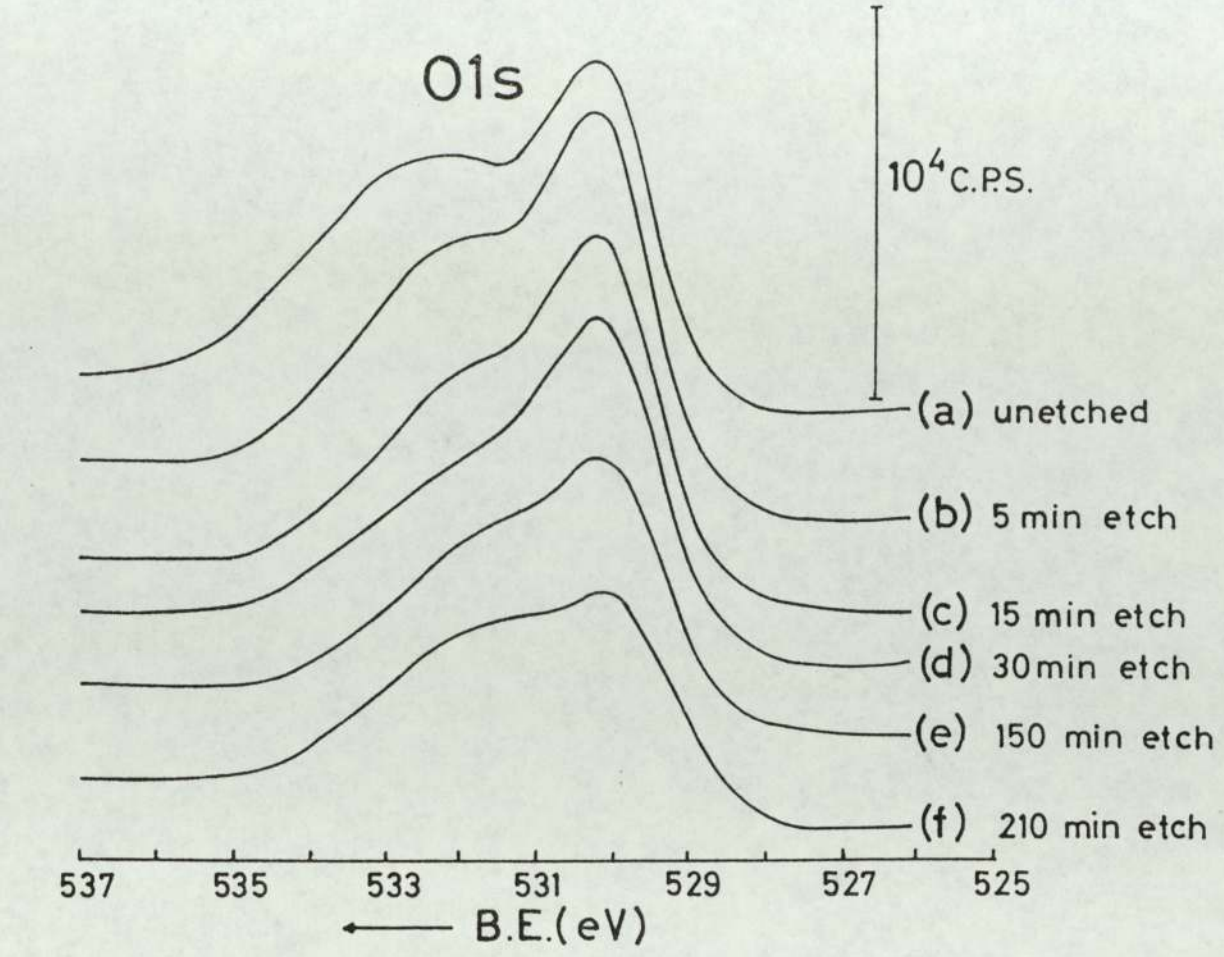

FIGURE 5.18 O1s Spectra of Worn Pin Surface from EN8/9% Cr Wear Test at 2.0ms^{-1}, 50N.

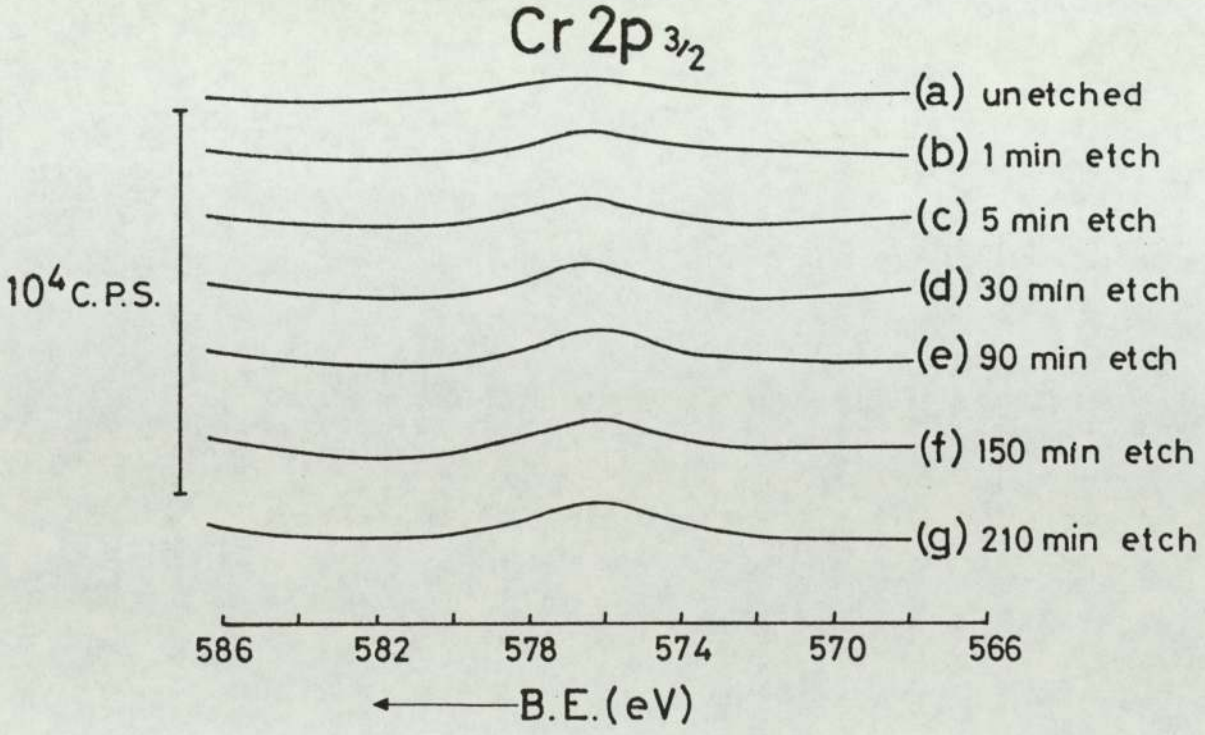

FIGURE 5.19 Cr 2p$_{3/2}$ Spectra of Worn Pin Surface from EN8/9% Cr Wear Test at 2.0ms^{-1}, 50N.

pin surface from the EN8 / 9% Cr wear test conducted at 2.0 ms^{-1} and 50 N.

5.3.5 XPS Analysis of Oxides Grown under Static Conditions

XPS analysis of oxides grown on low alloy steel surfaces under static conditions was considered useful since it was thought that comparison of the results with those obtained from analysis of tribologically produced oxides may give an insight into the differencies, or otherwise, in the growth mechanisms in each case.

This section describes the results obtained from the XPS analysis of oxides grown on low alloy steel in a heated furnace. Four oxide surfaces were investigated, these being produced at temperatures of 150°C, 260°C, 500°C and 650°C. The sample oxidized at 150°C was a finely polished disc of EN8 steel (section 3.3.4), while the other samples were rectangular strips of low alloy steel sheet (section 3.3.4). The results of each analysis will now be considered separately.

150°C for 1 hour

The results indicated that statically grown oxide surfaces are also susceptible to ion beam reduction, in addition to the powder and tribologically produced oxide surfaces.

The initial $Fe2p_{3/2}$ and $Fe2p_{1/2}$ photoelectron peaks occurred at binding energy values of 710.9 eV and 724.6 eV, while the

01s spectrum consisted of a peak at 532.3 eV due to an adsorbed species, and a very much less intense peak due to the oxide, visible as a low binding energy shoulder on the former peak. In addition well defined Fe3p and Fe3s peaks were observed having binding energies of 55.9 eV and 93.5 eV respectively. These results indicate that the surface of the oxide was α-Fe_2O_3, and also that there was a high degree of adsorption on the surface.

After thirty seconds of argon ion etching the $Fe2p_{3/2}$ and $Fe2p_{1/2}$ peaks had shifted to the lower binding energy values of 709.9 eV and 723.1 eV, slightly higher than those due to Fe^{2+} in FeO, while the higher binding energy peak in the 01s spectrum had diminished considerably in intensity and was now only visible as a shoulder on the high binding energy side of the 01s oxide peak at 530.1 eV. After one minute of etching the Fe2p peak binding energies were characteristic of Fe^{2+} species in FeO. Since FeO is not present in oxides formed on iron at oxidation temperatures below 570^{o}C (17) this indicates that a full reduction of Fe^{3+} ions to Fe^{2+} ions had occurred after only one minute of etching. Fe^{o} peaks were also just visible after one minute of etching. This may have been due to ion beam reduction, but was more likely due to the metallic substrate since the oxide was very thin.

Figure 5.20 shows the Fe2p spectra obtained from the XPS analysis of the polished EN8 sample oxidised at 150^{o}C, while figure 5.23 shows how rapidly the higher binding energy adsorption peak in the 01s spectrum disappeared on etching. The photoelectron peaks are more intense than those obtained from the analysis of powder and worn oxide surfaces since in

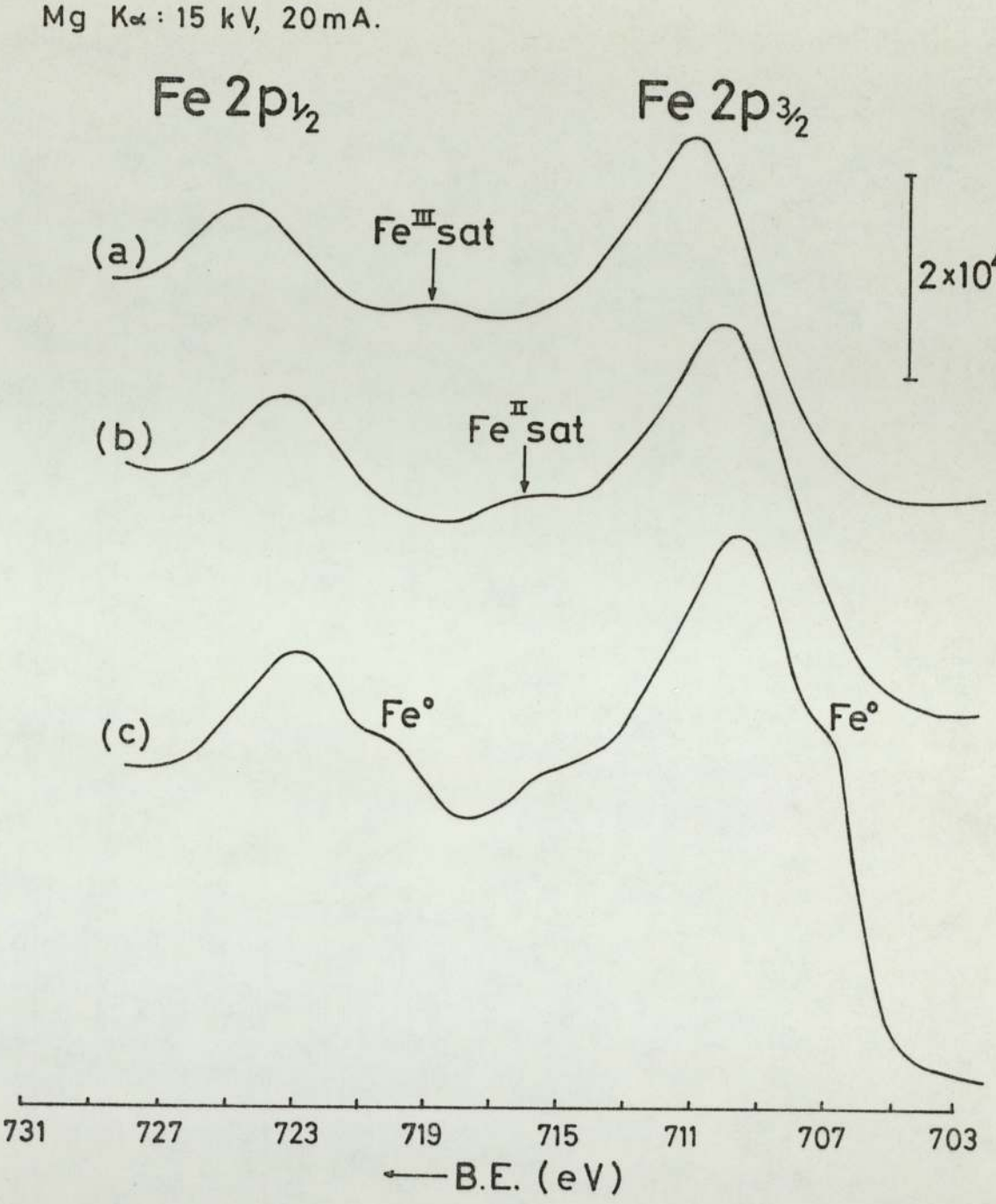

(a) unetched surface
(b) 30 sec etch
(c) 1 min etch

FIGURE 5.20 Fe 2p Spectra of Polished EN8 Steel Surface Oxidised at 150°C for 1 hour.

this case the surface was very much smoother.

260°C for 5 hours

The initial Fe2p, 3p and 3s photoelectron peak positions, together with an O1s peak at 530.1 eV having only a very slight high binding energy shoulder, indicates that the surface of the oxide was α-Fe_2O_3. After thirty seconds of argon ion etching the $Fe2p_{3/2}$ and $Fe2p_{1/2}$ peaks moved to the lower binding energy values of 710.1 eV and 723.2 eV respectively, indicating the presence of Fe^{3+} and Fe^{2+}. These peaks remained in the same position after etching for several minutes, until after approximately fifteen minutes they had shifted to lower binding energies characteristic of FeO. Again this indicated ion beam reduction, but in this case the effect was less pronounced since it took around fifteen minutes for a full reduction of Fe^{3+} to Fe^{2+}. Fe^{o} peaks from the underlying metal substrate were observable after around fifteen minutes of etching.

Figure 5.21 shows the Fe2p spectra obtained during the XPS analysis of the low alloy steel surface oxidized at a temperature of 260°C.

500°C for 8 hours

The results obtained in the XPS analysis of the surface oxide grown at 500°C were similar to those obtained during the analysis of the sample oxidised at 260°C except that in the present case Fe^{o} peaks appeared after around fifteen minutes of etching, but did not greatly increase in intensity

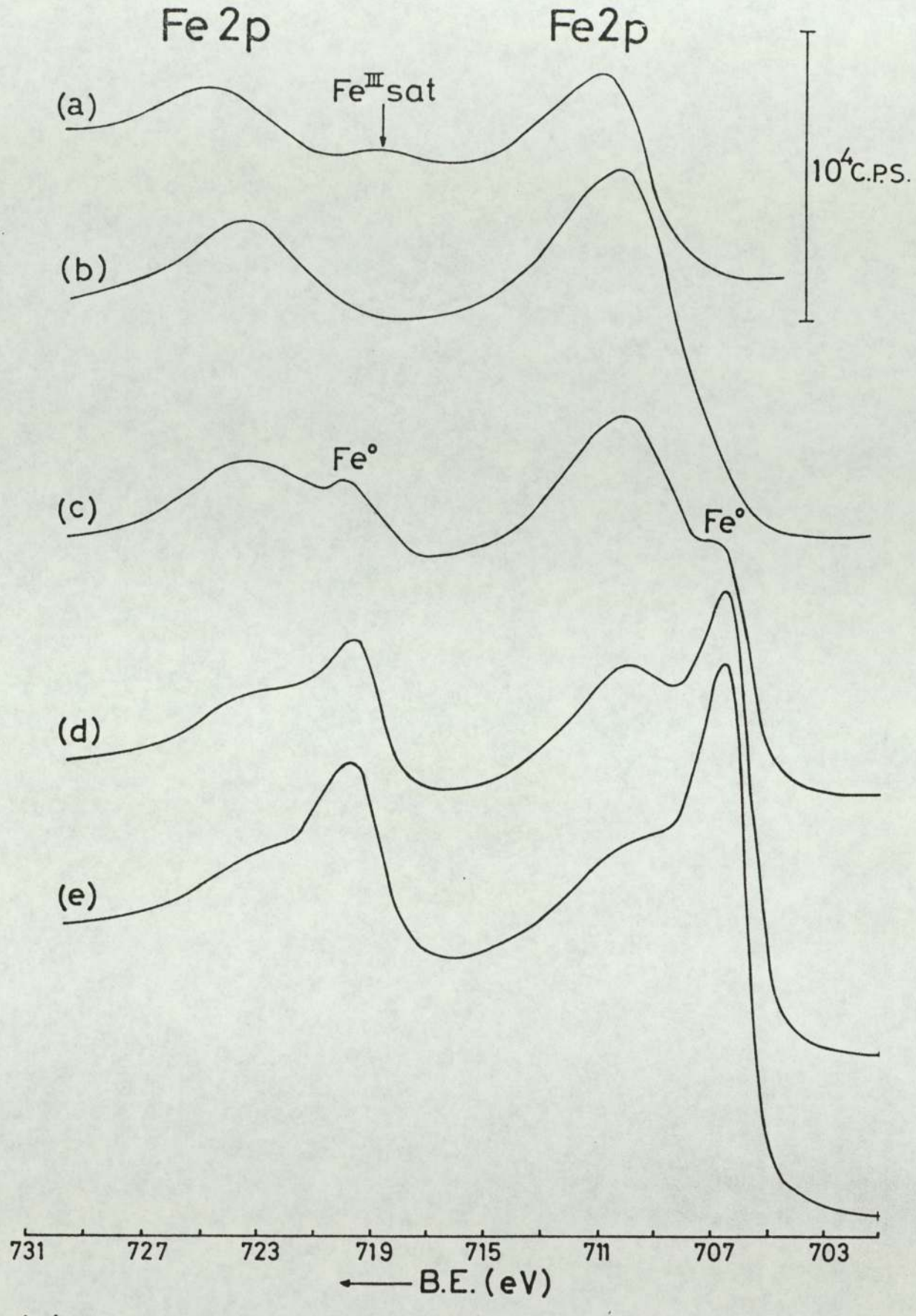

FIGURE 5.21 Fe 2p Spectra of Low Alloy Steel Surface Oxidised at 260°C for 5 hours.

after a further prolonged period of etching, even after eight hundred minutes. Figure 5.22 shows Fe2p spectra obtained during the XPS analysis of the low alloy steel surface oxidized at a temperature of 500°C.

The initial O1s spectrum obtained for the unetched oxide surface consisted of two peaks, the familiar oxide peak at 530.1 eV and a slightly less intense adsorption peak at 531.6 eV. This latter peak diminished rapidly upon etching as can be seen from figure 5.23.

650°C for 4½ hours

XPS analysis of this sample produced very similar results to those obtained from the analysis of the oxide grown at 500°C, discussed above. In this case, however, we would expect to detect FeO as it is formed in oxides on iron if the oxidation temperature is higher than 570°C, and its presence in this instance was confirmed by glancing angle x-ray diffraction. Unfortunately it was impossible to determine whether the initial detection of FeO was due to its presence in the oxide or whether it was due to the ion beam reduction of higher oxides in the surface layers.

The spectra obtained during the anlysis of this sample were very similar to those of figure 5.22 showing the Fe2p spectra for the sample oxidized at 500°C, and so are not presented here in order to avoid what would be virtual duplication.

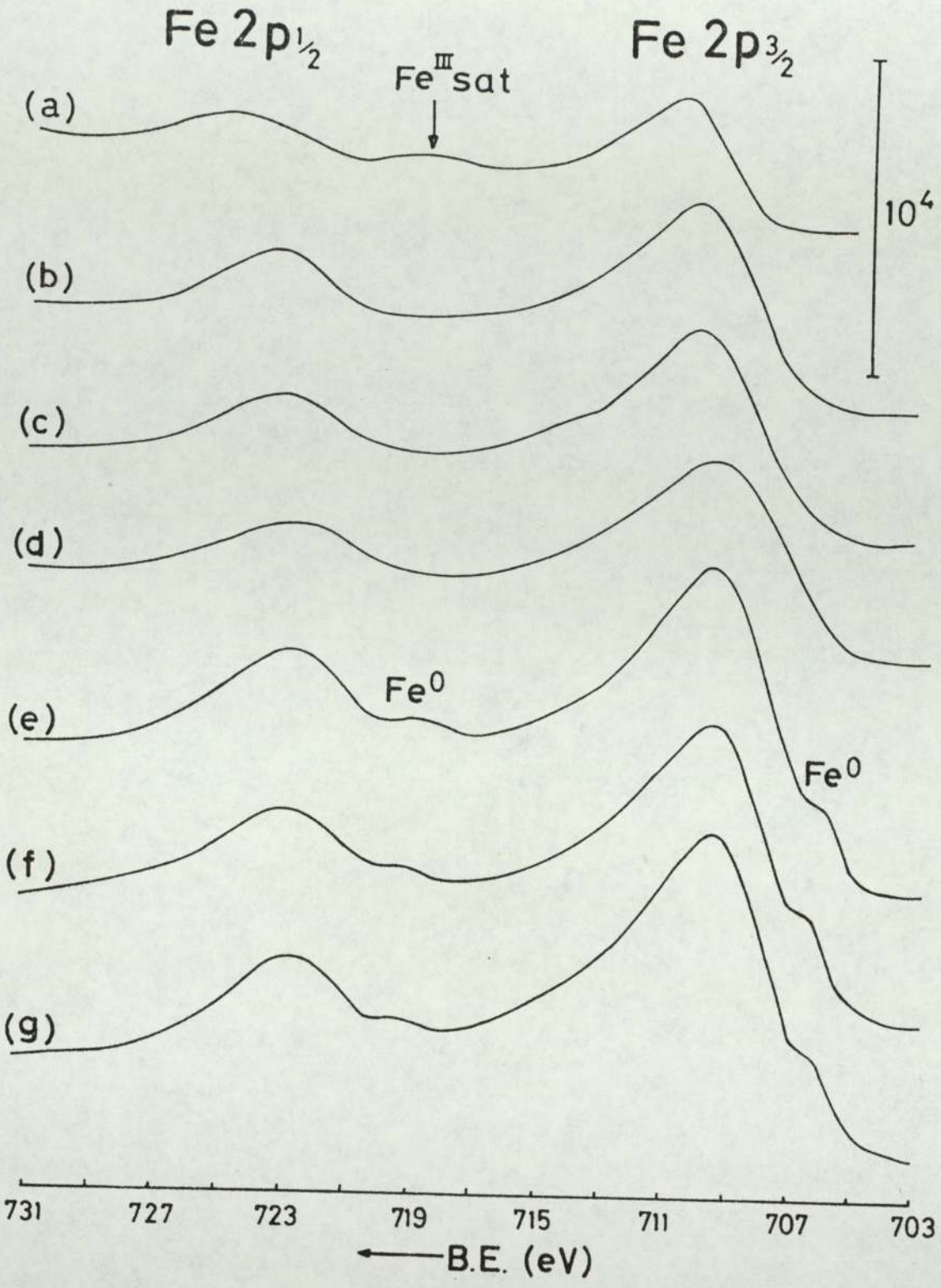

(a) unetched surface
(b) 1 min etch
(c) 5 min etch
(d) 15 min etch
(e) 60 min etch
(f) 120 min etch
(g) 800 min etch

FIGURE 5.22 Fe 2p Spectra of Low Alloy Steel Surface Oxidised at 500°C for 8 hours.

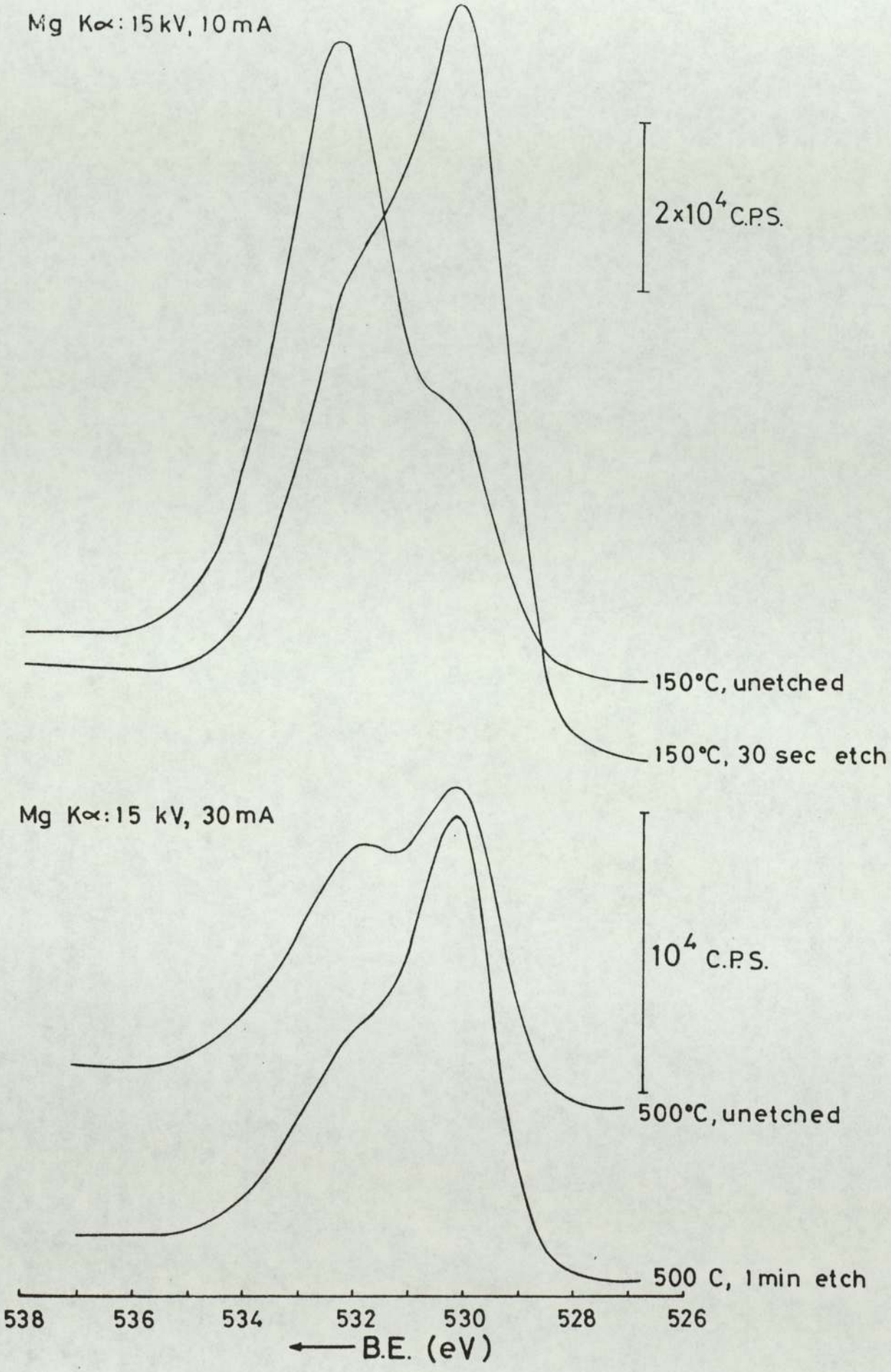

FIGURE 5.23 O1s Spectra of Surfaces Oxidised under Static Conditions.

5.4 Auger Electron Spectroscopy (AES) Results

5.4.1 AES of Worn Surfaces from EN8 Wear Tests

Elemental concentrations were calculated from peak to peak heights in the differentiated Auger spectra using an equation which gives the proportion of an element i in a matrix j:

$$X_i = \frac{\alpha_i I_i \cdot \frac{\lambda_i^{\circ}(E_i)}{\lambda_j(E_i)}}{\sum_j \alpha_j I_j \cdot \frac{\lambda_j^{\circ}(E_j)}{\lambda_j(E_j)}} \qquad (5.5)$$

where α_i = sensitivity factor of element i, defined by equation (6.17)

I_i = peak to peak height of Auger peak of element i in differentiated spectrum of matrix j

$\lambda_j(E_i)$ = inelastic mean free path of Auger electrons of element i in matrix j

and the superscript $^{\circ}$ denotes a pure element.

The origin of equation (5.5) for quantitative AES analysis is given in section (6.4). The λ terms are included in order to take into account the matrix dependence of the inelastic mean free path of electrons, which is discussed in section (6.4.2). Equations (6.27), (6.29) and (6.31) due to Seah (79) were used for the calculation of λ values. Correction factors for the matrix dependence of backscattering of the primary electron beam, and for instrumental effects should also be taken into account, but this was not possible in the present work as discussed in section (6.4). Sensitivity factors

were taken from the Handbook of Auger Electron Spectroscopy (80) and, in fact, the reciprocal of these values were used for α_i in the present work due to our definition of α_i in equation (6.17) being the inverse of the handbook definition.

Concentration versus depth profiles were obtained for selected worn pin and disc surfaces produced in the EN8 wear experiments at 2.0 ms^{-1} and 4.0 ms^{-1}. Examples of these are shown in figures 5.24, 5.25 and 5.26 for worn surfaces produced in experiments run at 2.0 ms^{-1}, while figures 5.27 and 5.28 are for surfaces produced in the 4.0 ms^{-1} wear tests. These particular examples were chosen because each one is representative of a separate distinct region in the wear rate versus load graphs of figures 4.1(a) and 4.1(b). For the sake of clarity only the oxygen levels have been plotted. Carbon levels were initially around 40% for the unetched surfaces, but fell to around 10% to 15% after approximately ten minutes of etching, after which the carbon concentration remained fairly constant. The iron levels were between 40% to 45% throughout the oxide layer so that the ratio of oxygen atoms to iron atoms present in the oxide was approximately 50:50. Once the ion beam etching had penetrated through the oxide to the metal base iron levels rose to around 75% to 80%. Figures 5.29(a), (b) and (c) show differentiated Auger spectra recorded at various depths through an oxide plateau on a worn pin surface.

It can be seen from the concentration versus depth profiles of figures 5.24 to 5.28 that oxygen concentrations remain reasonably uniform for around 100 minutes to 200 minutes etching time, after which they fall off fairly rapidly and

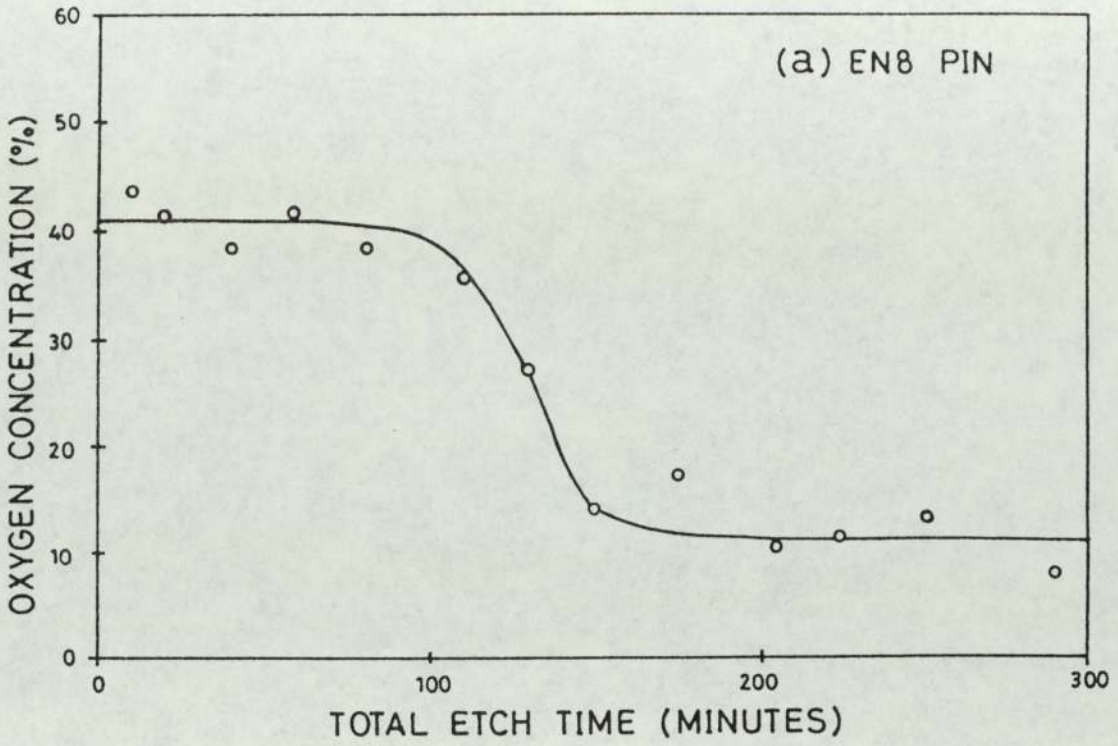

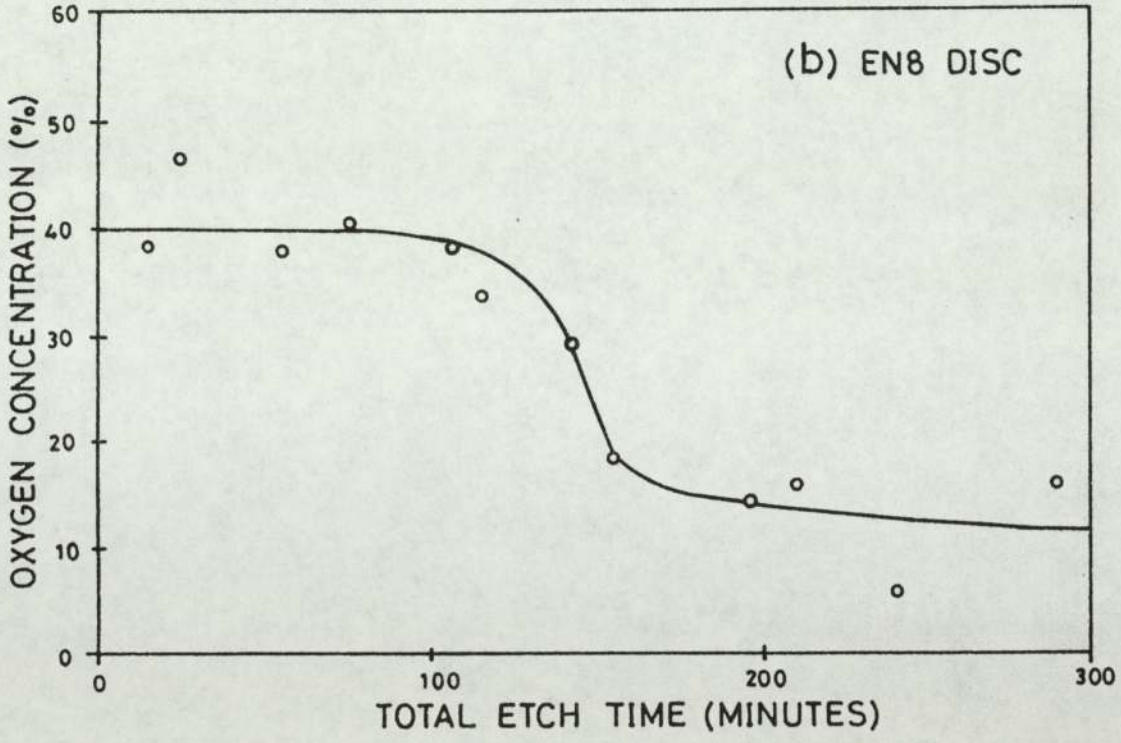

FIGURE 5.24 Concentration versus Depth Profiles for Worn Surfaces from EN8 Wear Test at 2.0ms^{-1}, 5N.

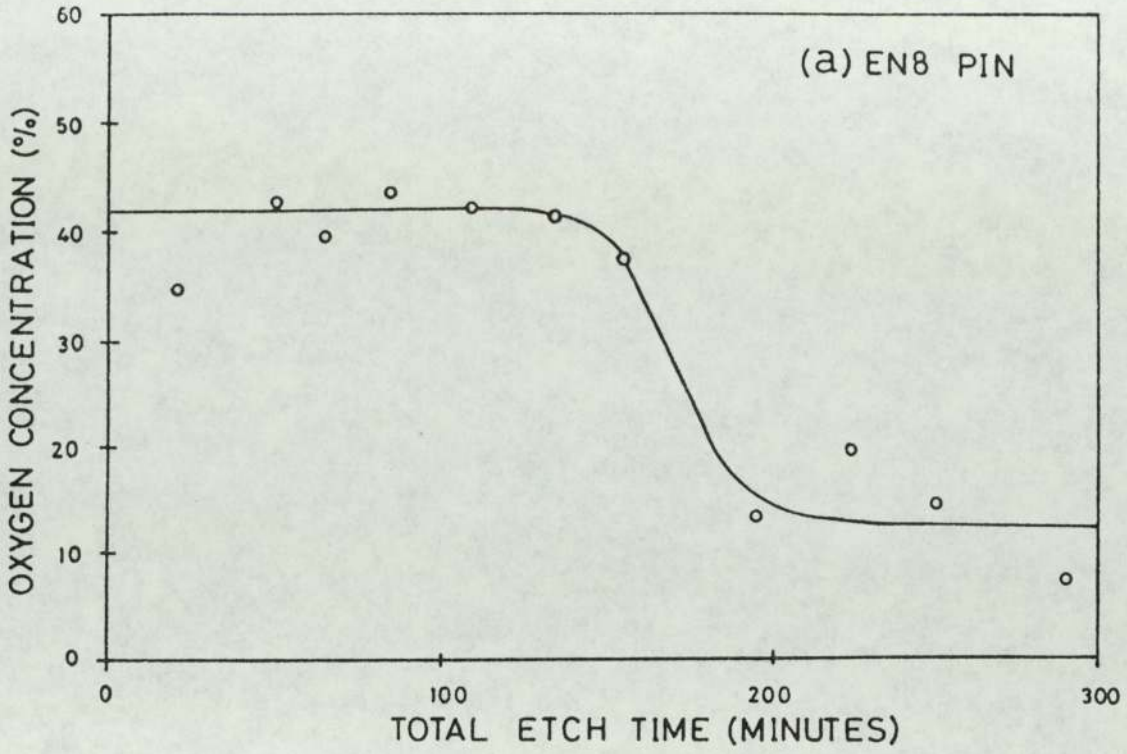

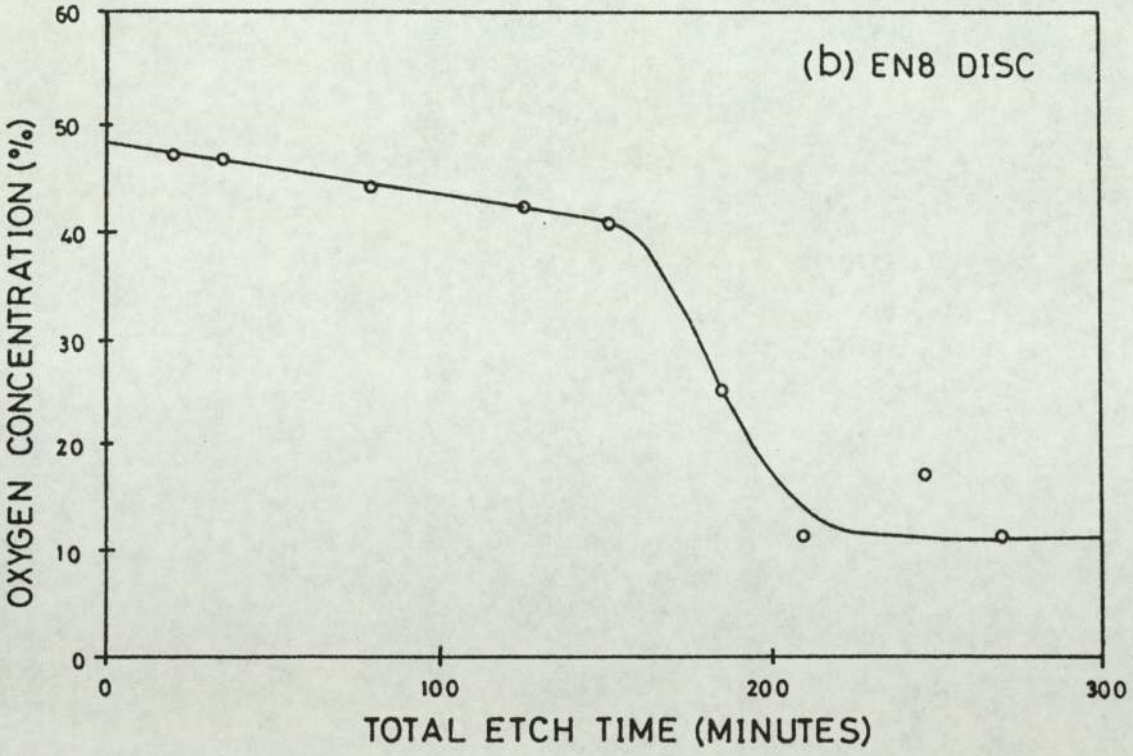

FIGURE 5.25 Concentration versus Depth Profiles for Worn Surfaces from EN8 Wear Test at 2.0 ms^{-1}, 25 N.

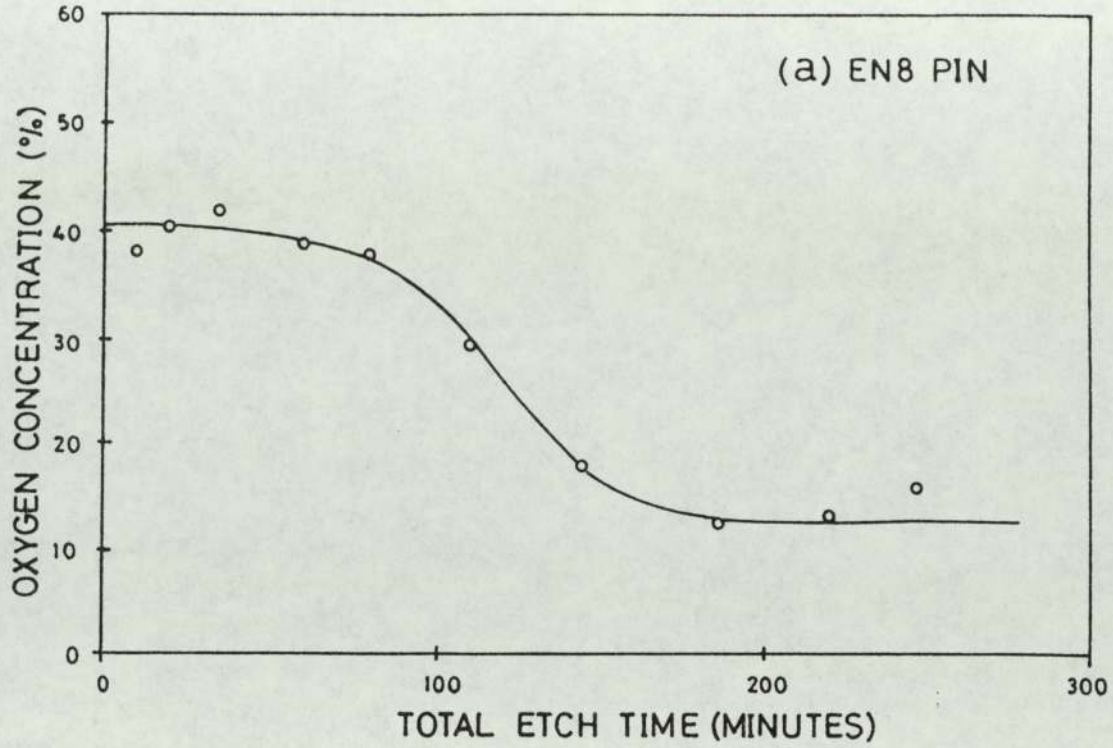

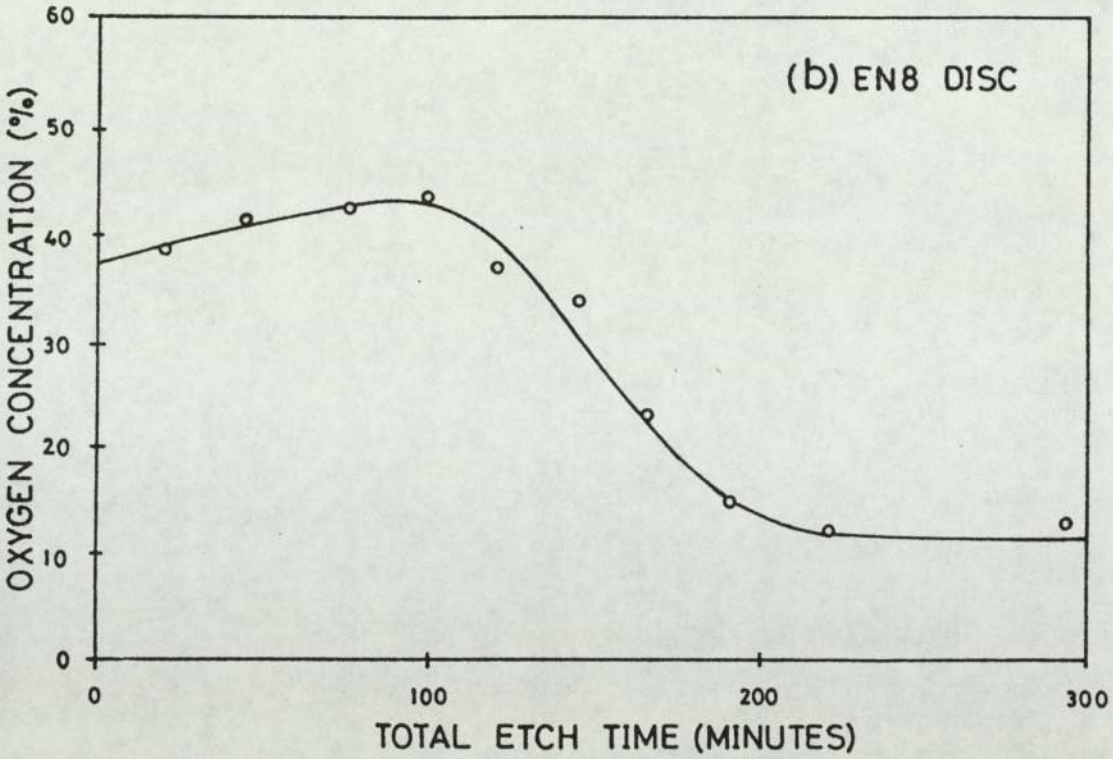

FIGURE 5.26 Concentration versus Depth Profiles for Worn Surfaces from EN8 Wear Test at $2.0 ms^{-1}$, 45 N.

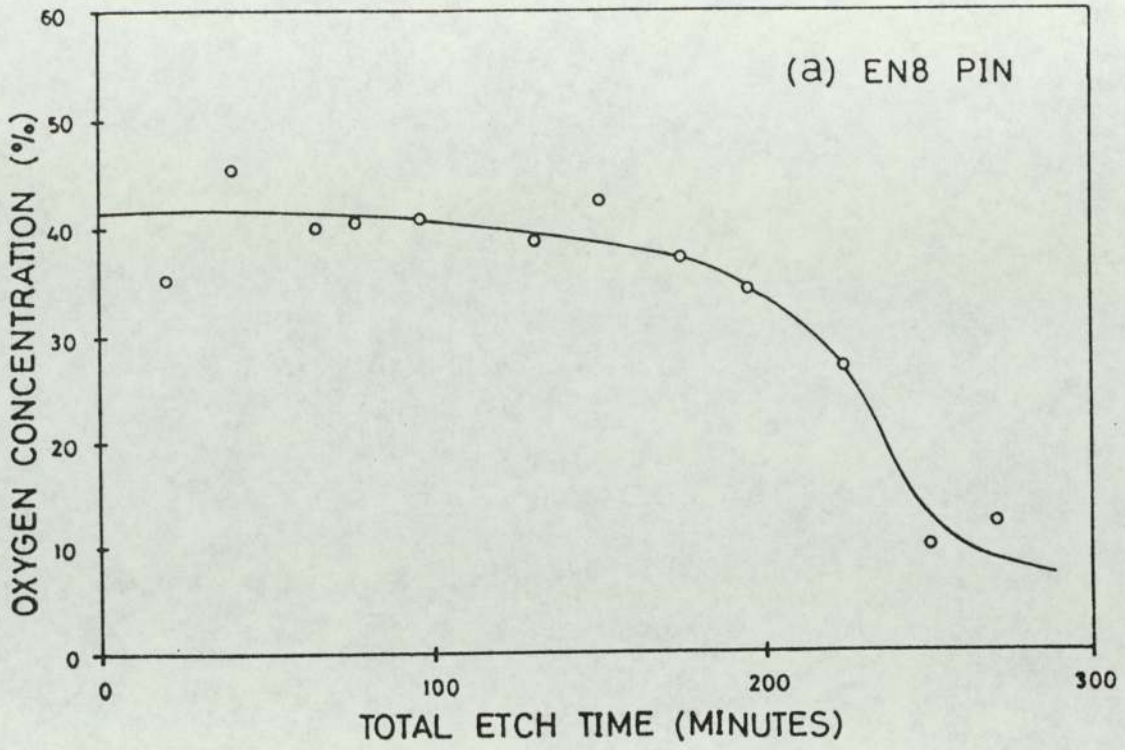

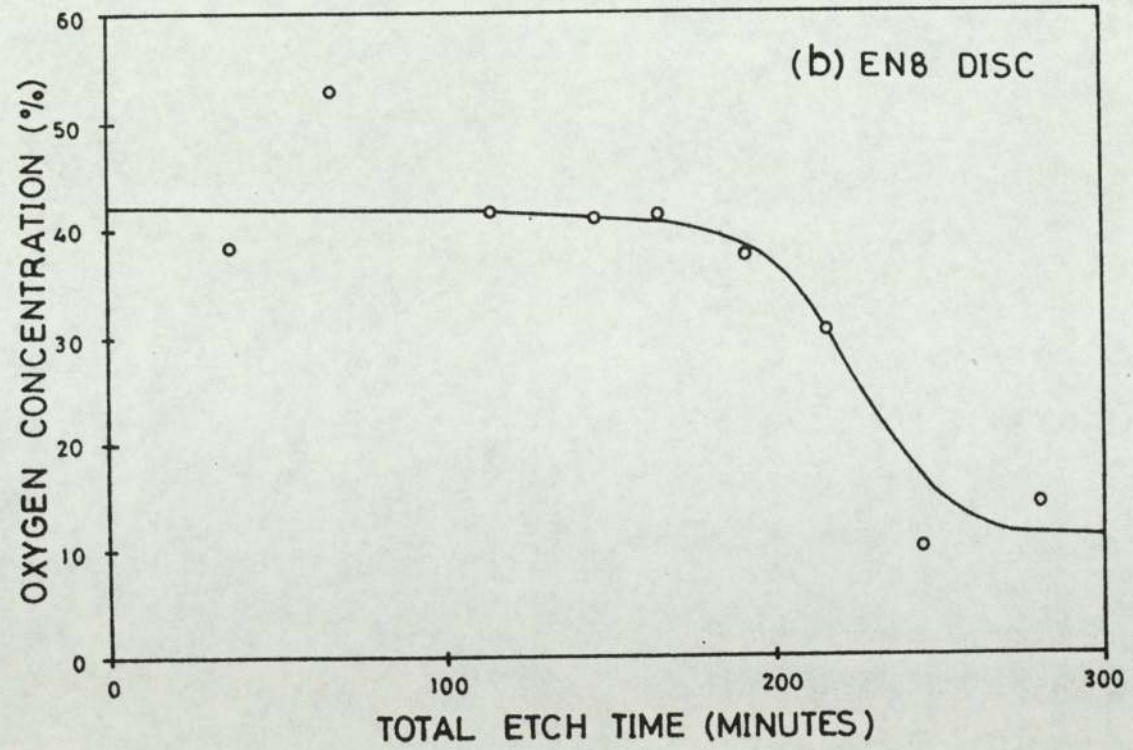

FIGURE 5.27 Concentration versus Depth Profiles for Worn Surfaces from EN8 Wear Test at 4.0 ms^{-1}, 30 N.

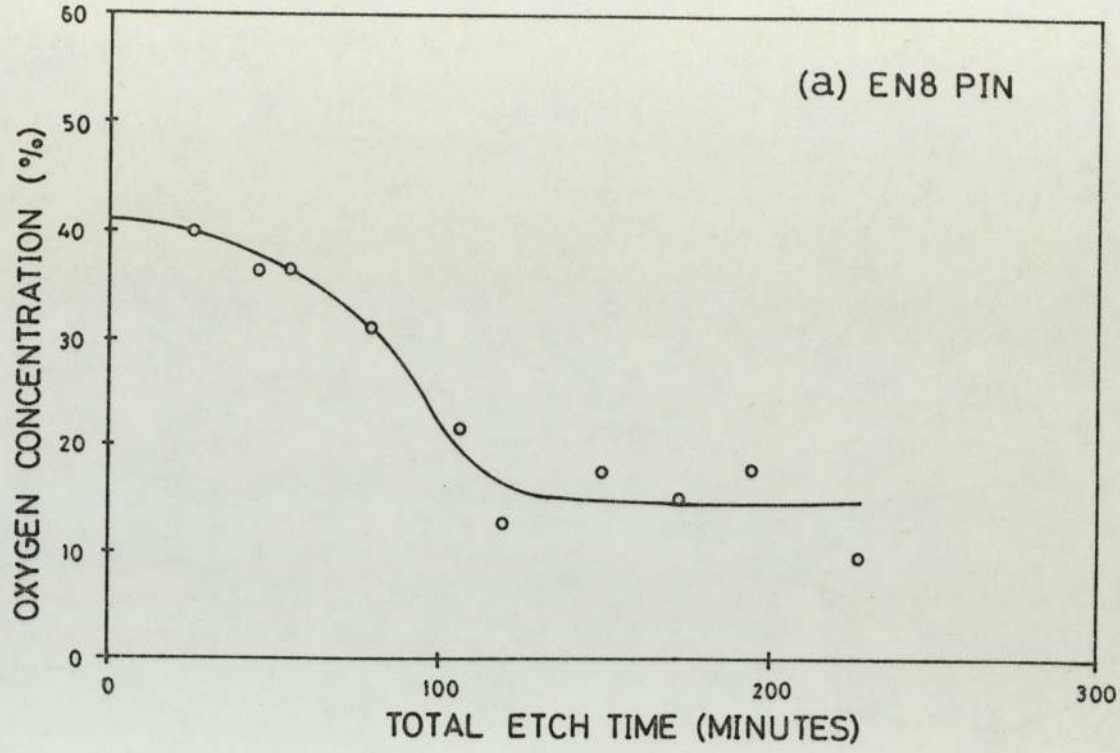

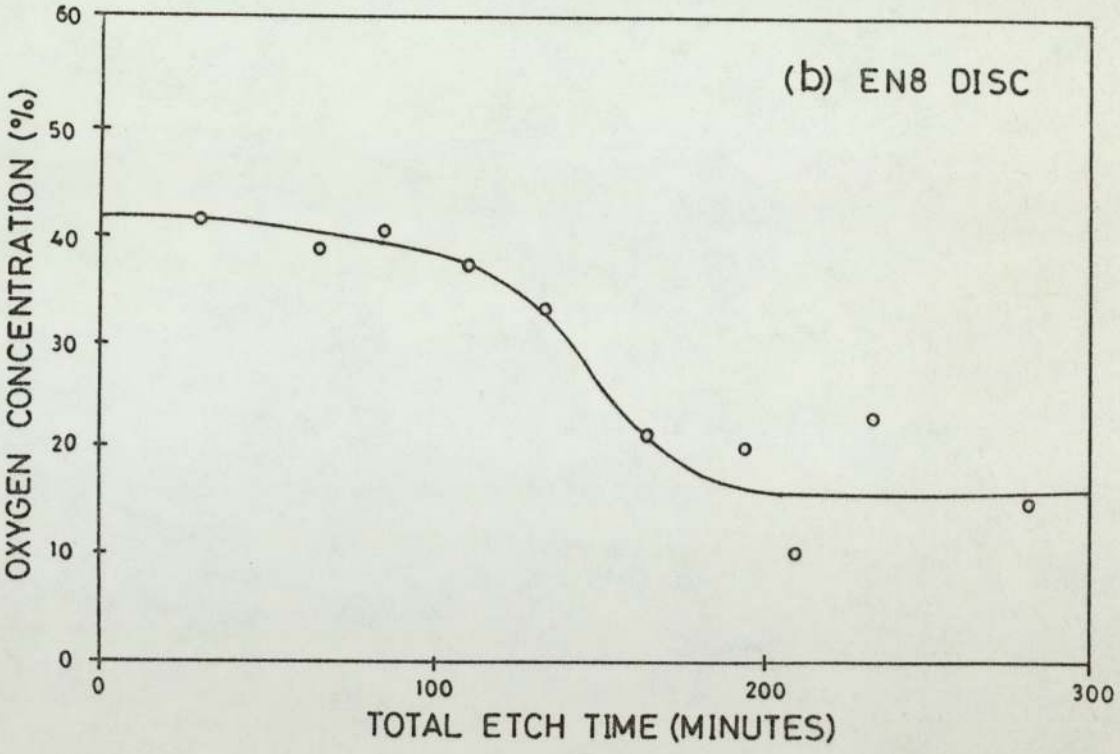

FIGURE 5.28 Concentration versus Depth Profiles for Worn Surfaces from EN8 Wear Test at 4.0 ms^{-1}, 45 N.

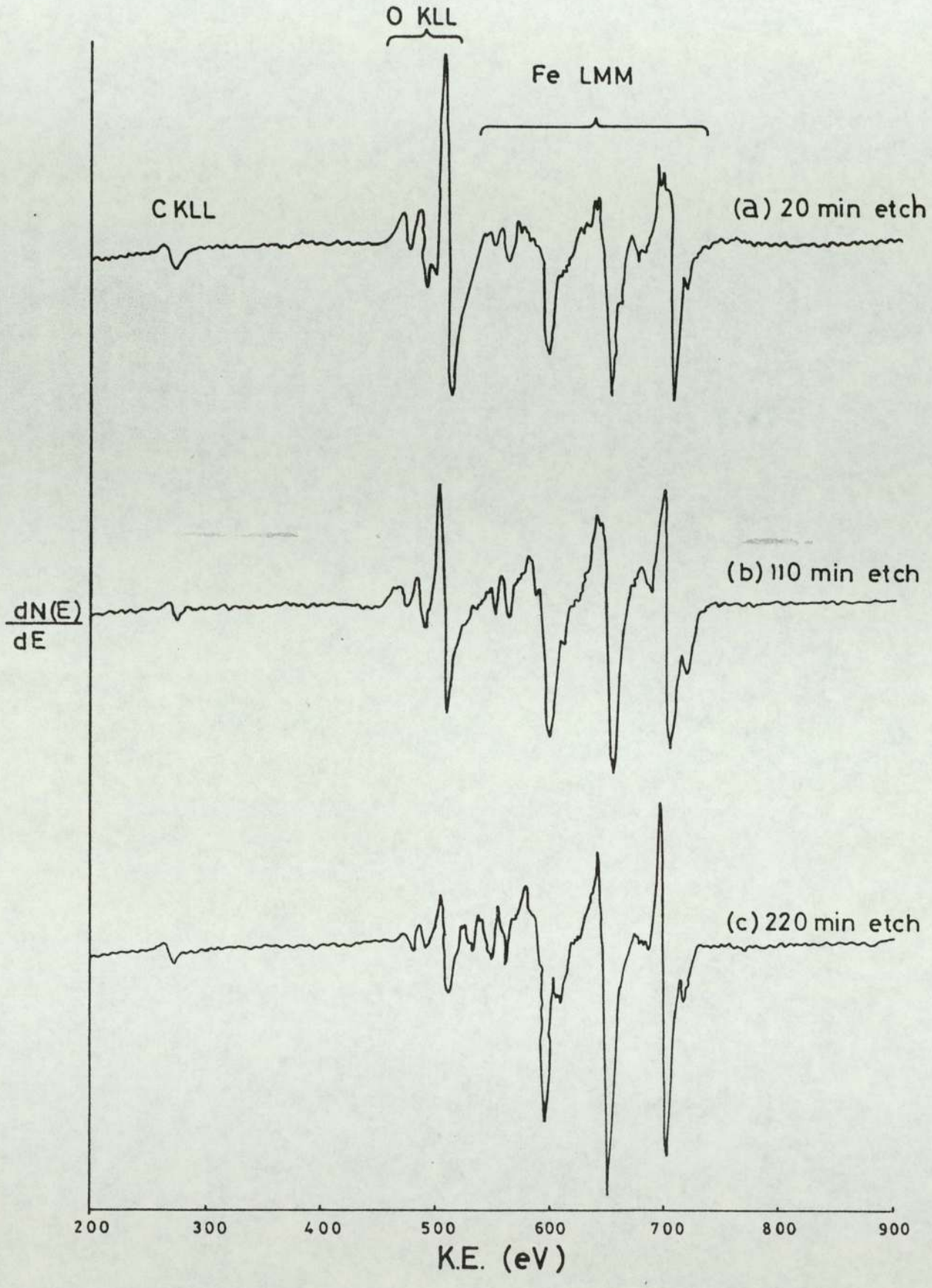

FIGURE 5.29 Auger Spectra Recorded for a Worn Pin Surface Generated in an EN8 Wear Test at 50N, 2.0ms^{-1}.

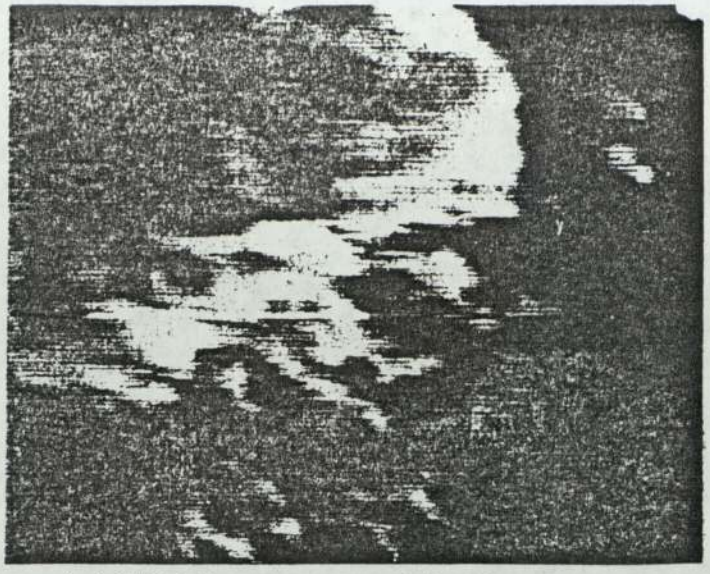

(a) SEM image, unetched

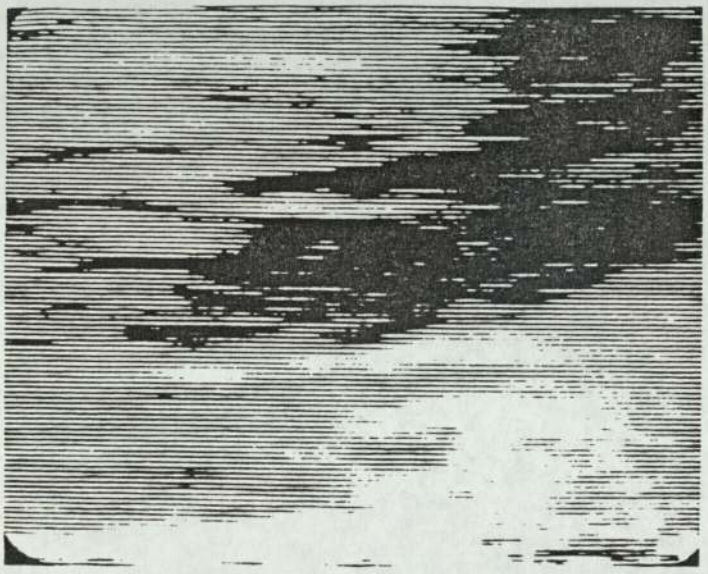

(b) oxygen map, 5 minute etch

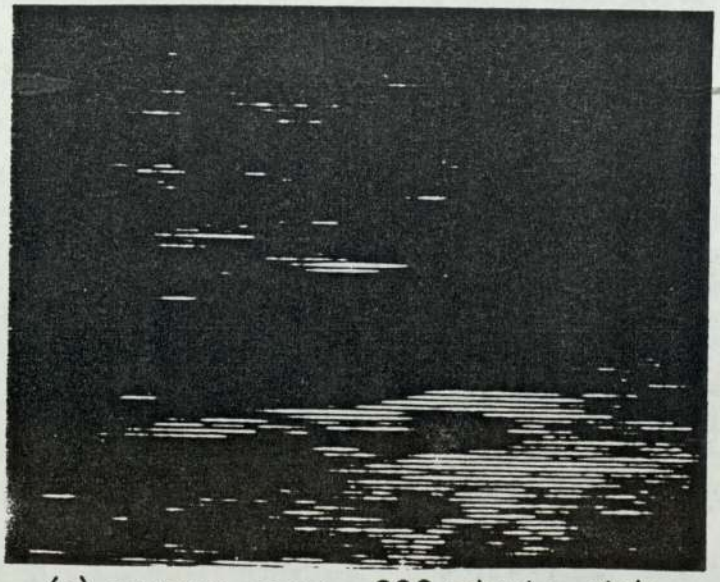

(c) oxygen map, 200 minute etch

FIGURE 5.30 Scanning Electron Micrograph and Corresponding Auger Oxygen Maps of Worn Disc Surface Generated at 2.0ms^{-1}, 10N.

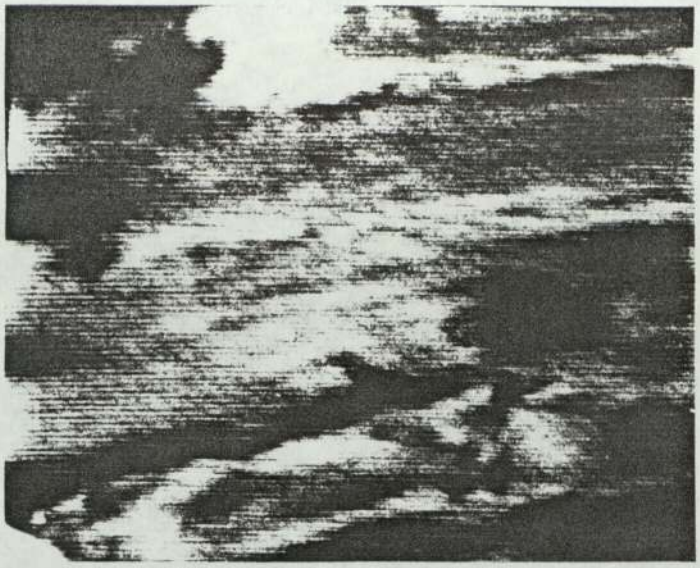

(a) SEM image unetched

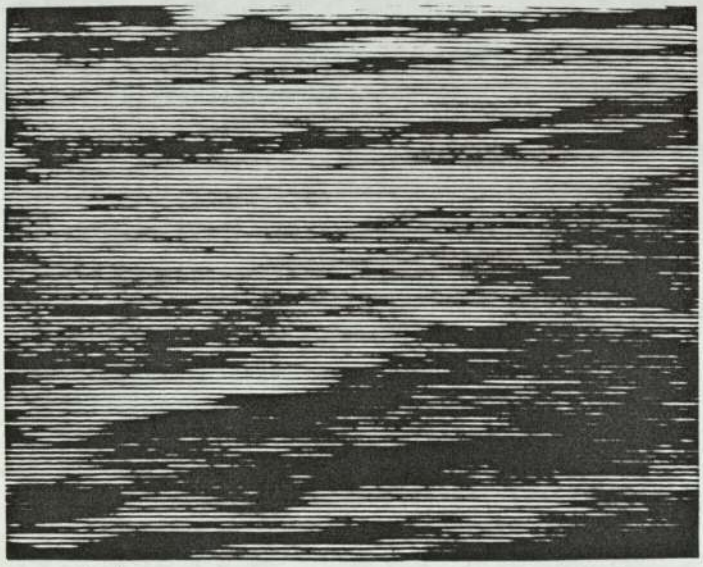

(b) oxygen map, 5 minute etch

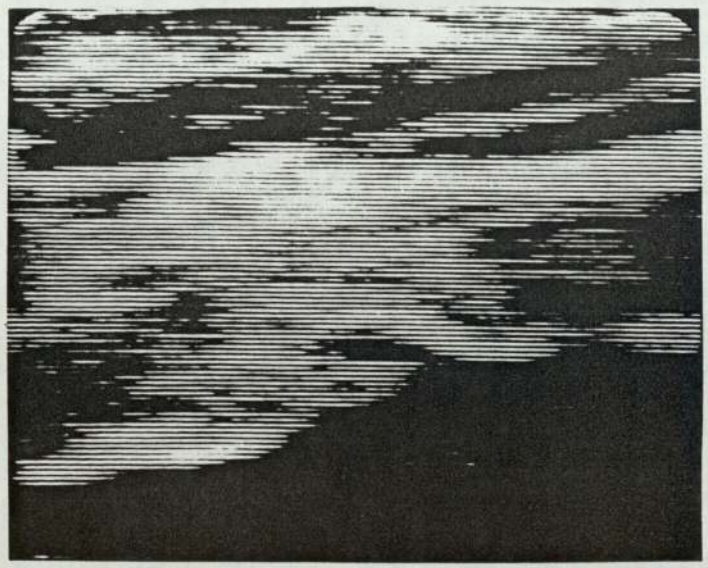

(c) oxygen map, 20 minute etch

FIGURE 5.31 Scanning Electron Micrograph and Corresponding Auger Oxygen Maps of Worn Disc Surface Generated at 2.0ms^{-1}, 25N.

(a) SEM image unetched

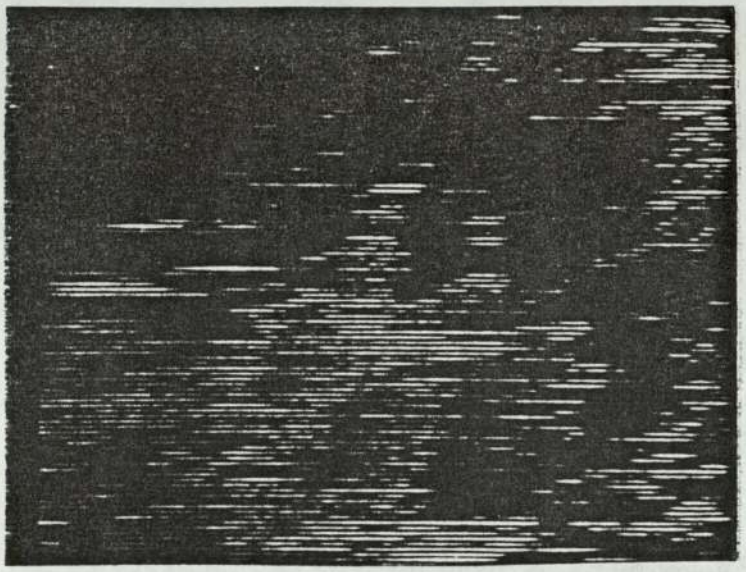

(b) oxygen map., 50 minute etch

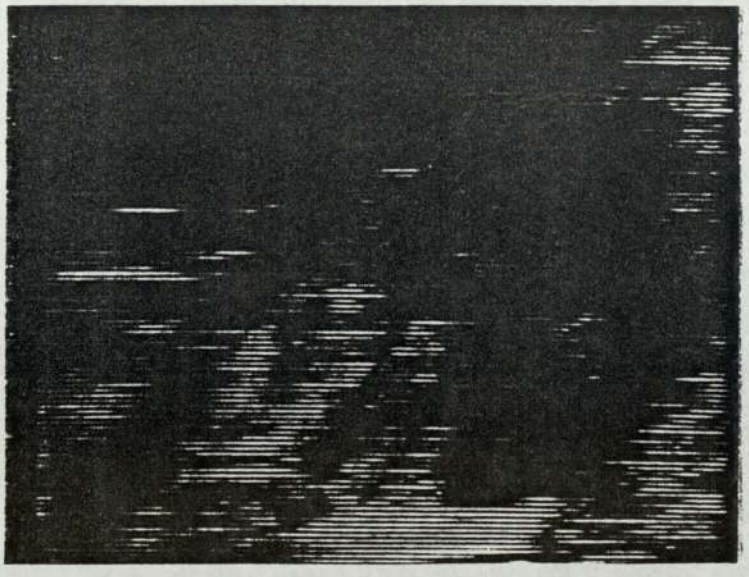

(c) oxygen map, 150 minute etch

FIGURE 5.32 Scanning Electron Micrograph and Corresponding Auger Oxygen Maps of Worn Disc Surface Generated at 2.0ms^{-1}, 55N.

level out at a concentration of approximately 10%. This tends to indicate that the plateaux present on the worn surfaces consist of a physically homogeneous oxide. In addition, the results indicate that the oxide films are thicker when Fe_3O_4 is the predominant oxide rather than α-Fe_2O_3 or FeO.

As mentioned earlier, scanning Auger oxygen maps recorded after various periods of etching of each worn surface indicated that plateaux consisted of oxide. Figures 5.30, 5.31 and 5.32 show SEM images plus corresponding oxygen maps recorded after various periods of etching for worn surfaces produced in wear tests at 2.0 ms^{-1} and loads of 10 N, 25 N and 55 N respectively.

5.4.2 AES of Worn Surfaces from EN8 / 9% Cr Wear Tests

The wear tests in which EN8 pins were worn against 9% chromium discs were conducted in order to determine if there was any transfer of oxide from disc to pin during oxidational wear. The concentration of chromium present in the oxide on the worn EN8 pin surface, determined by AES depth profiling, indicates whether oxide transfer has taken place or not. Figures 5.33, 5.34, 5.35 and 5.36 show the concentration versus depth profiles obtained by point Auger analysis of worn surfaces produced in EN8 / 9% Cr steel wear experiments run at a speed of 2.0 ms^{-1} and applied loads of 20 N, 30 N, 40 N and 50 N respectively. Depth profiles have been given for both pin and disc, since absence of chromium in the pin oxide would prove little if chromium was undetectable in the disc oxide also. For the sake of clarity only oxygen and

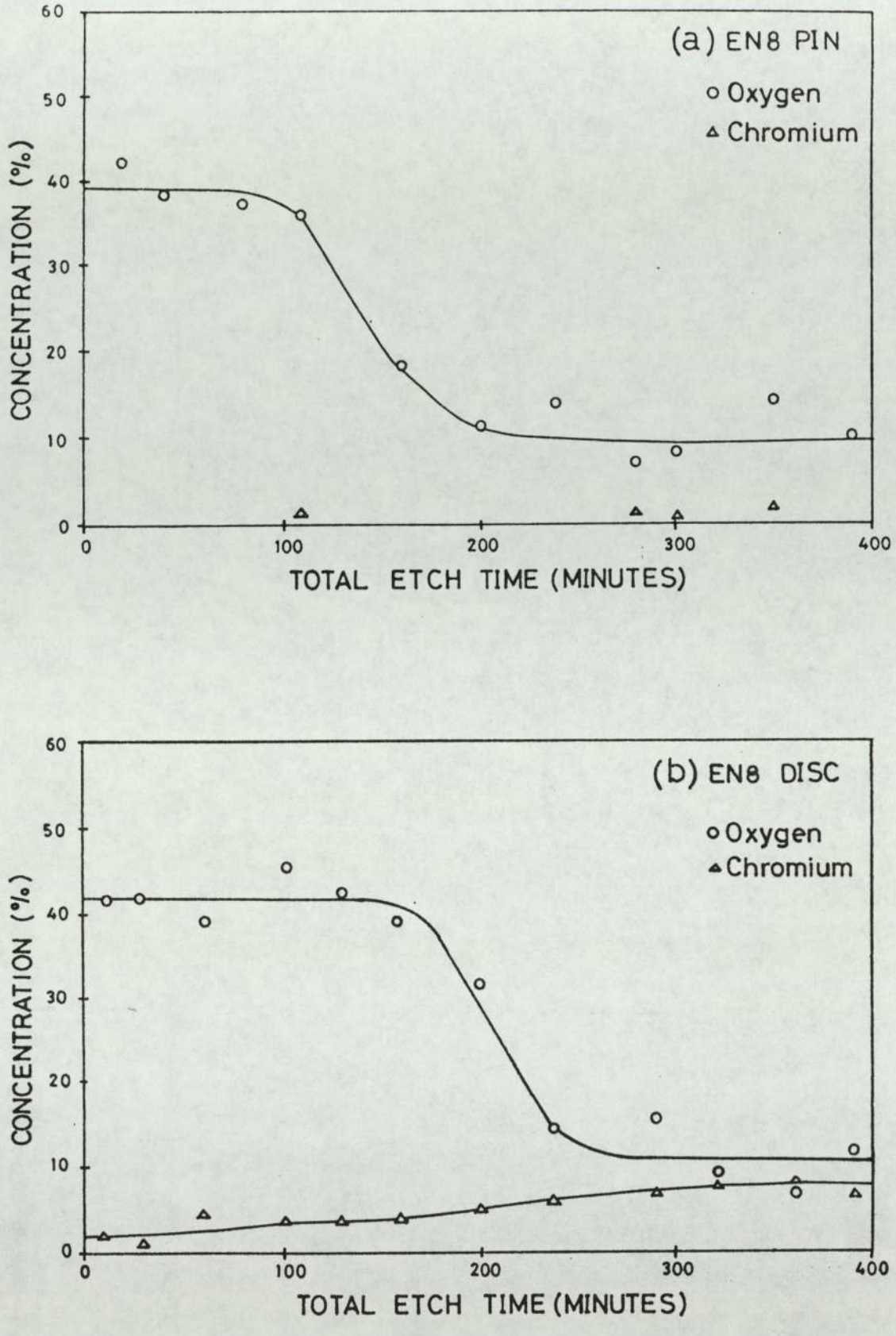

FIGURE 5.33 Concentration versus Depth Profile for Worn Surfaces from EN 8/9% Cr Wear Test at 2.0 ms^{-1}, 20N.

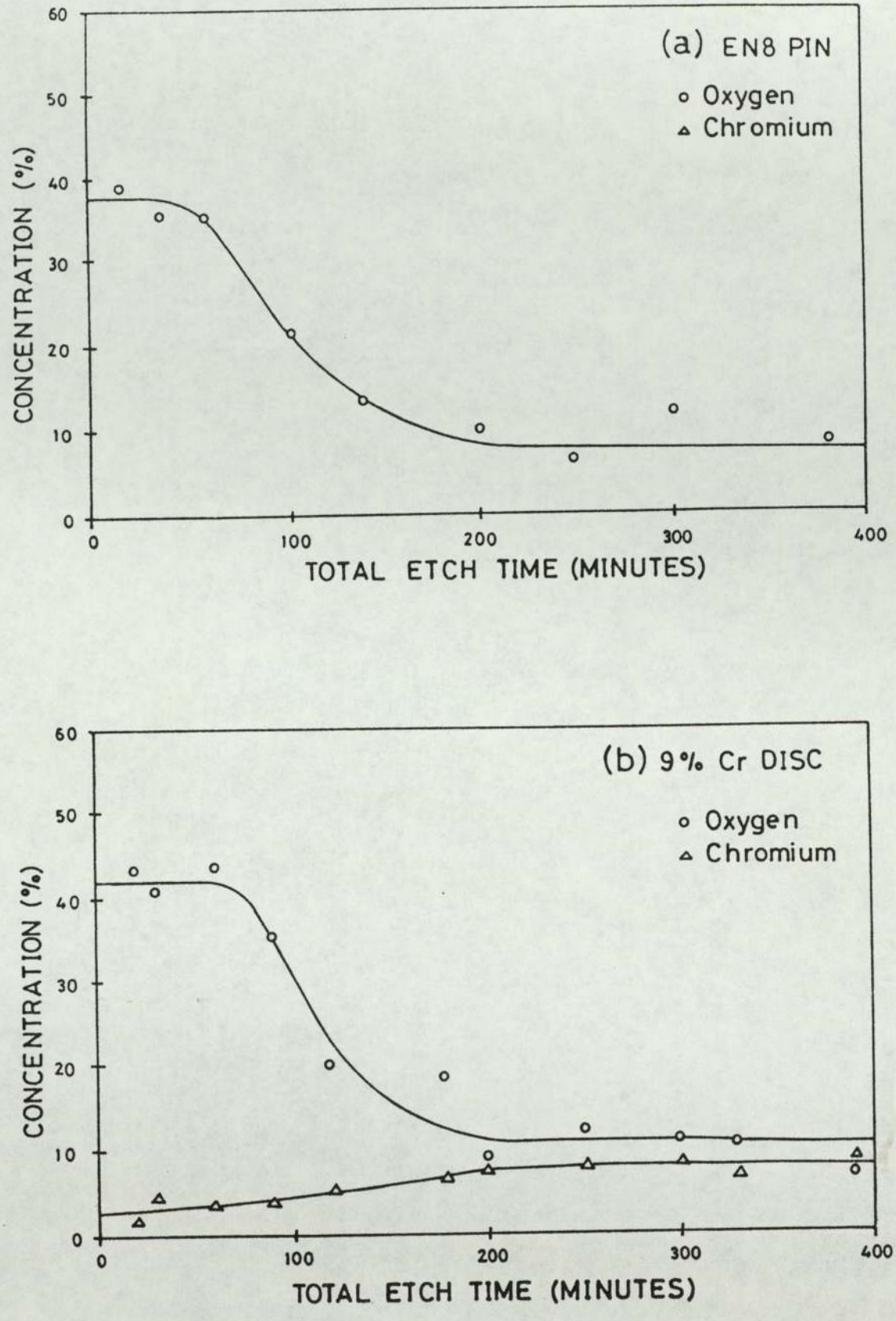

FIGURE 5.34 Concentration versus Depth Profiles for Worn Surfaces from EN8/9% Cr Wear Test at 2.0 ms^{-1}, 30 N.

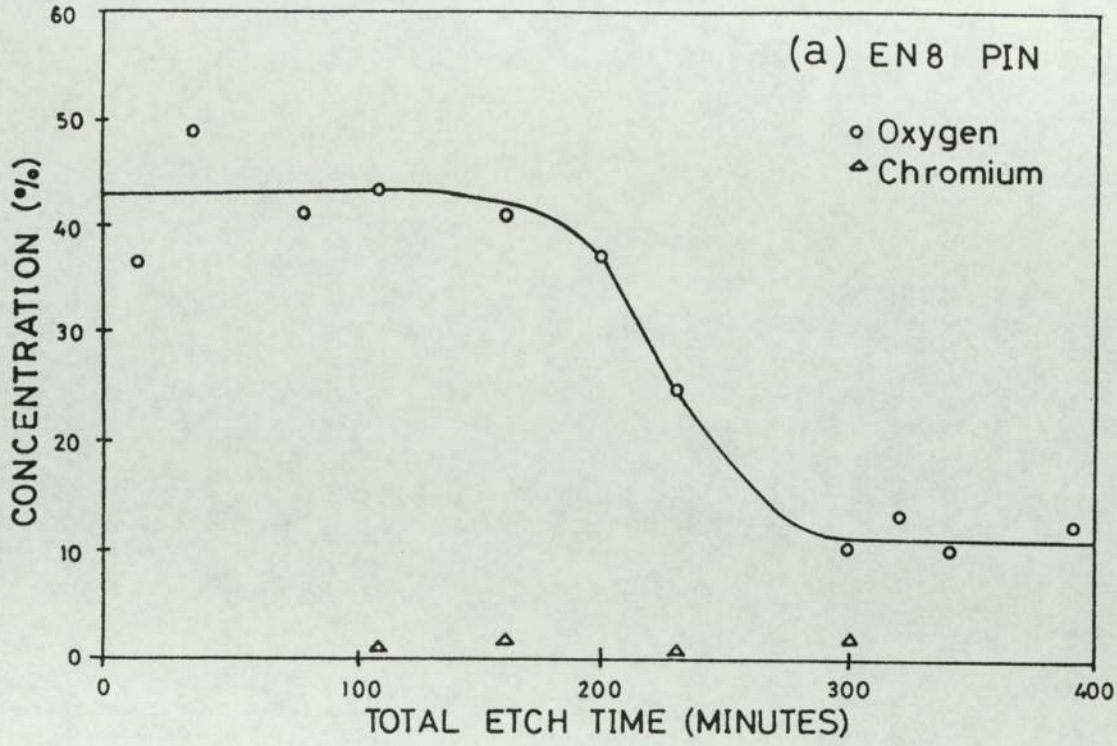

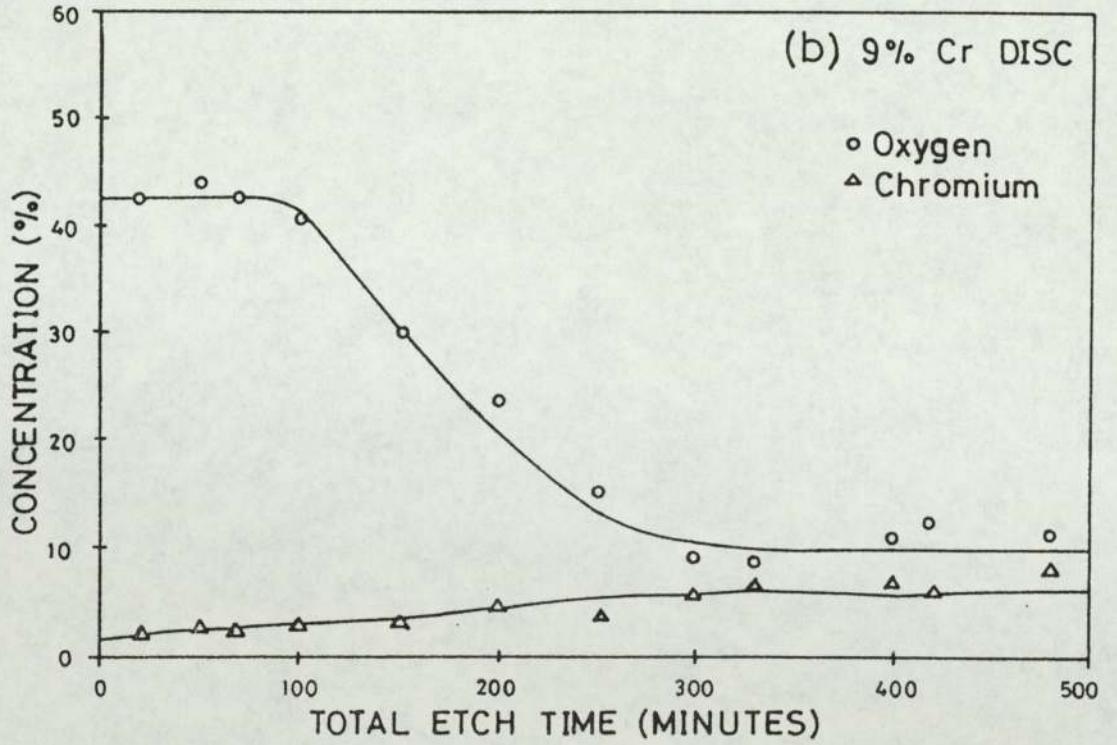

FIGURE 5.35 Concentration versus Depth Profiles for Worn Surfaces from EN8/9% Cr Wear Test at $2.0 ms^{-1}$, 40N.

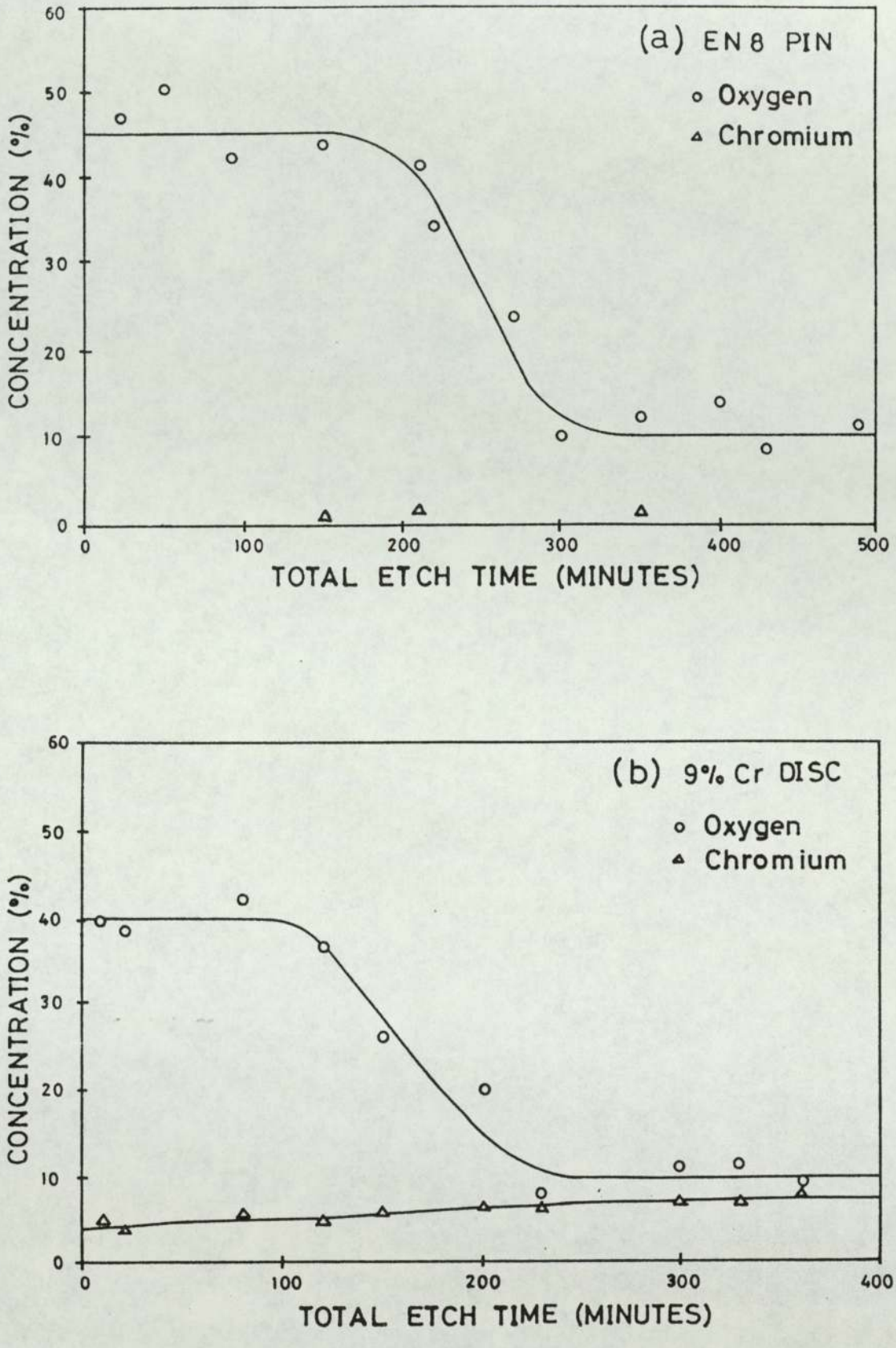

FIGURE 5.36 Concentration versus Depth Profiles for Worn Surfaces from EN 8/9% Cr Wear Test at 2.0 ms^{-1} 50 N.

chromium levels have been plotted.

Elemental concentrations were calculated using equation(5.5). Carbon levels were initially around 40% for the unetched surfaces, but fell to around 10% to 15% after approximately ten minutes of etching, after which the carbon concentration remained fairly constant. For all of the surfaces studied the iron levels remained approximately constant at around 40% to 45% throughout the oxide so that the ratio of oxygen atoms to iron atoms was close to 50:50. This is around what we would expect since x-ray diffraction of the debris from the EN8/ 9% Cr steel wear tests (section 5.2.3) indicated that FeO was always present in the oxide, probably being the major constituent. Once the oxide had been penetrated through to the metal base iron levels rose to around 70%.

Certain conclusions can be drawn from the Auger analysis of these surfaces. Firstly, the plateaux observable on the worn pin and disc surfaces consist of oxide. This is evident from the depth versus concentration profiles and from scanning Auger oxygen maps not presented here. Secondly, there is a marked difference between the levels of chromium detected on the pin and disc surfaces. The chromium concentration in the oxide on the worn disc is initially around 3% at the oxide surface, rising very gradually through the oxide until its value levels out at approximately 8% in the bulk metal. In addition, chromium was detected in the oxide at all depths. In the case of the oxide on the worn EN8 pins, however, the situation is very different. Here, chromium was only very occasionally detected and then its concentration was only around 1%. Figures 5.37 and 5.38 show Auger

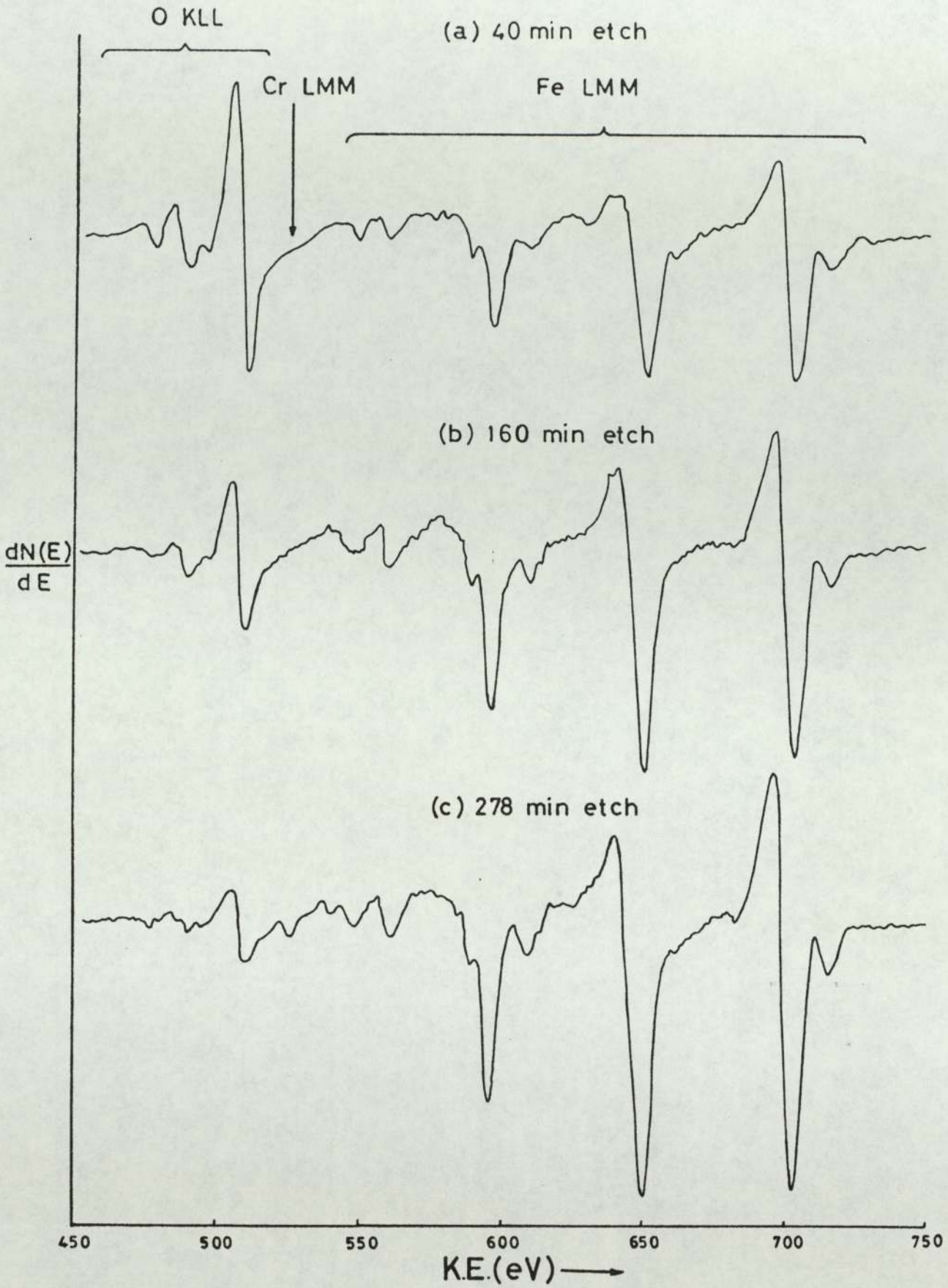

FIGURE 5.37 Auger Spectra Recorded for a Worn EN8 Pin Surface Generated in an EN8/9% Cr Wear Test at 20N, 2.0ms^{-1}

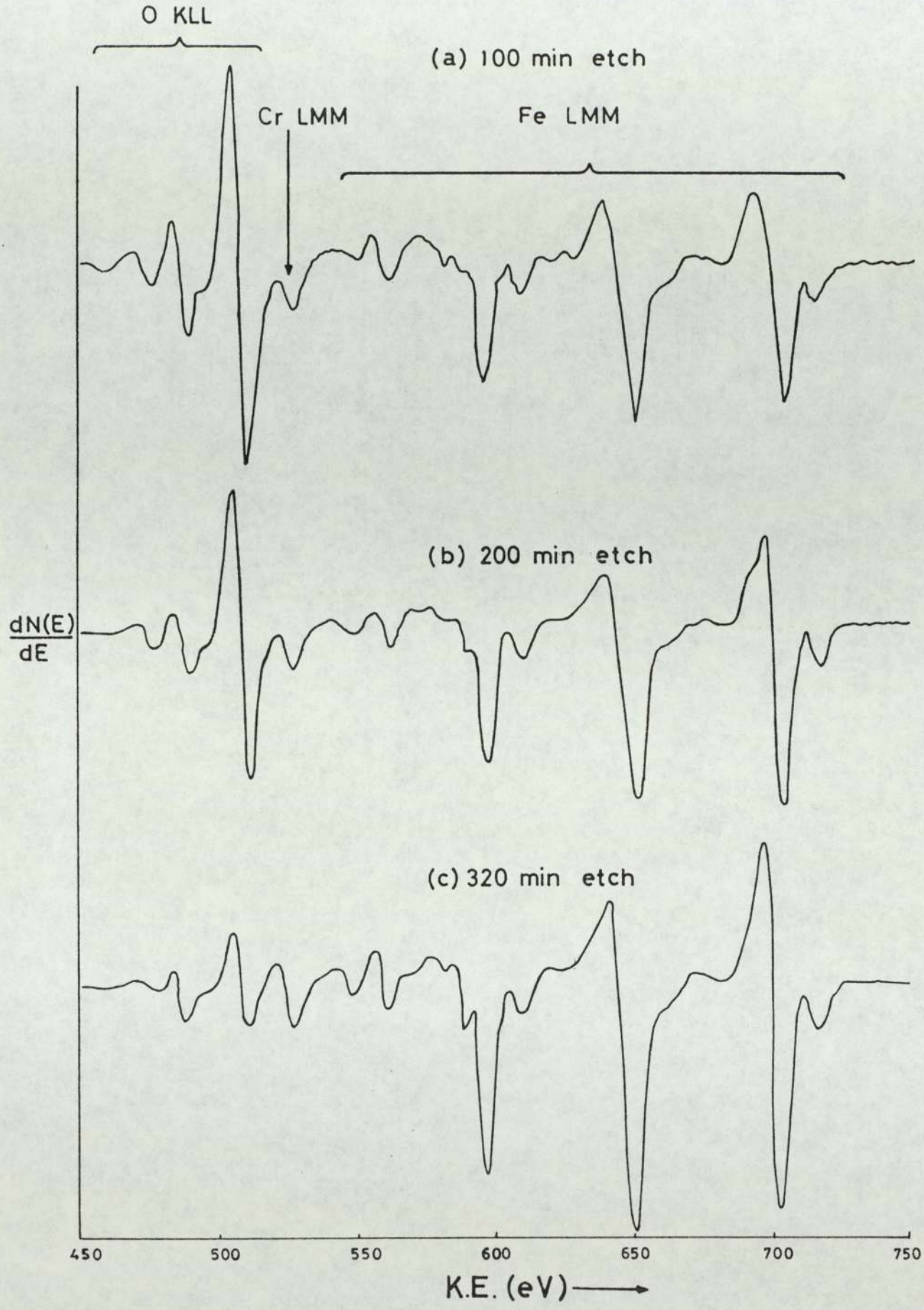

FIGURE 5.38 Auger Spectra Recorded for a Worn 9% Cr Disc Surface Generated in an EN8/9% Cr Wear Test at 20N, 2.0 ms^{-1}

spectra recorded at various depths through the oxide on an EN8 steel pin and a 9% chromium steel disc respectively, the surfaces of which were worn in an experiment conducted at 2.0 ms^{-1} and 50 N.

Thus, evidence from the AES analysis of worn surfaces produced in the EN8 / 9% Cr wear tests clearly show that transfer of oxide from the disc to the pin does not occur, indicating that the oxides on the worn pin and disc surfaces grow separately.

5.5 Scanning Electron Microscopy (SEM) Results

5.5.1 Analysis of Worn Surfaces from EN8 Wear Tests

The technique of scanning electron microscopy was invaluable for observing the general surface characteristics of, and measuring thicknesses of oxide on, worn pin and disc surfaces. Almost all of the worn surfaces from the EN8 wear tests were analysed in this manner.

An observation which was usually found to be true was that the worn pin surface from a given wear test appeared smoother with a higher surface area covering of oxide and less oxide disruption than the corresponding disc surface.

There was also found to be a correlation between the transitions in the wear rate versus load graphs (figures 4.1(a) and (b)) and the general appearance of the worn surfaces as observed by SEM. The scanning electron micrographs in figure 5.39 show worn disc surfaces from wear

FIGURE 5.39 Scanning Electron Micrographs of Worn Disc Surfaces Generated in EN8 Wear Tests Conducted at 2.0 ms^{-1}

(a) 58 N

(b) 25 N

(c) 5 N

a

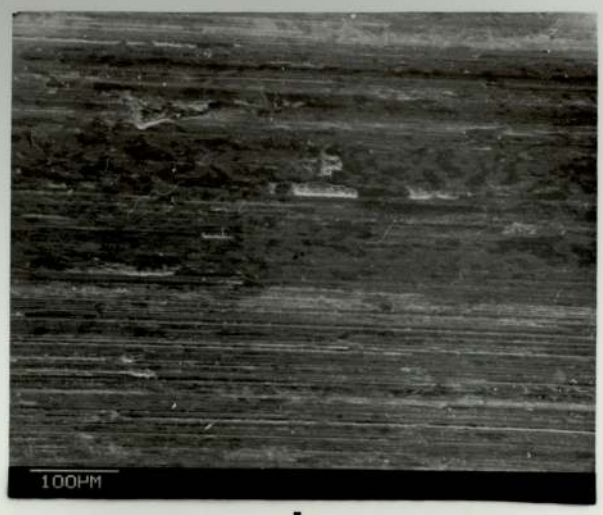

b

c

FIGURE 5.40 Scanning Electron Micrographs of Worn Pin Surfaces Generated in EN8 Wear Tests Conducted at 2.0 ms^{-1}

(a) 58 N

(b) 25 N

(c) 10 N

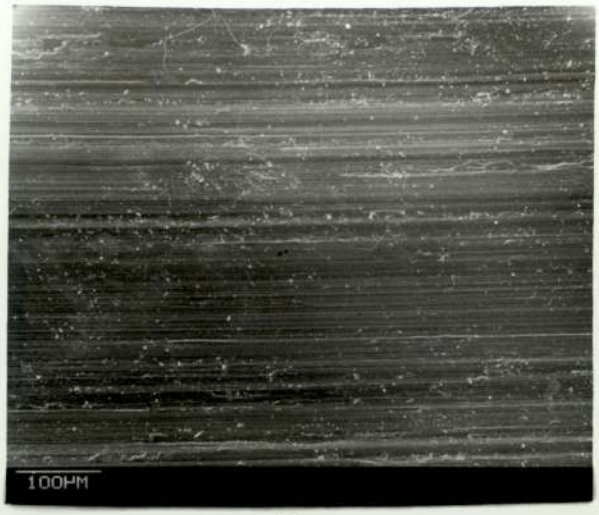

a

b

c

tests conducted at 2.0 ms^{-1}. Worn surfaces produced in each of the three different regions of the wear rate versus load graph of figure 4.1(a) are represented. Figure 5.39(c) is a micrograph of a worn disc surface generated in a wear experiment conducted at a load below the first transition, where the surface oxide is α-Fe_2O_3, and smooth oxide plateaux are visible standing above relatively rough, debris covered metallic areas. The micrograph of figure 5.39(b) illustrates the appearance of a worn disc surface produced in the intermediate region between loads of approximately 12 N and 38 N, where the surface oxide is a mixture of α-Fe_2O_3 and Fe_3O_4. In this case the worn surface appears smooth and is almost completely covered in oxide. The third micrograph of figure 5.39(a) shows a worn disc surface generated at a load higher than the second transition, and thus FeO was present in the surface oxide. Here, oxide plateaux can be seen standing above rough metallic areas which are heavily covered in debris. The corresponding pin surfaces characteristic of the three regions are shown in the micrographs of figure 5.40, and it can be seen that there is much less variation in the appearance of the pin surfaces, all of them being almost completely covered in a smooth oxide film.

The worn surfaces generated in the EN8 wear experiments conducted at 4.0 ms^{-1} similarly exhibited a variation in appearance according to whether the experimental load was above or below the transition in the wear rate versus load graph of figure 4.1(b). Figures 5.41(b) and (c) are micrographs of worn disc surfaces generated at loads lower than the transition load, corresponding to a surface oxide of α-Fe_2O_3 and Fe_3O_4, and it can be seen that the surfaces have an almost complete covering of smooth oxide. In complete

FIGURE 5.41 Scanning Electron Micrographs of Worn Disc Surfaces Generated in EN8 Wear Tests Conducted at $4.0 ms^{-1}$

(a) 58 N

(b) 25 N

(c) 10N

a

b

c

FIGURE 5.42 Scanning Electron Micrographs of Worn Pin Surfaces Generated in EN8 Wear Tests Conducted at $4.0\,ms^{-1}$.

(a) 58 N

(b) 25 N

(c) 15 N

a

b

c

contrast, the micrograph of figure 5.41(a) shows a worn disc surface produced at a load higher than the transition load, where FeO was present in the surface oxide, and it can be seen that there is now a much greater degree of surface disruption, with smooth oxide plateaux standing above relatively large rough areas which are heavily covered in debris. As for the surfaces generated in the $2.0\,ms^{-1}$ wear tests, there is much less variation in the appearance of the worn pin surfaces. Figure 5.42 shows micrographs of pin surfaces generated at loads above and below the transition load at 35 N, and it can be seen that in all cases the surfaces have an almost complete covering of smooth oxide.

Scanning electron microscopy was also used at a higher magnification in order to measure oxide thicknesses. As mentioned in section 3.6, the worn surfaces often had to be mechanically distorted in order to produce cracking of the almost complete covering of oxide so that oxide edges became visible for thickness measurements. The micrographs of figure 5.43 show how the surface oxide cracked under the applied stresses to reveal visible oxide edges, Figures 5.43(g) and 5.43(h) show two examples of how this method created an extensive visible edge to a complete sheet of oxide covering virtually the whole surface. It was considered that the thickness of the layer of oxide uplifted from the base was representative of the total thickness of oxide on the worn surface since point Auger depth profiling analysis of the underlying substrate, carried out for a few of the samples, indicated bulk metal after around five minutes of etching.

FIGURE 5.43 Scanning Electron Micrographs of Worn EN8 Surfaces Mechanically Stressed so as to Produce Cracking of the Surface Oxide.

(a) 4.0 ms^{-1}, 40 N, pin

(b) 4.0 ms^{-1}, 45 N, pin

(c) 2.0 ms^{-1}, 40 N, pin

(d) 4.0 ms^{-1}, 45 N, pin

(e) 4.0 ms^{-1}, 45 N, pin

(f) 4.0 ms^{-1}, 10 N, disc

(g) 2.0 ms^{-1}, 25 N, pin

(h) 4.0 ms^{-1}, 25 N, disc

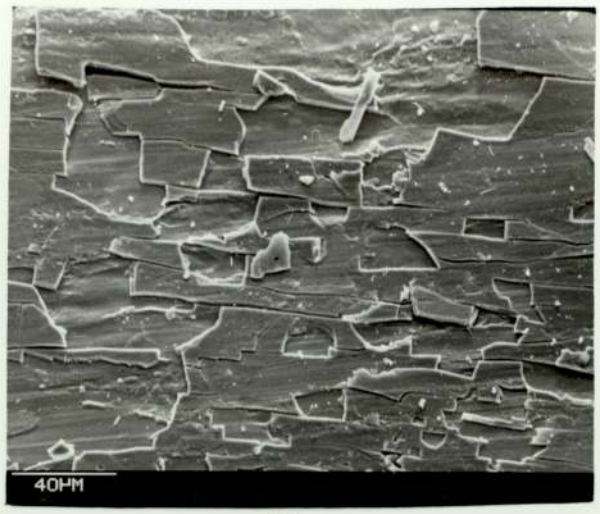

a

b

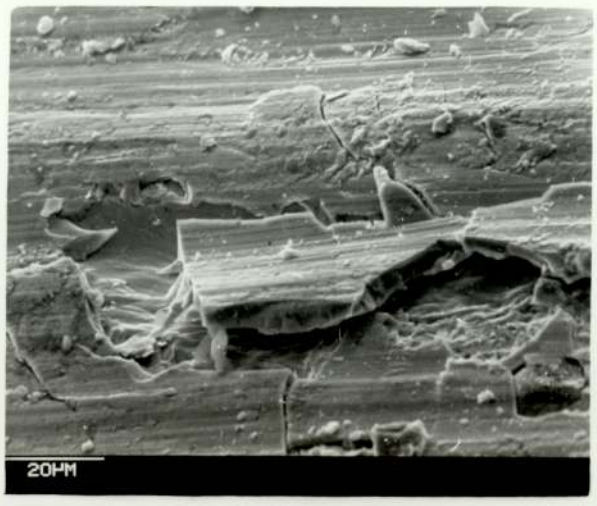

c

d

e

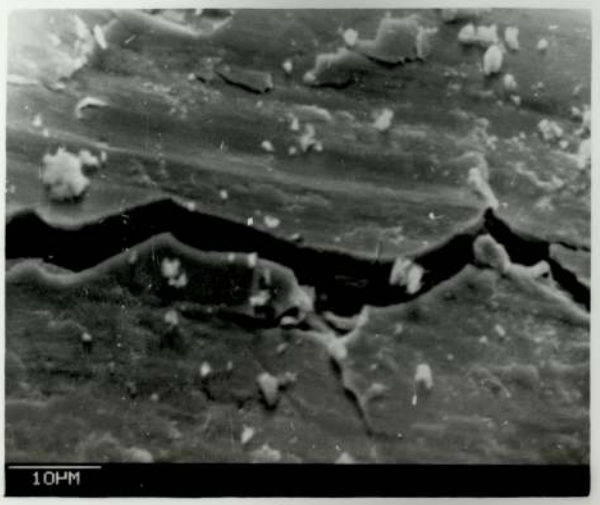

f

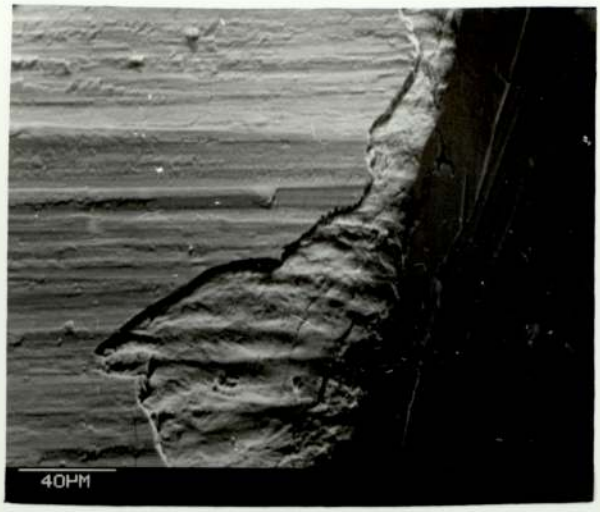

g

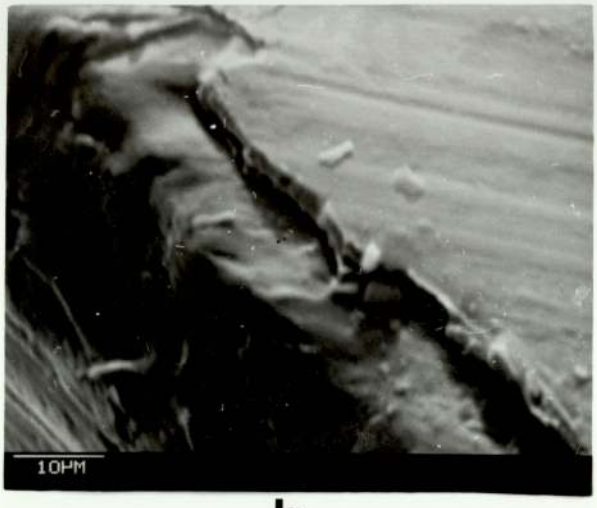

h

FIGURE 5.44 Scanning Electron Micrographs of Oxide Edges on Worn Surfaces from EN8 Wear Tests.

(a) 4.0 ms^{-1}, 45 N, disc

(b) 4.0 ms^{-1}, 25 N, disc

(c) 4.0 ms^{-1}, 10 N, disc

(d) 4.0 ms^{-1}, 20 N, disc

(e) 4.0 ms^{-1}, 10 N, disc

(f) 4.0 ms^{-1}, 45 N, disc

(g) 2.0 ms^{-1}, 40 N, disc

(h) 2.0 ms^{-1}, 40 N, pin

(i) 2.0 ms^{-1}, 35 N, pin

(j) 2.0 ms^{-1}, 35 N, disc

(k) 4.0 ms^{-1}, 55 N, pin

(l) 4.0 ms^{-1}, 55 N, pin

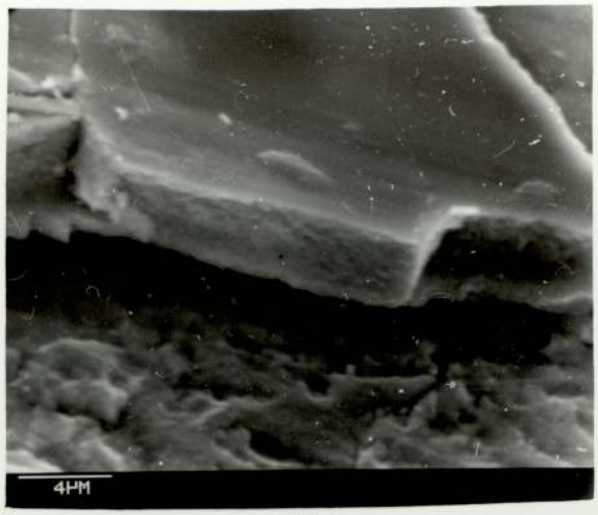

a

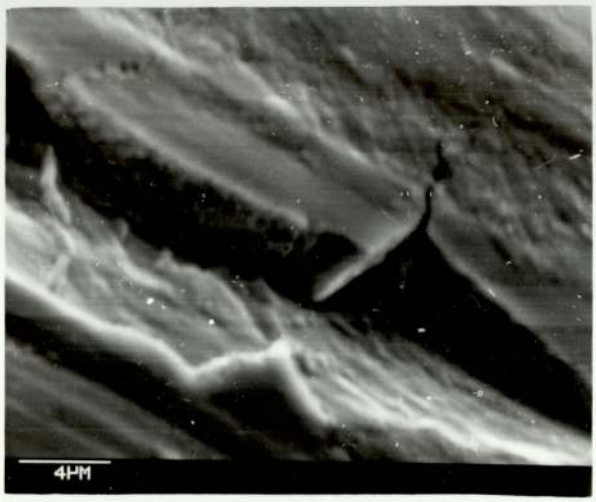

b

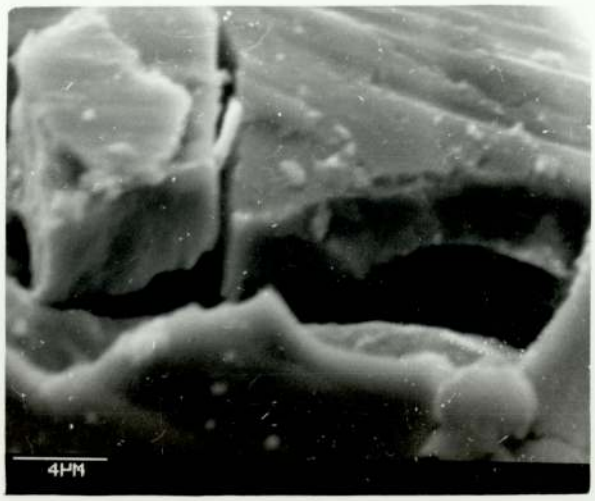

c

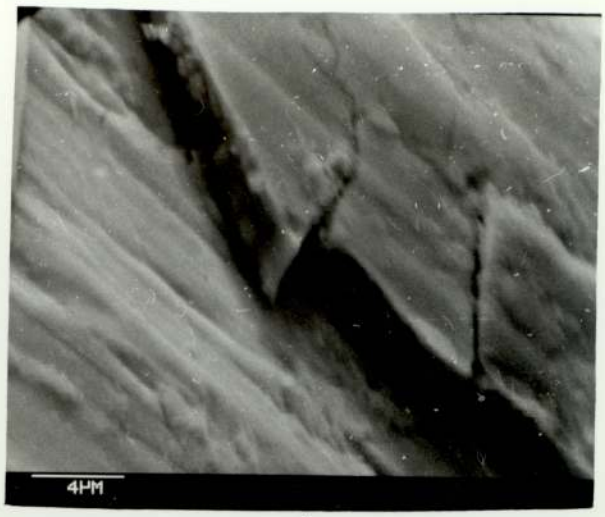

d

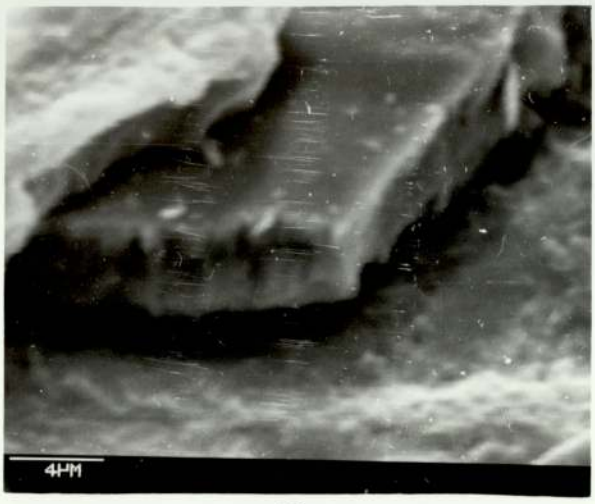

e

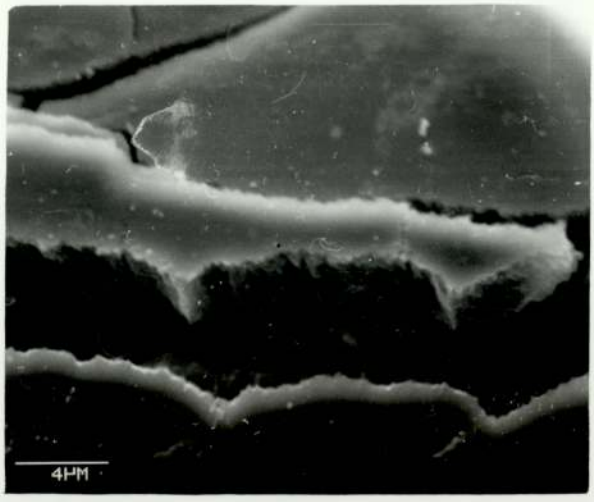

f

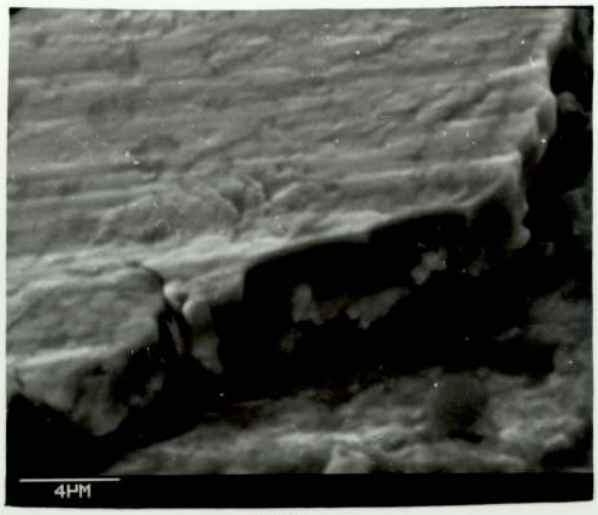

g

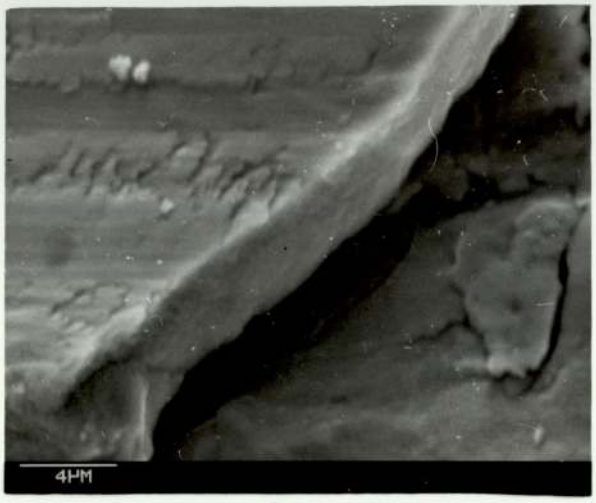

h

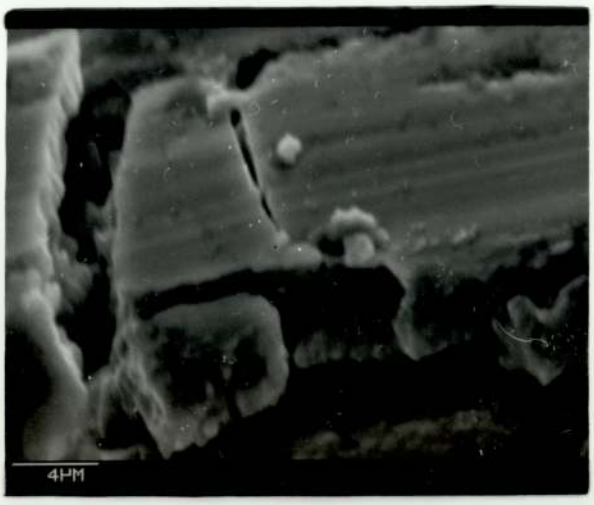

i

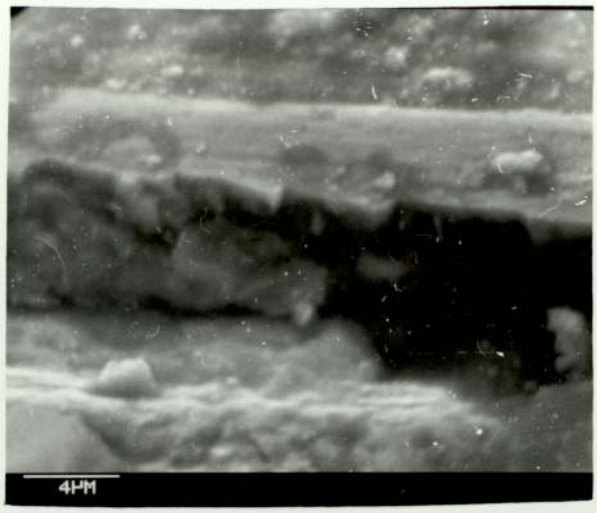

j

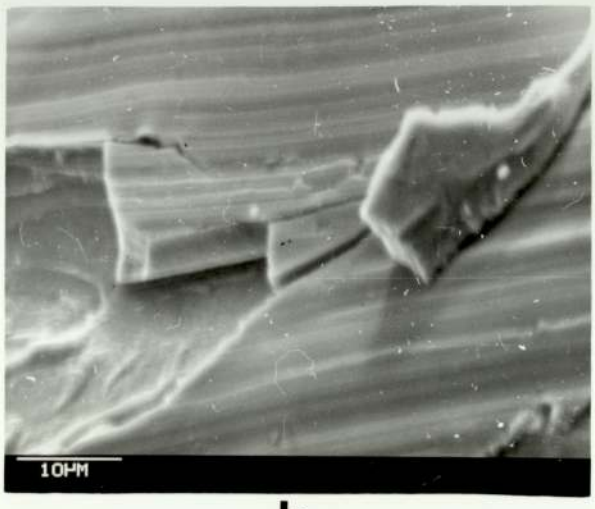

k

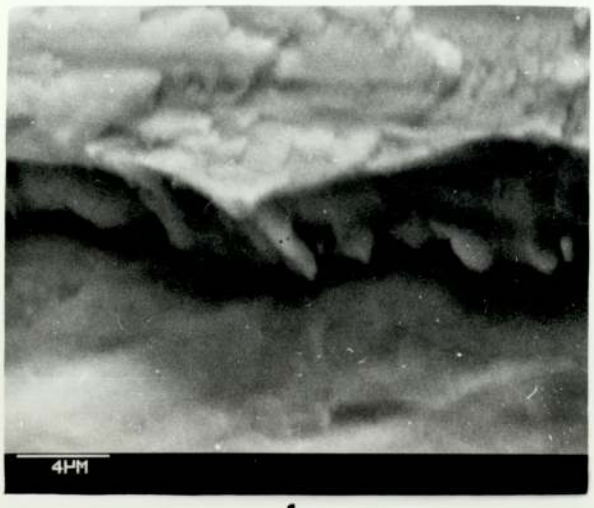

l

FIGURE 5.45 Scanning Electron Micrographs of Oxide Edges on Worn Surfaces Generated in Reciprocating Sliding Wear Tests at Elevated Temperatures.

(a)

(b)

(c)

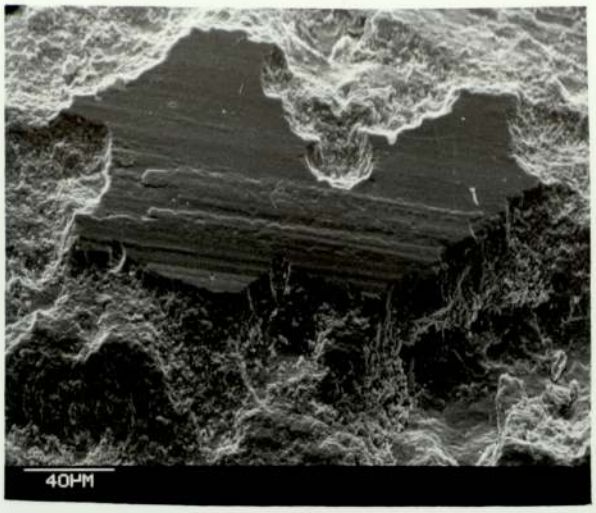

a

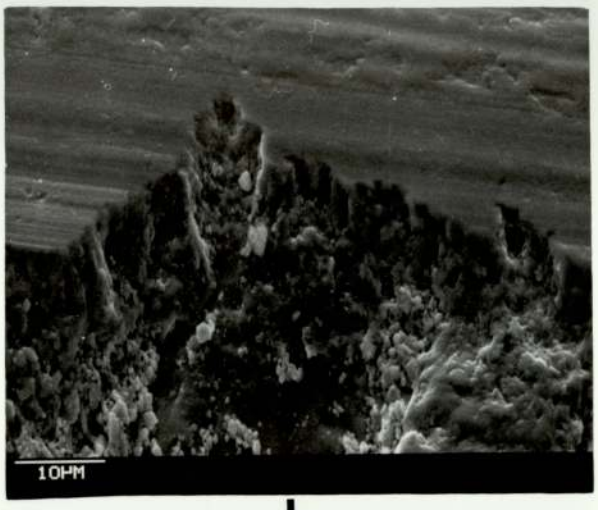

b

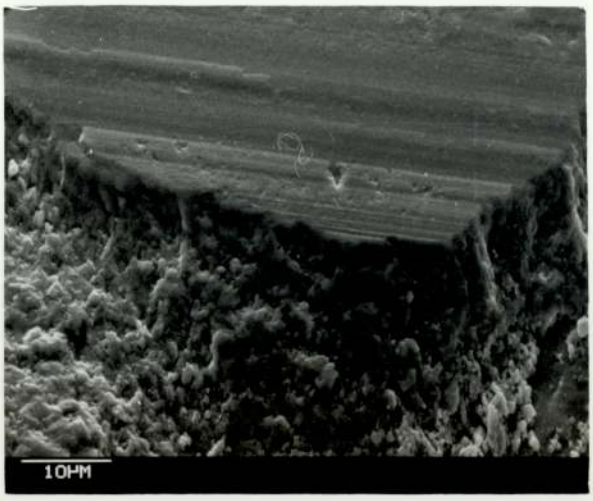

c

Micrographs of the actual oxide edges are shown in figure 5.44. Most of these edges were produced by cracking of the oxide by the method described in section 3.6. Observation of the oxide edges indicates that, for all loads, the oxide is a solid layer and does not consist of compacted oxide particles. In contrast, the micrographs of figure 5.45 show the edges of oxide plateaux formed on worn 9% Cr steel surfaces produced in reciprocating sliding wear experiments conducted at elevated temperatures (81). In this case it can be seen that the oxides consist of agglomerate layers.

Tables 5.10(a) and (b) give the measured oxide thicknesses for worn surfaces from EN8 wear tests carried out at 2.0 ms^{-1} and 4.0 ms^{-1} respectively. Around ten to fifteen thickness measurements were carried out on each surface and an average value calculated. In all cases the error stated was the standard deviation in the measurements. It can be seen that in all cases the oxide thickness on the pin and the disc was very similar. Figures 5.46 and 5.47 present the oxide thickness results graphically for worn surfaces from 2.0 ms^{-1} and 4.0 ms^{-1} wear tests respectively. It is clear from these figures that transitions occur in the oxide thicknesses which coincide with the transitions in the wear rate versus load graphs of figure 4.1. An additional trend noticeable in the oxide thickness versus load graphs is a slight increase in oxide thickness with increase in applied load within any given region.

EXPERIMENTAL LOAD (N)	OXIDE THICKNESS (μm)	
	DISC	PIN
5	—	3.6 ± 0.8
8	2.8 ± 0.8	3.0 ± 1.0
10	3.2 ± 0.8	3.2 ± 0.4
13	4.0 ± 0.6	3.9 ± 0.7
20	4.4 ± 0.7	4.2 ± 0.7
25	4.4 ± 0.4	4.0 ± 0.8
30	4.6 ± 0.8	4.5 ± 0.8
33	—	4.5 ± 1.3
35	4.0 ± 1.0	4.1 ± 1.2
38	3.5 ± 0.7	—
40	—	3.5 ± 0.4
45	—	3.0 ± 0.3
50	3.1 ± 0.9	2.9 ± 0.5
52	—	4.0 ± 1.2
55	3.4 ± 1.2	—
58	3.3 ± 1.0	3.1 ± 0.8

TABLE 5.10 Results of SEM Oxide Thickness Measurements
(a) EN8 Wear Tests carried out at $2.0\ ms^{-1}$.

EXPERIMENTAL LOAD (N)	OXIDE THICKNESS (μm) DISC	PIN
5	3.8 ± 0.5	—
10	—	3.6 ± 0.8
15	4.0 ± 0.5	3.6 ± 0.7
20	4.1 + 0.8	3.9 + 0.5
25	4.6 ± 0.7	3.8 ± 1.0
30	5.0 ± 0.9	5.2 ± 0.6
35	3.4 ± 0.9	2.8 ± 0.8
40	2.7 ± 0.9	—
45	3.6 ± 1.2	—
50	2.4 ± 1.2	2.6 ± 0.9
52	4.0 ± 0.9	3.2 ± 0.7
55	3.4 ± 0.7	—
58	2.9 ± 1.0	2.9 ± 1.0

TABLE 5.10 Results of SEM Oxide Thickness Measurements
(b) EN8 Wear Tests Carried Out at 4.0 ms^{-1}.

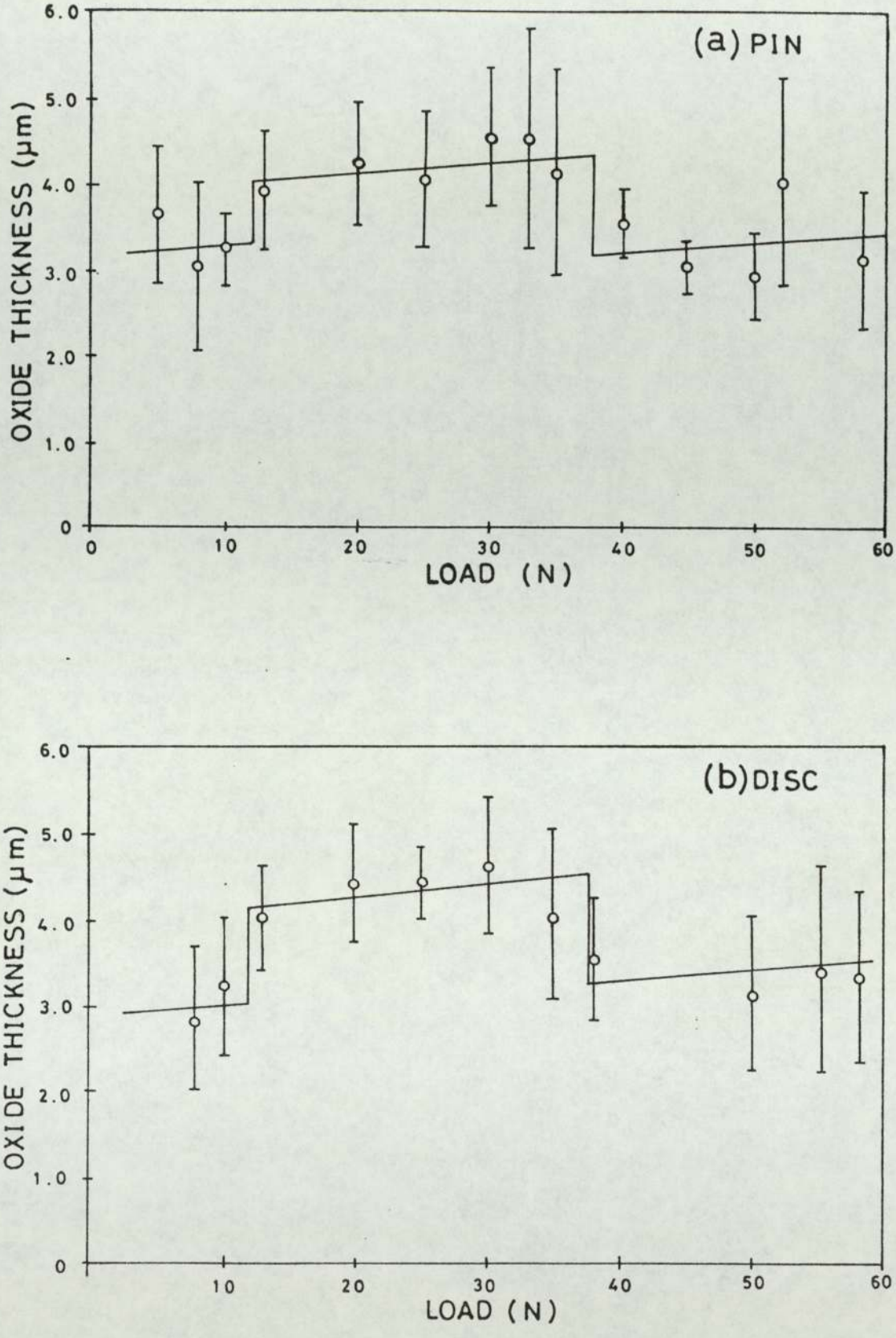

FIGURE 5.46 Variation in Oxide Thickness on Worn Surfaces with Applied Load for EN8 Wear Tests Conducted at 2.0ms^{-1}.

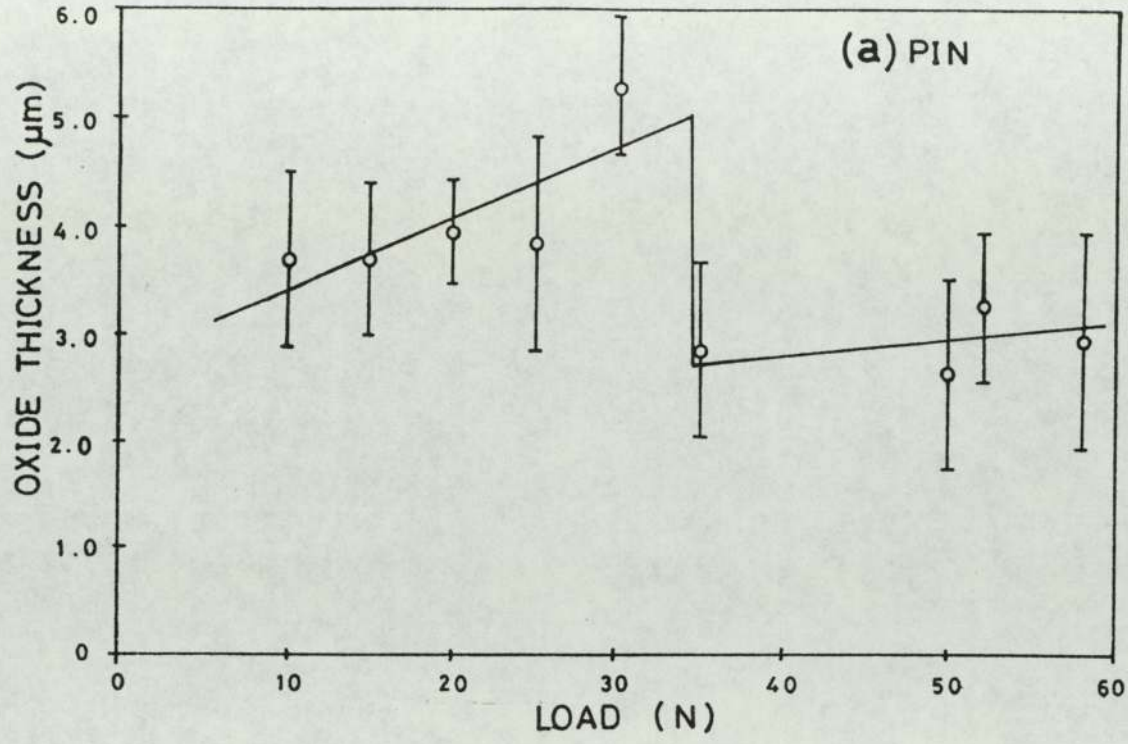

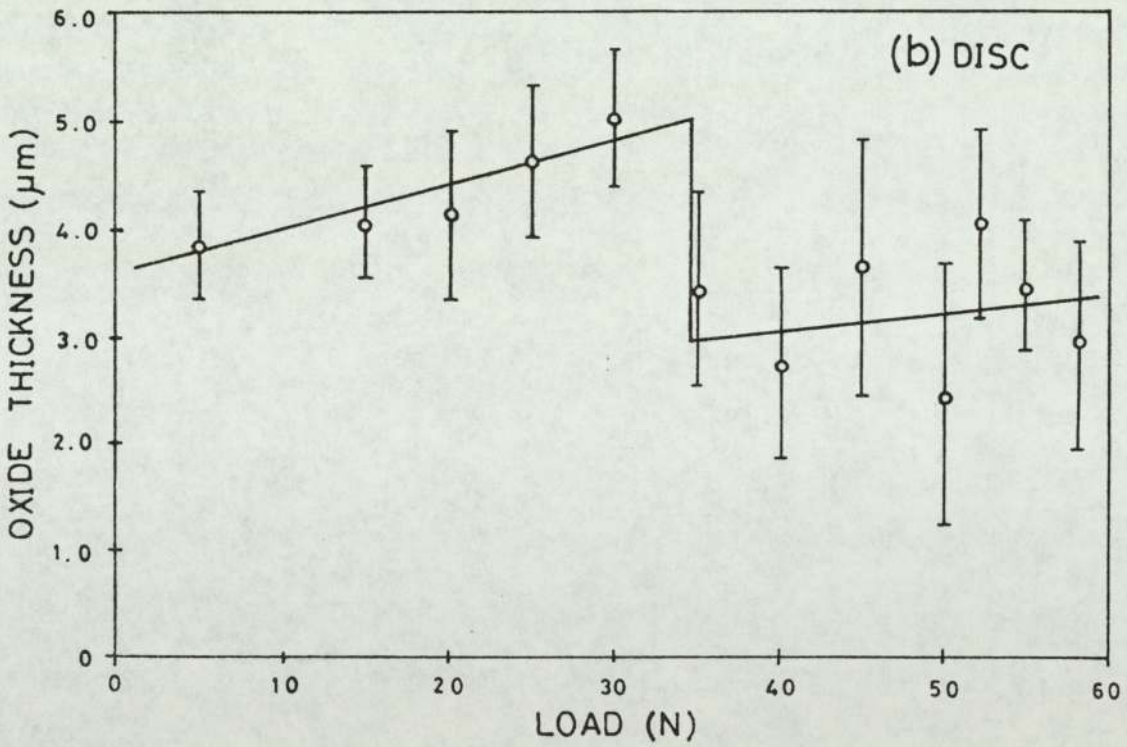

FIGURE 5.47 Variation in Oxide Thickness on Worn Surfaces with Applied Load for EN8 Wear Tests Conducted at 4.0ms^{-1}.

5.5.2 Analysis of Worn Surfaces from EN8 / 9% Cr Wear Tests

SEM was one of the techniques employed to confirm that the wear regime in the EN8 / 9% Cr wear tests was, in fact, mild, oxidational wear. The scanning electron micrographs of figures 5.48 and 5.49 show worn surfaces generated in these experiments. The general characteristics of the surfaces, with large, smooth plateaux observable in all cases indicated oxidational wear. This was confirmed by Auger electron spectroscopy in conjunction with argon ion depth profiling (section 5.4.2) which showed that the plateaux were, in fact, oxide.

5.5.3 Analysis of Low Alloy Steel Surfaces Oxidized under Static Conditions

Since a part of the aim of this project is to compare and contrast oxidation produced under static and tribological conditions in order that we may gain a better understanding of the mechanisms of tribological oxide growth, it was considered useful to analyse surfaces oxidized under static conditions by SEM.

Only a few of the statically oxidized surfaces were analysed. The micrographs in figure 5.50 show some interesting features. Both are of a low alloy steel surface oxidized at 600^{o}C for a period of six hours. Figure 5.50(a) shows the grain structure observable at the surface of the oxide, and gives a rough idea of the grain size. It would be interesting to compare this with the grain size of the tribologically

FIGURE 5.48 Scanning Electron Micrographs of Worn 9%Cr Disc Surfaces from EN8 9%Cr Wear Tests.

(a) 50 N

(b) 40 N

(c) 20 N

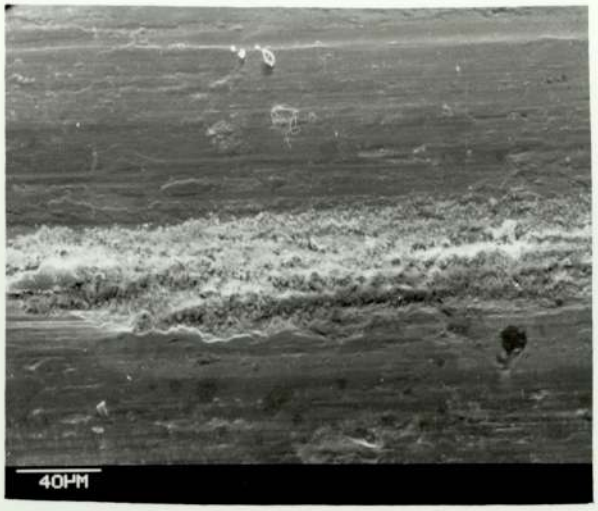

a

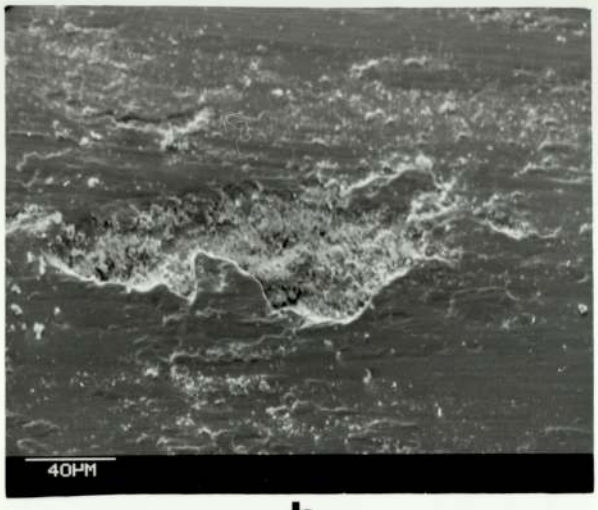

b

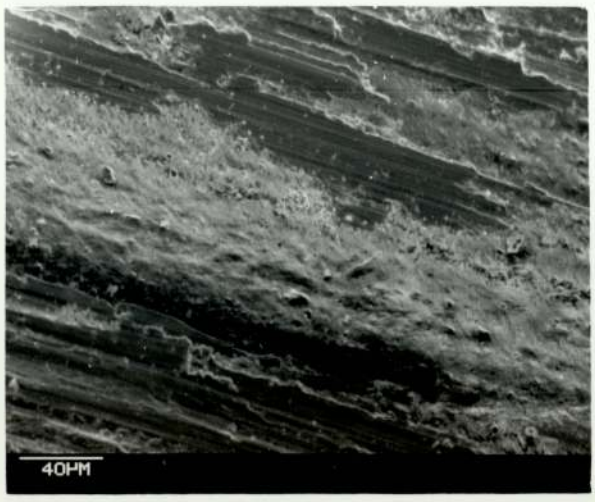

c

FIGURE 5.49 Scanning Electron Micrographs of Worn EN8 Pin Surfaces from EN8/9%Cr Wear Tests.

(a) 50 N

(b) 40 N

(c) 20 N

a

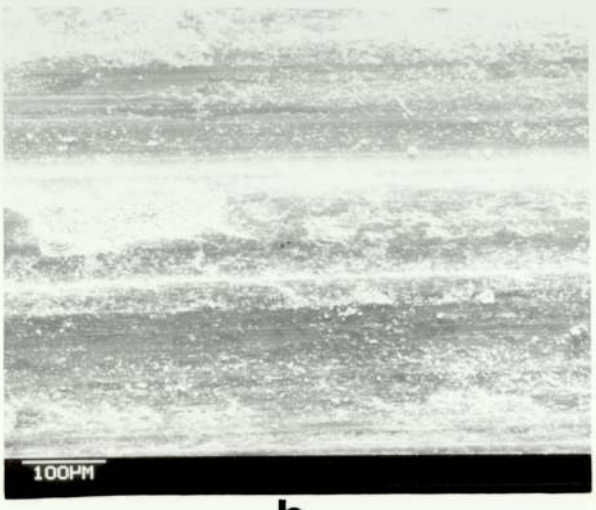

b

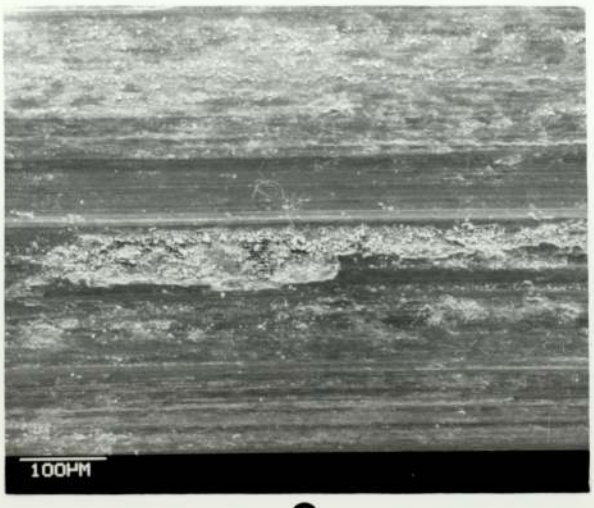

c

FIGURE 5.50 Scanning Electron Micrographs of Low Alloy Steel Surface Oxidized at 600°C for 6 Hours.

(a) magnification x5000
(b) magnification x100

a

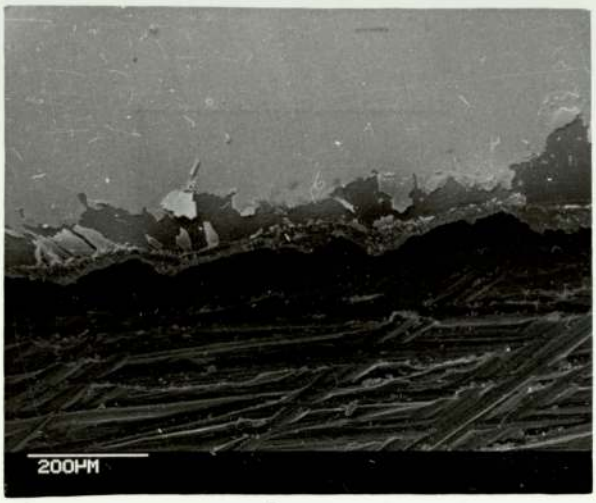

b

produced oxides, and this may be possible by detaching some of the oxide from the worn surface of a sample which has been stressed by the method described in section 3.6 (see micrograph of figure 5.43(e) for example of oxide which has become detached) and analysing it by the technique of transmission electron microscopy (TEM).

Figure 5.50(b) shows a part of the oxide which has been lifted slightly from the metallic substrate as a consequence of mechanically scraping away part of the oxide, this being the cause of the scars on the substrate. It can be seen that there is a layered structure to the oxide. Values for the electrical conductivity of iron oxides given in the literature vary somewhat (82), but it is likely that the oxide structure consists of a thin layer of α-Fe_2O_3 or Fe_3O_4 (Light charged) on top of a layer of FeO. This structure may have been present at the actual temperature of oxidation, for it is well known that oxide on iron usually forms a layered structure (17), or it may have arisen due to the oxidation of FeO on cooling.

CHAPTER 6

THEORETICAL CONSIDERATIONS

6.1 Introduction

The first part of this chapter is concerned with oxidation of worn surfaces produced during sliding wear conditions. Section 6.2. gives a brief outline of the oxidational theory of mild wear due to Quinn (83), while section 6.3 describes a method for calculating the activation energy and Arrhenius constant applicable to tribo-oxidation.

The second part of the chapter deals with quantitative Auger electron spectroscopy. Section 6.4.1 outlines the methods of obtaining quantitative information from Auger spectra, while sections 6.4.2 and 6.4.3 describe the corrections which should be made for the energy and matrix dependence of inelastic mean free path and backscattering factor respectively.

6.2 The Oxidational Theory of Mild Wear

The oxidational theory of mild wear was first proposed by Quinn (83) in order to explain the mild wear of unlubricated steel, and the theory will now be covered briefly.

The starting point of the theory is the Archard wear equation (84) given by:

$$\omega = K A \qquad (6.1)$$

where ω is the wear rate (measured in terms of volume removed per unit sliding distance), and A is the real area of contact between the sliding surfaces. The factor K is usually visualized as the probability of producing a wear particle per asperity encounter. Thus, 1/K asperity encounters are needed (at a given asperity contact), on the average, for a critical oxide film of thickness ξ to be built up before it becomes detached to form a wear particle. It was assumed that each encounter adds to the oxide thickness at a given asperity, so that the total time of contact, t_c, required to produce a wear particle of thickness ξ is given by:

$$t_c = \frac{\tau}{K} \qquad (6.2)$$

where τ is the duration of a single encounter. This latter quantity can be expressed in terms of the distance along which a wearing contact is made, d, and the speed of sliding, U, so that:

$$t_c = \frac{d}{UK} \qquad (6.3)$$

Quinn (83) assumed that the rate law describing the growth of oxide at the individual asperities was of a parabolic form, given by:

$$(\Delta m)^2 = k_p \cdot t_c \qquad (6.4)$$

where Δm is the mass per unit area of oxide, and k_p is the parabolic rate constant. This form of law is often used to describe the growth of thick oxide films produced under static oxidizing conditions, in which growth occurs by a diffusion mechanism (17). To a good approximation it can be assumed that:

$$\Delta m = f \rho \xi \qquad (6.5)$$

where ρ is density of the oxide on the worn surface and f is the mass fraction of the oxide which is oxygen. If we eliminate t_c in equation (6.4) and use the above expression for Δm, we have:

$$K = \frac{d k_p}{U \rho^2 \xi^2 f^2} \qquad (6.6)$$

The variation of the parabolic oxidation rate constant with oxidation temperature, T (in degrees K), is described by the Arrhenius equation (17):

$$k_p = A_p \exp(-Q_p / R T) \qquad (6.7)$$

where Q_p and A_p are the activation energy and Arrhenius constant for parabolic oxidation respectively, and R is the gas constant.

The oxidational wear theory assumes that the temperature responsible for the growth of oxide at the real areas of contact is the contact temperature, T_o. Thus, combining equations (6.6) and (6.7) and replacing T by T_o, we have:

$$K = \frac{d A_p \exp(-Q_p / R T_o)}{U \rho^2 \xi^2 f^2} \qquad (6.8)$$

Substituting this expression for K into equation (6.1), and assuming that the real area of contact is approximately given by W/P_m, in accordance with the plastic deformation hypothesis of Bowden and Tabor (49), we obtain a theoretical expression for the wear rate, namely:

$$\omega = \frac{2a W A_p \exp(-Q_p / R T_o)}{P_m U \rho^2 \xi^2 f^2} \qquad (6.9)$$

where d, the distance along which a wearing contact is

made, has been replaced by 2a, 'a' being the contact radius.

6.3 Activation Energy and Arrhenius Constant for the Mild Wear of Low Alloy Steel

Early applications of the oxidational theory to the mild wear of low alloy steels (83, 85) revealed discrepancies between the theoretical predictions of equation (6.9) and experimentally derived data. This has recently been shown by Sullivan et al (46) to be due to the incorrect assumption that the oxidational constants Q_p and A_p measured under static oxidation conditions could also be applied to oxidation under tribological conditions. They have shown that although the activation energies are likely to be similar for oxidation under static and sliding wear conditions, the Arrhenius constant, which depends upon the degree of disruption of the surface oxide, will be very different. Thus, the growth rate of an oxide at a given oxidation temperature will be different under static and tribological oxidizing conditions.

Values of Q_p for use in the oxidational wear theory have been calculated by Sullivan et al (46) from the results of a study of the oxidation of abraded iron by Caplan and Cohen (26). Careful plotting of the static oxidation rates versus the reciprocal of absolute temperature revealed three distinct regions, corresponding to three different oxide growth regimes. The results of x-ray diffraction analyses (31, 46, 69), including results presented in this thesis (section 5.2), show that these three distinct regions correspond to the predominant oxide being α-Fe_2O_3, Fe_3O_4 or

FeO. Sullivan et al (46) used the results from previous low alloy steel wear tests (59), together with the static oxidation Q_p values of Caplan and Cohen, to generate values of A_p for oxidation during sliding. Values of Q_p, and values of A_p for both static and sliding oxidizing conditions, resulting from the above calculations are given in tables 6.1(a) and 6.1(b), together with static (section 5.1) and sliding (section 6.3) values obtained in the present work.

Previous methods of obtaining Q_p and A_p for oxidation under sliding wear conditions have involved selecting a value of Q_p measured under static oxidizing conditions, and using this value of Q_p in the calculation of A_p (46 , 69). It is possible, however, to obtain a value for these two quantities from the results of wear tests, without assuming a statically derived Q_p value. This method, which will now be described, is based on simultaneous equations using equation (6.9).

First of all consider equation (6.9). This can be written:

$$s = \frac{\omega}{W} = \frac{2a A_p \exp(-Q_p / R T_o)}{P_m U f^2 \rho^2 \xi^2} \qquad (6.10)$$

where s is simply the slope of the wear rate versus load graph for a given sliding speed, U, and a particular surface oxide. In the present case s can be determined from the wear rate versus load graphs of figures 4.1(a) and 4.1(b), which were plotted for sliding speeds of $2.0\,ms^{-1}$ and $4.0\,ms^{-1}$ respectively. Consider the region in each of these graphs which corresponds to a particular surface oxide being predominant e.g. Fe_3O_4, and let the slopes of these graphs in this region be s_2 and s_4 for sliding speeds of $2.0\,ms^{-1}$ and $4.0\,ms^{-1}$

Q_P (kJ mol^{-1})

	OXIDE		
	α-Fe_2O_3	Fe_3O_4	Fe O
Static oxidation experiments (present work)	–	96	201
Static oxidation experiments (Caplan & Cohen[†])	208	96	210
tribologically derived values (present work)	–	74	–

TABLE 6.1 (a) Values of Activation Energy, Q_P, for Parabolic Oxidation.

A_P (kg^2 m^{-4} s^{-1})

	OXIDE		
	α-Fe_2O_3	Fe_3O_4	Fe O
Static oxidation experiments (present work)	–	3.7×10^{-3}	7.1×10^{3}
Static oxidation experiments (Caplan & Cohen[†])	1.5×10^{6}	3.2×10^{-2}	1.1×10^{5}
tribologically derived values (present work)	–	8.3×10^{3}	–
tribologically derived values (Sullivan et al[††])	10^{16}	10^{3}	10^{8}

TABLE 6.1 (b) Values of Arrhenius Constant, A_P, for Parabolic Oxidation.

† ref (26)

†† ref (46)

respectively. We can re-write equation (6.10) more specifically in order to represent sliding speeds of $2.0\,ms^{-1}$ and $4.0\,ms^{-1}$, thus:

$$s_2 = \frac{2a_2 A_p \exp(-Q_p / R T_2)}{P_{m2} U_2 f^2 \rho^2 \xi_2^2} : 2.0\,ms^{-1} \qquad (6.11a)$$

and

$$s_4 = \frac{2a_4 A_p \exp(-Q_p / R T_4)}{P_{m4} U_4 f^2 \rho^2 \xi_4^2} : 4.0\,ms^{-1} \qquad (6.11b)$$

The quantities Q_p, A_p, f and ρ will be the same in both of the above equations if the chemical composition of the oxide formed on the worn surfaces is similar in both cases. The hardness of the substrate metal, P_m, varies with temperature and so we would expect P_{m2} to be different from P_{m4}. However, it was shown in chapter 4 that P_m does not vary much over the range of general surface temperatures produced in the present wear tests, so that to a good approximation P_m can be assumed to be constant. Dividing equation (6.11a) by equation (6.11b) and cancelling like terms we have:

$$\frac{s_2}{s_4} = \frac{a_2 U_4 \xi_4^2}{a_4 U_2 \xi_2^2} \exp\left\{ \frac{-Q_p}{R} \left(\frac{1}{T_2} - \frac{1}{T_4} \right) \right\} \qquad (6.12)$$

Rearranging equation (6.12) we get an expression for the activation energy for parabolic oxidation, Q_p, namely:

$$Q_p = R \frac{T_2 T_4}{T_2 - T_4} \ln \left\{ \frac{s_2 a_4 U_2 \xi_2^2}{s_4 a_2 U_4 \xi_4^2} \right\} \qquad (6.13)$$

Theoretically, we could obtain a value of Q_p for all three iron oxides from this latter equation, simply by selecting the results from two wear tests, one run at $2.0\,ms^{-1}$ and the other at $4.0\,ms^{-1}$, in which the particular oxide of interest

was the predominant oxide on the worn surfaces. A set of Q_p values would then be obtained for each particular oxide, corresponding to different pairs of experimental results, and an average value could be obtained. In the present work, however, this has only been performed for the oxide Fe_3O_4. In the case of α-Fe_2O_3, the calculation of Q_p could not be carried out since a region for which α-Fe_2O_3 was the predominant oxide did not exist for the 4.0 ms^{-1} experiments, Fe_3O_4 being the main oxide at low loads due to the relatively high speed. For the FeO regions in figures 4.1 and 4.8, representing the variation of wear rate and contact temperature with load respectively, it can be seen that there is a relatively high scatter of points. This high degree of scatter leads to a large uncertainty in the slopes, s_2 and s_4, of the wear rate versus load graphs, and this is probably partly due to the lower loads in the FeO region being fairly close to the boundary between the Fe_3O_4 / FeO oxide regions. Due to this high degree of scatter and to the fact that the FeO region spans a relatively small range of loads in the present wear tests, it was decided that determination of Q_p for FeO from the present data was not really feasible.

As an example of the calculation performed for the determination of Q_p corresponding to a predominantly Fe_3O_4 surface oxide, consider the experiments run at 13 N, 2.0 ms^{-1} and 30 N, 4.0 ms^{-1}. We have:

13 N, 2.0 ms^{-1}	30 N, 4.0 ms^{-1}
$s_2 = 2.00 \times 10^{-14}\ m^3 m^{-1} N^{-1}$	$s_4 = 1.33 \times 10^{-14}\ m^3 m^{-1} N^{-1}$
$U_2 = 2.0\ ms^{-1}$	$U_4 = 4.0\ ms^{-1}$
$a_2 = 6.16 \mu m$	$a_4 = 3.12 \mu m$
$\xi_2 = 3.9 \mu m$	$\xi_4 = 5.2 \mu m$
$T_2 = 700\ K$	$T_4 = 829\ K$

and $R = 8.314 \times 10^{-3}\ kJ\ mol^{-1} K^{-1}$

Using equation (6.13) we have:

$$\ln \left\{ \frac{s_2 a_4 U_2 \xi_2^2}{s_4 a_2 U_4 \xi_4^2} \right\} = -1.541$$

and

$$\frac{T_2 T_4}{T_2 - T_4} = -4498.4\ K$$

so that

$$Q_p = 57.7\ kJ\ mol^{-1}$$

The values used for ξ_2 and ξ_4 were the pin oxide thicknesses, ξ_p, in both cases since s_2 and s_4 are the slopes of the wear rate versus load graphs for the pin. Where ξ_p had not been measured ξ_D was used. The value of Q_p calculated above was then substituted into equation (6.11a) (or alternatively equation (6.11b) could have been used) to yield a value for A_p of $5.7\ kg^2\ m^{-4}\ s^{-1}$. The values of Q_p and A_p for Fe_3O_4 calculated by this method, using various pairs of experimental results, are shown in table 6.2.

The variation in activation energy values is reasonable when we consider the errors involved in the calculations. The largest source of error in calculating Q_p from equation

EXPERIMENTAL PAIR	Q_P ($kJ\ mol^{-1}$)	A_P ($kg^2 m^{-4} s^{-1}$)
30N, $4.0 ms^{-1}$ / 13N, $2.0 ms^{-1}$	57.7	5.7
30N, $4.0 ms^{-1}$ / 20N, $2.0 ms^{-1}$	73.2	5.4×10^1
30N, $4.0 ms^{-1}$ / 25N, $2.0 ms^{-1}$	65.6	1.8×10^1
25N, $4.0 ms^{-1}$ / 13N, $2.0 ms^{-1}$	52.4	2.3
25N, $4.0 ms^{-1}$ / 20N, $2.0 ms^{-1}$	80.8	1.9×10^2
20N, $4.0 ms^{-1}$ / 13N, $2.0 ms^{-1}$	57.6	5.6
30N, $4.0 ms^{-1}$ / 30N, $2.0 ms^{-1}$	122.9	7.3×10^4
25N, $4.0 ms^{-1}$ / 25N, $2.0 ms^{-1}$	64.9	1.6×10^1
20N, $4.0 ms^{-1}$ / 20N, $2.0 ms^{-1}$	90.9	9.9×10^2
AVERAGE VALUE	74.0	8.3×10^3
STANDARD DEVIATION	22.0	2.4×10^4

TABLE 6.2 Activation Energy and Arrhenius Constant Calculated from Equations (6.13) and (6.11a).

(6.13) is the difference in contact temperatures in the denominator of the equation. For the example calculation given earlier, an uncertainty of ±10 K in each of the contact temperatures T_2 and T_4 results in a percentage error of 18.1% for the $T_2T_4 / (T_2-T_4)$ term in equation (6.13), and this increases to 36.2% for a temperature uncertainty of ±20 K. For this reason experimental pairs for which T_2 was very close to T_4 were not used in the calculations of Q_p. Looking at table 6.2 it can be seen that there is a much greater variation in the values of A_p, and this is due to the fact that moderate variations in Q_p result in much larger variations in the exponential term and hence in A_p.

6.4 Quantitative Auger Electron Spectroscopy

6.4.1 Methods of Quantification

The current of Auger electrons, I_i, of kinetic energy E_i, from an element i homogeneously distributed in a matrix j, may be expressed as:

$$I_i = I_o \sigma_i(U_i) \psi_i \{1 + r_j(U_i)\} T(E_i) D(E_i) N_i \lambda_j(E_i) \cos\Theta \quad (6.14)$$

where:

I_o = primary electron beam current

U_i = reduced energy, E_p/E_c, where E_c is the ionization energy of the initial core level electron of an atom of i involved in the Auger process, and E_p is primary electron energy

$\sigma_i(U_i)$ = ionization cross section of initial core level electron

ψ_i = Auger transition probability factor

$r_j(U_i)$ = ratio of Auger electrons produced by the back-scattered flux of electrons to those produced by the primary electrons directly

$T(E_i)$ = analyser transmission efficiency

$D(E_i)$ = electron detector efficiency

N_i = atomic density of element i

$\lambda_j(E_i)$ = inelastic mean free path of Auger electrons of element i in matrix j

θ = angle of emission of Auger electrons with respect to the local normal at the sample surface.

It should be possible to determine N_i from equation (6.14) by determination of all of the other factors in the equation. In practice, however, this is very difficult since many of the factors are not known, or cannot be measured, to the required degree of accuracy. For this reason, quantitative Auger analysis from first principles is not considered practical at the present time.

The most accurate method of quantitative Auger analysis involves the use of external standards. In this method, Auger spectra from the specimen of interest are compared with those from a standard having a known concentration of the element of interest. Usually the standard is a pure element. By comparison of the Auger spectra of element i, which is present in a matrix j, with the Auger spectra from a pure elemental standard of i, we have from equation (6.14):

$$\frac{I_i}{I_i^\circ} = \frac{\{1 + r_j(U_i)\}\ \lambda_j(E_i)}{\{1 + r_i^\circ(U_i)\}\ \lambda_i^\circ(E_i)} \cdot \frac{N_i}{N_i^\circ} \qquad (6.15)$$

where the superscript $\circ$ denotes a pure element. It is

frequently assumed in Auger analysis that:

$$\lambda_j(E_i) \simeq \lambda_i^{\circ}(E_i) \quad \text{and} \quad r_j(U_i) \simeq r_i^{\circ}(U_i)$$

but this is almost certainly incorrect in most cases, and for accurate quantitative analysis the variation of inelastic mean free path, λ, and backscattering factor, r, with matrix should be taken into account. An advantage of this method is that it is not necessary to know the factors σ, Ψ, T, D and $\cos\theta$ as they cancel out in equation (6.15). Since Auger current is reduced to a relative measurement I_i may be taken as any parameter of the Auger electron signal which is proportional to its intensity. It is now customary to use the peak to peak height in the differential Auger spectrum for this purpose (64). If the spectrometer operating conditions are not identical for the two measurements, then corrections for this fact must also be added.

To eliminate the process of having to compare directly with an elemental standard every time an analysis is performed, a less accurate method of quantitative analysis based on the use of elemental sensitivity factors can be employed. This was the method used to obtain the quantitative AES results presented in this thesis. This method will now be considered fully.

The proportion of an element i in a matrix j may be written:

$$X_i = \frac{I_i/I_i^{\circ}}{\sum_j I_j/I_j^{\circ}} \qquad (6.16)$$

We can define the Auger sensitivity of element i, α_i, relative to that of silver by the equation:

$$\alpha_i I_i^\circ = I_s^\circ \qquad (6.17)$$

where I_i° and I_s° are the Auger signals, generated under identical experimental conditions, from pure samples of the element i and silver respectively. Then from equation (6.16) and (6.17) we have:

$$X_i = \frac{\alpha_i I_i}{\sum_j \alpha_j I_j} \qquad (6.18)$$

where from equations (6.14) and (6.17) it follows that:

$$\alpha_i = \frac{\sigma_s(U_s)\,\psi_s\left\{1 + r_s^\circ(U_s)\right\}\,T(E_s)\,D(E_s)\,N_s^\circ\,\lambda_s^\circ(E_s)}{\sigma_i(U_i)\,\psi_i\left\{1 + r_i^\circ(U_i)\right\}\,T(E_i)\,D(E_i)\,N_i^\circ\,\lambda_i^\circ(E_i)} \qquad (6.19)$$

First consider the case where the sensitivity factors have been measured on the same instrument that is used for the analysis. By substituting equations (6.14) and (6.19) in equation (6.18) and cancelling like terms, we have:

$$X_i = \frac{\left[\left\{1 + r_j(U_i)\right\}\,\lambda_j(E_i) \Big/ \left\{1 + r_i^\circ(U_i)\right\}\,\lambda_i^\circ(E_i)\right]\frac{N_i}{N_i^\circ}}{\sum_j \left[\left\{1 + r_j(U_j)\right\}\,\lambda_j(E_j) \Big/ \left\{1 + r_j^\circ(U_j)\right\}\,\lambda_j^\circ(E_j)\right]\frac{N_j}{N_j^\circ}} \qquad (6.20)$$

Thus a correction factor, γ_i, given by:

$$\gamma_i = \frac{\left\{1 + r_i^\circ(U_i)\right\}\,\lambda_i^\circ(E_i)}{\left\{1 + r_j(U_i)\right\}\,\lambda_j(E_i)} \qquad (6.21)$$

should be applied for accurate quantitative analysis, so that:

$$X_i = \frac{\gamma_i\,\alpha_i\,I_i}{\sum_j \gamma_j\,\alpha_j\,I_j} \qquad (6.22)$$

Again, γ_i is usually assumed to be equal to unity, neglecting

the matrix dependence of λ and r. Electron inelastic mean free paths have been calculated for the iron oxide surfaces which are the subject of Auger analysis in the present study, and these are presented later in this chapter.

If the sensitivity factors were measured on a different instrument to that used for the analysis then the situation is more complex since the instrumental terms $T(E_i)$ and $D(E_i)$, which will usually be different for the two spectrometers, must also be taken into consideration. This situation corresponds to the method used for quantitative Auger analysis in the present project: analysis was performed on a Kratos XSAM 800 Spectrometer at theUniversity of Aston, while sensitivity factors were obtained from the Handbook of Auger Electron Spectroscopy (80), a PHI spectrometer having been employed for their measurement. If we denote the sensitivity of element i on the spectrometer used for the analysis as α_{iA}(University of Aston, XSAM 800 spectrometer), and the sensitivity of the same element on the spectrometer used to produce the data bank of sensitivity factors as α_{iH} (Handbook of Auger Electron Spectroscopy, PHI spectrometer) then from equation (6.19), after cancelling like terms, we have:

$$\frac{\alpha_{iA}}{\alpha_{iH}} = \frac{T_A(E_s)\, D_A(E_s)\, T_H(E_i)\, D_H(E_i)}{T_A(E_i)\, D_A(E_i)\, T_H(E_s)\, D_H(E_s)} \qquad (6.23)$$

Now for Auger analysis on the Aston spectrometer equation (6.22) should be written:

$$X_i = \frac{\gamma_i\, \alpha_{iA} I_i}{\sum_j \gamma_j\, \alpha_{jA} I_j} \qquad (6.24)$$

From equations (6.23) and (6.24) above we have:

$$X_i = \frac{\beta_i \gamma_i \alpha_{iH} I_i}{\sum_j \beta_j \gamma_j \alpha_{jH} I_j} \qquad (6.25)$$

where the correction factor, β_i, is given by:

$$\beta_i = \frac{T_H(E_i) D_H(E_i)}{T_A(E_i) D_A(E_i)} \qquad (6.26)$$

Thus we really need to know the transmission function and detector efficiency for both the XSAM 800 spectrometer used for the analysis and the PHI spectrometer used in the measurement of sensitivity factors, in order to estimate how great an effect the β term has on the quantitative Auger results presented in this thesis. However, β_i correction factors could not be determined in the present work as explained in section (6.2.4).

The correction factors which have arisen in deriving the equations which form the basis of quantitative Auger electron spectroscopy will now be covered more fully in the following sections.

6.4.2 Inelastic Mean Free Path (λ)

Only a small proportion of the Auger electrons produced in a sample surface will reach the external electron energy analyser without being scattered, either elastically or inelastically. Elastic scattering need not usually be considered as in general as many electrons will be scattered elastically into a particular emergent direction as will be scattered out of it (86), and so the problem reduces to

that of inelastic scattering. Furthermore, since the average loss of energy associated with each inelastic scattering event ($\sim$15 eV) is usually much greater than the Auger peak width of 1 to 10 eV, a single scattering event is sufficient to remove a given Auger electron from the measured peak (87). Auger electrons which have been inelastically scattered contribute to the background on the low kinetic energy side of the Auger peak.

A quantity which gives a measure of the degree of inelastic scattering of electrons in solids is the inelastic mean free path (IMFP), $\lambda(E)$. It is defined as the path length for which an electron with energy E has a probability equal to 1-1/e of being scattered inelastically (87). The probability that a measured Auger electron came from a depth x in the surface is then given by the simple expression $\exp(-x/\lambda(E))$.

Various methods have been used to determine $\lambda(E)$ experimentally and a review is given by Powell (86).

Certain general points can be made from the numerous experimental determinations and empirical expressions about the variation of IMFP with electron energy and material. Firstly, the value of $\lambda(E)$ is relatively high at low electron energies, falls to a minimum around 50-100 eV, and then rises gradually again with further increase in energy. Secondly, $\lambda(E)$ is not too strongly dependent upon matrix and a 'universal curve' can be used to give an approximate representation of the variation of $\lambda(E)$ with electron energy for all materials.

Expressions for $\lambda(E)$ as a function of energy and matrix have been given by various workers, those due to Penn (88), Powell (86), and Seah and Dench (79) being well-known examples.

Seah and Dench (79) have compiled all published measurements of electron IMFP's in solids for energies in the 0-10 keV range, numbering nearly 350 in total. The data were not critically evaluated or weighted and no account was taken of estimates of error. A statistical analysis of the data resulted in an empirical expression for the IMFP of an electron of energy E_i in an element i, which is:

$$\lambda_i^{\circ}(E_i) = \frac{538}{E_i^2} + 0.41(m_i E_i)^{1/2} \quad \text{monolayers} \qquad (6.27)$$

where the monolayer thickness, m_i (nanometres), is given by:

$$m_i^3 = \frac{A_i}{\rho_i N} \times 10^{24} \qquad (6.28)$$

where:

A_i = atomic weight of element i

ρ_i = bulk density of element i ($kg\ m^{-3}$)

N = Avogadro's number

Equation (6.27) gives a value for $\lambda_i^{\circ}(E_i)$ in monolayers, and although an equation for λ in nanometres is also given by Seah and Dench (79), they point out that equation (6.27) above gives least scatter of the compiled experimental points about the empirical curve.

A similar expression is given for inorganic compounds. The IMFP of an electron from element i in an inorganic compound

matrix j is given by:

$$\lambda_j(E_i) = \frac{2170}{E_i^2} + 0.72(m_j E_i)^{1/2} \qquad (6.29)$$

where the monolayer thickness, m_j (nanometres), is given in this case by:

$$m_j^3 = \frac{A_j}{\rho_j N n} \qquad (6.30)$$

where A_j and ρ_j now represent the molecular weight and density of the compound j, and the term n represents the number of atoms in a molecule of j.

In the case of organic compounds the experimental data is more scarce and scatter of points is greater, but the lowest r.m.s. scatter factor occurs for the equation:

$$\lambda_j(E_i) = \frac{49}{E_i^2} + 0.11E_i^{1/2} \text{ mg m}^{-2} \qquad (6.31)$$

In this case $\lambda_j(E_i)$ is expressed in terms of mg m^{-2}, and not monolayers, as a meaningful value of m_j cannot be defined.

At low electron energies the first term in equations (6.27), (6.29) and (6.31) dominates and we observe an E^{-2} dependence. Above approximately 75 eV the second term becomes dominant and an $E^{1/2}$ law is obeyed. The matrix dependency of λ is provided for by the 'm' factors in equations (6.27) and (6.29).

Of the expressions given in the literature for calculating electron IMFP's in solids those of Seah and Dench (79) provide the smallest r.m.s. scatter of data points about their empirical curves, their equations are applicable over a large energy range, and all classes of solids are repres-

ented. For these reasons they probably represent the most accurate procedure for determining IMFP's in solids at the present time, and as such were used in determining the matrix correction factors involved in the quantitative Auger analysis in this thesis.

The IMFP's of principal Auger electrons in the matrices of interest in the present study have been calculated from equations (6.27) to (6.31) due to Seah and Dench (79), and the results are summarised in table 6.3. Atomic and molecular weights, and densities were obtained from Kaye and Laby (89), while energies of the principal Auger electrons of interest (E_i) and elemental sensitivity factors (α_{iH}) were taken from "The Handbook of Auger Electron Spectroscopy" (80). In fact, the inverse of the data bank elemental sensitivity factor values were used to represent α_{iH} in equation (6.25) since the present definition of α_i, given by equation (6.17), is the inverse of the definition in reference (80). In the case of the correction factor for the OKL_2L_3 Auger electron we are correcting for the fact that the IMFP of the electron in iron oxide differs from that in an elemental matrix of oxygen i.e. solid oxygen. Thus the density of oxygen was taken as 1460 kg m^{-3}, its value at -252.7°C (89).

Figure 6.1 shows the variation of IMFP with electron energy in FeO and Fe metal, plotted using equations (6.27) and (6.29) due to Seah and Dench (79). The curves for the three oxides of iron are virtually identical and so the plotted curve for FeO can also be taken as representative of Fe_3O_4 and α-Fe_2O_3. Also present on the figure are

MATRIX	AUGER ELECTRON C KL_2L_3 272eV	O KL_2L_3 503eV	Fe $L_3M_{4,5}M_{4,5}$ 703eV	Cr $L_3M_{2,3}M_{4,5}$ 529eV
C	3.08 (1.44)*			
O		4.72		
Fe			5.19	
Cr				4.52
Fe_2O_3		7.52	8.88	7.71
Fe_3O_4		7.58	8.95	7.77
FeO		7.56	8.93	7.75
Cr_2O_3		7.47	8.82	7.65
organic compound	(1.99)*			

TABLE 6.3 Inelastic Mean Free Path Values in Monolayers, Calculated from Seah and Dench Equations (79).

* bracketted values are expressed in mg m^{-2}.

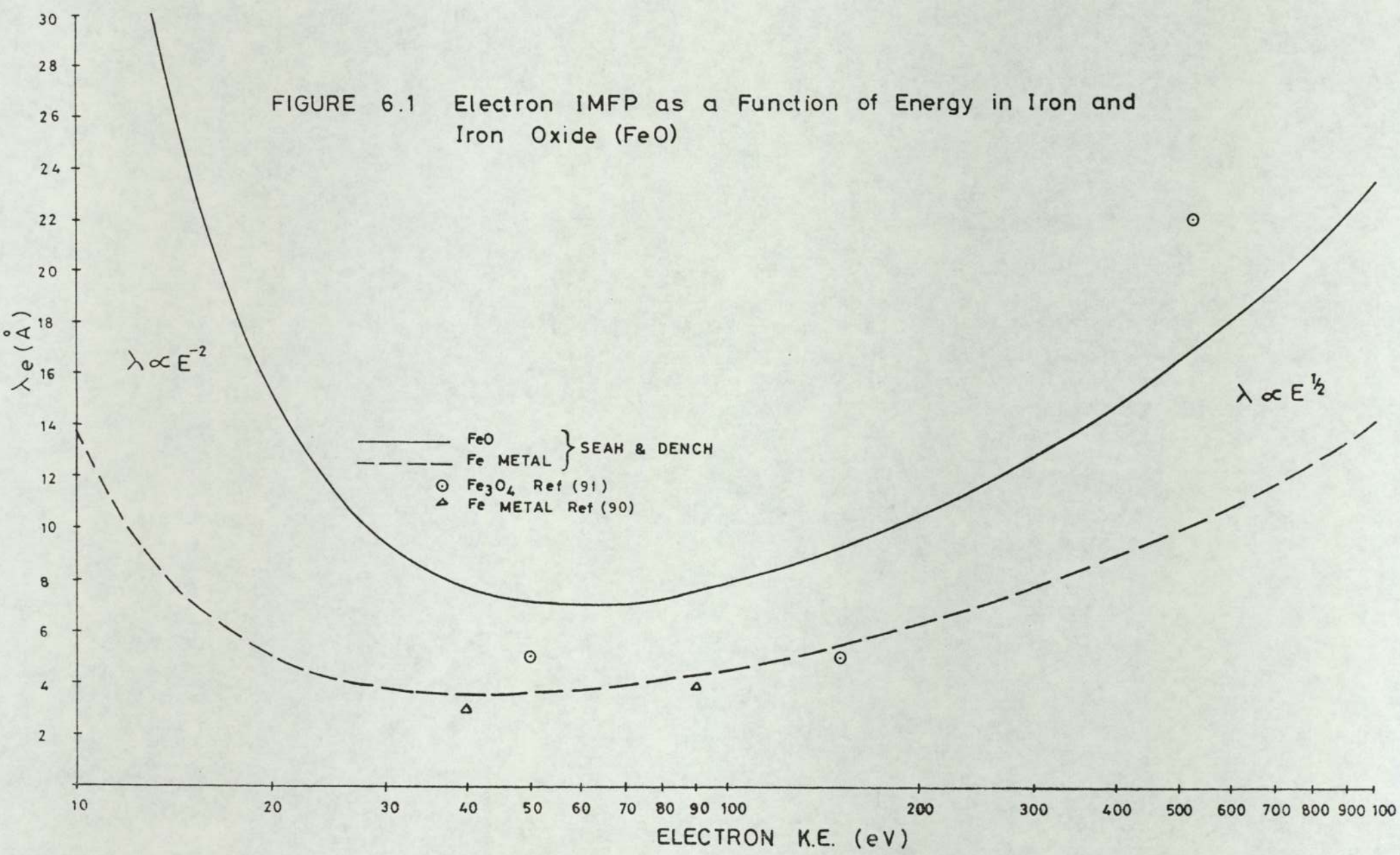

FIGURE 6.1 Electron IMFP as a Function of Energy in Iron and Iron Oxide (FeO)

experimentally determined values of IMFP's for Fe and Fe_3O_4, all determined by the overlayer technique (90 , 91).

A typical example will now be given which demonstrates the effect of the matrix dependence of $\lambda(E)$ on the quantitative AES results in the present work. The peak to peak heights in the differentiated Auger spectrum of a worn EN8 surface generated at 2.0 ms^{-1} and 25 N, plotted after 30 minutes of argon ion etching, are shown below together with the relevant elemental Auger sensitivity (80):

element	p:p height (mm)	elemental sensitivity factor, α_{iH}
carbon	6.0	7.14
oxygen	75.0	2.50
iron	45.0	4.55

The value of the demominator in equation (6.25), neglecting the correction factors γ_j and β_j, is given by:

$$\sum_j \alpha_{jH} I_j = (7.14 \times 6.0) + (2.50 \times 75.0) + (4.55 \times 45.0)$$
$$= 435.1 \text{ mm}$$

Again neglecting the correction factors γ_i and β_i in equation (6.25), we have for the atomic fraction, X, and corresponding elemental concentration, C:

$X_C = (7.14 \times 6.0) / 435.1 = 0.098 : C_C = 9.8\%$

$X_O = (2.50 \times 75.0) / 435.1 = 0.431 : C_O = 43.1\%$

$X_{Fe} = (4.55 \times 45.0) / 435.1 = 0.471 : C_{Fe} = 47.1\%$

where the subscripts denote the chemical symbol of the element concerned.

Now we can calculate the corresponding concentrations which result by applying corrections for the matrix dependence of $\lambda(E_i)$ (but neglecting all other corrections). The value of the denominator in equation (6.25) is now given by:

$$\sum_j \frac{\lambda_j^\circ(E_j)}{\lambda_j(E_j)} \alpha_{jH} I_j = \left(\frac{1.44}{1.99} \times 7.14 \times 6.0\right) + \left(\frac{4.72}{7.56} \times 2.50 \times 75.0\right) + \left(\frac{5.19}{8.93} \times 4.55 \times 45.0\right) = 267.1 \text{ mm}$$

Thus from equation (6.25) we have for the atomic fraction, X, and concentration, C:

$$X = \left\{\frac{\lambda_i^\circ(E_i)}{\lambda_j(E_i)} \alpha_{iH} I_i\right\} \Big/ 267.1$$

so that:

$$X_C = \left\{\frac{1.44}{1.99} \times 7.14 \times 6.0\right\} \Big/ 267.1 = 0.116 : C_C = 11.6\%$$

$$X_O = \left\{\frac{4.72}{7.56} \times 2.50 \times 75.0\right\} \Big/ 267.1 = 0.438 : C_O = 43.8\%$$

$$X_{Fe} = \left\{\frac{5.19}{8.93} \times 4.55 \times 45.0\right\} \Big/ 267.1 = 0.446 : C_{Fe} = 44.6\%$$

IMFP values used in this calculation were taken from table 6.3. The correction factors employed in these calculations correct for the fact that the O KL_2L_3 and Fe $L_3M_{4,5}M_{4,5}$ Auger electrons were travelling through an oxide matrix, in which their IMFP's differ from those in elemental O and Fe respectively. This is a slightly simplified picture since a layer of hydrocarbon contamination was present on the surface of the oxide, so that an Auger electron generated in the oxide had to pass through the hydrocarbon layer before it left the sample surface. However, in the present case the thickness of the contaminant layer was small compared with

the IMFP of the O KL_2L_3 and Fe $L_3M_{4,5}M_{4,5}$ Auger electrons in a hydrocarbon matrix, and so the correction for the effect of this layer on the IMFP of these two Auger electrons will be very small and can be neglected.

The C KL_2L_3 Auger electron was generated in the hydrocarbon surface film, and so the $\lambda_i^{\circ}(E_i)/\lambda_j(E_i)$ term for the carbon Auger signal corrects for the fact that the IMFP of the C KL_2L_3 Auger electron in elemental carbon is different from that in a hydrocarbon compound. Since the correction factor consists of a ratio of λ values, both $\lambda_i(E_i)$ and $\lambda_j(E_i)$ were represented by values expressed in mg m^{-2} for the case of the C KL_2L_3 electron. It was not necessary to know the exact chemical composition of the surface hydrocarbon in order to calculate a value for the term $\lambda_j(E_i)$, since the empirical relation given by equation (6.31) due to Seah and Dench (79) is based on limited data, and gives $\lambda_j(E_i)$ as a function of E_i for all organic compounds.

In the case of the worn 9% Cr steel disc surfaces generated in the EN8 / 9% Cr wear tests (section 4.2.2) chromium ions were also present in the iron oxide. However, due to the very similar atomic weights and densities of Fe and Cr the IMFP's of Auger electrons of any given energy in iron oxide and chromium oxide are almost identical (see table 6.3), and so no correction for the presence of chromium in the iron oxide need be made.

The effect which correcting for the matrix dependence of the IMFP of Auger electrons has on the quantitative Auger results in the present work is illustrated by the previously

given example, and this example is fairly typical. The corrections have a relatively small effect on the concentrations of the elements detected on the worn surfaces, the concentration of iron being reduced slightly, while that of carbon increases slightly. The ratio of O:Fe was always around 50:50, which is the ratio we would expect for FeO.

6.4.3 Backscattering Factor (r)

A primary electron beam which is incident on a surface produces Auger electrons not only by direct impact of the primary electrons, but also as a result of some of the primary electrons being backscattered by the solid back into the surface layers. The backscattering factor, r, accounts for the effect of these backscattered electrons on the Auger electron yield.

Experimental investigations of electron backscattering in elements and alloys have been performed by various workers, and these are summarised in a review by Jablonski (92). No information was found in the literature concerning the experimental measurement of backscattering factors in oxides, and so the quantitative Auger results presented in this thesis are uncorrected for the matrix dependence of r. According to Hofmann (93), however, the electron backscattering in AES is only a second order effect compared to the IMFP, except in extreme cases, so that neglect of r in equation (6.25) on the calculated elemental concentrations will probably be small.

6.4.4 Instrumental and Ion Beam Effects

Application of the instrumental correction factor, β_i, defined by equation (6.26), to the calculated elemental concentrations was not possible since determination of the factors $T(E_i)$ and $D(E_i)$ for the XSAM 800 spectrometer was beyond the scope of the present project. For an HSA (XSAM 800 spectrometer) or a CMA (PHI spectrometer) operated in the FRR mode, $T(E_i)$ is simply proportional to E_i (94). $D(E_i)$ will also vary with E_i for an electron energy analyser operated in the FRR mode, but the form of this variation is generally unknown (94).

In addition to the above mentioned factors, changes in the relative concentrations of iron and oxygen in the surface layers of the oxide will also probably occur as a result of the Ar^+ ion etching process (93).

CHAPTER 7

DISCUSSION

In this chapter all of the experimental results obtained in the present study are discussed, and a model based on the evidence of these results is proposed for the mild wear of low alloy steel. This model is then discussed in relation to other past and current models of mild wear.

In all of the EN8, pin on disc wear tests (section 4.2.1) the resulting wear of the steel surfaces was mild. Abrupt changes were found to occur in the magnitude of the wear rate at certain loads, while wear rate was found to be directly proportional to applied load, consistent with the Archard wear law (32), for the load regions between these abrupt transitions. This was true for both the 2.0 ms^{-1} wear tests and for those conducted at 4.0 ms^{-1} (figures 4.1(a) and 4.1(b) respectively). This pattern of wear behaviour has been observed in previous work (31 , 46 , 69). Sullivan and Athwal (31), using an experimental wear test rig very similar to that used in the present work, reported transitions in the mild wear characteristics of EN31 steel at various temperatures. These workers have attributed the abrupt changes in wear rate to a change in the chemical composition of the oxide on the worn surfaces, this conclusion being based largely on the findings of x-ray diffraction of the surface oxides and debris. The predominant oxide which is present on a worn steel surface will depend upon the temperature at which oxidation occurs: for temperatures less than about 200°C it is α-Fe_2O_3, between 200°C and 570°C it is Fe_3O_4, and for temperatures above 570°C it is FeO (95). If there is an

increase in load such that the corresponding change in oxidation temperature results in a different oxide on the worn surfaces, then an abrupt change in wear rate occurs. These workers have also shown that the temperature responsible for the growth of wear protective oxides (with no external heating) is the "hot-spot" temperature produced at the contacting asperities between the two surfaces, and it will be seen later that the same conclusion has to be drawn from the present work.

The explanation of the observed transitions in the wear rate of low alloy steel in terms of the chemical composition of the oxide present on the worn surfaces is supported by the findings of x-ray diffraction analysis of surface oxides (section 5.2.2) and debris (section 5.2.1) in the present work. In the case of the 2.0 ms^{-1} wear tests we can compare table 5.7(a), summarising the debris XRD results, with figure 4.1(a), showing the variation of wear rate with applied load. It can be seen that the transition at a load of approxiamtely 12 N coincides with the first appearance of Fe_3O_4 in the oxide, while the higher transition around 35 N coincides with the first appearance of FeO. For the wear tests run at 4.0 ms^{-1} comparison of table 5.7(b) with figure 4.1(b) reveals that the transition in wear rate at a load of around 35 N coincides with the first appearance of FeO in the oxide debris.

Another feature which becomes evident from the above mentioned results is that whenever Fe_3O_4 is the predominant oxide on the worn surfaces, as opposed to α-Fe_2O_3 or FeO, wear rates are lower. Considering figure 4.1(a), extrapolation of the portion of the curve below 12 N, in which the oxide on

the worn surfaces is α-Fe_2O_3, into the Fe_3O_4 region leads to a wear rate of around 1.9 times the measured value. This means that, under similar conditions, if it were possible to have either α-Fe_2O_3 or Fe_3O_4 as the oxide present on the worn surfaces, then Fe_3O_4 would be expected to result in a wear rate 1.9 times less than that associated with α-Fe_2O_3. Similarly for FeO, extrapolation of the FeO portions of the wear rate curves in figures 4.1(a) and 4.1(b) back into the Fe_3O_4 regions results in wear rates of approximately 3.4 and 2.9 times those measured for the 2.0 ms^{-1} and 4.0 ms^{-1} wear tests respectively. These points indicate that Fe_3O_4 forms a more protective surface oxide than either α-Fe_2O_3 or FeO. Good and Godfrey (96), Bisson et al (97), and Clark et al (98) have all shown that Fe_3O_4 forms a more wear protective surface oxide than α-Fe_2O_3, and thus that wear rates are lower when Fe_3O_4 is predominant, in agreement with the present findings. Davies et al (14), in studies of the oxidation of iron under static oxidizing conditions, have found that compressional stresses resulting from the volume change associated with oxidation are greater in α-Fe_2O_3 than in Fe_3O_4, so that mechanical breakdown of the former oxide occurs much more readily than the latter. In agreement with the present work, Tsuji (99) and Hurricks (100) found definite increases in wear at temperatures at which FeO starts to appear but, in contradiction of this, both Bisson et al (97) and Cornelius et al (101) found FeO to be protective.

Scanning electron micrographs of worn disc surfaces generated in the EN8 wear tests (figures 5.39 and 5.41) lend further support to the view that the oxide Fe_3O_4 has greater

wear protective properties than either α-Fe_2O_3 or FeO by revealing that in the former case the oxide layer is more extensive, covering virtually the whole worn surface, and is also smoother in appearance than in the case of the latter two oxides. The micrographs of the worn pins (figures 5.40 and 5.42), however, show that all of the worn pins surfaces were relatively smooth with a high degree of oxide coverage, irrespective of oxide type. This is not unexpected, however, since the variations in thermal and mechanical stresses experienced by the pin and disc will be very different. Since the pin surface is always in contact with the disc surface, but any region of the disc surface is only periodically in contact with that of the pin, then we would expect a pin surface which is more extensively oxidized and less disrupted than that of the disc.

The friction results are presented in figures 4.3(a) and 4.3(b) for the 2.0 ms^{-1} and 4.0 ms^{-1} wear test respectively, and it can be seen that μ initially increases, peaks at a relatively low load of around 10-20 N, and then gradually decreases. The scatter of the experimental points is rather large, making it rather difficult to assign curves to represent the variation of with load, but it is considered that the form of the curves in figures 4.3(a) and 4.3(b) is correct, especially in view of the fact that Athwal (47) has obtained numerous such curves from similar wear tests conducted on EN8 and EN31 steels. A decrease of μ with applied load for unlubricated sliding steels has also been reported by other workers (68 , 102 , 103).

The current friction results can be explained on the basis

of the adhesion theory of friction due to Bowden and Tabor (49). Equation (1.14) states that μ is given by the ratio of the shear strength of the welded junctions at the interface, S_i, to the hardness of the bulk metal, P_m. The temperature governing the value of S_i is the contact temperature, T_o, since we are considering the forces at the contacting asperities, whereas the temperature governing the bulk property P_m is the general surface temperature, T_s. Both S_i and P_m tend to vary with temperature in a similar manner (49) and, in addition, T_s increases with load in a similar manner to that of T_o (figures 4.5 and 4.8 respectively). With these facts in mind we would expect μ to remain approximately constant as the load is varied, and this is approximately true for the 4.0 ms^{-1} wear tests results, the decrease in μ with load being very small. However, a ploughing term contributes to the frictional force in addition to the shearing term and, furthermore, talysurf profiles of worn surfaces (47) have shown that surface roughness is greater at low loads indicating a greater contribution of the ploughing term to the total frictional force. At higher loads the contacting asperities become flattened under the influence of the applied load. Thus, the gradual decrease in μ with load could be due to the decreasing contribution from the ploughing component of the frictional force.

The heat flow results, presented in section 4.4, give us valuable information on the state of the worn surfaces, particularly when compared with the findings of SEM and XRD. It can be seen from tables 4.1(a) and 4.1(b) that the experimental division of heat, δ_{exp} , although remaining

approximately constant for given ranges of loads, changes abruptly at certain load values. This results from the fact that both H_1, the heat flow rate into the pin, and H_T, the rate of generation of frictional heat, increase steadily with load, but H_1 also changes sharply at certain applied loads. The load at which the H_1 transition occurs is around 35 N for both the 2.0 ms^{-1} and the 4.0 ms^{-1} wear tests , corresponding to the first appearance of FeO in the oxide debris, but no H_1 transition is observable for the 2.0 ms^{-1} wear tests at around 12 N corresponding to the change from α-Fe_2O_3 to Fe_3O_4.

These changes in heat flow rate are understandable on the basis of a sudden change in oxide thickness, or an increase in the degree of intermetallic contact, or a combination of both. From figures 5.46 and 5.47, representing the variation of oxide thickness with load for the 2.0 ms^{-1} and 4.0 ms^{-1} wear test respectively, it is evident that at a load of around 35 N in both cases there is a sudden fall in oxide thickness. This decrease in thickness will allow more heat to be conducted through the asperities of the pin, with a resultant increase in H_1 and T_s. In addition to this, Athwal (**47**), after conducting proportional analysis of wear debris from sliding wear tests on mild steel, has reported an increase in the amount of α-Fe in the debris when the predominant oxide changes from Fe_3O_4 to FeO. This indicates an increase in the degree of intermetallic contact, and since a change of predominant oxide from Fe_3O_4 to FeO coincided with the H_1 transitions in the present work, this could also be responsible for these transitions.

The highest general surface temperature recorded in the EN8

wear tests was 253°C, and yet FeO was the oxide detected by XRD at the higher loads employed, indicating that temperatures in excess of 570°C had been produced (17). These higher temperatures are the "hot-spot" temperatures generated by frictional heating at the contacting surface asperities. The fact that the surface oxides detected by XRD can be correlated with the contact tmeperatures (evaluated by the technique described in section 4.5.3), and not with the much lower general surface temperatures, indicates that T_o, and not T_s, is the temperature responsible for the growth of the surface oxide and thus for controlling the magnitude of the wear rate. This is true for wear tests carried out at room temperature, but it has been shown that if external heating is applied then so-called out of contact oxidation (occurring at T_s) becomes increasingly important the higher the temperature (31).

From the above it is evident that knowledge of the temperature T_o is very important in understanding oxidational wear. It can be seen from figures 4.8(a) and 4.8(b) that T_o varies linearly with load in a given range and, furthermore, the results have been interpreted as having abrupt transitions at certain loads, as for many of the other parameters. That these transitions in T_o do, in fact, occur is not certain since the scatter of the points is fairly high, but such an interpretation gives a closer fit to the points than does a simple linear variation without transitions. Moreover, in the light of the oxide thickness measurements shown in figures 5.46 and 5.47 we would perhaps expect such transitions in T_o since the greater thicknesses produced when Fe_3O_4 is the predominant surface oxide would lead to better insulation and so higher temperatures at the surface asperities.

One of the most important features emerging from the theoretical analysis of section 4.5 is that the predicted contact temperatures can be correlated with the oxides present on the worn surfaces as revealed by XRD. Whether we interpret figures 4.8(a) and 4.8(b) as having transitions or not, it is clear in both figures that the T_o value corresponding to a load of 35-40 N is around 550°C to 600°C. Now it is well known that the oxide FeO only forms at temperatures in excess of 570°C (17), so that if our predicted T_o values are a good representation of the actual temperatures at which the wear protective oxides grow then we would expect FeO to begin to appear in the oxide at a load of approximately 35-40 N. This is exactly what was found, the first detection of FeO occurring at a load of 40 N in the case of the 2.0 ms^{-1} wear tests, and at the slightly lower load of 35 N for the 4.0 ms^{-1} tests.

The fact that the FeO produced at the surface asperities does not oxidize to Fe_3O_4 on cooling after an asperity contact can be attributed to rapid quenching of the oxide due to T_s being much lower than T_o. In wear tests carried out at elevated temperatures by Sullivan and Athwal (31) FeO was not detected at expected contact temperatures in excess of 570°C, and this was attributed to the much slower cooling of the oxide formed at the asperities, allowing the oxidation of FeO to higher oxides to occur.

In the case of the 2.0 ms^{-1} wear tests α-Fe_2O_3 was the only oxide detected by XRD at the lower loads. The contact temperature corresponding to a load of around 12 N is between 300°C and 400°C, as can be seen from figure 4.8(a), and this

is the load at which Fe_3O_4 was first detected in the oxide debris by XRD. Unlike the case of FeO, however, there is no general agreement regarding the temperature at which Fe_3O_4 first begins to appear in the oxide on iron, making it more difficult to comment on the correlation between the predicted T_o values and the findings of XRD at the lower loads. Davies et al (14), in an investigation of the low temperature oxidation of iron under static conditions, found that Fe_3O_4 begins to appear at a temperature of around 250°C, while Vernon et al (104), in similar studies, detected Fe_3O_4 at temperatures of 200°C and above. Sullivan et al (46), by careful plotting of the static oxidation results of Caplan and Cohen (26), found three distinct regions on an Arrhenius plot, and the regions above and below 450°C were thought to correspond to the growth of Fe_3O_4 and α-Fe_2O_3 respectively. Thus, although the exact temperature at which Fe_3O_4 first appears in the oxide on an iron surface cannot be given and probably varies somewhat according to surface pretreatment, hardness etc., the findings of the above investigations show that such a temperature of around 300°C to 400°C is not unreasonable.

Other surface parameters which were calculated in the theoretical analysis of section 4.5 are the number of surface asperities in contact, N, and the average contact radius, a. The total real area of contact between the two wearing surfaces is $N\pi a^2$, and the two parameters are related to each other and to the applied load through equation (4.3), due to Bowden and Tabor (49), which is based on the assumption that the surface asperities are all deformed plastically. The calculated values of N suggest that N

increases smoothly with load as shown in figures 4.10(a) and 4.10(b), while figures 4.9(a) and 4.9(b) show that 'a' decreases with load. The decrease in 'a' over the load range studied is much less marked than the increase in N and, in fact, in the case of the 4.0 ms^{-1} wear tests 'a' was found to be very nearly constant. This finding, that the increase in real area of contact with increasing load arises mainly as a result of an increase in N, with changes in 'a' being much less significant, has been reported previously by Kragelskii (105), and Archard and Hirst (32). Quinn et al (69), using an iterative technique based on the oxidational wear theory, calculated values of 'a' for the wear of EN8 and EN31 steels at various sliding speeds. They found values of 'a' ranging from 2μm to 10μm, which is in good agreement with the values calculated in the present work. Furthermore, they suggested that 'a' is approximately constant for a given material combination and surface oxide, so that in order to obtain the necessary proportionality between N, and thus the real area of contact, and load it was necessary to assume that abrupt changes occurred in the value of N when the predominant oxide present on the surface changed from α-Fe_2O_3 to Fe_3O_4 or from Fe_3O_4 to FeO. In the present work it is difficult to determine if such transitions exist in figures 4.10(a) and 4.10(b), showing the variation of N with load, since the scatter of points at the higher loads is much greater than that at the lower loads where the curve is approximately linear. However, no reason could be found as to why the number of contacting asperities should depend upon the chemical composition of the oxide present on the worn surfaces, so that the curves drawn in figures 4.10(a) and 4.10(b) show a smooth variation of N with load.

The calculations of Athwal (47) show perhaps the closest agreement with the values of N and 'a' resulting from the present work, but this is probably due largely to the similarities in the methods used to calculate these quantities. Unlike the present results, however, Athwal interpreted the variation of N with load as being linear, attributing the increased curvature of the N versus load curve at higher loads as being due to increased softening of the steel (a decrease in P_m) as T_s becomes greater than around 300^oC (see figure 4.6). However, this explanation cannot be applied in the present case as T_s values were always less than 300^oC. This suggests that the curves shown in figures 4.10(a) and 4.10(b) represent the true form of variation of N over the range of loads employed in the present work, the more rapid increase in N at the higher loads not being due to an increased softening of the substrate. This form of variation is perfectly acceptable if we represent the variation of 'a' with load by the curves shown in figures 4.9(a) and 4.9(b), since in this case the proportionality between real area of contact and load is maintained.

There are two ways in which the results of the theoretical analysis of section 4.5 can be compared with experiment. Firstly we can compare the theoretically and experimentally determined values for the division of heat at the pin/disc interface, δ_{th} and δ_{exp} , and secondly we can compare the calculated values of T_o with those to be expected on the basis of the oxides present as revealed by XRD. The second method of comparison has revealed very good agreement between theory and experiment, as discussed earlier in this

chapter. The first method, of comparing δ_{th} and δ_{exp}, has also led to very good agreement as can be seen from tables 4.2(a) and 4.2(b), but an interesting point which arises is that δ_{th} was always found to be slightly greater than δ_{exp}. Sullivan and Athwal (31) used an iterative technique based on the oxidational theory of mild wear, in which both temperature and oxide thickness were varied, and the iteration process was terminated when T for calculating the thermal conductivity of the oxide was equal to the contact temperature, and δ_{th} was equal to δ_{exp}. These calculations were performed for low alloy steel wear tests carried out at room temperature and various elevated temperatures, and the agreement between theoretically calculated parameters (such as T_o and oxide thickness) and experimentally determined results (such as oxide composition and oxide thickness) were generally very good. However, in the case of the wear tests carried out without external heating the calculated values of oxide thickness were always found to be greater than those actually measured by SEM (typically 2μm greater), and this is exactly what was found to happen in the present study if such an iteration process was used. In view of the large number of oxide thickness measurements performed as part of the present study it seems unlikely that these measurements underestimate the true oxide thickness, especially as AES depth profiling has indicated that regions of the worn surfaces not covered by oxide plateaux have only a very thin covering of oxide. In addition, due to the relative complexity, although unavoidable, of equation (2.3) used in the calculation of H_1, and thus δ_{exp}, it is considered likely that inaccuracies occur in the calculation of δ_{exp}. Bearing these last two points in mind it was decided

to use the experimentally measured values of oxide thickness in the calculations of section 4.5, and to use the agreement between δ_{th} and δ_{exp} as a good indication of the agreement between theory and experiment rather than incorporate an exact agreement as a necessary condition in the calculations. This latter point is especially important when we consider that a relatively small change in the value of δ_{th} leads to a significantly larger change in the calculated values of T_o, ξ and N.

The calculation of the surface parameters was carried out by assuming that the oxide properties K_o and χ_o should be taken at the contact temperature, T_o, and not the general surface temperature, T_s, and it is instructive to see what affect this assumption has on the results of the calculations. Table 7.1 gives the results of the calculations obtained by evaluating K_o and χ_o at T_s. In this case an iterative process was not needed in the calculations of T_o, N, a and δ_{th} since T_s was known, having been evaluated by equation (2.2). Comparison of this table with table 4.2(a) shows that taking the oxide properties at T_s rather than T_o does not have a marked effect on the calculated values of T_o, N, a and δ_{th}. Calculated values of T_o are around 20-100^{o}C lower than when the oxide properties are evaluated at T_s rather than T_o and, furthermore, T_o and N increase less rapidly with load. The values of T_o calculated in this way indicate that the first appearance of FeO should occur at a load of around 50-55 N, whereas XRD has shown that this occurs at the lower load of 35 N. In contrast to this, the T_o values shown in table 4.2(a) show good correlation with the XRD results since they indicate that FeO should appear around 35 N, and this finding

LOAD (N)	K_o ($Wm^{-1} K^{-1}$)	a (μm)	N	T_o (^oC)	δ_{th} (%)
5	6.33	11.76	5	216	10.6
8	6.24	11.21	8	275	12.0
10	6.22	12.00	9	238	8.2
13	3.77	7.10	32	387	11.7
20	3.76	7.25	47	414	10.4
25	3.75	7.25	59	404	10.6
30	3.74	7.14	73	450	10.8
33	3.71	6.83	88	516	12.7
35	3.69	6.04	119	548	18.1
38	3.68	5.86	137	498	19.5
40	3.65	6.07	135	562	17.6
45	3.63	6.02	154	546	17.7
50	3.61	5.49	207	555	22.3
52	3.61	5.37	224	657	22.1
55	3.58	5.61	217	626	20.2
58	3.57	5.30	257	643	23.1

TABLE 7.1 Values of Surface Parameters Calculated by taking Oxide Properties K_o and γ_o at T_s.

supports the present view that the oxide properties K_o and χ_o should be evaluated at T_o and not T_s. Athwal (47) has also investigated the effect of evaluating K_o and χ_o at various temperatures between T_s and T_o, and it was shown that if the properties are evaluated at T_s then the calculated contact temperature is unrealistically high ($>6000^oC$). This does not conflict with the present findings, however, since the value of oxide thickness was varied in the work of Athwal, as mentioned previously, in order to maintain exact agreement between δ_{th} and δ_{exp}. Very high values of calculated oxide thickness ($>100\mu m$) were obtained in this way and it will now be shown that the value of oxide thickness also has a marked effect upon T_o in the present work.

The effect of varying the value of oxide thickness on the pin in the calculations of section 4.5 is illustrated by tables 7.2(a) and 7.2(b) for the 2.0 ms^{-1} wear tests. Table 7.2(a) summarises the results obtained by taking the pin oxide thickness as the average measured thickness value minus the standard deviation in the measurements for each load (see table 5.10(a)), while table 7.2(b) gives the corresponding results obtained for the pin oxide thicknesses equal to the average measured value plus the standard deviation. As a typical example consider the wear test which was carried out at a load of 35 N. The oxide thickness determined by SEM measurements was found to be $4.1 \pm 1.2\mu m$. Thus, it can be seen that an increase in ξ_p of $1.2\mu m$ has resulted in an increase of 196^oC in T_o, while a decrease in ξ_p of $1.2\mu m$ has led to a decrease in T_o of 158^oC. Hence, relatively small changes in ξ_p have a considerable effect on the value of T_o. The correlation between the values of T_o

LOAD (N)	ξ_p (um)	K_0 ($Wm^{-1}K^{-1}$)	a (μm)	N	T_0 (°C)	δ_{th} (%)
5	4.4	4.75	8.58	8	283	10.6
8	4.0	3.76	6.40	24	432	11.7
10	3.6	4.72	9.04	15	285	8.1
13	4.6	3.19	5.85	47	495	11.5
20	4.9	3.15	5.96	70	527	10.2
25	4.8	3.16	5.98	87	519	10.4
30	5.3	3.06	5.72	114	585	10.5
33	5.8	2.82	4.97	166	761	12.2
35	5.3	2.73	4.12	256	828	17.3
40	3.9	2.91	4.75	220	697	16.9
45	3.3	2.97	4.87	236	651	17.0
50	3.4	2.90	4.26	342	698	21.1
52	5.2	2.42	3.28	601	1057	20.6
58	3.9	2.61	3.65	542	908	21.4

TABLE 7.2 Effect of Value of Pin Oxide Thickness (ξ_p) on Calculated Values of Surface Parameters.

(a) ξ_p taken as average value of thickness measurements plus standard deviation in measurements.

LOAD (N)	ξ_p (μm)	K_o ($Wm^{-1}K^{-1}$)	a (um)	N	T_o (°C)	δ_{th} (%)
5	2.8	5.26	10.02	6	200	10.7
8	2.0	5.01	9.44	11	238	12.1
10	2.8	5.01	9.78	13	239	8.2
13	3.2	3.36	6.51	38	361	11.7
20	3.5	3.32	6.55	58	393	10.4
25	3.2	3.35	6.65	70	370	10.8
30	3.7	3.28	6.42	91	426	10.9
33	3.2	3.25	6.29	104	443	13.0
35	2.9	3.21	5.72	133	474	18.5
40	3.1	3.08	5.31	176	574	17.6
45	2.7	3.10	5.32	198	558	17.6
50	2.4	3.13	5.07	242	537	22.5
52	2.8	3.07	5.13	246	578	22.7
58	2.3	3.06	5.01	288	588	23.7

TABLE 7.2 Effect of Value of Pin Oxide Thickness (ξ_p) on Calculated Values of Surface Parameters.

(b) ξ_p taken as average value of thickness measurements minus standard deviation in measurements.

calculated in this way and the oxide composition as revealed by XRD is not too bad, but if the value of ξ_p is changed by more than a few μm then the correlation becomes poor. In contrast, only a very small change in the value of δ_{th} results from a change in ξ_p of a few μm so that agreement between δ_{th} and δ_{exp} is still good. Changes in the value of oxide thickness on the disc, ξ_D, unlike changes in ξ_p, only have a small effect on the calculated values of T_o eg. an increase or decrease of 1 μm in ξ_D for the wear test run at 25 N and 2.0 ms^{-1} only results in a respective increase or decrease in the value of T_o of approximately 1^oC. This results from the fact that N and 'a' vary in opposition with ξ_D such that the product Na^2 remains very nearly constant, and changes in the product Na are very small. As a result of this variations in the second and third terms of equation (4.9), used in the calculation of T_o, with ξ_D are very small.

The results discussed so far do not give any indication of the way in which the oxide films are formed during wear, although it has been established that growth occurs at, or near, T_o. A technique which proved invaluable in the examination of the physical structure of the oxide films is SEM. Figures 5.44(a) to 5.44(1) are scanning electron micrographs which effectively show "sections" through the oxide plateaux. Most of these sections are not true plateaux edges, but were produced by causing the oxide to crack by the method described in section (3.7). Oxide "sections" produced in this way gave a much clearer picture of the structure of the oxide films than did the true plateaux edges, since these were often obscured with loose oxide debris or else were very few in number. The micrographs in figures 5.43 show the way

in which the surface oxide cracked to reveal these oxide sections. In particular, figures 5.43(g) and 5.43(h) show the edges of an oxide sheet which clearly extends to cover virtually the whole of the worn surfaces in both cases.

Observation of the oxide films in figures 5.44(a) to 5.44(l) reveals a very important point regarding the physical structure of the films, and that is that they are physically homogeneous and do not consist of a layer of compacted debris, which has been shown to be the case in some mild wear tests (40 , 106). This latter type of oxide formation is illustrated by the micrographs in figure 5.45, taken of worn surfaces generated in reciprocating wear tests at elevated temperatures (106). Clearly the structure of the two types of oxide is very different, indicating that the mechanism of formation is also very different. In the present case the physical homogeneity of the oxide films suggests that growth occurs by a diffusion controlled mechanism, as for thick oxides grown under static oxidizing conditions. If this is so then a question arises as to whether the activation energy, Q, and Arrhenius constant, A, determined from oxidation experiments carried out under static oxidizing conditions are applicable to oxidation produced during wear. In order to answer this question we must consider the factors upon which Q and A depend, and compare values of Q and A calculated from static oxidation experiments with those calculated from the results of the present wear tests (table 6.1).

The contact temperatures generated in the present wear tests ranged from 230^{o}C to 750^{o}C, and the rate law for the growth

of thick oxide films on iron or low alloy steel in this range is parabolic (17). Both the activation energy, Q_p, and Arrhenius constant, A_p, for parabolic oxidation will depend upon whether the oxide is predominantly α-Fe_2O_3, Fe_3O_4 or FeO, since the diffusing species will be different in each case: α-Fe_2O_3 grows by the diffusion of oxygen ions, Fe_3O_4 by the diffusion of both oxygen and iron ions, and FeO by the diffusion of iron ions (24).

Quinn et al (46 , 69) have postulated that values of Q_p derived from static oxidation experiments can be applied to oxidation produced during wear, but that A_p values so derived cannot. This belief is based on the expectation that the parabolic rate constant, k_p, for oxidation produced during wear is dependent upon the diffusion coefficient, D, of the relevant diffusing species in the oxide, given by:

$$D = D_o \exp(-Q_D / R T) \qquad (7.1)$$

where D_o is a constant often known as the frequency factor, and Q_D is the activation energy for diffusion. If k_p is indeed dependent upon D then from equation (6.7) and (7.1) we can see that A_p depends upon D_o, while Q_p depends upon Q_D. Q_D, and thus Q_p, is dependent upon the relative potential barrier heights for diffusion in the oxide lattice and so will not differ greatly in static and tribological conditions. However, D_o, and hence A_p, depends upon the entropy of the system which will almost certainly be greater for the tribologically produced oxides than for the statically grown oxides. An important point which must be made regarding this view, however, is that Q_D is only dependent upon relative potential barrier heights alone if movement of ions through

the oxide occurs by so-called lattice diffusion i.e. ions diffuse via a vacancy or interstitial mechanism through the bulk of the oxide. If, however, an appreciable amount of diffusion occurs along grain boundaries or dislocations then Q_p will be smaller since the energy required for diffusion via these paths is smaller than that for lattice diffusion (19). Thus, while the value of A_p will probably be considerably greater for tribo-oxidation than for static oxidation due to the tribologically produced oxide having a highly disrupted crystalline structure brought about by mechanical and thermal stresses associated with the rubbing action, it may also be that Q_p for tribo-oxidation will be lower. Obviously oxides grown under static conditions will also exhibit a grain structure so that grain boundary diffusion will also play a part in the total transfer of reactants across the oxide film, but the point of interest in the present discussion is how sensitive is the value of Q_p to changes in crystalline structure. Owing to the lower activation energy for grain boundary and dislocation diffusion, this form of diffusion becomes increasingly important for decreasing temperature, and according to Hauffe (18) this "short-circuit" diffusion does not play a significant role at high temperatures.

Values of Q_p and A_p for the oxidation or iron or low alloy steel determined from various sources are summarised in tables 6.1(a) and 6.1(b) respectively. The values of Q_p determined from the static oxidation experiments conducted as part of the present work agree very closely with those of Caplan and Cohen (26) for the oxidation of iron which had been cold worked by abrasion. We would have perhaps expected

Caplan and Cohen's value of Q_p appropriate to the temperature range where Fe_3O_4 is the predominant oxide to be somewhat less than the corresponding value determined in the present study, since they have shown that surface abrasion lowers the activation energy for oxidation. However, this can be accounted for by the error of $\pm 25\ kJ\ mol^{-1}$ in the value of Q_p from the present study. For the FeO oxidation region, Caplan and Cohen (26) have shown that Q_p is not dependent on the degree of disruption of the surface, as FeO can deform plastically in order to collapse any pores which might form. It can be seen from table 6.1(a) that for the FeO oxidation region the agreement between the Q_p value of Caplan and Cohen and that calculated for static oxidation in the present study is very good, although it must be remembered that the maximum error in the latter value, estimated from figure 5.4, is $\pm 20\ kJ\ mol^{-1}$.

The value of Q_p for tribo-oxidation calculated from equation (6.13) for the Fe_3O_4 temperature range is $74 \pm 22\ kJ\ mol^{-1}$ (standard deviation). Comparison of this value with $96\ kJ\ mol^{-1}$ obtained from the results of Caplan and Cohen (26) for the oxidation of abraded iron, and $96 \pm 25\ kJ\ mol^{-1}$ for the static oxidation of low alloy steel from the present study, shows that there is reasonable agreement between the tribologically and statically derived values. The value for tribo-oxidation is around $20\ kJ\ mol^{-1}$ lower than that for static oxidation, but this difference is not great when we consider the uncertainties associated with these values. In the case of the values of Q_p calculated for tribo-oxidation it must be realised that these values are quite sensitive to relatively small changes in T_o and ξ in

equation (6.13), e.g. in the example calculation in section 6.3 a decrease of 30% in the value of Q_p results from any one of the following changes: an increase in ξ_2 of 1μm, a decrease in ξ_4 of 1.1μm, an increase in T_4 of 71°C, or a decrease in T_2 of 44°C. However, bearing in mind that the relatively high number of calculations of Q_p (nine values) resulted in a standard deviation of only 22 kJ mol^{-1} it is considered that the average value of 77 kJ mol^{-1} gives an indication of the order of Q_p for the tribo-oxidation of low alloy steel when Fe_3O_4 is the predominant oxide. These results show that there is some truth in the assumption of Quinn and co-workers (46 , 69) that the value of Q_p relevant to tribo-oxidation does not differ greatly from that relevant to oxidation under static conditions. Molgaard and Srivastava (95), having performed similar calculations of Q_p for the tribo-oxidation of steel, have reached the same conclusion.

In contrast to the above findings, comparison of statically and tribologically derived values of A_p show that the Arrhenius constant differs greatly in the two cases. The A_p value obtained from the work of Caplan and Cohen (26) for the predominantly Fe_3O_4 temperature range is 3.2×10^{-2} kg^{2}m^{-4}s^{-1}, and this is in reasonable agreement with the static oxidation value of 3.7×10^{-3} kg^{2}m^{-4}s^{-1} from the present study. The A_p value calculated for tribo-oxidation, however, was 8.3×10^3 kg^{2}m^{-4}s^{-1} i.e.some six to seven orders of magnitude higher than that for static oxidation. This indicated that the value of A_p appropriate to oxidation under sliding wear conditions is much higher than that for oxidation under static conditions. Thus it appears that the much higher rate

of oxidation produced during the sliding wear of low alloy steel over that produced under static oxidizing conditions is a result of the considerably greater value of A_p relevant to tribo-oxidation, the values of Q_p relevant to both cases being of similar value.

The results of the AES analyses reinforced the view that the plateaux present on the worn surfaces consisted of a physically homogeneous oxide layer. This is evident from figures 5.24 to 5.28 which show profiles of oxygen concentration versus etching time for oxide plateaux produced on worn EN8 surfaces at various selected loads. It has not yet been possible to accurately calibrate etching time in terms of depth of penetration into the oxide, but comparison of the profiles with the SEM oxide thickness measurements (tables 5.10(a) and 5.10(b)) should give an approximate calibration factor. All of the profiles show the same basic shape: oxygen concentration remains approximately constant at around 40-45% for an etching time of about 100 to 200 minutes after which it falls off fairly abruptly, and levels out at a concentration of around 10%. Further prolonged etching produced no further change in the elemental concentrations indicating that we had effectively etched through the oxide to the bulk metal below. Very similar oxygen concentration versus depth profiles have been reported by Sullivan and Athwal (31) for worn EN31 steel surfaces. In contrast to this, however, Sullivan and Granville (106) have shown that the concentration versus depth profiles of surface plateaux produced in the reciprocating wear of 9% Cr steel are very different. In this case the oxygen concentration falls off very gradually with etching time, while those of iron and

chromium increase very gradually. Clearly the structure of these latter films is very different to that of the oxide films produced in the present study and, in fact, they consist of an agglomerate layer of wear debris. Sullivan and Granville (106) have explained the concentration versus depth profiles on the basis of the compacted wear debris being mainly oxide at the surface of the plateaux and mainly metallic at the base. The SEM micrograph of figure 5.45 was supplied by one of these workers (107) and clearly shows the structure of the agglomerate layer.

The Auger oxygen maps and corresponding micrographs shown in figures 5.30 to 5.32 confirm that the plateaux produced on the worn surfaces in the present wear tests consist of oxide.

In addition to establishing the nature of the plateaux, AES depth profiling was also able to reinforce the findings of XRD and SEM by indicating how the thickness of the oxide film differs according to the predominant oxide of iron which is present. Although only a very small area of each surface was analysed during point Auger analysis depth profiling and there will be some variation in oxide thickness over the surface, nevertheless it was found generally that when Fe_3O_4 was the predominant surface oxide, the oxide layer tended to be thicker than when the predominant surface oxide was α-Fe_2O_3 or FeO. This can be seen from comparison of the oxygen concentration versus depth profiles in figures 5.24 to 5.28. This is in agreement with the SEM oxide thickness measurements shown in figures 5.46 and 5.47.

In order to obtain any meaningful conclusions from the EN8/9% Cr

wear tests it was first necessary to establish that the wear regime in these wear tests was in fact, oxidational wear. This was accomplished by SEM and AES analyses, and it is evident from the micrographs of figures 5.48 and 5.49 and the concentration versus depth profiles of figures 5.33 to 5.36 that both the EN8 pin surfaces and the 9% Cr disc surfaces were covered by smooth oxide plateaux. The significant feature of the concentration verus depth profiles is the difference in the levels of chromium in the oxide on the pin surface from that of the oxide on the disc surface. In the case of the oxide film on the 9% Cr discs chromium was detected in the surface oxide at all depths, rising from approximately 3% at the oxide surface to approximately 8% in the bulk. In the case of the oxide film on the EN8 pin surfaces, however, chromium was only occassionally detected and then its concentration was around 1%. The detection of very small traces of chromium in the oxide on the pin surface is to be expected anyway since there will be some transfer of chromium from the disc surface to the pin surface during the initial severe"running-in" stage. This occurs due to plastic shearing of the surface junctions resulting in metallic particles being transferred from one surface to the other (108). This view was supported by the fact that if chromium was detected in the oxide plateaux on the pins, it was not detected in the initial layers of the oxide but well into the oxide near the oxide/metal interface. This would suggest that chromium was transferred from the disc to the pin during the severe wear of the running in period, followed by diffusion of chromium ions into the oxide once mild, oxidational wear had ensued. Chromium was probably incorporated into the iron oxide lattice by the

formation of mixed oxides such as $(Fe,Cr)_2O_3$ and $FeCr_2O_4$ (18). Hence, evidence from the AES analysis of worn surfaces generated in the EN8/9% Cr wear tests shows that transfer of oxide from the disc surface to the pin surface does not occur and so it must be concluded that, under the experimental wear test conditions described in this thesis, the oxides grow separately on the pin and disc surfaces by a diffusion process. This is in full agreement with other results discussed.

In the analysis of oxide films on the worn EN8 surfaces the ratio of oxygen to iron was always found to be near 50:50, and while this is expected for FeO, we would expect higher ratio of around 57:43 and 60:40 for the oxides Fe_3O_4 and α-Fe_2O_3 respectively. A possible reason for this is that the results are uncorrected for variations in backscattering factor, r, and inter-spectrometer variations, as discussed in section 6.4. However, if this was the reason for the discrepancy, then we would perhaps expect the ratio of oxygen to iron calculated from the Auger spectra to always be lower than the true value, whereas this was only found to be so for oxides which were predominantly α-Fe_2O_3 or Fe_3O_4. Concentrations calculated from Auger spectra of oxide films which were predominantly FeO, as revealed by glancing angle XRD, gave O:Fe ratios very close to 50:50. Hence, the inter-spectrometer correction factor, β_i , defined by equation (6.26) is not the major cause of this error since the instrumental factors $T(E_i)$ and $D(E_i)$ only depend upon electron energy, and not upon the chemical composition of the iron oxides (although there will possibly be small chemical shifts). Furthermore, if we assume that the values of r, for a given

electron energy, are similar for the three iron oxides, then this also cannot explain the discrepancies.

A much more likely cause of the lower than expected O:Fe ratios for oxides which were mainly α-Fe_2O_3 or Fe_3O_4 is the ion etching process. According to Hofmann (93) ion bombardment inevitably induces changes in the topography and in the composition of the surface region of the sample. The composition of the surface layers of a multicomponent sample is generally changed during sputtering due to the different atomic sputtering yields of the constituent elements. In compounds, preferential sputtering of one component is linked with the change in the chemical state of the sample constituents, and many oxides are reduced to lower oxidation states, as revealed by XPS (109). In the present study XPS analysis of a range of iron oxide surfaces revealed that ion beam reduction of Fe^{3+} to Fe^{2+} occurred very rapidly. After a short period of etching with Ar^+ ions, typically a few minutes, the surface layers of oxides which were predominantly α-Fe_2O_3 or Fe_3O_4 had been largely or fully reduced to Fe^{2+}. This would explain why the O:Fe ratio calculated from the Auger spectra obtained from oxide plateaux was always around 50:50, irrespective of whether the oxide was α-Fe_2O_3, Fe_3O_4 or FeO. Further reduction to atomic Fe did take place, but this occurred to a much lesser extent than the reduction of Fe^{3+} to Fe^{2+}. It is worth noting that reduction of oxides by the incident electron beam used in AES has also been reported (110).

A major part of the study was the use of x-ray photoelectron spectroscopy for the investigation of surface oxide films.

In many areas the technique has not proved to be as successful as had originally been hoped. The results of this part of the investigation, however, have very important implications for any future electronspectroscopic oxidation study and hence they will be discussed in detail here.

Table 5.9 gives a summary of the core-level electron binding energies in iron and its three oxides determined from the present study, together with photoelectron peak widths expressed as full width at half maximum (FWHM). For comparison table 7.3 summarises the core-level electron binding energies reported by a number of other workers (73,74, 111,112,113,114) the values having been corrected with respect to $Au4f_{7/2}$ = 84.0 eV or C1s = 284.8 eV. The binding energy values obtained in the present study agree very closely with those of McIntyre and Zetaruk (74), although it can be seen from table 7.3 that variation between different sets of results is often quite large, hence justifying the need for the present study. These variations probably result largely from differences in sample type (e.g. powder, crystalline) and surface pretreatment, since iron oxide surfaces are susceptible to oxidation and adsorption of water on exposure to air, and from differences in spectral interpretation. The results are further complicated by the reduction of surface oxides due to ion beam etching, which is usually necessary in order to remove adsorbed layers or surface layers which have become oxidised. It is evident from the present study, and from most of the other studies, that the difference between the electron binding energies of the Fe^{o}, Fe^{2+} and Fe^{3+} species is sufficient to enable their identification, and thus the identification of iron oxides

	Fe $2p_{3/2}$	Fe $2p_{1/2}$	Fe 3p	Fe 3s	O1s	REF
Fe metal	706.9	-	53.0	90.9	-	74
	707.3	720.3	-	-	-	73
	707.0	-	-	-	-	111
	706.82	719.92	52.9	91.4	-	112
	707.0	-	-	-	-	113
FeO	709.5		54.9	92.5	530.0	74
	710.3	723.8	-	-	530.1	73
	709.7	-	-	-	530.1	111
	709.0	-	54.4	-	-	112
	709.6	-	-	-	530.4	113
Fe_3O_4						
Fe^{2+}/Fe^{3+}	711.4	724.9	-	-	530.1	73
Fe^{2+}	709.5	-	-	-	530.1	111
Fe^{3+}	711.2	-	-	-	-	
Fe^{2+}/Fe^{3+}	710.95	723.98	56.2	93.6	530.17	112
Fe^{2+}/Fe^{3+}	710.4	724.4	-	-	-	114
Fe_2O_3	711.0	-	55.7	93.6	529.8	74
	711.4	724.6	-	-	530.1	73
	711.2	-	-	-	530.1	111
	710.97	724.30	55.8	93.8	529.98	112
Fe OOH	711.9	-	56.6	94.2	530.3 & 531.4	74
	711.0	724.5	-	-	530.1 & 531.8	73
	711.2	-	-	-	530.1 & 531.1	111

TABLE 7.3 Core Level Electron Binding Energies for Iron and Iron Oxides Obtained from the Literature.

themselves.

The O1s spectra of the oxide surfaces could usually be resolved into two peaks approximately 1 eV apart. The lower binding energy peak was due to oxygen ions in an Fe-O-Fe bond and, unlike the case of the Fe photoelectron peaks, had an invariant binding energy of 530.1 ± 0.2 eV. For this reason it cannot be used in the identification of the different oxides of iron. The findings of other workers (73 , 74 , 111) confirm this fact. The higher binding energy peak, which occurred at around 531.4 eV, disappeared rapidly upon etching. This peak was almost certainly due to the presence of hydroxyl species as a result of the dissociative chemisorption of water on the air exposed surfaces (73 , 115). Occassionally it was noticeable that the O1s peak at around 531.4 eV was considerably more intense than the O1s peak at 530.1 eV (e.g. figure 5.11(b)). In such cases it appears that the higher binding energy peak is characteristic of the hydroxide, $Fe(OH)_3$, rather than the oxy-hydroxide, FeOOH, since in the latter case we would expect the two O1s peaks to be of equal intensity (FeOOH), or a 530.1 eV peak which was more intense than the peak at 531.4 eV (FeOOH plus oxide detected). In view of these findings the contaminant layer is given as being a hydroxide in table 5.9, although this is not absolutely certain. In the case of air exposed Fe metal the higher binding energy peak was approximately 2 eV above the oxide peak, which would seem to indicate a different adsorbed species to that previously discussed. This may have been due to adsorbed oxygen rather than water (73). In view of the high concentration of carbon on the unetched sample surfaces it may also be possible that these O1s peaks

could be due to a hydrocarbon contaminant layer. Figure 5.11 shows the O1s spectra of the air exposed surfaces.

The widths of the O1s photoelectron peaks were 3.6±0.2 eV (FWHM) for the peak doublets characteristic of the unetched state. This was true for all three oxides studied. The O1s peak doublet of the unetched Fe metal surface had the slightly greater FWHM of 4.0 eV, which was to be expected since the separation of the two oxygen peaks was greater. Upon etching, the higher binding energy peak due to the adsorbed species rapidly diminished, being visible as a shoulder on the high binding energy side of the O1s oxide peak. Complete removal of this peak left the O1s peak due to the oxide having a FWHM of 2.0±0.2 eV. Figure 5.12 shows the effect of argon ion etching upon the O1s spectrum of an Fe_3O_4 powder surface.

The phenomenon of multiplet splitting associated with photoelectron peaks is due to the presence of unpaired valence electrons, resulting in an exchange interaction which affects differently the remaining spin-up or spin-down core electrons (116). In the case of high spin states the phenomenon is heightened, and for the high spin states Fe^{2+} and Fe^{3+} we observe broadening of the Fe2p peaks due to unresolved multiplet splitting. In this present study $Fe2p_{3/2}$ and $Fe2p_{1/2}$ peak widths of between 4.0 eV and 5.0 eV were observed, in good agreement with Brundle et al (111), who report a value of 4.5 eV for Fe^{2+} and Fe^{3+} states, and the Fe2p peak width of 4.1 eV for Fe_2O_3 falls within the limits given by Allen et al (73) who concluded that we should expect to observe Fe2p peak widths of between 3.8 eV and 4.4 eV for the Fe^{3+} state. Also evident from table 5.9 is a noticeable broadening

as we go from α-Fe_2O_3 (Fe^{3+} ions) to Fe_3O_4 (Fe^{2+} and Fe^{3+} ions).

Another characteristic feature of the oxide spectra, which has been empirically observed for other high spin states of transition metal ions (117), is the presence of satellite peaks. These shake-up core-level satellites are caused by an incident x-ray photon giving up a discrete portion of its energy to the excitation of a second electron rather than imparting its entire quantum of energy to the primary, photo-ejected electron. This photoelectron will thus have lost a small amount of energy and will appear at a slightly higher binding energy than the parent peak. From the results of the present XPS study of iron oxides it is evident that a satellite occurring at approximately 8.0 eV above the $Fe2p_{3/2}$ peak maximum is characteristic of an Fe^{3+} species, while the occurrence of a satellite at approximately 6.0 eV above the $Fe2p_{3/2}$ peak is characteristic of an Fe^{2+} species. Brundle et al (111) observed Fe^{2+} and Fe^{3+} satellites at 6.0 eV and 8.5 eV above the $Fe2p_{3/2}$ peak respectively, lending good support to the findings of the present study.

In addition to oxide surfaces being contaminated by an adsorbed layer, it appears that the lower oxides FeO and Fe_3O_4 were subject to surface oxidation effects. This can clearly be seen in the case of the Fe_3O_4 powder surface from the spectra obtained while heating the sample under UHV conditions (figure 5.8). It seems likely that the surface of the FeO powder sample was also oxidized to form α-Fe_2O_3 but, if so, was masked by the presence of an adsorption layer.

Ion beam reduction was found to be a serious drawback in the analysis of oxide surfaces which had been ion etched. This phenomena was observed for all three iron oxides studied and, in the case of Fe_3O_4 (figure 5.7), complete reduction of the Fe^{3+} ions to Fe^{2+} had occurred within only a few minutes of ion etching. This problem has been reported previously in XPS studies of iron oxide surfaces. Brundle et al (111) observed a significant increase in the Fe^{2+} concentration, and the appearance of Fe^{o}, after etching an α-Fe_2O_3 surface for only a few minutes, even though the sputtering rate was only a few Å per minute. In addition, McIntyre and Zetaruk (74) found that bombardment of an α-Fe_2O_3 surface resulted in an almost complete reduction to FeO during the first few minutes of ion sputtering. Kim et al (109) have shown that the suseceptibility of an oxide to Ar^+ reduction can be predicted from the value of its free energy of formation, and on this basis the reduction of iron oxides is expected.

In the case of the worn surfaces it had been intended to use XPS in conjunction with argon ion etching in order to determine the chemical state of the oxide at various depths into the oxide plateaux. In this way it was hoped that information could be gained on the chemical structure of the oxide films and, in particular, the relative proportions of α-Fe_2O_3, Fe_3O_4 and FeO and their positions in the film. However, this was almost totally prevented due to the reduction of the surface oxides caused by ion beam etching. Due to this reduction the results obtained from the XPS analysis of a range of worn surfaces were all similar. Fe2p spectra obtained for the unetched worn surfaces were characteristic of the Fe^{3+} state due to the presence of α-Fe_2O_3, while the

initial O1s spectra also indicated the presence of an adsorbed species. Upon argon ion etching for a few minutes the Fe2p peaks shifted to the lower binding energies characteristic of Fe^{2+} ions in FeO, irrespective of whether FeO was present in the unetched oxide film or not (which was revealed by XRD).

An interesting feature which emerged from the analysis of the worn surfaces was the different energies which were observed for the O1s photoelectron peak associated with the adsorbed species. In most cases this peak occurred at a binding energy of 531.4 eV, but in the case of the pin surface generated in the 33 N wear test the adsorption peak occurred at 532.1 eV, a difference of almost 1 eV. Results of SEM and AES depth profiling analysis of the surfaces indicate that the physical nature of the oxide on the worn surfaces was similar for all of the wear tests conducted, and so we cannot explain the difference in adsorption behaviour on this basis. It could be, however, that the difference in adsorption behaviour is associated with differences in the chemical composition of the surface oxides, which were revealed by XRD (sections 5.2.1 and 5.2.2). In the case of the 33 N wear test the oxide produced was predominantly Fe_3O_4, and this might favour the adsorption of a species having a binding energy of 532.1 eV in the O1s spectrum, whereas oxides which were predominantly α-Fe_2O_3 (10 N, 2.0 ms^{-1}) or FeO (50 N, 2.0 ms^{-1}) might favour adsorption of a species having the lower O1s binding energy of 531.4 eV. This is by no means certain and more work on a wide range of worn surfaces would be required before any definite conclusion could be reached. An O1s adsorption peak at 532.4 eV was also observed for an unetched Fe metal

surface. However, if the above idea is correct this may not necessarily indicate that the oxide on the metal surface is Fe_3O_4 since physical differences between the surfaces of tribologically and statically produced oxides will also have some bearing on adsorption behaviour.

The purpose of the XPS analysis of oxides grown under static oxidizing conditions was one of comparison. It was hoped that comparison of the results obtained from the analysis of the two types of surfaces would reveal any similarities, or otherwise, in the structure of the oxides, and thus provide information on the way in which the oxide films grow during wear. Unfortunately this was not possible due to ion beam reduction of both types of oxide.

The rate of reduction of the statically oxidized surfaces varied. In the case of the highly polished low alloy steel surface oxidized at 150°C complete reduction of Fe^{3+} to Fe^{2+} had occurred after only one minute of etching. In contrast, ion beam reduction of the thicker oxides formed at higher temperatures (260°C, 500°C) was much less rapid. Complete reduction to Fe^{2+} had not occurred until after around 15 minutes of etching. Further reduction to metallic Fe was evident from the appearance of the Fe^{o} 2p photoelectron peak which also occurred after around 15 minutes of etching. This could not have been due to a signal from the metallic substrate since the oxides were very thick and, furthermore, continued prolonged etching for a period of fourteen hours did not result in any great further increase in the Fe^{o}2p peak intensity.

The O1s spectra obtained from the analysis of the statically oxidized samples revealed an interesting feature regarding the origin of the photoelectron peak arising from an adsorbed species. The O1s peak at around 531.4 eV, which was observed for most of the unetched oxide surfaces, was earlier attributed to the adsorption of water. This tentative assumption was based on the fact that when the 531.4 eV peak was intense relative to the O1s oxide peak at 530.1 eV, observable shifts to a higher binding energy occurred in the Fe2p photoelectron peaks, and this could be explained on the basis of hydroxide formation. If we consider the O1s spectrum obtained for the unetched metal surface oxidized at 150^{o}C, however, although the O1s adsorption peak, which occurred at the higher binding energy values of 532.3 eV, was much more intense than that due to the oxide, the corresponding Fe2p spectrum was still characteristic of an α-Fe_2O_3 surface. This could be due to the fact that the adsorbed species in this instance may have been oxygen rather than water (73).

Clearly ion beam reduction was a major limiting factor in the identification of oxidation states as a function of depth for all of the oxides analysed in the present study. However, the characterisation of the XPS spectra of the standard iron oxide surfaces and the measurement of core-level electron binding energies, together with the analysis of a range of tribologically and statically produced oxides, has laid the foundations for further work in this area. Kim et al (109) have shown that in certain cases ion beam reduction can be prevented by the use of O_2^+ ions. However, an additional complication which often occurs is the oxidation of surfaces by a chemical reaction with the incident oxygen

ions. Depth profiling by means of ball cratering (118) can only be achieved with the very small spot size employed in AES, and even then an initial etching of the surface is usually required to remove surface contamination. A systematic study of the effect of sputtering conditions (e.g. ion species and ion energy) on the occurrence and extent of oxide reduction may be worthwhile. However, although such a study was beyond the scope of the present project, XPS analysis of a few selected oxide surfaces which had been sputtered by 0.5 keV Ar^+ ions revealed that reduction still occurred at this much lower energy.

In view of the experimental evidence discussed so far it is possible to propose a mechanism for the mild wear of low alloy steel under dry, unlubricated,unidirectional sliding conditions. It is considered that the plateaux present on the worn surfaces are physically homogeneous oxide films which grow by diffusion of iron and oxygen ions through the film. The temperature at which the wear reducing oxide films are formed is the "hot-spot" temperature produced at the contacting asperities, or a temperature close to this. Each encounter adds to the oxide thickness at a given asperity, and the thickness builds upto a critical value of around 3-4μm after which it becomes detached to form a wear particle. The mechanism of wear particle formation is probably a fatigue mechanism in which thermal and mechanical stresses cause detachment of the oxide at the oxide/metal interface (31). This view is supported by SEM micrographs due to Athwal (47), from which it can be seen that the thickness of wear fragments produced in oxidational wear tests is approximately the same as the thickness of the surface oxide film. The α-Fe which was

always detected in the wear debris by XRD does not conflict with the view of predominantly oxide/oxide contact if we take into account the differing magnitudes of the Archard K-factor for metallic wear and oxidational wear, since this shows that only 1 in 100 encounters are needed,on average, to produce a metallic wear particle, whereas 1 in 100,000 are needed to produce an oxide wear particle.

Other theories of mild wear have been proposed (37 , 43) in which oxidation of the worn surfaces is assumed to occur by means of a diffusion process. Tenwick and Earles (43) assumed that the oxide film on a worn surface builds up to a critical thickness before becoming detached, as in the present model. However, oxidation rates were assumed to be linear, and this is incorrect for temperatures above 200^{o}C since the rate law characteristic of high temperature oxidation is parabolic (17). Linear rate laws are only observed for the thick films formed at high temperatures if cracks appear in an oxide film so that the thick film diffusion process becomes unimportant. Furthermore, these workers considered that the wear protective oxides are formed at the general surface temperature rather than the "hot-spot" temperature, since if consecutive collisions of a given asperity are infrequent then the time spent at T_s is much greater than the time spent at T_o. The findings of the present study have shown however, that for wear tests carried out at room temperature (i.e. without external heating) the important temperature is T_o. By calculations of the relative contributions from "in-contact" and "out-of-contact" oxidation based on a modified form of Quinn's oxidational wear equation (equation (6.9)), Athwal (47) has shown that

out of contact oxidation is not important at room temperature but becomes the dominant mechanism at ambient temperatures above 300°C. Hence, T_s may well have been the temperature at which the majority of oxide formed in the wear tests of Tenwick and Earles since T_s values as high as 500°C were recorded.

The activation energies resulting from the model of Tenwick and Earles (43) was around 10-30 kJ mol^{-1} and these low values were attributed to the effect of the pin and track substrates on the oxidation of the pin. Tao (37) calculated a value of activation energy for oxidation during wear of 14.1 kJ mol^{-1} , and he attributed this low value to the effect of the rubbing action producing blisters and voids which enhance diffusion. The findings of the present study, however, indicate that the activation energy for oxidation during wear is considerably higher, and does not differ greatly from that applicable to static oxidation.

In contrast to physically homogeneous thick oxide films in which growth is diffusion controlled, Stott et al (40) have reported oxide films which consist of a layer of compacted oxide particles underneath a smooth oxide glaze. The micrographs of figure 5.45 show the structure of such an oxide film (107). These films were produced in reciprocating wear conditions in which the test plate was horizontal so that any loose wear particles which are formed cannot easily escape. The trapped wear particles become further fragmented during sliding, giving rise to a smooth wear topography above an agglomeration of oxide particles. However, in the present wear tests a horizontal pin was loaded against a

vertical disc (figure 2.3) so that the majority of the loose oxide particles formed were removed from the sliding interface due to gravity. Therefore the conditions of the present wear tests were unfavourable for the formation of an agglomerate oxide layer.

CHAPTER 8

CONCLUSIONS

Mild wear was observed for all of the EN8 pin-on-disc wear tests carried out as part of the present study. Abrupt transitions occurred in the magnitude of wear rate at certain applied loads, and wear rate was found to be directly proportional to applied load for load regions between the transitions. Analysis of the surface oxides and debris by x-ray diffraction indicate that the abrupt changes in wear rate were due to changes in the composition of the oxide on the worn surfaces. The transitions observed at loads of around 12 N and 35 N in the 2.0 ms^{-1} wear test results were due to a change in the predominant oxide from α-Fe_2O_3 to Fe_3O_4 and from Fe_3O_4 to FeO respectively, while the single transition at around 38 N in the 4.0 ms^{-1} wear test results was due to a change in the predominant oxide from Fe_3O_4 to FeO. It was found that wear rates were considerably lower when Fe_3O_4 was the main constituent of the surface oxide as opposed to α-Fe_2O_3 or FeO. Results indicate that if it were possible, under identical conditions of load and speed, to have either α-Fe_2O_3 or Fe_3O_4 as the main constituent of the oxide on the worn surface then Fe_3O_4 would give rise to a wear rate which is around 1.9 times less than that resulting from α-Fe_2O_3. Similarly, if it were possible to have either Fe_3O_4 or FeO as the main surface oxide, then the wear rate resulting from Fe_3O_4 would be around 3.2 times less than that resulting from FeO.

Scanning electron micrographs of the worn disc surfaces

provide further evidence that Fe_3O_4 has greater wear protective properties than either α-Fe_2O_3 or FeO by showing that oxide films which were mainly composed of Fe_3O_4 had a much higher surface coverage than films which were mainly α-Fe_2O_3 or FeO.

Variations in the coefficient of friction, μ, were found to be small. This was to be expected from equation (1.14) since S_i and P_m vary with temperature in the same manner. The small decrease in μ with increasing applied load may be due to a decrease in the contribution from the ploughing term as load increases.

Abrupt increases in heat flow rate into the pin, H_1, and thus the experimentally determined division of heat, δ_{exp}, were observed at a load of around 35 N for both the 2.0 ms^{-1} and 4.0 ms^{-1} wear tests. The increase in H_1 is considered to be due to the sudden decrease in oxide thickness at these loads, as revealed by SEM measurements, while an increase in intermetallic contact could also have been a contributing factor. The cause of this sudden change in oxide thickness was a change in the composition of the oxide, since Fe_3O_4 was found to form thicker films than either α-Fe_2O_3 or FeO. As a result of the abrupt changes in H_1, abrupt changes were also noted in the value of the general surface temperature, T_s.

A theoretical analysis was developed which enabled the estimation of the parameters T_o, a, N and δ_{th}. The calculated values of contact temperature, T_o, were found to increase linearly with load for given load ranges and, furthermore,

it is considered that sharp transitions occur in the magnitude of T_o at certain applied loads which are associated with the observed transitions in the wear rate verus load plots. The increase in T_o when Fe_3O_4 was the main surface oxide is considered to be due to the greater insulation provided by the thicker Fe_3O_4 oxide films. Correlation between the calculated values of T_o and the expected temperatures at which oxide growth occurred on the basis of oxide composition is very good. This points strongly to the fact that T_o is the temperature governing the growth of the oxides on the worn surfaces and hence the magnitude of the wear rate, and not the much lower T_s.

Calculated values of the number of asperities in contact, N, were found to increase smoothly with load, while the average asperity contact radius, a, decreased with load, any decrease in 'a' being much less marked than the corresponding increase in N. Hence, the increase in the real area of contact due to an increase in applied load results mainly from an increase in N.

The correlation between the theoretically deduced surface parameters and the experimentally measured results is very good: transitions are observable in the T_o versus load curves which correspond to transitions in the experimentally determined values of wear rate, T_s and oxide thickness, and these transitions can be explained on the basis of a change in oxide composition as revealed by x-ray diffraction. Furthermore, the agreement between theoretically determined values of division of heat, δ_{th}, and its experimental counterpart, δ_{exp}, is good. In view of this it is considered that

the surface model utilized in the present study yielded useful information regarding the processes occurring at the sliding interfaces.

Measurements of oxide thickness, ξ, by means of SEM has revealed that values of ξ were around 2-6μm, and that the oxide thickness on the pin did not differ greatly from that on the disc. Fe_3O_4 was found to produce thicker oxide films than either α-Fe_2O_3 or FeO, while a slight increase in ξ with load was observable in any given oxide region. A very important point which is evident from scanning electron micrographs of oxide edges is that the oxide films are physically homogeneous, and this suggests that film growth occurs by a diffusion mechanism.

Values of activation energy, Q_p, and Arrhenius constant, A_p, relevant to the parabolic oxidation of low alloy steel surfaces under static oxidizing conditions have been experimentally determined. Comparison of these values with corresponding values determined for oxidation during the sliding wear of low alloy steel indicates that while Q_p does not differ greatly in the two cases, A_p for tribo-oxidation is considerably greater than that for static oxidation resulting in correspondingly higher growth rates.

Concentration versus depth profiles and oxygen maps obtained from AES analyses reveal that the plateaux present on the worn surfaces consist of oxide. In particular the shape of the oxygen concentration versus depth profiles provides further evidence that the oxide films have a physically homogeneous structure. The AES results also indicate that

Fe_3O_4 formsthicker oxide films than either α-Fe_2O_3 or FeO, in agreement with SEM measurements.

The wear tests in which EN8 pins were worn against 9% Cr steel discs resulted in mild wear. Scanning electron micrographs show that the worn surfaces were covered with smooth plateaux, while AES results show that these plateaux consist of oxide. The relative concentrations of chromium detected in the oxides on the EN8 pins and 9% Cr discs indicates that transfer of oxide from the disc to the pin did not occur during mild wear. This suggests that the oxide films grow separately on the two wearing surfaces.

X-ray photoelectron spectroscopy has been used to study the core-level electrons in iron and its three oxides. The characteristic core-level photoelectron spectra for α-Fe_2O_3, Fe_3O_4 and FeO powder surfaces and for an Fe metal surface have been obtained. The binding energies of the photoelectron peaks have been measured and those due to Fe can be used to provide identification of Fe^{2+} and Fe^{3+} species and of iron oxides themselves. The use of the more intense $Fe2p_{3/2}$ and $Fe2p_{1/2}$ peaks plus associated satellite peaks are particularly useful for this purpose.

The O1s spectra of the oxide surfaces invariably consisted of two overlapping peaks. The lower binding energy peak was due to oxygen ions in the oxide, and had an almost invariant binding energy with a value of around 530.1 eV. For this reason it cannot be used in the identification of iron oxides. The higher binding energy peak was usually around 531.4 eV, and it is considered that this peak was due to

oxygen ions in hydroxyl groups, present as a result of the adsorption of water on the air exposed surfaces. Occassionally the higher binding energy peak was observed at around 532.1 eV, indicating a different adsorbed species, and this is tentatively attributed to adsorbed oxygen.

Etching of the oxide surfaces with Ar^+ ions led to a rapid reduction of Fe^{3+} ions to Fe^{2+}, and of further reduction to Fe^{o}. Results indicate that etching of an Fe_3O_4 powder surface with 5.0 keV Ar^+ ions resulted in a complete reduction of Fe^{3+} to Fe^{2+} after only a few minutes.

The XPS spectra of worn surfaces indicate that the iron in the surface layers of the oxide was invariably in an Fe^{3+} state, present in α-Fe_2O_3, or in a hydroxide produced by adsorption of water, or more probably a combination of both. Usually the higher binding energy O1s photoelectron peak occurred at around 531.4 eV, but it occassionally appeared at approximately 532.1 eV indicating a different adsorbed species. This difference in adsorption behaviour might be due to differences in the composition of the underlying oxide.

The XPS spectra of unetched statically oxidized surfaces are similar to those obtained for the worn surfaces, again indicating the presence of α-Fe_2O_3 and an Fe^{3+} adsorption produced contaminant layer. The higher binding energy photo-electron peak in the O1s spectrum usually occurred around 531.4 eV, but in the case of the highly polished steel surface oxidized at 150°C this peak was observable at 532.3 eV and is tentatively attributed to the adsorption of oxygen rather than water.

Identification of chemical states at various depths into the tribologically and statically produced oxides was rendered impossible in the present study by ion beam reduction. All of the oxide surfaces studied by XPS exhibited reduction by Ar^+ ions, but in the case of the thick oxides produced under static oxidizing conditions the rate of reduction was less rapid than for the powder and tribologically produced oxides.

In conclusion, it is felt that the present study has provided useful information regarding the process of mild wear for unlubricated low alloy steel surfaces under certain experimental conditions. In particular, an insight has been gained into the physical and chemical nature of the plateaux present on the worn surfaces, and thus into the mechanism by which these plateaux grow.

Since ion beam reduction was a serious drawback in the spectroscopic analysis of oxide surfaces, a useful extension of this project would be a systematic study of the effect of etching conditions (e.g. etching species, energy) on the reduction of iron oxide surfaces. If conditions could be found which enable sputtering to be performed without oxide reduction then it would be extremely useful to investigate the chemical composition of the oxide plateaux at successive depths into the plateaux. This could then be repeated for oxides grown under static conditions so that a comparison of the two sets of results would reveal any similarities, or otherwise, in the two oxide types e.g. it is well known that statically grown oxides on iron have an air/α-Fe_2O_3/Fe_3O_4/FeO/Fe layered structure, so it would be interesting to see if such a structure exists in the tribologically

produced oxides. If it did then this would reinforce the present view that the oxides grow by a diffusion mechanism. It would also be worthwhile to investigate the O1s photo-electron spectra from a wide range of oxidized surfaces since the results presented in this thesis suggest that the position of the higher binding energy peak, resulting from surface adsorption, might depend upon the chemical composition of the underlying oxide. Transmission electron microscopy is a technique which could be used to examine tribologically and statically produced oxides in order to gain information on the grain structure in the two types of oxide. Small pieces of surface oxide which were uplifted from the worn surfaces due to the method of cracking described in this thesis could be used for this purpose.

It would also be worthwhile to extend the investigation of tribo-oxidation to study the initial stages of film formation rather than the equilibrium films. Furthermore, a more detailed comparison of the oxide films formed under different sliding conditions e.g. unidirectional and reciprocating sliding, by a range of analytical techniques would be very useful in establishing the different mechanisms by which wear protective oxide films are formed.

APPENDIX

```
100 REM PROGRAM "SURF PARAMETERS"
110 REM PROGRAM TO FIND A,N,TC,D THEORY
120 PM=2.56E9:U=2.00:KD=52:KP=52
130 OPEN1,4
140 PRINT"LOAD VALUE"
150 INPUTW
160 PRINT"FRICTION VALUE"
170 INPUTF
180 PRINT"H1 VALUE"
190 INPUTH1
200 PRINT"TS VALUE"
210 INPUTTS
220 PRINT"TD VALUE"
230 INPUTTD
240 PRINT"DISC THICKNESS VALUE"
250 INPUTZD
260 PRINT"PIN THICKNESS VALUE"
270 INPUTZI
280 HD=U*F-H1
290 Y=PM/W
300 T=TS
301 GOTO 310
305 T=TC
310 KO=4.03-0.00137*(T+273)
340 CH=KO/3880338
350 A=(Y*U*HD)/(20*CH*KD)
360 B=-Y*(0.86*HD/KD-H1/KP-(U*HD*ZD)/(20*CH*KO))
370 C=-Y*(0.86*HD*ZD/KO-H1*ZI/KO)+TS-TD
380 BB=B↑2
390 CC=4*A*C
400 IF BB<CCTHEN590
410 AR=(-B+SQR(BB-CC))/(2*A)
415 REM AR IS RADIUS OF CONTACT
420 IF AR<0THEN610
430 N=1/(3.14159*Y*AR*AR)
435 REM N IS NO OF CONTACTS
440 T1=TS+(Y*H1*AR)/KP
450 TC=T1+(Y*H1*ZI)/KO
455 REM TC IS CONTACT TEMP
456 IFTC<(T-10)THEN305
457 IFTC>(T+10)THEN305
460 AL=0.96-(U*AR)/(20*CH)
470 X=Y*U*F
480 D=(AL*X*AR/KD)+(AL*X*ZD/KO)
490 P=(X*AR/KP)+(X*ZI/KO)
495 REM D AND P ARE FLASH TEMPS
500 DT=(D*100)/(P+D)
505 REM DT IS THEORETICAL DI'WEAT
506 PRINT#1,"            T=";T
510 PRINT#1,"           KO=";KO
520 PRINT#1,"          CHI=";CH
530 PRINT#1,"            A=";AR
540 PRINT#1,"            N=";N
550 PRINT#1,"           TC=";TC
560 PRINT#1,"DELTA THEORY=";DT
570 PRINT#1,
580 GOTO650
590 PRINT#1,"NO REAL VALUE"
600 GOTO 620
610 PRINT#1,"VALUE OF A IS NEGATIVE"
620 PRINT#1,
640 CLOSE1
650 STOP
READY.
```

REFERENCES

1. LAWLESS K.R., 'the Oxidation of Metals', Reports on Progress in Physics 37(1974)231.

2. OUDAR J., 'The Physics and Chemistry of Surfaces', Blackie and Sons Ltd. (1975).

3. BERNARD J., 'The Oxidation of Metals and Alloys', Metallurgical Reviews 9(No.36)(1964)473

4. LUSTMAN B., 'The Rate of Film Formation on Metals', Trans. Electrochem. Soc. 81(1942)359

5. CABRERA N. and MOTT N.F., 'Theory of the Oxidation of Metals', Reports on Progress in Physics 12(1948-49)163.

6. FEHLNER F.P. and MOTT N.F. in 'Oxidation of Metals and Alloys', Metals Park: ASM (1971)37.

7. HAUFFE K. in 'The Surface Chemistry of Metals and Semiconductors', Ed. Gatos H.C., John Wiley and Sons (New York) (1960)

8. FROMHOLD A.T. and COOK E.L., 'Kinetics of Oxide Film Growth of Metal Crystals: Electron Tunnelling and Ionic Diffusion', Phys. Rev. 158(1967)600.

9. MOTT N.F., 'The Theory of the Formation of Protective Oxide Films on Metals II', Trans. Faraday Soc. 36(1940)472

10. LANDSBERG P.T., 'On the Logarithmic Rate Law in Chemisorption and Oxidation', J. Chem. Phys. 23(1955)1079.

11. RITCHIE I.M. and HUNT G.L., 'The Kinetics and Pressure Dependence of Surface Controlled Metal Oxidation Reactions', Surf. Sci. 15(1969)524.

12. WAGNER C., 'Beitrag zur Theorie des Anlaufvorgangs', Z. Physik. Chem. B21(1933)25.

13. FROMHOLD A.T. and COOK E.L., 'Kinetics of Oxide Film Growth on Metal Crystals: Thermal Electron Emission and Ionic Diffusion', Phys. Rev. 163(1967)650.

14. DAVIES D.E., EVANS U.R. and AGAR N.J., 'The Oxidation of Iron at 175 to 350^{o}C', Proc. Roy. Soc. (London) A225 (1954)443

15. EVANS U.R., 'The Corrosion and Oxidation of Metals' Edward Arnold Ltd. (London) (1960)

16. HARRISON P.L., 'Oxidation by Transport through Blocking Pores', J. Electrochem. Soc. 112(1965)235

17. KUBACHEWSKI O. and HOPKINS B.E., 'Oxidation of Metals and Alloys', Butterworths (London) (1953).

18. HAUFFE K., 'Oxidation of Metals', Plenum Press (New York) (1965)

19. KOFSTAD P., 'High Temperature Oxidation of Metals', John Wiley and Sons (1966).

20. PILLING N.B. and BEDWORTH R.E., 'The Oxidation of Metals at High Temperatures', J. Inst. Metals 29(1923)529.

21. SCHOTTKY W., 'Reaktionstypen bei der Oxydation von Legierungen', (Discussion) 63(1959)784.

22. DUNN J.S., 'The High Temperature Oxidation of Metals', Proc. Roy. Soc. A111(1926)203.

23. CAPLAN D., SPROULE G.I., HUSSEY R.J. and GRAHAM M.T., 'Oxidation of Fe-C Alloys at 500°C', Oxid. Met. (USA). 12(No.1)(1978)67.

24. BOLTAKS B.I., 'diffusion in Semiconductors', Infosearch (London) (1963).

25. LUSTMAN B., 'The Resistance of Metals to Scaling', Metal Progress (1946) 850

26. CAPLAN D. and COHEN M., 'Effect of Cold Work on the Oxidation of Iron from 400-650°C', Corr. Sci. 6(1966)321.

27. AZZAM R.M.A. and BASHARA N.M., 'Ellipsometry and Polarized Light', North-Holland (1977).

28. SIEGBAHN K., ESCA - 'Atomic, Molecular and Solid State Structure Studied by means of Electron Spectroscopy', Almquist and Wiksella (Uppsala) (1967).

29. FADLEY C.S., HAGSTROM S.B.M., KLEIN M.P. and SHIRLEY D.A. 'Chemical Effects on Core-Electron Binding Energies in Iodine and Europium', J. Chem. Phys. 48(1968)3779.

30. BETZ G., WEHNER G.K., TOTH L.E. and JOSHI A., 'Composition versus Depth Profiles Obtained with Auger Electron Spectroscopy of Air-Oxidized Stainless Steel Surfaces', J. Appl. Phys. 45(1974)5312.

31. SULLIVAN J.L. and ATHWAL S.S., 'Mild Wear of a Low Alloy Steel at Temperatures up to 500°C, Tribology International (1983)123.

32. ARCHARD J.F. and HIRST W., 'The Wear of Metals under Unlubricated Conditions', Proc. Roy. Soc., A236(1956)397.

33. BURWELL J.T. and STRANG C.D., 'Metallic Wear', Proc. Roy. Soc., 212(1952)470.

34. BURWELL J.T., 'Survey of Possible Wear Mechanisms', Wear 1(1957)119.

35. RABINOWICZ E., 'The Friction and Wear of Materials', John Wiley and Sons (New York) (1965).

36. QUINN T.F.J., 'Role of Oxidation in the Mild Wear of Steel', Brit. J. Appl. Phys. 13(1962)33.

37. TAO F.F., 'A Study of Oxidation Phenomena in Corrosive Wear', ASLE trans. 12(1969)97.

38. RABINOWICZ E., DUNN L.A. and RUSSELL P.G., 'A Study of Abrasive Wear under 3 Body Conditions', Wear 4(1961)345.

39. BARNETT R.S., 'Fretting and Fretting Corrosion', Lubrication 41(1955)85.

40. STOTT F.H and WOOD G.C., 'The Influence of Oxides on the Friction and Wear of Alloys', Tribology International 11(1978)211.

41. WELSH N.C., 'The Dry Wear of Steels', Parts I and II, Phil. Trans. Roy. Soc. (London) A257(1965)31.

42. YOSHIMOTO G. and TSUKIZOE T., 'On the Mechanism of Wear between Metal Surfaces', Wear 1(1957-58)472.

43. TENWICK N. and EARLES S.W.E., 'A Simplified Theory of Oxidative Wear', Wear 18(1971)381.

44. QUINN T.F.J., 'Oxidational Wear', Wear 18(1971)413

45. ARCHARD J.F., 'Contact and Rubbing of Flat Surfaces', J. Appl. Phys. 24(1953)981.

46. SULLIVAN J.L., QUINN T.F.J. and ROWSON D.M., 'Developments in the Oxidational Theory of Mild Wear', Tribology International 13(4) (1980)153.

47. ATHWAL S.S., 'Wear of Low Alloy Steels at Elevated Temperatures', Ph.D. Thesis, University of Aston (1983).

48. STOTT, F.H., LIN D.S. and WOOD G.C., 'The Structure and Mechanism of Formation of the 'Glaze' Oxide Layers Produced on Nickel-Based Alloys during Wear at High Temperatures', Corr. Sci. 13(1973)449.

49. BOWDEN F.P. and TABOR D., 'The Friction and Lubrication of Solids', Clarendon Press (Oxford) Part I (1954), Part II (1964).

50. WHITEHEAD J.R., 'Surface Deformation and Fracture of Metals at Light Loads', Proc. Roy. Soc. A201 (1950)109.

51. WILSON J.E., SOTT F.H. and WOOD G.C., 'The Development of Wear Protective Oxides and their Influence on Sliding Friction', Proc. Roy. Soc. (London) A369(1980)557.

52. RIGNEY D.A. and HIRST J.P., 'Plastic Deformation and Sliding Friction of Metals', Wear 53(1979)345.

53. BOWDEN F.P. and RIDLER K.E.W., 'A Note on the Surface Temperature of Sliding Metals', Proc. Roy. Soc. A151(1936)431.

54. FUREY M.J., 'Surface Temperatures in Sliding Contact', Trans. ASLE 1(1964)133.

55. BLOK H., 'Theoretical Study of Temperature Rise at Surfaces of Actual Contact under Oiliness Lubricating Conditions', Inst. Mechn. Engrs. (Proc. General Discussion on Lubrication and Lubricants) 2(1937)222.

56. JAEGER J.C., 'Moving Sources of Heat and the Temperature at Sliding Contacts', Proc. Roy. Soc. (New South Wales) 56(1942)203.

57. ARCHARD J.F., 'The Temperature of Rubbing Surfaces', Wear 2(1959)438.

58. GROSBERG P. and MOLGAARD J., 'Aspects of the Wear of Spinning Travellers : the Division of Heat at Rubbing Surfaces', Proc. Instn. Mechn. Engrs. 181(3L)(1966-67)16.

59. QUINN T.F.J., 'The Division of Heat and Surface Temperature at Sliding Steel Interfaces and their Relation to Oxidational Wear', Trans. ASLE 21(1978)78.

60. McCRACKIN F.L., PASSAGLIA E., STROMBERG R.R. and STEINBERG H.L., 'Refractive Index of Very Thin Films and the Optical Properties of Surfaces by Ellipsometry', J. of Research of the National Bureau of Standards 67A(1963)363

61. DITCHBURN R.W., 'Some New Formulas for Determining the Optical Constants from Measurements on Reflected Light', J. Opt. Soc. Am. 45(1955)743.

62. MUSA A.H., 'Optical Properties of some Surfaces for Solar Energy Application', Ph.D. Thesis, University of Aston (1980)

63. SEAH M.P., 'Quantitative Auger Electron Spectroscopy : Modulating the Spectrometer', Surface and Interface Analysis 1(No.3) (1979)91.

64. SEAH M.P., 'Quantitative Auger Electron Spectroscopy : Via the Energy Spectrum or the Differential?', Surface and Interface Analysis 1(No.3) (1979)86.

65. CHANG C.C., 'Auger Electron Spectroscopy', Surf. Sci. 25(1971)53.

66. XSAM 800 Operators Handbook, Kratos.

67. Powder Diffraction Data File of the American Society for Testing and Materials (ASTM).

68. DUNCKLEY P.M. and QUINN T.F.J., 'The Effect of Elevated Temperatures and Speed upon the Wear of Mild Steel', Trans. ASLE 19(3) (1978)221.

69. QUINN T.F.J., ROWSON D.M. and SULLIVAN J.L., 'Application of the Oxidational Theory of Mild Wear to the Sliding Wear of Low Alloy Steel', Wear 65(1980)1.

70. SMITHELLS C.J., 'Metals Reference Handbook', Volume 3, 4th Edition, Butterworths (1967).

71. MOLGAARD J. and SMELTZER W.W., 'Thermal Conductivity of Magnetite and Haematite', J. Appl. Phys. 42(9) (1971)3644.

72. 'Handbook of Chemistry of Physics', Chemical Rubber Company, 44th Edition.

73. ALLEN G.C, CURTIS M.T., HOOPER A.J. and TUCKER P.M., 'X-Ray Photoelectron Spectroscopy of Iron-Oxygen Systems', J. Chemical Soc. (Dalton) (1974) 1525.

74. McINTYRE N.S. and ZETARUK D.G., 'X-Ray Photoelectron Spectroscopic Studies of Iron Oxides', Analytical Chemistry 49(No.11) (1977)1521.

75. SCOFIELD J.H., 'Hartree-Slater Subshell Photoionisation Cross-sections at 1254 and 1487 eV', J. Electron. Spectrosc. and Related Phenom. 8(1976)129.

76. EVANS S., PRITCHARD R.G. and THOMAS J.M., 'Relative Differential Subshell Photoionisation Cross-sections (MgKα) from Lithium to Uranium', J. Electron Spectrosc. and Related Phenom. 14(1978)341.

77. REILMAN R.F., MSEZANE A. and MANSON S.T., 'Relative Intensities in Photoelectron Spectroscopy of Atoms and Molecules', J. Electron Spectrosc. and Related Phenom. 8(1976)389.

78. OLEFJORD I., 'ESCA Studies of the Composition Profile of Low Temperature Oxide Formed on Chromium Steels - Part I. Oxidation in Dry Oxygen', Corr. Sci. 15(1975)687.

79. SEAH M.P. and DENCH W.A., 'Quantitative Electron Spectroscopy of Surfaces : a Standard Data Base for Electron Inelastic Mean Free Paths in Solids', Surface and Interface Analysis 1(No.1) (1979)1.

80. DAVIES L.E., McDONALD N.C., PALMBERG P.W., RIACH G.E. and WEBER R.E., 'Handbook of Auger Electron Spectroscopy', Physical Electronic Industries (Minnesota) (1976).

81. GRANVILLE N.W., 'Reciprocating Sliding Wear of 9% Cr Steel in Carbon Dioxide at Elevated Temperatures', Ph.D. Thesis (in preparation), University of Aston (1984).

82. SAMSONOV G.V., 'The Oxide Handbook', Plenum Press (1973).

83. QUINN T.F.J., 'The Effect of Hot Spot Temperatures on the Unlubricated Wear of Steel', Trans. ASLE 10(1967)158.

84. ARCHARD J.F., 'Single Contacts and Multiple Encounters', J. Appl. Phys. 32(1961)1420.

85. QUINN T.F.J., 'An Experimental Study of the Thermal Aspects of Sliding Contacts and their Relation to the Unlubricated Wear of Steel', Proc. Instn. Mechn. Engrs. 183(3P) (1968-69)129.

86. POWELL C.J., 'Attenuation Lengths of Low Energy Electrons in Solids', Surf. Sci. 44(1974)29.

87. TRACY J.C. and BURKSTRAND J.M., in 'Critical Reviews in Solid State Sciences', Schuele D.E. and Hoffman R.W., vol.4., issue 3, CRC Press.

88. PENN D.R., 'Quantitative Chemical Analysis by ESCA', J. Electron Spectrosc. and Related Phenom. 9(1976)29.

89. KAYE G.W.C. and LABY T.H., 'Tables of Physical and Chemical Constants', 14th Edition, Longman (1973).

90. RIDGWAY J.W.T. and HANEMAN D., 'Auger Spectra and LEED Patterns from Vacuum Cleaned Silicon Crystals with Calibrated Deposits of Iron', Surf. Sci. 24(1971)451.

91. NEEDHAM P.B. and DRISCOLL T.J., 'Determination of Auger Electron Cross Sections and Ranges using Proton-Excited X-Rays', J. Vac. Sci. Technol. 11(1974)278.

92. JABLONSKI A., 'Backscattering Effects in Auger Electron Spectroscopy : a Review', Surface and Interface Analysis 1(4) (1979)122

93. HOFMANN S., in 'Practical Surface Analysis by Auger and X-Ray Photoelectron Spectroscopy', ed. Briggs D. and Seah M.P., Wiley and Sons (1983).

94. SEAH M.P., 'A Quantitative Framework for the Analysis of Surfaces by AES and XPS' (Analusis) 9(5) (1981) 171.

95. MOLGAARD J. and SRIVASTAVA V.K., 'The Activation Energy of Oxidation in Wear', Wear 41(1977)263.

96. GOOD J.N. and GODFREY D., 'Changes Found on Run-in and Scuffed Surfaces of Steel, Chrome Plate and Cast Iron', NASA Technical Note 1432(1947).

97. BISSON E.F., JOHNSON R.L. and SWIBERT M.A., 'Friction, Wear and Surface Damage of Metals as Affected by Solid Films', NASA Technical Note 3444(1955).

98. CLARK W.T., PRITCHARD C. and MIDGLEY J.W., 'Mild Wear of Unlubricated Hard Steels in Air and Carbon Dioxide', Proc. Inst. Mechn. Engrs. 182(1967)99.

99. TSUJI E., 'Research on the Wear of Carbon Steel from 200^{o}C to 500^{o}C', Trans. N.R.I.M. 9(1967)301.

100. HURRICKS P.L., 'The Fretting Wear of Mild Steel from 200^{o}C to 500^{o}C', Wear 30(1974)189.

101. CORNELIUS D.F. and ROBERTS W.H., 'Friction and Wear of Metals in Gases up to 600^{o}C', ASLE Trans. 4(1961)20.

102. EARLES S.W.E. and POWELL D.G., 'Variation in Friction and Wear between Unlubricated Steel Surfaces', Proc. Inst. Mechn. Engrs. 182(3N) (1968)167.

103. QUINN T.F.J., BAIG A.R., HOGARTH C.A. and MULLER H., 'Transitions in the Friction Coefficients, the Wear Rates, and the Composition of the Wear Debris produced in the Unlubricated Sliding of Chromium Steels', Trans. ASLE 16(4) (1972)239.

104. VERNON W.H.J., CALNAN E.A., CLEWS C.J.B. and NURSE T.J., 'The Oxidation of Iron around 200^{o}C', Proc. Roy. Soc. A216(1953)375.

105. KRAGELSKII I.V., 'Friction and Wear', Butterworths (London) (1965).

106. SULLIVAN J.L. and GRANVILLE N.W., 'Reciprocating Sliding Wear of 9% Cr Steel in Carbon Dioxide at Elevated Temperatures', Tribology International (1984)63.

107. GRANVILLE N.W., Private Communication, (1984).

108. CHILDS T.H.C., 'The Sliding Wear Mechanisms of Metals, Mainly Steels', Tribology International (1980)285.

109. KIM K.S., BAITINGER W.E., AMY J.W. and WINOGRAD N., 'ESCA Studies of Metal-Oxygen Surfaces using Argon and Oxygen Ion Bombardment', J. Electron Spectrosc. and Related Phenom. 5(1974)351.

110. OOSTROM A.V., 'Some Aspects of Auger Microanalysis', Surf. Sci. 89(1979)615.

111. BRUNDLE C.R., CHUANG T.J. and WANDELT K., 'Core and Valence Level Photoemission Studies of Iron Oxide Surfaces and the Oxidation of Iron', Surf. Sci. 68 (1977)459.

112. ASAMI K. and HASHIMOTO K., 'The X-Ray Photoelectron Spectra of Several Oxides of Iron and Chromium', Corr. Sci. 17(1977)559.

113. GRENET G., JUGNET Y., TRAN MINH DUC and KIBLER M., 'On the FeO Valence Band Photoemission Spectra', J. Chem. Phys. 72(1) (1980)1.

114. OKU M. and HIROKAWA K., 'X-Ray Photoelectron Spectroscopy of Co_3O_4, Fe_3O_4, Mn_3O_4 and Related Compounds', J. Electron Spectrosc. and Related Phenom. 8(1976)475.

115. ASAMI K., HASHIMOTO K., and SHIMODAIRA S., 'X-Ray Photoelectron Spectrum of Fe^{2+} State in Iron Oxides', Corr. Sci. 16(1976)35.

116. FADLEY C.S., in 'Electron Spectroscopy', Ed. Shirley D.A., North Holland (Amsterdam) (1972).

117. FROST D.C., McDOWELL C.A. and WOOLSEY J.S., 'X-Ray Photoelectron Spectra of Cobalt Compounds', Mol. Phys. 27(1974)1473.

118. WALLS J.M., HALL D.D. and SYKES D.E., 'Composition Depth Profiling and Interface Analysis of Surface Coatings using Ball Cratering and the Scanning Auger Microprobe', Surface and Interface Analysis 1(6) (1979)204.

J. Phys. D: Appl. Phys., 16 (1983) 723–732. Printed in Great Britain

A study of the core level electrons in iron and its three oxides by means of x-ray photoelectron spectroscopy

P Mills and J L Sullivan
Department of Physics, University of Aston in Birmingham, Birmingham B4 7ET, UK

Received 9 November 1982

Abstract. The core level electrons in iron and its three oxides FeO, Fe_3O_4 and α-Fe_2O_3 have been studied by means of x-ray photoelectron spectroscopy. The main features of the spectra have been identified and electron binding energies have been measured. The Fe 2p peaks of the oxide spectra are broadened (FWHM ~ 4.5 eV) due to unresolved multiplet splitting, and shake-up satellites can be observed for both Fe^{II} and Fe^{III} species. For all the samples studied the O 1s spectra consist of two overlapping peaks, one due to the oxide and a higher binding energy peak due to an adsorbed species. The higher binding energy peak was frequently dominant indicating a high degree of adsorption on the oxide surfaces. The effect of argon ion etching on the surfaces has also been investigated and the results indicate that the analysis of surfaces by means of ion etching in conjunction with XPS can give misleading results.

1. Introduction

The core electrons of the molecular bonded atoms in compounds are basically in atomic orbitals, their binding energies being characteristic of the atoms. However, slight changes occur in the core-level binding energies with changes in chemical environment. This is a result of alterations in the valence shell electron density, since the valence shell electrons contribute to the net force experienced by the core-level electrons. A positive change in oxidation state produces a slight increase in binding energy and vice versa for a negative change in oxidation state. We therefore expect small differences in the binding energy values of the core-electrons of the three oxides FeO, Fe_3O_4 and α-Fe_2O_3 since they contain Fe^{II} and Fe^{III} ions in differing amounts. FeO contains exclusively Fe^{II} ions, the ions being octahedrally coordinated in a cubic lattice. Fe_3O_4 contains both Fe^{II} and Fe^{III} ions in an inverse cubic spinel structure, with the Fe^{II} ions in octahedral sites and Fe^{III} ions half in octahedral and half in tetrahedral sites. α-Fe_2O_3 contains exclusively Fe^{III} ions in a lattice having the rhombahedral Al_2O_3 structure.

It is the purpose of this present work to study the spectra of iron and its oxides and to measure these small changes in binding energy. The binding energy values so produced can then be used as reference values to facilitate the identification of oxides grown on iron and steels.

2. Experimental details

The oxides studied were commercially obtained powders. All were first bulk characterised by x-ray diffraction. The iron studied was in the form of a thin sheet (0.5 mm thickness) 99.9% pure, supplied by Goodfellow Metals, Cambridge.

Oxide surfaces were prepared by intimately mixing oxide powder with gold powder and pressing into lead sheet. All binding energy measurements were then made with reference to the Au $4f_{7/2}$ line at 84.0 eV.

Samples were first studied in the air-exposed form. They were then successively etched with an argon ion gun operated at 5 kV, 25 μA producing a specimen current of approximately 20 μA, spectra being recorded at the end of each etching period. The analysis was carried out in a Kratos XSAM 800 ESCA–Auger Spectrometer, using Mg Kα as the exciting radiation. The pressure inside the experimental chamber was *ca.* 10^{-9} Torr. Each analysis was performed several times to test for reproducibility of results.

3. Results

Fe $2p_{3/2}$, $2p_{1/2}$, 3p, 3s, O ls and Au $4f_{7/2}$ spectra were recorded. Binding energy measurements were made relative to the Au $4f_{7/2}$ peak at 84.0 eV. It was also considered useful to record the C 1s spectra due to hydrocarbons on the sample surfaces as the binding energy of this line is often used as a reference value in XPS work.

The C 1s peak was invariably the most intense spectral peak for all samples in the unetched state. Measurements for this peak and for the Fe $2p_{3/2}$ peaks for FeO, Fe_3O_4 and α-Fe_2O_3 show relative intensities of 4.6, 5.6 and 3.2 respectively in the unetched condition. Estimated values of carbon present in all three cases, expressed as an atomic fraction, were about 0.7. These are semi-quantitative estimates based on peak area measurements, and cross-section values due to Scofield (1976). No account was taken of photoelectron angular intensity distributions or analyser or detector efficiency variations with photoelectron energy.

These latter quantities have as yet not been reliably determined for the instrument used in this investigation. More reliable quantitative results may perhaps be obtained from the very comprehensive data of Evans *et al* (1978) recorded on an AEI ES-200 spectrometer together with angular intensity distributions taken from the work of Reilman *et al* (1976), however, serious quantitative analyses should be attempted only when a full appraisal of the XSAM-800 instrumental characteristics has been undertaken.

After a period of about 1 min of ion etching under the conditions previously stated the carbon peak had fallen to a negligible level, indicating that carbon contamination had been effectively removed.

Figure 1 shows the Fe $2p_{3/2}$ and Fe $2p_{1/2}$ spectra of FeO, Fe_3O_4 and α-Fe_2O_3 powder surfaces. Figure 1(A), showing the spectrum of air-exposed FeO, is very similar to figure 1(C), showing the spectrum of Fe_3O_4, indicating the presence of Fe^{III} species on the FeO surface. Both these spectra differ from that of α-Fe_2O_3 in figure 1(D) and so the similarity is not due to a covering of α-Fe_2O_3 as is often the case with FeO and Fe_3O_4 surfaces which have been exposed to air. These results lead us to the conclusion that the FeO surface was initially covered by a layer of Fe_3O_4. Upon etching the FeO sample surface very briefly with Ar^+ ions, the binding energy of the peaks shifted to a lower value, and

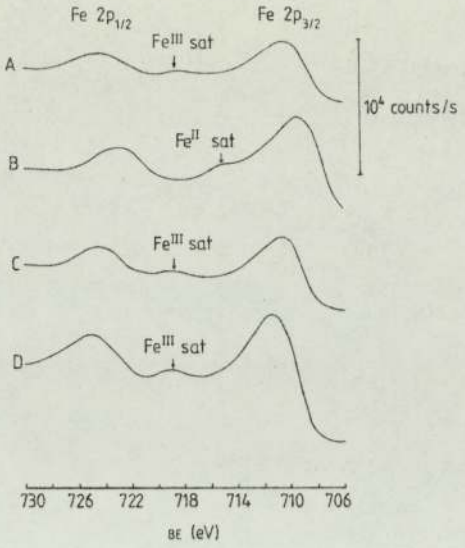

Figure 1. Fe $2p_{3/2}$ and Fe $2p_{1/2}$ spectra of iron oxide surfaces. Curves: (A) air-exposed FeO powder; (B) sample of (A) briefly etched (1 min); (C) air-exposed Fe_3O_4 powder; (D) air-exposed α-Fe_2O_3 powder.

the satellite peak previously present disappeared, being replaced by another satellite peak at a lower binding energy. Further etching did not alter the position of the maxima of the Fe $2p_{3/2}$ and Fe $2p_{1/2}$ peaks, nor did the lower binding energy satellite peak disappear. It was concluded from these results that figure 1(B) is representative of the Fe 2p spectrum of an FeO surface. The spectra C and D in figure 1 are considered to represent the Fe 2p spectra of Fe_3O_4 and α-Fe_2O_3 surfaces respectively.

Figure 2 shows the spectra recorded for air-exposed Fe metal, before and after argon

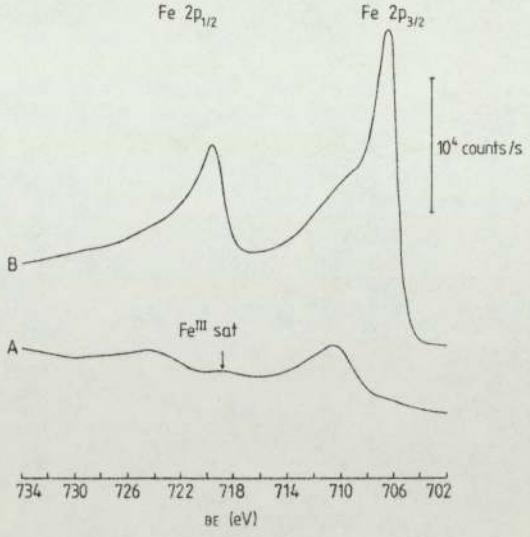

Figure 2. Fe $2p_{3/2}$ and Fe $2p_{1/2}$ spectra of Fe sheet. Curves: (A) air-exposed spectrum; (B) sample of (A) briefly etched (5 min).

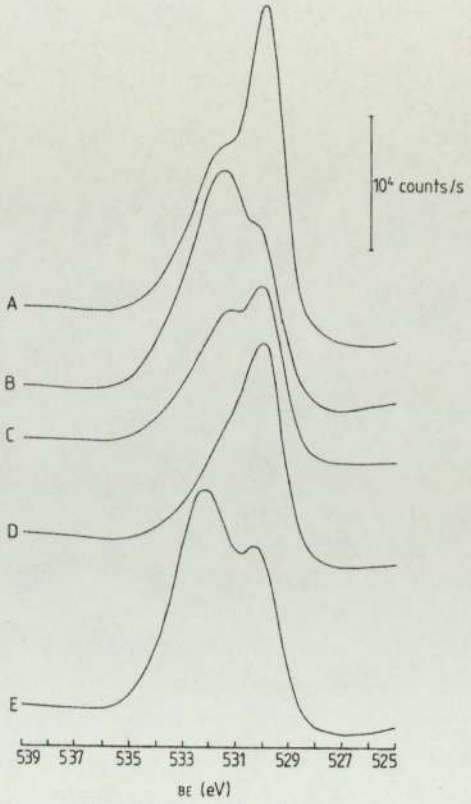

Figure 3. O 1s spectra of iron and iron oxides. Curves: (A) air-exposed α-Fe_2O_3 powder; (B) air-exposed Fe_3O_4 powder; (C) air-exposed FeO powder; (D) sample of (C) briefly etched (1 min); (E) air-exposed Fe sheet.

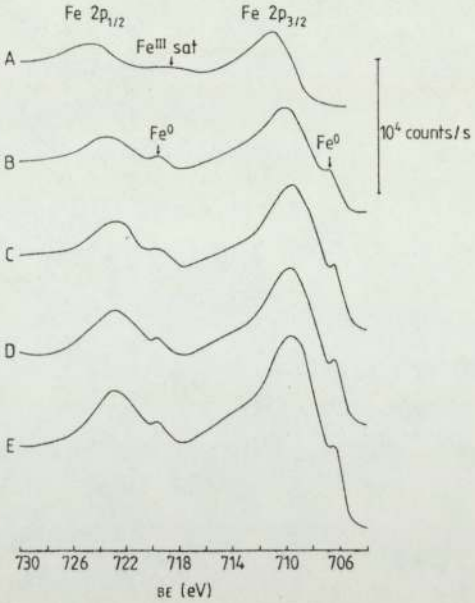

Figure 4. Effect of Ar^+ ion etching on Fe_3O_4 powder sample. Curves: (A) unetched, air-exposed sample; (B) 1 min etch; (C) 5 min etch; (D) 15 min etch; (E) 60 min etch. Ion gun 2 kV; specimen current 20 μA.

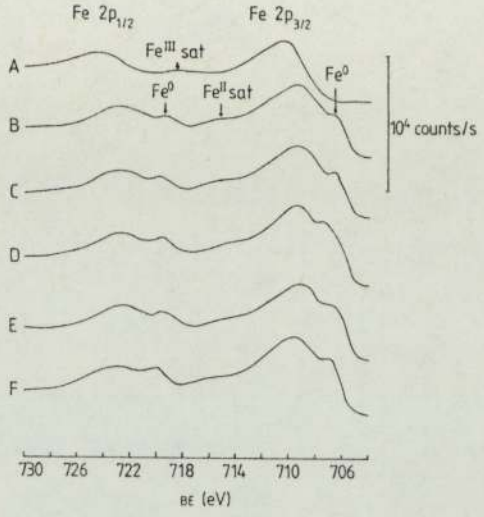

Figure 5. Effect of Ar^+ ion etching on FeO powder sample. Curves: (A) unetched, air-exposed sample; (B) 15 min etch; (C) 30 min etch; (D) 45 min etch; (E) 60 min etch; (F) 90 min etch. Ion gun 2 kV; specimen current 20 μA.

ion etching. The spectrum of the unetched Fe surface in figure 2(A) closely resembles that due to Fe_3O_4 in figure 1(C), indicating a covering of Fe_3O_4 on the air-exposed Fe surface. Upon etching, the sharply defined peaks due to the metal surface rapidly become prominent as illustrated in figure 2(B). The high binding energy shoulders of these peaks show the presence of some remaining oxide.

The O 1s spectra of the oxide surfaces are shown in figure 3. In each case the spectra

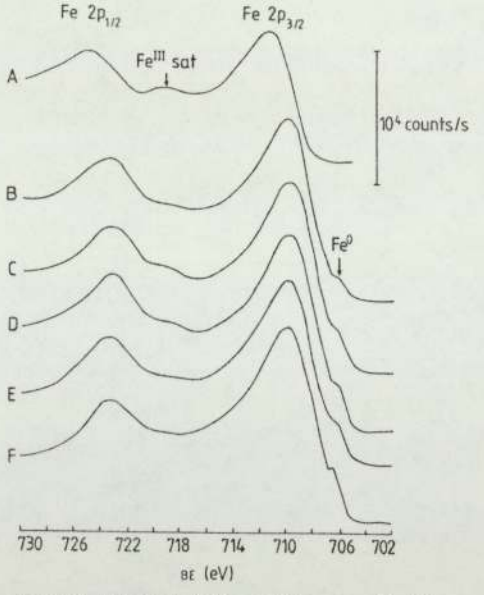

Figure 6. Effect of Ar^+ ion etching on α-Fe_2O_3 powder sample. Curves: (A) unetched, air-exposed sample; (B) 1 min etch; (C) 5 min etch; (D) 15 min etch; (E) 30 min etch; (F) 60 min etch. Ion gun 2 kV; specimen current ~20 μA.

consist of two overlapping peaks, one due to the oxide and one approximately 1 eV higher in binding energy. The binding energy values of the oxide peaks for the three oxides are almost identical. The O 1s spectrum for air-exposed Fe metal is shown in figure 2(E). Again two peaks are observable, but in this case the higher binding energy peak is about 2 eV above the oxide peak.

The intensities of the O 1s peak due to the absorbed species was greater than that of the Fe $2p_{3/2}$ peak for samples in their unetched, air-exposed form. Relative peak intensities for FeO, Fe_3O_4 and α-Fe_2O_3 samples being 2.8, 5.2 and 1.7 respectively. Upon etching the peaks due to the contaminant layer rapidly diminished, with the Fe $2p_{3/2}$ becoming the more intense of the two. The oxide O 1s peaks were always found to be more intense than the Fe $2p_{3/2}$ peaks; however, with the limited information on instrumental characteristics available, it is felt that an estimate of relative atomic concentration of these elements might be misleading at this stage.

The effects of argon ion etching on the Fe 2p spectra are shown in figures 4, 5 and 6. In each instance an ion gun operated at 5 kV and 25 mA was used, producing a specimen current of around 20 μA. For all three oxide surfaces examined, ion bombardment resulted in a shift in the binding energy of the Fe $2p_{3/2}$ and Fe $2p_{1/2}$ peaks to a lower value, and the Fe^0 peaks of iron metal appeared quite rapidly. The effect of etching on the O 1s spectra was to cause a rapid diminishing of the higher binding peak, leaving the peak due to the oxide remaining.

The binding energy values of the core-level electrons in FeO, Fe_3O_4, α-Fe_2O_3 and Fe metal resulting from this study are listed in table 1.

4. Discussion

Certain general points can be made for the spectra of the iron oxides.

The phenomenon of multiplet splitting associated with photoelectron peaks is due to the presence of unpaired valence electrons, resulting in an exchange interaction which affects differently the remaining spin-up or spin-down core electrons. In the case of high spin states this phenomenon is heightened, and for the high spin states Fe^{II} and Fe^{III} we observe broadening of the Fe 2p peaks due to unresolved multiplet splitting. In this present study Fe $2p_{3/2}$ and Fe $2p_{1/2}$ peak widths (FWHM) of *ca.* 4.5 eV are observed, irrespective of oxide, in good agreement with Brundle *et al* (1977), who also report a value of *ca.* 4.5 eV for Fe^{II} and Fe^{III} states, and Allen *et al* (1974) who state that we should expect to observe Fe 2p peak widths of between 3.8 eV and 4.4 eV for the Fe^{III} state.

Table 1. Core-level binding energies (BE) in eV for iron and iron oxides.

	Fe $2p_{3/2}$		Fe $2p_{1/2}$		Fe 3p	Fe 3s	O 1s	C 1s
	BE (±0.2)	FWHM	BE (±0.2)	FWHM	BE (±0.2)	BE (±0.2)	BE (±0.2)	BE (±0.2)
Fe metal	706.5	3.9	719.7	4.5	52.9	91.3	530.1 (and 532.4)	284.9
FeO unetched	710.7	4.4	724.4	4.2	56.0	93.6	530.0 (and 531.3)	284.9
FeO etched	709.6	5.0	722.9	4.4	54.8	93.3 ± 0.5	530.1 (and 531.4)	284.9
Fe_3O_4	710.8	4.0	724.7	3.6	56.4	94.0	530.3 (and 531.4)	285.0
α-Fe_2O_3	711.6	5.0	725.1	4.4	56.6	94.0	529.9 (and 531.4)	285.2

Asami *et al* (1976) have studied the Fe^{II} state in iron oxides by deconvolution of the Fe^{III} peak from spectra obtained from a mixture of FeO, Fe_3O_4 and α-Fe_2O_3. The value they obtained of around 2.0 eV for the width of the Fe $2p_{3/2}$ peak is much too small.

Another characteristic feature of the oxide spectra, which has been empirically observed for other high spin states of transition metal ions (Frost *et al* 1974) is the presence of satellite peaks. These shake-up core-level satellites are caused by an incident x-ray photon giving up a discrete portion of its energy to the excitation of a second electron rather than imparting its entire quantum of energy to the primary, photoejected electron. This photoelectron will thus have lost a small amount of energy and will appear at a slightly higher binding energy than the parent peak. Satellite peaks are observable for both the Fe^{II} and Fe^{III} states in this present study.

The O 1s spectra could invariably be resolved into two peaks approximately 1 eV apart. The lower binding peak due to the oxide has an almost constant value of around 530.1 eV, irrespective of oxide, in agreement with the results of Brundle *et al* (1977) and Allen *et al* (1974). The second peak, which occurs around 531.4 eV, disappeared rapidly upon argon ion etching. This peak was almost certainly due to the presence of hydroxyl species as a result of chemisorption of water on the air-exposed surfaces. This view is shared by Allen *et al* (1974), who also found their oxide surfaces to be highly susceptible to adsorption, with an O 1s adsorption peak occurring around 531.9 eV. Asami *et al* observed a peak at 531.5 eV and attributed it to the presence of iron oxy-hydroxide. Brundle *et al* (1977), while agreeing that this peak could be due to a hydroxyl species, also believe it could represent non-stoichiometric surface oxygen atoms since they have still observed its presence on surfaces which have not been air-exposed. In the case of air-exposed Fe metal the higher binding energy peak is approximately 2 eV above the oxide peak, which would seem to indicate a different adsorbed species to that just discussed. Allen *et al* (1974) reported an O 1s spectrum for FeO that was consistently dominated by a peak at around 532.2 eV, higher than that for other oxide surfaces, which they considered may have been due to adsorbed oxygen rather than water. In view of the high concentration of carbon on the unetched sample surfaces it may also be possible that these O 1s peaks could be due to a hydrocarbon contaminant layer. The oxide spectra will now be considered in detail.

4.1. FeO—Wustite

The Fe 2p spectrum for air-exposed FeO is shown in figure 1(A). There is a marked similarity between this spectrum and that of figure 1(C) due to Fe_3O_4. The Fe $2p_{3/2}$ and Fe $2p_{1/2}$ binding energies of the former are 710.7 eV and 724.4 eV respectively, while the respective values of the latter are 710·8 eV and 724.7 eV. A satellite peak is observable at approximately 8.0 eV above the parent Fe $2p_{3/2}$ peak in both cases. Although FeO and Fe_3O_4 are thermodynamically unstable in air and tend to be covered with a layer of α-Fe_2O_3, the evidence in this instance supports the fact that our freshly crushed FeO powder surface was covered in a layer of Fe_3O_4. Upon etching, the peaks shifted to a lower binding energy and the satellite peak previously observed disappeared, to be replaced by one at a lower binding energy approximately 6 eV above the Fe $2p_{3/2}$ peak maximum. This occurred after etching for less than 1 min. Further etching did not result in a further shift in the binding energy values of the maxima of the Fe $2p_{3/2}$ and Fe $2p_{1/2}$ peaks, but the low binding energy peak shoulders due to the formation of Fe^0 were quickly observed, as witnessed by figure 5. From these results we believe the spectrum of figure 1(B) to be characteristic of an FeO surface. The binding energies of the

Fe $2p_{3/2}$ and Fe $2p_{1/2}$ peaks are 709.6 eV and 722.9 eV respectively. This is in good agreement with Brundle *et al* (1977), who give a value of 709.7 eV for the more intense peak, but the values of 710.3 eV and 723.8 eV reported by Allen *et al* (1974) are considerably higher.

From the satellite peaks observed on the etched and unetched FeO surfaces together with satellite peaks observed on the other oxide samples it was evident that a satellite occurring at approximately 8.0 eV above the Fe $2p_{3/2}$ peak is characteristic of an Fe^{III} species, while the occurrence of a satellite at approximately 6.0 eV above the Fe $2p_{3/2}$ peak is characteristic of an Fe^{II} species. Brundle *et al* (1977) observed Fe^{II} and Fe^{III} satellites at 6.0 eV and 8.5 eV above the Fe $2p_{3/2}$ peak respectively, lending good support to the results obtained in the present study.

The two peaks observable in the O 1s spectrum of the air-exposed FeO surface shown in figure 3(*c*) are of almost equal intensity. The maxima of the peaks occur at 531.4 eV and 530.1 eV, the combination of peaks having a FWHM of 3.5 eV. The peak due to the adsorbed species disappeared rapidly upon etching, leaving the oxide peak at 530.1 eV with a FWHM of 2.2 eV.

4.2. *Fe_3O_4—magnetite*

The Fe 2p spectrum of air-exposed Fe_3O_4 powder surface is shown in figure 1(C). Again the results indicate that air oxidation of the surface to α-Fe_2O_3 had not occurred. The Fe $2p_{3/2}$ and Fe $2p_{1/2}$ binding energy values are 710.8 eV and 724.7 eV respectively. The value of 710.8 eV agrees well with that of 711.0 eV due to Allen *et al* (1974) for an ion etched magnetite mineral surface, although they find the value for Fe_3O_4 powder to be identical to that for α-Fe_2O_3 (711.4 eV) even after heating the Fe_3O_4 sample under vacuum to decompose the surface layer of α-Fe_2O_3. Argon ion etching the Fe_3O_4 surface for a few minutes caused a shifting of the Fe $2p_{3/2}$ and Fe $2p_{1/2}$ peaks to the lower binding energy values of 709.6 eV and 722.9 eV respectively. These values are identical to those established for an FeO surface, indicating that a reduction of the Fe^{III} ions present in Fe_3O_4 to Fe^{II} had taken place. Further etching did not result in any further change in the binding energy values of the maxima of these peaks, although the peak due to the further reduction to Fe^0 soon became clearly visible.

The O 1s spectrum of the air-exposed Fe_3O_4 is dominated by the peak due to the hydroxyl oxygen occurring at a binding energy of 531.4 eV, as is evident from figure 3(B). The peak due to oxide is observable as a shoulder on the low binding energy side of the main peak, combining to give a broad peak of width 3.8 eV. The peak due to the adsorbed species disappeared rapidly upon etching, in common with the spectra examined for the other oxides.

4.3. *α-Fe_2O_3*

The Fe 2p spectrum of an α-Fe_2O_3 powder surface is shown in figure 1(D). The Fe $2p_{3/2}$ peak has a binding energy of 711.6 eV and that due to the Fe $2p_{1/2}$ peak is 725.1 eV. This is in good agreement with the previously published results of 711.5 eV due to Carver *et al* (1972) and 711.4 eV due to Allen *et al* (1974) and in reasonable agreement with that of 711.2 eV reported by Brundle *et al* (1977). A small Fe^{III} satellite peak is observable in the spectrum centred at approximately 8.0 eV above the Fe $2p_{3/2}$ peak. Figure 6 shows the effect of argon ion bombardment on the α-Fe_2O_3 Fe 2p spectrum. The peaks showed a shift to lower binding energies after etching for less than 1 min. Further etching for up

to 1 h duration produced no further shift in the peaks, the Fe $2p_{3/2}$ and Fe $2p_{1/2}$ binding energy values remaining at 710.0 eV and 723.3 eV respectively. This is in contrast to Fe_3O_4 for which the results indicated that a full reduction of the Fe^{III} ions to Fe^{II} had occurred within only 5 min of ion etching.

The O 1s spectrum of the α-Fe_2O_3 samples was dominated by the oxide peak at 529.9 eV. The peak due to adsorbed water was observable as a shoulder on the high binding energy side of the oxide peak (figure 3). This shoulder diminished rapidly upon etching.

4.4. Fe metal

Figure 2 shows the Fe 2p spectra recorded for Fe metal. The spectrum in figure 2(A) corresponding to the air-exposed oxidised surface is virtually identical to that of figure 1(C) for an Fe_3O_4 surface, indicating the presence of a layer of this oxide on the surface. Argon ion etching rapidly produced the narrow intense peaks due to Fe metal as shown in figure 2(B). The measured binding energy values of the Fe $2p_{3/2}$ and Fe $2p_{1/2}$ peaks are 706.5 eV and 719.7 eV respectively. Identical values were obtained for work carried out on iron surfaces oxidised under both static and tribological conditions not discussed here. These values are considerably lower than those reported in earlier studies by Allen *et al* (1974) and Fadley (1972) of 707.3 eV and 720.3 eV, and by Brundle *et al* (1972) who quote a value of 707.0 eV for the more intense Fe $2p_{3/2}$ peak.

Figure 3(E) shows the O 1s spectrum of an air-exposed iron surface. The maxima of the two peaks are clearly visible, although the higher binding energy peak is more intense. In this case the higher binding energy peak is approximately 2 eV above the photoelectron peak due to the oxide, in contrast to the separation of approximately 1 eV observed for the oxide powder surfaces. This clearly indicates a different adsorbed species to that present on the oxide powder surfaces, and has tentatively been attributed to the presence of adsorbed oxygen by Allen *et al*.

5. Conclusions

The characteristic core-level photoelectron spectra for FeO, Fe_3O_4 and α-Fe_2O_3 oxide powder surfaces and for an Fe metal surface have been obtained. The binding energies of the photoelectron peaks have been measured and those due to Fe can be used to provide an identification of Fe^{II} and Fe^{III} species and of iron oxides themselves. The use of the more intense Fe $2p_{3/2}$ and Fe $2p_{1/2}$ peaks plus associated satellite peaks are particularly useful for this purpose.

The O 1s spectra of the oxide surfaces invariably consisted of two overlapping peaks. The lower binding energy peak was due to the oxygen atoms in the oxide, and had an almost invariant binding energy with a mean value of around 530.1 eV. For this reason it cannot be used in the identification of iron oxides. The higher binding energy peak at around 531.4 eV was due to oxygen atoms present in a contaminant layer.

Etching the oxide surfaces with Ar^+ ions leads to a rapid reduction of Fe^{III} species to Fe^{II}, and of further reduction to Fe^0. Results indicate that etching of an Fe_3O_4 powder surface under the conditions stated in the report results in a complete reduction of Fe^{III} to Fe^{II} after only a few minutes. Beam effects such as this should be taken into account when using XPS to identify successive layers of an oxide which have been stripped away by ion beam etching.

References

Allen G C, Curtis M T, Hooper A J and Tucker P M 1974 *J. Chem. Soc.* 1525–30
Asami K, Hashimoto K and Shimodaira S 1976 *Corrosion Sci.* **16** 35–45
Brundle C R, Chuang T J and Wandelt K 1977 *Surface Sci.* **68** 459–68
Evans S, Pritchard R G and Thomas J M 1978 *J. Electron Spectrosc.* **14** 341–52
Carver J C, Schweitzer G K and Carlson T A 1972 *J. Chem. Phys.* **57** 973–82
Fadley C S 1972 *Electron Spectroscopy* ed. D A Shirley (Amsterdam: North Holland) pp 781–801
Frost D C, McDowell C A and Woolsey J S 1974 *Mol. Phys.* **27** 1473–89
Reilman R F, Msezane A and Manson S T 1976 *J. Electron Spectrosc.* **8** 389–96
Scofield J H 1976 *J. Electron Spectrosc.* **8** 129–38